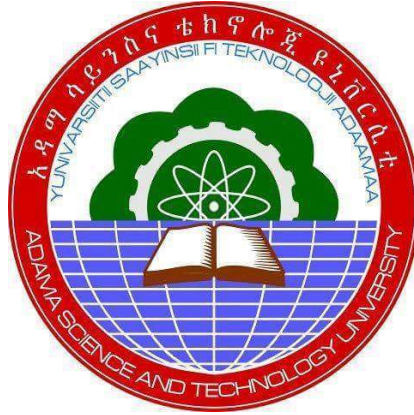


COMPUTATIONAL ANALYSIS OF BOUNDARY LAYER FLOW OF  
MAGNETIC NANOFUID WITH HEAT AND MASS TRANSFER  
CHARACTERISTICS



Feleke Buta Tadesse

A Dissertation Submitted to the Department of Applied Mathematics  
School of Applied Natural Sciences

Presented in Fulfillment of the Requirement for the Degree of Doctor of Philosophy in  
Applied Mathematics(Specialization in Computational Fluid Dynamics)

Office of Graduate Studies  
Adama Science and Technology University

August, 2022  
Adama, Ethiopia

COMPUTATIONAL ANALYSIS OF BOUNDARY LAYER FLOW OF MAGNETIC  
NANOFLUID WITH HEAT AND MASS TRANSFER CHARACTERISTICS

Feleke Buta Tadesse

Supervisor: Oluwole Daniel Makinde (Professor)

Co-Supervisor: Lemi Guta Enyadene (PhD)

A Dissertation Submitted to the Department of Applied Mathematics  
School of Applied Natural Sciences

Presented in Fulfillment of the Requirement for the Degree of Doctor of Philosophy in  
Applied Mathematics(Specialization in Computational Fluid Dynamics)

Office of Graduate Studies  
Adama Science and Technology University

August, 2022  
Adama, Ethiopia

## Declaration

I declare that "Computational Analysis of Boundary Layer Flow of Magnetic Nanofluid with Heat and Mass Transfer Characteristics" is my own work, that it has not been submitted before for any degree or examination at any other university, and that all sources I have used or quoted have been indicated and acknowledged by complete references.

Mr. Feleke Buta Tadesse  
Name of Student

\_\_\_\_\_  
Signature

\_\_\_\_\_  
Date



# Approval Page

We hereby certify that the recommendations and suggestions made by the board of examiners are appropriately incorporated into the final version of the dissertation entitled **”Computational Analysis of Boundary Layer Flow of Magnetic Nanofluid with Heat and Mass Transfer Characteristics”** and developed by Feleke Buta Tadesse.

<u>Professor Oluwole Daniel Makinde</u>		
Main Supervisor	Signature	Date

<u>Dr. Lemi Guta Enyadene</u>		
Co-Spervisor	Signature	Date

We, the undersigned, members of the Board of Examiners of the dissertation open defense by Feleke Buta Tadesse have read and evaluated the dissertation entitled **”Computational Analysis of Boundary Layer Flow of Magnetic Nanofluid with Heat and Mass Transfer Characteristics”** and examined the candidate during open defense. This is, therefore, to certify that the dissertation is accepted for partial fulfillment of the requirement of the degree of Doctor of Philosophy in Applied Mathematics.

Chairperson	Signature	Date
-------------	-----------	------

Internal Examiner 1	Signature	Date
---------------------	-----------	------

Internal Examiner 2	Signature	Date
---------------------	-----------	------

External Examiner 1	Signature	Date
---------------------	-----------	------

External Examiner 2	Signature	Date
---------------------	-----------	------

Finally, approval and acceptance of the dissertation is contingent upon submission of its final copy to the Office of Postgraduate Studies (OPGS) through the candidate’s Department Graduate Council (DGC) and School Graduate Committee (SGC).

Department Head	Signature	Date
-----------------	-----------	------

School Dean	Signature	Date
-------------	-----------	------

Office of Postgraduate Studies, Dean	Signature	Date
--------------------------------------	-----------	------

# ACKNOWLEDGEMENTS

This work was successful with the help of the almighty God. Glory be to His name . I would like to express my sincere gratitude and appreciation to my first supervisor, Professor Oluwole Daniel Makinde, who painstakingly guided and directed the study at a time when he could barely make any time for anything else than his work. I must admit that without him, this far was difficult to reach. His guidance during the program was excellent, and it is my hope that he will continue to lend his vast experience and knowledge to me even after this program. God will pay you back, and I will always pray that He blesses him abundantly as he continues helping other students.

I also wish to thank my second supervisor, Dr. Lemi Guta Enyadene. His unwavering support and advice during the program cannot be over appreciated.

I extend my sincere thanks to my family, my wife, Hirut Gebreegziabher, and our kids, Afomia Feleke and Eyuel Feleke, for their moral support, patience, and unconditional love.

Furthermore, I would like to express my gratitude to my best friend, Dr. Getachew Teshome, for his overall valuable support from the beginning of the study; Shambel Tadesse for his support during the study time; all my best friends and staff of the applied Mathematics department that supported and encouraged me when I needed it the most.

Finally, I am also grateful for the financial support of Adama Science and Technology University as well as for sponsoring my PhD study.

# Dedication

It is dedicated to my family.

## Abstract

*Due to the advancement of thermal devices in engineering systems, the utilization of nanofluid has been playing a vital role in the process of cooling electronic devices and heat transfer enhancement in many industrial manufacturing processes. Thus, the study of a boundary layer flow of a magnetic nanofluid has gained considerable interest owing to its extensive engineering applications. Therefore, in this dissertation, the combined applications of boundary layer flow of magnetic nanofluid and porous medium (Darcian and non-Darcian porous medium) in the process of heat and mass transfer enhancement cases are investigated. Following this, computational analysis is done on specific fluid flow problems such as mixed convection flow of a radiating magnetic nanofluid past a convectively heated stretching/shrinking sheet in Darcian porous medium, Magnetite Ferrofluid ( $Fe_3O_4-H_2O$ ) flow past a convectively heated permeable stretching/shrinking sheet in a Darcy-Forchheimer porous medium and temporal stability analysis of unsteady slip flow of chemically reactive and radiative magnetic nanofluid past a convectively heated permeable stretching/shrinking sheet in a non-Darcian porous medium. Using appropriate similarity transformations the governing nonlinear partial differential equations are converted into a system of nonlinear ordinary differential equations and then solved numerically using the shooting method with Runge-Kutta-Fehlberg fourth-fifth order integration procedure in MAPLE software. Dual solutions are observed numerically, and their characteristics are analyzed through a hydrodynamic stability analysis. The effects of the pertinent parameters on velocity, temperature, and species concentration profiles are discussed thoroughly. Furthermore, the effects of these parameters on the skin friction coefficient, the Nusselt number, and the Sherwood number are analyzed through graphs and tables. The stability analysis indicates that a stable and physically realizable solution appeared in the upper branch solutions, whereas the second solution is unstable. Moreover, a positive smallest eigenvalue in the upper branch solutions is obtained*

**Keywords:** Stagnation point flow; Porous medium; Shrinking/Stretching sheet; Convective heating; Dual Solutions; Magnetic Nanofluid; Stability analysis.

## List of Publications

This PhD dissertation contributed the following original papers which were published (to be published) in peer reviewed journals and indexed in Scopus to the scientific community in the field of applied mathematics.

1. Tadesse, F. B., Makinde, O. D., & Enyadene, L. G. (2021). Mixed Convection of a Radiating Magnetic Nanofluid past a Heated Permeable Stretching/Shrinking Sheet in a Porous Medium. *Mathematical Problems in Engineering*, 2021.  
<https://doi.org/10.1155/2021/6696748>
2. Tadesse, F. B., Makinde, O. D., & Enyadene, L. G. (2021). Hydromagnetic stagnation point flow of a magnetite ferrofluid past a convectively heated permeable stretching/shrinking sheet in a Darcy-Forchheimer porous medium. *Sadhana*, 46(3) 1-17.  
<https://doi.org/10.1007/s12046-021-01643-y>
3. Temporal Stability Analysis of Unsteady Slip Flow of Magnetic Nanofluid Past a Heated Permeable Stretching/Shrinking Sheet in a Non-Darcian Porous Medium. (Submitted)

# Contents

Declaration	i
Recommendation	ii
Approval Sheet	iii
Acknowledgements	iv
Dedication	v
Abstract	vi
List of Publications	vii
Table of Contents	x
List of Tables	xi
List of Figures	xv
Nomenclatures	xvi
<b>1 Introduction to the Dissertation</b>	<b>1</b>
1.1 Background of the Study . . . . .	1
1.1.1 Magnetohydrodynamic and its Applications . . . . .	1
1.1.2 Heat and Mass Transfer . . . . .	3
1.1.3 Viscous Dissipation . . . . .	7
1.1.4 Chemical Reaction . . . . .	7
1.1.5 Slip Boundary Condition . . . . .	8
1.1.6 Porous Medium . . . . .	9
1.1.7 Nanofluid and its Applications . . . . .	10
1.2 Statement of the Problem . . . . .	13
1.3 Objectives of the Study . . . . .	14
1.3.1 General Objective of the Study . . . . .	14
1.3.2 Specific Objectives of the Study . . . . .	14
1.4 Significance of the Study . . . . .	15

1.5	Scope of the Study . . . . .	15
1.6	Organization of the Dissertation . . . . .	16
<b>2</b>	<b>Literature Review</b>	<b>17</b>
2.1	Boundary Layer Flow . . . . .	17
2.2	Boundary Layer Flow Past a Stretching/Shrinking Sheet . . . . .	19
2.3	Boundary Layer Flow in a Porous Medium . . . . .	24
2.4	Stagnation Point flow of Magnetic Nanofluid Flow in a Porous Medium . . . . .	25
<b>3</b>	<b>Research Methodology</b>	<b>29</b>
3.1	Governing Equations . . . . .	29
3.1.1	The Continuity Equation . . . . .	29
3.1.2	The Momentum Equation (Navier-Stokes Equation) . . . . .	30
3.1.3	The Energy Equation . . . . .	33
3.1.4	The Species Concentration Equation . . . . .	39
3.2	Methods of Solution . . . . .	40
3.2.1	Computational Techniques for Solving BVPs . . . . .	41
<b>4</b>	<b>Mixed Convection Flow of a Radiating Magnetic Nanofluid Past a Heated Permeable Stretching/Shrinking Sheet in a Porous Medium</b>	<b>45</b>
4.1	Introduction . . . . .	45
4.2	Mathematical Model Formulation . . . . .	46
4.3	Similarity Transformation . . . . .	52
4.4	Important Engineering Parameters . . . . .	58
4.5	Numerical Procedures . . . . .	59
4.6	Results and Discussion . . . . .	60
4.6.1	Velocity Profiles with Parameter Variations . . . . .	61
4.6.2	Temperature Profiles with Parameter Variations . . . . .	63
4.6.3	Nanoparticle Volume Fraction Profiles with Parameter Variations . . . . .	65
4.6.4	Skin Friction, Reduced Nusselt and Reduced Sherwood Number . . . . .	66
4.6.5	Dual Solutions . . . . .	69
<b>5</b>	<b>Magnetite Ferrofluid flow Past a Convectively Heated Permeable Stretching/Shrinking Sheet in a Darcy-Forchheimer Porous Medium</b>	<b>72</b>

5.1	Introduction . . . . .	72
5.2	Mathematical Model Formulation . . . . .	73
5.3	Similarity Transformation . . . . .	77
5.4	Important Engineering Parameters . . . . .	81
5.5	Stability Analysis . . . . .	82
5.6	Numerical Procedures . . . . .	85
5.7	Results and Discussion . . . . .	86
<b>6</b>	<b>Temporal Stability Analysis of Unsteady Slip Flow of Magnetic Nanofluid Past a Heated Permeable Stretching/Shrinking Sheet in a Non-Darcian Porous Medium</b>	<b>98</b>
6.1	Introduction . . . . .	98
6.2	Mathematical Model Formulation . . . . .	99
6.3	Similarity Transformation . . . . .	102
6.4	Important Engineering Parameters . . . . .	108
6.5	Stability Analysis . . . . .	109
6.6	Numerical Procedures . . . . .	112
6.7	Results and Discussion . . . . .	112
<b>7</b>	<b>Summary, Conclusion and Recommendation</b>	<b>125</b>
7.1	Summary . . . . .	125
7.2	Conclusion . . . . .	126
7.3	Recommendation and Suggestions for Future Research . . . . .	129
7.3.1	Recommendation . . . . .	129
7.3.2	Suggestions for Future Research . . . . .	129
	<b>References</b>	<b>131</b>
	<b>Appendix</b>	<b>158</b>

# List of Tables

4.6.1 Computations showing the effects of buoyancy, magnetic, viscous dissipation, convective heating and stretching/shrinking parameters on dimensionless temperature, shear stress, heat and mass transfer rates when $Pr = 6.2, Le = 3, Nb = Nt = 0.3, Nc^* = 0.1, R = 0.1, Da = 1, S = 0.1$ . . .	68
4.6.2 Computations showing the effects of Brownian, suction/injection, thermophoresis, convective mass transfer, radiation and the porous media parameters on dimensionless temperature, shear stress, heat and mass transfer rates when $Pr = 6.2, Le = 0.1, Nr = 1, M = 1, Ec = Nc = \lambda = 0.1$	69
4.6.3 Computation showing critical shrinking parameter( $\lambda_c$ ) when $Pr = 6.2$ .	70
4.6.4 Comparison of values for skin friction and Nusselt number for different values of $\lambda$ and $Nr$ with $M = 1, Ec = 0.1, Nc = 1$ for the case of $Da = Nc^* = \infty, R = 0, S = 0$ . . . . .	71
5.2.1 Nanoparticle and base fluid thermophysical properties . . . . .	77
5.7.1 The computation showing $Re_x^{1/2}C_f$ and $Re_x^{-1/2}Nu$ for different stretching/shrinking parameter value with $Pr = 1$ for $\phi = 0$ (Regular fluid), $M = 0, S = 0, Da = \infty, F_n = 0, Bi = \infty, Ec = 0$ . . . . .	87
5.7.2 The computation showing skin friction and critical shrinking parameter for various values of $\phi$ and $\lambda$ when $M = 0.1, S = 1, Da = 0.5, F_n = 1$ . . .	90
5.7.3 The computation showing impact of parameters variation on skin friction and critical shrinking parameter for $Fe_3O_4 / H_2O$ when $\phi = 0.1$ . . . . .	91
5.7.4 The computation of smallest eigenvalue ( $\beta$ ) for both lower and upper branch solutions for $Fe_3O_4 / H_2O$ . . . . .	96
6.7.1 The computation showing impact of parameters variation on the skin friction and the critical shrinking parameter . . . . .	120
6.7.2 The computation of smallest eigenvalue ( $\beta$ ) for both lower and upper branch solutions . . . . .	121

# List of Figures

1.1.1 Interaction among magnetic field, Current and plasma flow. . . . .	2
1.1.2 Nanofluids synthesis . . . . .	11
2.1.1 Boundary layer flow( <a href="https://www.grc.nasa.gov">https://www.grc.nasa.gov</a> ) . . . . .	18
4.2.1 Flow diagram of the model . . . . .	47
4.6.1 (a) Influence of $Nr$ and $M$ on the velocity profile (b) Influence of $Da$ and $S$ on the velocity profile. . . . .	62
4.6.2 (a) Influence of $\lambda$ on the velocity profile (b) Influence of $Nc$ on the velocity profile. . . . .	62
4.6.3 (a) Influence of $\lambda$ and $M$ on the temperature profile (b) Influence of $Da$ and $\delta$ on the temperature profile. . . . .	63
4.6.4 (a) Influence of $Nr$ on the temperature profile (b) Influence of $R$ and $Ec$ on the temperature profile. . . . .	64
4.6.5 (a) Influence of $\lambda$ and $M$ on the concentration profile (b) Influence of $Nt$ and $Nb$ on the concentration profile. . . . .	65
4.6.6 (a) Variation of skin friction with $M$ for different values of $Nr$ and $R$ (b) Variation of skin friction with $Nc$ for different values of $Nb$ and $S$ . . . . .	66
4.6.7 (a) Variation of reduced Nusselt number with $M$ for different values of $Nr$ and $\lambda$ (b) Variation of reduced Nusselt number with $Nc$ for different values of $Nb$ and $S$ . . . . .	67
4.6.8 (a) Variation of $Sh$ with $M$ for different values of $Nr$ and $R$ (b) Variation of $Sh$ with $Nt$ for different values of $Nb$ and $Nr$ . . . . .	67
4.6.9 (a) Impact of $M$ on $\lambda_c$ and skin friction. (b) Impact of $Da$ on $\lambda_c$ and skin friction. . . . .	70
5.2.1 Flow diagram of the model. . . . .	74
5.7.1 (a) Variation of skin friction for different values of magnetite nanoparticle volume fraction, $\phi$ (b) Variation of skin friction for different values of suction parameter, $S$ . . . . .	87
5.7.2 (a) Variation of skin friction for different values of porous media parameter, $Da$ (b) Variation of skin friction for different values of magnetic field parameter, $M$ . . . . .	88

5.7.3 (a) Variation of skin friction for different values of second-order porous resistance parameter, $F_n$ (b) Variation of skin friction for different values of injection parameter, $S$ . . . . .	88
5.7.4 (a) Dual solution for velocity profiles with nanoparticles concentration, $\phi$ . (b) Dual solution for velocity profiles with suction parameter, $S$ . . .	89
5.7.5 (a) Dual solution for velocity profiles with porous media parameter, $Da$ . (b) Dual solution for velocity profiles with magnetic field parameter, $M$ . . .	89
5.7.6 (a) Dual solution for velocity profiles with shrinking parameter, $\lambda$ . (b) Dual solution for velocity profiles with second-order porous resistance parameter, $F_n$ . . . . .	90
5.7.7 (a) Dual solution for temperature profiles with nanoparticles concentration, $\phi$ (b) Dual solution for temperature profiles with viscous dissipation, $Ec$ . . . . .	92
5.7.8 (a) Dual solution for temperature profiles with porous medium parameter, $Da$ (b) Dual solution for temperature profiles with second-order porous resistance parameter, $F_n$ . . . . .	92
5.7.9 (a) Variation of local Nusselt number for different values of magnetite nanoparticle volume fraction, $\phi$ (b) Variation of local Nusselt number for different values of suction parameter, $S$ . . . . .	95
5.7.10 (a) Variation of local Nusselt number for different values of porous media parameter, $Da$ (b) Variation of local Nusselt number for different values of second-order porous resistance parameter, $F_n$ . . . . .	95
5.7.11 Heat transfer enhancement rate with nanoparticles concentration when $S = F_n = 1, Bi = Ec = M = 0.1, Da = 0.5$ . . . . .	96
6.2.1 Flow diagram of the model. . . . .	100
6.7.1 (a) Variation of skin friction for different values of unsteadiness parameter, $A$ (b) Variation of skin friction for different values of porous medium parameter, $Da$ . . . . .	113
6.7.2 (a) Variation of skin friction for different values of second-order porous resistance parameter, $F_n$ (b) Variation of skin friction for different values of slip parameter, $\gamma$ . . . . .	114

6.7.3 (a) Variation of skin friction for different values of suction parameter, $S$	
(b) Variation of skin friction for different values of Magnetic field parameter, $M$	114
6.7.4 (a) Dual solution for velocity profiles with unsteadiness parameter, $A$ .	
(b) Dual solution for velocity profiles with porous medium parameter, $Da$ .	115
6.7.5 (a) Dual solution for velocity profiles with second-order porous resistance parameter, $F_n$ .	
(b) Dual solution for velocity profiles with velocity slip parameter, $\gamma$ .	115
6.7.6 (a) Dual solution for velocity profiles with suction/injection parameter, $S$ .	
(b) Dual solution for velocity profiles with Magnetic field parameter, $M$ .	116
6.7.7 (a) Dual solution for temperature profiles with porous medium parameter, $Da$	
(b) Dual solution for temperature profiles with unsteadiness parameter, $A$ .	116
6.7.8 (a) Dual solution for temperature profiles with radiation parameter, $R$	
(b) Dual solution for temperature profiles with Magnetic field, $M$ .	117
6.7.9 (a) Dual solution for temperature profiles with viscous dissipation, $Ec$	
(b) Dual solution for temperature profiles with suction/injection parameter, $S$ .	117
6.7.10 (a) Influence of $Nt$ and $Nb$ on the concentration profile	
(b) Influence of $\delta$ and $Sc$ on the concentration profile.	118
6.7.11 (a) Influence of $A$ and $\lambda$ on the concentration profile	
(b) Influence of $S$ and $\gamma$ on the concentration profile.	118
6.7.12 (a) Variation of local Nusselt number for different values of porous medium parameter, $Da$	
(b) Variation of local Nusselt number for different second-order porous resistance parameter, $F_n$	119
6.7.13 (a) Variation of local Nusselt number for different values of unsteadiness parameter, $A$	
(b) Variation of local Nusselt number for different values of velocity slip parameter, $\gamma$ .	119
6.7.14 (a) Variation of local Nusselt number for different values of suction/injection, $S$	
(b) Smallest eigen value $\beta$ for various values of, $\lambda$ .	120

6.7.15(a) Variation of local Sherwood number for different values of  $S$  and  $A$

(b) Variation of local Sherwood number for different values of  $Da$  and  $Fn$ <sup>121</sup>

## Nomenclatures

$a$ Constant	$Ra_x$ Local Rayleigh number
$B_0$ Magnitude of magnetic field	$Pr$ Prandtl number
$D_B$ Brownian diffusion coefficient	$Le$ Lewis number
$D_T$ Thermophoresis diffusion coefficient	$Nc$ Convective parameter
$\phi$ Dimensionless nanoparticle volume fraction	$T$ Temperature
$k$ Effective thermal conductivity of nanofluid	$T_f$ Local fluid temperature
$h_f$ Heat transfer coefficient	$T_\infty$ Ambient temperature
$k_p$ Thermal conductivity of nanoparticles	$f$ Dimensionless stream function
$k_f$ Thermal conductivity of base fluid	$g$ Acceleration due to gravity
$Nb$ Brownian motion parameter	$U_\infty$ External velocity
$Nu$ Reduced Nusselt number	$u, v$ Velocity components along $x$ and $y$ -axis
$Sh$ Reduced local Sherwood number	$x, y$ Coordinate along the plate and normal to it
$K$ Porous medium permeability	
$k^*$ Mean absorption coefficient	
$q_w''$ Wall heat flux	
$q_m''$ Wall mass flux	

### Greek symbols

$\beta$ Volumetric thermal expansion coefficient	$(\rho C)_p$ Heat capacity of the nanoparticle
$\alpha_f$ Thermal diffusivity of fluid	
$\lambda$ Stretching/shrinking parameter	$\theta$ Dimensionless temperature
$C$ Nanoparticle volume fraction	$\psi$ Stream function
$C_w$ Nanoparticle volume fraction at the wall	$\sigma$ Electrical conductivity
$\eta$ Similarity variable	

# Chapter 1

## Introduction to the Dissertation

### 1.1 Background of the Study

In this chapter, basic definitions of the physical properties in fluid flow needs to describe the boundary layer flow of magnetic nanofluid with heat and mass transfer characteristics is introduced. Along with the fundamental laws of conservation, they can be used to solve specific problems related to fluid flow problems in different physical conditions.

#### 1.1.1 Magnetohydrodynamic and its Applications

Fluid dynamics, like the study of any other branches of science, need mathematical analysis as well as experimentation. The analytical approach helps us finding the solution of certain idealized and simplified problems and understands the unity behind apparently dissimilar phenomena as stated by [Chand \(2017\)](#). The field is very vast and has given birth to other subjects like meteorology, Newtonian flows, non-Newtonian flows, gas dynamics and magnetohydrodynamics (MHD), etc.

Magnetohydrodynamic (MHD) denotes the study of the dynamics of electrically conducting fluids in a magnetic fields. The field of MHD was initiated by the Swedish Physicist Hannes Olof Alfvén (1908-1995), who received the Nobel Prize in Physics in 1970 for fundamental work and discoveries in magnetohydrodynamics with fruitful applications in different parts of plasma physics ([Falthammar, 1997](#)). MHD establishes a coupling between the Navier-Stokes equations for fluid dynamics and Maxwell's for electromagnetism. The main concept behind magnetohydrodynamics is that magnetic fields can induce currents in a moving electrically conductive fluids but non-magnetic fluids such as liquid sodium, electrolytes, molten salts, plasmas (highly ionized gases), among others as mentioned by [Sarojini et al. \(2013\)](#) and [Zakaria et al. \(2009\)](#) which in turn creates forces on the fluid and influence the magnetic field itself. This makes the problem highly nonlinear.

Faraday discovered the law of electromagnetic induction in 1831 and gave its mathematical description which is the production of an electromotive force (emf) across a conductor when it is exposed to a time varying magnetic field ([Davidson, 2002](#)). The

fundamental concept behind MHD is that magnetic fields can induce currents in a moving conductive fluid, which in turn creates forces on the fluid and changes the magnetic field itself. As a result, these currents experience a mechanical force, known as Lorentz force, due to the presence of magnetic field which tends to modify the original fluid motion. Thus, the essential feature of the physical situation is the mutual interaction between the fluid motion and magnetic field which forms the basis of all MHD fluid flow problems. Thus, the science of MHD covers several natural phenomena and various engineering processes.

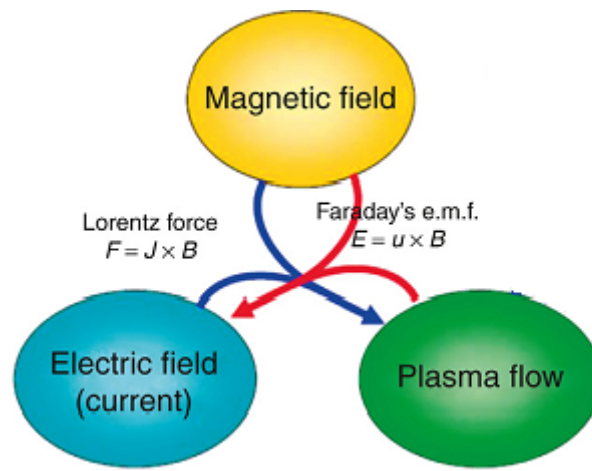


Figure 1.1.1: Interaction among magnetic field, Current and plasma flow.  
(Sheikholeslami and Ganji, 2016)

The principles of MHD are highly relevant in today's engineering processes and biomedical applications; research on methods to target chemotherapy drugs in the human body includes the analysis of bio-compatible magnetic nano carrier systems, for example magnetic liquids such as ferrofluids. Models developed to investigate the effects of an external magnetic field and its interaction with blood flow containing a magnetic carrier substance are based on the principles of MHD which clearly shows the importance of MHD in magnetic drug targeting as explained in the paper by Gupta (2016a).

The most widespread applications of MHD is in metallurgical process viz. electromagnetic stirring, casting and levitation. In casting operations, magnetic fields are used to dampen the motion of the liquid metal to promote a more quiescent process, thus minimizing contamination (Mortuja Sarkar and Sahoo, 2021). Other applications of MHD in metallurgy include, electromagnetic (non-contact) casting of aluminum, vacuum-arc re-melting titanium and nickel-based super alloys, electromag-

netic removal of non-metallic inclusions from melts, electromagnetic launchers and the so called cold-crucible induction melting process, in which the melt is protected from the crucible walls by thin solid crust of its own material. A detailed explanation about MHD applications is obtained in [Davidson \(2002\)](#).

Hartman in 1937 presented an excellent idea which cemented the direction of modern research in MHD flow ([Hartman, 1937](#)). He was the first person who studied the flow of a viscous, incompressible and electrically conducting fluid within a parallel plate channel in the presence of transverse magnetic field. The experimental investigation of modern MHD flow in laboratory was performed by [Hartman and Lazarus \(1937\)](#) who designed a magnetic pump to put mercury in motion in the presence of transverse magnetic field. After these famous investigations, a series of experiments were performed by engineers and applied physicists to study the basic features of MHD flow and to find its applications in fluid engineering, namely, power generation ([Steg and Sutton, 1960](#)), accelerators, induction type pumps used in nuclear reactor ([Blake, 1959](#)), mechanical engineering manufacturing process ([Ryabinin and Khozhainov, 1967](#)) and plasma aerodynamics ([Takenouchi, 1985](#)).

MHD technology is commonly used today by engineers, for instance, in heat transfer systems, in the production of shock absorbers, production of flow meters, process of stirring molten metals during solidification, dampen undesired convection-driven flow during casting, filter out impurities, melt and even levitate metals , petroleum industries, MHD power generator designs, design for cooling of nuclear reactors, and construction of heat exchangers ([Gautam et al., 2020](#)),([Ibrahim and Tulu, 2019](#)), ([Makinde, 2008](#)), ([Griesse and Kunisch, 2006](#)).

### **1.1.2 Heat and Mass Transfer**

Temperature imbalance between layers of fluid or between boundary and the surrounding environment results in temperature variations within the fluid. The temperature gradient within the system may also arise from viscous dissipation, absorption of thermal radiations and release of energy when vaporized fluid condenses ([Seth et al., 2016](#)) and ([Kumar et al., 2017b](#)). The quantity that transfers from one system to another system at lower temperature, by virtue of the temperature difference, when the two are brought into contact is called heat ([Kreith et al., 2011](#)). Heat transfer is considered

as a primary process of energy transportation which forms a foundation for thermal power generation, and is commonly encountered in industrial and engineering systems, namely, chemical and food plants, in designing of power stations, aerodynamic heating, extraction of energy from atomic piles, cooling of high power motors, high speed aircraft, atmospheric re-entry of vehicles, utilization of heat stored in the subterranean layer of the earth, heat exchangers using liquid metal coolant, etc. (Dessie and Kishan, 2014) and (Kumar et al., 2018)

There are three types of thermal energy transport: conduction, convection and radiation. In various types of studies related to heat transfer or thermal transport, considerable effort has been directed in the convection mode, in which heat transfer process takes place with the motion of the fluid.

Conduction is the process of heat transfer by molecular motion, supplemented in some cases by the flow of free electrons, through a body (solid) from a region of high temperature to a region of low temperature (Holman, 2009). Heat transfer by conduction also takes place across the interface between two bodies in contact when they are at different temperature. Conduction is greater in solids, where atoms are in contact. In liquids (except liquid metals) and gases, the molecules are usually further apart, giving a lower chance of molecules colliding and passing on thermal energy. The heat transfer rate must be vanished when the medium is equilibrium.

Conduction heat transfer is described macroscopically by Fourier's law, which is

$$\vec{q} = -k(T)A\nabla T, \quad (1.1.1)$$

where  $\vec{q}$  is the quantity of heat transmitted,  $T$  is the temperature,  $k(T)$  is the transport property known as thermal conductivity,  $A$  is the area through which the heat is flowing,  $\nabla = \vec{i}\frac{\partial}{\partial x} + \vec{j}\frac{\partial}{\partial y} + \vec{k}\frac{\partial}{\partial z}$  is the vector differential operator. The magnitude of thermal conductivity for a given substance mainly depends on its microscopic structure and also tends to vary somewhat with temperature. Metals are usually the best conductors of thermal energy. However, fluids (liquids and gasses), except liquid metals, are not typically good conductors. This is due to the large distance between atoms in a gas: fewer collisions between atoms means less conduction. As density decreases so does conduction. Conductivity of gases increases with temperature but only slightly with pressure near and above atmosphere. Conduction does not occur at all in a perfect

vacuum.

Convection is a mode of heat transfer in fluids, wherein the moving fluid particles carry heat in the form of internal energy (Holman, 2009). Convection arises due to body forces acting within the fluid, e.g. gravity (buoyancy) or surface forces acting at the boundary of the fluid. Convection heat transfer rate is described by Newton's law of cooling, which is

$$\vec{q} = hA(T_f - T), \quad (1.1.2)$$

where  $\vec{q}$  is the quantity of heat transmitted,  $T$  is the temperature,  $h$  is the material property known as convective heat transfer,  $A$  is the area through which the heat is flowing.

Three types of convective heat transfer occur, viz. free or natural convection, forced convection and mixed convection. A convection process, where fluid motion is induced by buoyancy forces resulting from density variation caused by temperature differences in the fluid, is termed free or natural convection while a convection process, where the fluid motion is created by external influences such as pressure drop or an agitator, is known as forced convection. When both the free and forced convections occur simultaneously, the convection process is termed as mixed convection.

Radiation is the energy emitted by matter in the form of electromagnetic waves (or photons) as a result of the changes in the electronic configurations of the atoms or molecules (Holman, 2009). Unlike conduction and convection, the transfer of heat by radiation does not require the presence of an intervening medium. This allows heat to be transferred between two bodies over great distances. In this way the earth receives a large energy flow from the sun. In heat transfer studies we are interested on electromagnetic radiation that is propagated as a result of a temperature difference; this is called thermal radiation (Cengel and Ghajar, 2007). It differs from other forms of electromagnetic radiation such as x-rays, gamma rays, microwaves, radio waves, and television waves that are not related to temperature. All bodies at a temperature above absolute zero emit thermal radiation. The phenomenon of radiative heat transfer is important with regard to various applications in manufacturing design of nuclear power plants and various engineering processes (Kumar et al., 2017a). The proper understanding of mechanism of solar radiation has major importance in the design of advanced energy conversion systems performed at higher temperature. Examples of

such systems include astrophysical flows, space vehicle re-entry, solar power technology and fossil fuel combustion energy (Kumar et al., 2018). The radiation heat transfer phenomenon is described macroscopically by a modified form of the Stefan-Boltzmann law, which is

$$\bar{Q} = \bar{\epsilon}\sigma^*T_s^4, \quad (1.1.3)$$

where  $\bar{Q}$  is the rate at which energy is released per unit area,  $\sigma^*$  is the Stefan-Boltzmann constant and  $\bar{\epsilon}$  is a radiative property of the surface termed emissivity that characterizes how effectively the surface radiates with values in the range of  $0 \leq \bar{\epsilon} \leq 1$  and  $T_s$  is the absolute temperature of the surface. Thermal radiation takes place according to the fourth power of the absolute temperature of the surface. Controlling the effects of radiation in fluid flow and heat transfer problems has vigorous significance in engineering processes, nuclear plants, space vehicles, gas turbines, and satellites involving high temperatures needed in designing specific equipment (Jamil et al., 2020).

Mass transfer is the transport of one or more components of a mixture, of fluid or solid material, within a fluid-fluid interface or a fluid-solid interface. Mass transport within a fluid-fluid interface or a fluid-solid interface is called mass transfer (Baehr and Stephan, 2011). The driving forces for mass transfer are concentration, temperature or pressure gradients. The most common of these three is mass transfer due to a concentration gradient. As experience tells us, the components of a mixture move from regions of higher concentration to those with lower concentration. Equilibrium with respect to mass transfer is realised when the driving force, in this case the concentration difference, has disappeared.

Mathematically mass diffusion can be described by the diffusion equation. This equation is derived from Fick's law, which states that the net movement of diffusing substance from higher concentration to lower concentration, per unit area of cross section (the flux) is proportional to the concentration gradient (Bergman et al., 2011).

$$\vec{J}_A = -D_{AB}\nabla C_A, \quad (1.1.4)$$

where  $\vec{J}_A$  is the molar flux relative to the molar average velocity,  $D_{AB}$  is the mass diffusivity or diffusion coefficient for component  $A$  diffusing through component  $B$  which depends on the diffusing species and the material through which diffusion occurs and  $\nabla C_A$  is the concentration gradient. An analogous statement of Fick's law, for

heat instead of concentration, is Fourier's law.

Mass transfer processes can be found in various ways in both nature and technology. For instance, in highly developed plants and animals there is a circulatory systems which serve the supply of nutrition and energy, separation processes in chemical engineering such as the drying of solid materials, distillation and extraction are all affected by the processes of mass transfer, in the production of materials in order to obtain the desired properties of a substance, and also in chemical reactions including combustion processes are often decisively determined by mass transfer ([Baehr and Stephan, 2011](#)).

### 1.1.3 Viscous Dissipation

The irreversible conversion of mechanical energy to internal energy or heat due to viscous effects is known as viscous dissipation of energy ([Rashad et al., 2014](#)). Viscous dissipation affects heat transfer and temperature distribution in the flow regime by playing a role like an energy source, which leads to affect heat transfer rate and hence it is sometimes important to consider the effects of viscous dissipation in fluid flow and heat transfer problems ([Ibrahim and Tulu, 2019](#)). A fluid flowing past a stretching/shrinking sheet embedded in porous medium gains some velocity as well as kinetic energy and this kinetic energy is converted into the heat energy which leads to the inclusion of porous dissipation term in addition to viscous dissipation term in energy equation ([Kausar et al., 2019](#)).

Viscous dissipation is of significance in natural convection in various devices that are subjected to large variations of gravitational force or that operate at high rotational speeds ([Rashad et al., 2014](#)). Currently, different researchers are investigating MHD boundary layer flows in porous media with the effect of viscous dissipation on free, mixed, and forced convective flows.

### 1.1.4 Chemical Reaction

A fluid flow is affected by chemical reactions that take place in it. When chemical reactions occur either energy is used or dissipated resulting in processes known as endothermic and exothermic reactions ([Jan et al., 2019](#)). Consequently, fluid properties are affected . Boundary layer flow of nanofluid with heat and mass transfer problems in the presence of chemical reaction are of importance in many processes and have,

therefore, received considerable amount of attention in recent times ([Sehra et al., 2021](#)).

Chemical reactions can be modeled as either homogeneous or heterogeneous processes. This depends on whether they occur at an interface or as a single phase volume reaction. A homogeneous reaction is one that occurs uniformly throughout a given phase. The species generation in a homogeneous reaction is the same as an internal source of heat generation. On the other hand, a heterogeneous reaction takes place in a restricted area or within the boundary of a phase. It can therefore be treated as a boundary condition similar to the constant heat flux condition in heat transfer.

The study of heat and mass transfer with chemical reaction is of great practical importance to engineers and scientists because of its universal occurrence in many branches of science and engineering ([Mahdy, 2010](#)). Quite a number of physical phenomena involve free convection driven by heat generation. The study of heat generation in moving fluids is important in view of several physical problems such as those dealing with chemical reactions and those concerned with dissociating fluids. Possible heat generation effects may change the temperature distribution and, therefore, the particle deposition rate. This may occur in such applications related to nuclear reactor cores, fire and combustion modeling, electronic chips and semi conductor wafers. Furthermore, the addition of chemical reaction in the boundary layer flow has huge applications in air and water pollution, fibrous insulation, atmospheric flows and many other chemical engineering problems ([Najib et al., 2014](#)).

### **1.1.5 Slip Boundary Condition**

In many practical problems in Science and Engineering, boundary conditions have an essential role so that a meaningful solution is obtained. The two boundary conditions observed in fluid flow phenomena are boundary conditions with slip and no-slip ([Sehra et al., 2021](#)). If there is no relative motion between the wall and the fluid immediately in contact with the wall, then it is called no-slip boundary condition. This condition is extensively used because it simplifies complex situations, but it has some limitations. If there are some surfaces which are sufficiently smooth where the fluid (liquid) cannot be in contact with the wall and slip against the wall, then it is called slip boundary condition.

In different works the conventional no slip boundary conditions are used at the wall

surface over which fluid flow but there are some situations where no slip conditions lead to unrealistic behavior-for example, the spreading of a liquid on a solid substrates, corner flow and the extrusion of polymer melts from a capillary tube (Thompson and Troian, 1997). No slip condition must be replaced by slip condition when fluid flows around microfluidic and nanofluidic (Nguyen et al., 2019). The slip flow region for the fluid problem is very significant in the era of modern sciences and technology (Jan et al., 2019). Furthermore, in the fluid flow problems slip condition has very important role in industries and chemical sciences (Sehra et al., 2021).

### 1.1.6 Porous Medium

A porous medium is a material consisting of a solid matrix with an interconnected voids (Nield and Bejan, 2017). The fraction of the void space to the total volume is named as porosity. The interconnection of the pores allows the flow of one or more fluids through the material. Natural materials such as sandstone, limestone, beach sand, wood, biological tissues, and human lung and industrially made materials such as ceramics, composite materials, and high porosity metallic foams etc are few examples of porous medium (Nazari et al., 2019). The ability of the fluid to flow across a porous medium is determined by the permeability or porosity of the medium.

Fluid flow in porous media is governed not only by the magnitude of the potential gradient across the media but also the drag forces such as the surface drag(friction), and the form drag (due to solid obstacles) which are experienced by the fluid within the porous media (Noghrehabadi et al., 2013). The Darcy equation accounts for the surface drag only. Darcy's law is generally recognized as the macroscopic equation of motion for Newtonian fluids in porous media at small Reynolds numbers. According to this law the flow is linearly dependent upon the pressure gradient. Mathematically,

$$V = -\frac{K}{\mu}\nabla P, \quad (1.1.5)$$

where  $K$  is the permeability of the porous medium which is to be determined experimentally and has the dimension of length squared and  $\mu$  is the dynamic viscosity. For the case of isotropic porous medium permeability is a scalar and the equation  $V = -\frac{K}{\mu}\nabla P$  can be simplified to  $\nabla P = -\frac{\mu}{K}V$ , which is of potential flow form and is valid when  $K$  is very large (Nield et al., 2006). Under situations in which inertial forces

are dominant, drag force becomes comparable to the surface drag. Forchheimer added a modification term to Darcy equation to account for the pressure drop due to the form drag, which was ignored by Darcy. The Forchheimer-extended Darcy equation is as follows:

$$\nabla P = -\frac{\mu}{K}V - \frac{C_F}{\sqrt{K}}\rho_f|V|V, \quad (1.1.6)$$

where  $C_F$  is a dimensionless form drag constant, and  $\rho_f$  is the density of the fluid (Nield et al., 2006).

Fluid flows through porous media have widespread applications in various areas of science and engineering applications, viz. Purification and filtration processes, seepage of water in river beds, migration of pollutants into the soil and aquifers, drying of porous materials in textile industries, the movement of moisture through and under engineering structures, the saturation of porous materials by chemicals, and heat and mass transport in packed bed reactor columns are among many other applications (Kausar et al., 2019). Moreover the analysis and simulation of momentum and heat transport problems in porous media has many important engineering and geophysical applications such as the prediction of natural convection heat transfer characteristics from heated bodies embedded in a porous medium is crucial to the design of canisters for nuclear wastes disposal (Noghrehabadi et al., 2013).

### 1.1.7 Nanofluid and its Applications

In the world of advanced technology, nanotechnology is considered to be one of the significant forces that contribute to the next major industrial revolution. Nanofluids have been largely studied to mitigate the problem of heat transfer in high technology industries. The term nanofluid has been first proposed by Choi (Choi and Eastman, 1995) to indicate engineered colloids consist of nanoparticles dispersed in a base fluid.

A recent development in fluid mechanics has been the study of nanofluids which possess superior thermal conductivity properties and enhance heat transfer in fluids. Nanofluids are a new class of fluids engineered by dispersing nanometer-sized materials (nanoparticles, nanofibers, nanotubes, nanowires, nanosheets, or droplets) in base fluids. In other words, nanofluids are nanoscale colloidal suspensions containing condensed nanomaterials. They are two-phase systems with one phase (solid phase) in another (liquid phase). Nanofluids have been found to possess enhanced thermophysical

properties such as thermal conductivity, thermal diffusivity, viscosity, and convective heat transfer coefficients compared to those of base fluids like oil or water (Scherer and Figueiredo Neto, 2005).

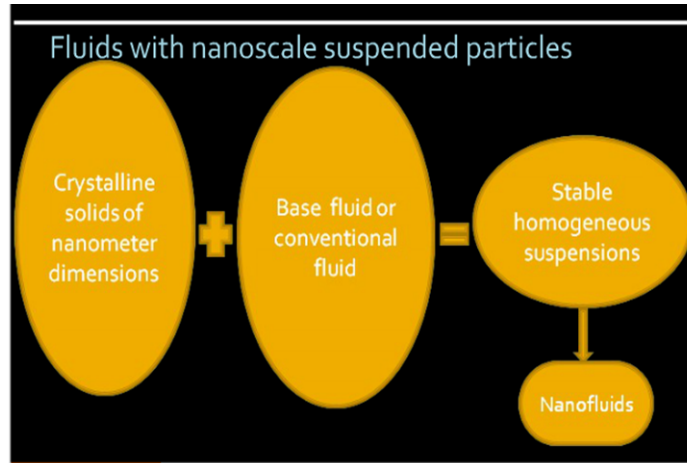


Figure 1.1.2: Nanofluids synthesis

Recently nanofluid has gained significant attention due to its great potential for enhancing the thermal conductivity of the base fluids with a remarkable improvement in the convective heat transfer coefficient. Various researchers have been experimentally and theoretically make a research on the performance of nanofluid. An innovative technique to improve convective heat transfer is to introduce nanoscale particles to the base fluid (Mukhopadhyay, 2012). During the past decades, the technology to make particles in nanometer dimensions was improved and a new kind of solid liquid mixture that is called nanofluid was appeared (Salman et al., 2014).

Convective heat transfer by nanofluid is also one of the current focuses in computational fluid dynamics field in which the percentage of nanoparticles and the types of nanoparticles (thermal conductivity) are the important parameters. Many researchers have devoted their focus to investigate the applicability of the nanofluid which is the new innovation of heat transfer fluid in real engineering applications (Kothandapani and Prakash, 2015).

In nanofluids, it is recognized that nanoparticles do not follow the fluid streamlines passively. In fact, there are some reasons that induce a slip velocity between the nanoparticles and the base fluid. Movements of nanoparticles have significant impact on rheological and thermophysical properties of the nanofluids. Therefore, investigating

the nanoparticles motion is critical for evaluating the performance of nanoparticles inclusion to the base fluid as a heat transfer medium (Lok et al., 2006).

Brownian and thermophoretic diffusivities are the main slip mechanisms in nanofluids as explained by Buongiorno (2006). Brownian diffusion is due to random drifting of suspended nanoparticles in the base fluid which originates from continuous collisions among the nanoparticles and liquid molecules. Thermophoresis induces nanoparticle migration from warmer to colder region (in opposite direction of the temperature gradient), making a non-uniform nanoparticle volume fraction distribution.

A good nanofluid is characterized by high thermal conductivity and low viscosity which was explained by Choi and Eastman (1995). The main reason why nanofluid possess enhanced thermal properties is because of the suspended nanoparticles increase the effective thermal conductivity of the fluid. The key building blocks of nanofluid are nanoparticles, so research on nanofluid become a topic of major contemporary interest because of the development of nanotechnology in general and availability of nanoparticles in particular.

Ferrofluids, are colloidal suspension made up of nanoscale ferromagnetic/paramagnetic nanoparticles suspended in a nonmagnetic base fluid, constitute a special class of nanofluids exhibiting both magnetic and fluid properties (Liu et al., 2009). In these suspensions, also known as smart or functional fluids all features such as fluid flow, particles movement and heat transfer process can be controlled by applying magnetic fields (Odenbach, 2004). However, in these types of fluids, there are chances of aggregation/agglomeration of the particles due to Vander wall interaction and magnetic interaction between the particles. In order to overcome this situation, the nanoparticles are coated by a surfactant layer (Tynjälä et al., 2006). The tiny particles are thoroughly coated with a layer of surfactant. A surfactant is a compound that lowers the surface tension (or interfacial tension) between two liquids or between a liquid and a solid. Surfactants may act as detergents, emulsifying agents and dispersants (Gupta, 2016b).

The most common ferromagnetic particles used in the preparation of ferrofluids are Mn-Zn ferrite, iron and cobalt  $Fe_3O_4$  (Arulmurugan et al., 2006), (Sun and Zeng, 2002). One the unique properties of ferrofluid flow is the flow velocity and heat flow may be controlled by the applied external magnetic fields (Odenbach, 2003) and (Jordan

et al., 1999). The ferrofluid flow is applicable in various fields ranging from medical to engineering processes. Ferrofluid are widely applied in chemotherapy such as localized drug targeting for cancer treatments and hyperthermia (Lübbe et al., 1999) and (Hirgeist et al., 1999), detection of Ammonia (Shen and Liou, 2008), use of magnetic seals in computer hard disk drives, high vacuum systems, chemical plants and oil refineries (Kim et al., 1999), (Liu et al., 2005), in display devices such as CD, DVD players (Raj et al., 1995), in heat transfer in various industrial and commercial applications (Stoian et al., 2003).

## 1.2 Statement of the Problem

The study of magnetic nanofluid flow problems with heat and mass transfer characteristics has a wide range of applications in science and engineering processes. Technology associated with stagnation point flow of magnetic nanofluid is currently finding favor in the manufacturing industries, where it has attracted many experimental and theoretical studies. The main goals of those studies are to improve and enhance the performance of different systems arising from engineering, including lubrication, cooling systems, power generation, etc., and observe how the behavior of the flow varies with the change of embedded parameters.

Several authors have studied boundary layer flow of nanofluid problems with heat and mass transfer characteristics in different domains and orientations. However, the study of the boundary layer flow of magnetic nanofluids in porous media with the consideration of different physical parameters cannot be overlooked and requires critical investigation since the problem of thermal management of heat-generating electronics devices for optimal performance has been an active area of research in recent years. Heat accumulation in electronics devices may lead to operation failure, thermal runaway, and loss of life and properties. Furthermore, due to the nonlinearity occurring in the fluid flow problems, there may be more than one solution; those solutions that exist are difficult to visualize (Raza et al., 2016). This can cause researchers to fail to notice the multiple solutions that might exist within the flows, which is an important aspect of fluid mechanics. Therefore, a mathematical computation and analysis of such a boundary layer flow are required to determine the existence of multiple solu-

tions. Specifically, the boundary layer flow of magnetic nanofluid in a porous medium was investigated in this dissertation.

1. Mixed Convection of a Radiating Magnetic Nanofluid Past a Heated Permeable Stretching/Shrinking Sheet in a Porous Medium.
2. Magnetite Ferrofluid(  $\text{Fe}_3\text{O}_4\text{-H}_2\text{O}$ ) flow Past a Convectively Heated Permeable Stretching/Shrinking Sheet in a Darcy-Forchheimer porous Medium.
3. Temporal Stability Analysis of Unsteady Slip Flow of Magnetic Nanofluid Past a Heated Permeable Stretching/Shrinking Sheet in a Non-Darcian Porous Medium.

The significance of such computational modeling analysis as well as multiplicity of fluid flows as highlighted above leads us to the objectives of the present study as given in the following section.

## **1.3 Objectives of the Study**

### **1.3.1 General Objective of the Study**

The general objective of this study is to present boundary layer flow of magnetic nanofluid with heat and mass transfer characteristics.

### **1.3.2 Specific Objectives of the Study**

The specific objectives of this study are to:

- i.** develop a mathematical model for mixed convection of a radiating magnetic nanofluid past a heated permeable stretching/shrinking sheet in a porous medium
- ii.** formulate a mathematical model for magnetite ferrofluid flow past a convectively heated permeable stretching/shrinking sheet in a Darcy-Forchheimer porous medium
- iii.** develop a mathematical model of unsteady slip flow of magnetic nanofluid past a heated permeable stretching/shrinking sheet in a non-Darcian porous medium
- iv.** determine the effects of embedded parameters on the velocity, temperature and concentration profiles as well as on the skin friction coefficient, the heat transfer rate and the mass transfer rate.

- v. investigate the existence of dual/multiple solutions and establish the temporal stability analysis of the basic flows.

## 1.4 Significance of the Study

The study is significant for the following reasons:

- Help to understand the heat and flow characteristics in metallurgical processing, metal-working processes, operation of heat-exchange apparatus, nuclear reactors and other applications so that the finished product meets the desired quality and specifications.
- Used in the investigation of electrical conductivity, heat transfer characteristics and biomedical applications of different nanofluids in the presence of a magnetic field.
- Used as a supplementary work in the designing process of many industrial applications such as MHD generators, pumps, flow meters, cooling of nuclear reactors, geothermal energy extractors, nuclear waste disposal and heat exchangers.
- Act as a benchmark for further research on boundary layer flow of magnetic nanofluid with heat and mass transfer characteristics and form a base for further studies on related issue.

## 1.5 Scope of the Study

The present study is confined to the problem of two-dimensional steady and unsteady external laminar boundary layer flow with convective heat and mass transfer of a viscous, incompressible, fluid flow along a flat plate (horizontal or vertical) in Darcian and non-Darcian porous media. Some prescribed parameters, such as permeability, velocity slip, thermal convective, radiation, viscous dissipation and porous dissipation, magnetic field, buoyancy ratio, chemical reaction, thermophoresis, Brownian motion, unsteadiness, and suction/injection are included in the study of the boundary layer behavior. For porous media, the governing PDEs are approximated by Darcy and non-Darcy flow models.

The thermophoresis and Brownian motion effects are incorporated into the nanofluids model. The similarity transformations are used to transform similarity equations with boundary conditions. The numerical scheme, the Runge-Kutta-Fehlberg fourth-fifth (RK45) order method, along with the shooting technique, is used to solve the similarity equations. The study finds applications in boundary layer control, in the polymer industry, cooling problems, solar power technology, nuclear reactors, polymeric materials processing, and reducing the drag in aerodynamics, etc. The detailed applications for each problem are given in the relevant chapters.

## **1.6 Organization of the Dissertation**

The remaining parts of the dissertation are organized as follows. Some important related literature reviews are presented in chapter 2. Chapter 3 presents the derivations of fluid flow governing equations based on conservation laws and relevant mathematical tools used for solving boundary value problems. An investigation into the mixed convection of a radiating magnetic nanofluid towards a permeable stretching/shrinking sheet in a porous medium is presented in chapter 4. In chapter 5, a single flow model is used to study magnetite ferrofluid flow past a convectively heated permeable stretching/shrinking sheet in a Darcy-Forchheimer porous medium. Chapter 6 performs a temporal stability analysis of unsteady slip flow of magnetic nanofluid flow over a permeable stretching/shrinking sheet in a non-Darcian porous medium. Finally, the main results of the dissertation and conclusions drawn are presented in chapter 7.

# Chapter 2

## Literature Review

This chapter reviews the studies that have been carried out concerning boundary layer fluid flow under various fluid flow conditions. The first subsection presents studies regarding boundary layer flow in general. The following subsections examine several studies on boundary layer flow of nanofluids past a stretching/shrinking sheet and boundary layer flow in a porous medium.

### 2.1 Boundary Layer Flow

The concept of boundary layer flow, introduced in 1904 by Prandtl, is a popular field of study in fluid mechanics for engineers, physicists, and mathematicians. The concept of boundary layer emphasizes that flows at high Reynolds numbers can be divided up into two unequal regions. In the bulk of the flow region, the viscosity can be neglected, and the flow corresponds to the inviscid limiting solution called the inviscid outer flow. The second region is the very thin boundary layer at the wall where the viscosity must be taken into account [Schlichting and Gersten \(2003\)](#).

Many of Prandtl's papers become a baseline for different works on skin friction, heat transfer, and boundary layer separation. Due to viscous shearing, the fluid velocity immediately adjacent to the surface is zero and the fluid layer next to the surface becomes attached to the surface. This is referred to as the no slip condition [Kundu and Cohen \(2002\)](#).

The layers of fluid above the surface are moving, hence there is shearing taking place between the layers of the fluid, which was examined by [Nisar et al. \(2008\)](#). The wall shear stress, denoted by  $\tau_w$ , is the shear stress acting between the wall and the first moving layer next to it. This thin layer adjacent to the surface of a body or a solid wall in which viscous forces affect the flow is called the boundary layer (shear layer). The boundary layer theory has wide application in numerous problems of fluid dynamics and has provided a powerful tool for the analysis of problems of fluid resistance. A lot of work has been done on the boundary layer theory in view of different scenarios. There are two classical boundary layer flows in the literature. The first one is the flow along a horizontal, motionless plate due to a constant free stream ([Blasius, 1907](#)). The

second is the flow induced by a horizontal plate moving with constant velocity inside a calm fluid (Sakiadis, 1961). The thickness of the boundary layer is a function of the ratio between inertial forces and viscous forces, that is, the Reynolds number. At a low Reynolds number, viscous forces govern the entire boundary layer and the flow is laminar. However, at high Reynolds numbers, inertia forces dominate the boundary layer and the fluid becomes turbulent. Generally, there are two types of boundary layers: hydrodynamic (velocity) boundary layers and thermal boundary layers. The hydrodynamic boundary layer is the region in which the fluid velocity changes from its free stream flow value to zero at the body surface.

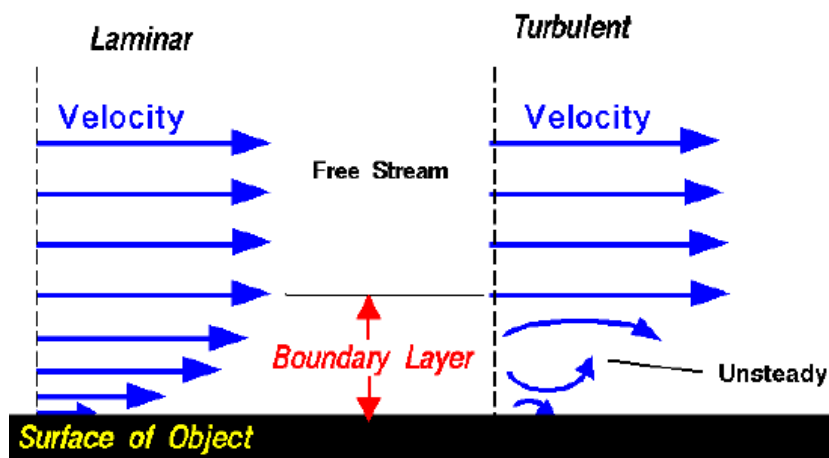


Figure 2.1.1: Boundary layer flow(<https://www.grc.nasa.gov>)

Heat will flow between a wall and the fluid adjacent to it when a temperature gradient is established between the wall and the fluid. Just like the fluid velocity increases from zero at the surface to the mainstream, the temperature changes from that at the wall to that in the free stream. The result is that the fluid temperature adjacent to the wall is assumed to be equal to the surface temperature of the wall at the interface and is equal to the bulk fluid temperature at some point in the fluid. This thin layer near the surface of the body is known as the thermal boundary layer.

Concentration is a measure of how much of a given species is dissolved in another substance per unit volume. A concentration boundary layer manifests itself when a species concentration difference exists between the solid-fluid interface and the free stream region of the fluid. The region in which the species concentration gradient exists is known as the concentration boundary layer. Species transfer takes place through the process of diffusion and convection and is governed by the properties of

the concentration boundary layer as described in [Baag et al. \(2017\)](#).

The drag on ships and missiles, the efficiency of compressors and turbines in jet engines, and the effectiveness of air intakes for ram and turbojets depend on the concept of the boundary layer and its effects on the main flow as reported by [Zeitoun et al. \(2013\)](#).

## 2.2 Boundary Layer Flow Past a Stretching/Shrinking Sheet

The laminar boundary layer flow over a stretching sheet has important industrial applications, for example, in metallurgical processes such as drawing of continuous filaments through quiescent fluids, annealing and tinning of copper wires, wire drawing and continuous casting and levitation. In addition to these, there are a wide range of applications in many engineering processes such as polymer extrusion, manufacturing of plastics and rubber sheets, crystal growing, continuous cooling, fiber spinning, manufacturing of foods and paper, glass fiber production, stretching of plastic films, and many more ([Ibrahim et al., 2013](#); [Makinde et al., 2013](#); [Freidoonimehr et al., 2016](#); [Bhatti et al., 2017](#); [Makinde et al., 2017](#); [Rehman et al., 2017](#); [Jusoh and Nazar, 2018](#); [Sharma et al., 2018](#); [Soid et al., 2018](#); [Waini et al., 2019](#)). During the manufacture of these sheets, the melt issues from a slit and is subsequently stretched to achieve the desired thickness. The final product with the desired characteristics strictly depends upon the stretching rate, the rate of cooling in the process, and the process of stretching ([Veera Krishna, 2020](#)). Related to this facts, [Crane \(1970\)](#) started the study of boundary layer flow of a viscous and incompressible fluid over a linearly stretching sheet (i.e., the velocity of the sheet varies linearly with the distance from a fixed point on the sheet) and obtained a similarity solution in closed analytical form. Since then, a wide variety of problems dealing with heat and fluid flow over a stretching or shrinking sheet have been studied with both Newtonian and non-Newtonian fluids with the inclusion of magnetic fields, different thermal boundary conditions, and power law variation of the stretching or shrinking velocity.

A stagnation point is a point where the field of a flow regarding a body and the fluid particles has zero velocity with respect to the body ([Haq et al., 2015](#)). A stagnation

point exists at the surface of objects in the flow field, where the fluid is brought to rest by the object. Stagnation point flow and heat transfer problems towards a stretching sheet have attracted the attention of many researchers due to their wide applications in a large class of industrial manufacturing and engineering processes such as cooling of electronic devices by fans, cooling of nuclear reactors during emergency shutdown, solar central receivers exposed to wind currents, polymer extrusion, wire drawing, and drawing of plastic sheets (Makinde et al., 2013). The study of a stagnation point flow towards a solid surface in moving fluid was first studied by Hiemenz (1911). He studied two-dimensional stagnation point flow on a stationary plate using a similarity transformation to reduce the well-known Navier-Stokes equations to non-linear ordinary differential equations. Thereafter, many scientific researchers are investigating the idea of stagnation point flow problems towards a stretching/shrinking surface in connection with different physical situations. To mention some, Bhattacharyya (2013) investigated heat transfer in boundary layer stagnation-point flow towards a shrinking sheet with non-uniform heat flux and obtained dual solutions. His result indicates that for direct variation of heat flux along the surface, the thermal boundary layer thickness reduces and for inverse variation of heat flux, a wavy nature in temperature profiles is found. The analysis also reveals that the velocity ratio parameter and the Prandtl number act as the enhancers or suppressors of this unusual nature of temperature due to the presence of non-uniform heat flux. Ismail et al. (2017) numerically investigated stagnation point flow over a stretching sheet with convective boundary conditions and shown that how the Prandtl number, stretching parameter and conjugate parameter affect the values of the surface temperature and skin friction coefficient.

The diffusion of spices with chemical reaction in the boundary layer flow has huge applications in water and air pollution, fibrous insulation, atmospheric flows and many other chemical engineering problems (Prasad et al., 2017). Taking this fact into account, Dash et al. (2016) studied boundary layer stagnation-point flow, taking into account chemical reactions of diffusing species and internal heat generation/absorption. Zaimi and Ishak (2016) numerically investigated the effects of partial slip on stagnation-point flow and heat transfer due to a stretching vertical sheet, and the effect of slip and buoyancy parameters on the fluid flow and heat transfer characteristics was observed. Bhattacharyya et al. (2011) analyzed the effects of partial slip on the steady bound-

ary layer stagnation-point flow of an incompressible fluid and heat transfer towards a shrinking sheet. Their study reveals that the increase in slip increases the range of velocity ratio parameters for the existence of dual solutions.

Imposition of magnetic field in fluid flow with or without heat transfer has been studied extensively by many researchers owing to its many industrial applications such as MHD generator, pumps, cooling of nuclear reactors, cooling of electronic components, combustion modeling, fire engineering, geo-thermal energy extractors, thermal insulators, nuclear waste disposal, heat exchangers, petroleum and polymer technology, and heat transfers involving metallurgical processes (Pal and Mondal, 2012; Chu et al., 2020). Keeping in view the importance of such topics, a number of researchers have investigated hydromagnetic natural, forced and mixed convection flows by considering different aspects of the problem. Singh and Makinde (2013) studied MHD slip flow of viscous fluid over an isothermal reactive stretching sheet. Shen et al. (2015) investigated MHD mixed convection flow near a stagnation-point region over a nonlinear stretching sheet with velocity slip and prescribed surface heat flux. Sharma et al. (2018) considered the effects of heat generation/absorption on MHD mixed convective stagnation point flow along a vertical stretching sheet in the presence of external magnetic field.

Hydromagnetic natural convection flow with radiative heat transfer becomes significant in many scientific and engineering problems such as casting and levitation, design of fins, thermo-nuclear fusion, steel rolling, turbine blade heat transfer, furnace design, glass production etc. Prasad et al. (2006) studied effects of radiation on transient hydromagnetic free convection flow past an impulsively started vertical plate with uniform heat and mass flux. Ogulu and Makinde (2008) analyzed the effects of viscous dissipation and thermal radiation on unsteady hydromagnetic free convection flow past a vertical plate with constant heat flux.

Chemical reactions between foreign mass and the ambient fluid often occur in several chemical engineering processes such as polymer production, manufacturing of ceramics and glassware, food processing, etc. In fact, chemical reactions greatly affect buoyancy driven flows and as a result the interaction between chemical reaction and convection plays a decisive role in fluid flow characteristics. Taking into consideration this fact, Mabood et al. (2015) considered the study of combined heat and mass transfer by MHD stagnation point flow towards a permeable stretching surface in the presence of

a first order chemical reaction.

Nanofluids attract a great deal of interest with their enormous potential to provide enhanced performance properties, particularly with respect to heat transfer. Nanofluids are used for cooling of microchips in computers and other electronics equipment which use microfluidic applications. Using nanofluids as coolants would allow for the radiators with smaller sizes and better positioning. An innovative technique, which uses a mixture of nanoparticles and the base fluid, was first introduced by [Choi and Eastman \(1995\)](#) in order to develop advanced heat transfer fluids with substantially higher conductivities. The main property of nanofluids is to increase the thermal conductivity of the base fluid. A comprehensive survey of convective transport in nanofluids has been made by [Buongiorno \(2006\)](#), who gave a satisfactory explanation for the abnormal increase of the thermal conductivity.

[Makinde and Aziz \(2011\)](#) explained the effects of a convective boundary condition on boundary layer flow, heat transfer, and nanoparticle fraction over a stretching surface in a nanofluid. According to their analysis, the thermal boundary layer thickness increases with a rise in the local temperature due to Brownian motion, thermophoresis, and convective heating. The effects of Lewis number on the temperature distribution are minimal compared to other parameters. Natural convective boundary layer flow of a nanofluid past a convectively heated vertical plate was investigated numerically by [Aziz and Khan \(2012\)](#). Based on their investigation, they have obtained that the velocity, temperature and solid volume fraction of the nanofluid profiles in the boundary layer depend on six dimensionless parameters, namely Prandtl number, Lewis number, Brownian motion parameter  $N_b$ , thermophoresis parameter, buoyancy parameter, and convective parameter.

[Ibrahim et al. \(2013\)](#) investigated effects of magnetic field on stagnation point flow and heat transfer due to nanofluid towards a stretching sheet and obtained that heat transfer rate at the surface increases with the magnetic parameter when the free stream velocity exceeds stretching velocity of the sheet. Extending this idea, [Makinde et al. \(2013\)](#) studied the combined effects of buoyancy force and convective heating and showed the existence of a dual solution for shrinking cases. [Rashidi et al. \(2014\)](#) investigated heat transfer of a steady, incompressible water-based nanofluid flow over a stretching sheet in the presence of a transverse magnetic field with thermal radiation

and buoyancy effects. [Makinde et al. \(2017\)](#) numerically investigated the combined effects of buoyancy forces, homogeneous chemical reaction, thermal radiation, partial slip, heat source, thermophoresis and Brownian motion on hydromagnetic stagnation point flow of nanofluid with heat and mass transfer over a stretching convective surface by assuming the stretching velocity and the ambient fluid velocity are assumed to vary linearly with the distance from the stagnation point. Furthermore, several other studies are presented by incorporating other physical aspects. To mention some, [Mustafa et al. \(2017\)](#) analyzed buoyancy effects on the MHD nanofluid flow past a vertical surface with chemical reaction and activation energy. [Mustafa et al. \(2020\)](#) numerically investigated the problem of hydromagnetic flow due to shrinking sheet and calculated dual solutions against velocity ratio parameter in case of shrinking sheet. A stability analysis is performed for the purpose of checking which solution is stable. [Rosali et al. \(2020\)](#) numerically analyzed the combined effects of velocity and thermal slip on the unsteady boundary layer stagnation point flow and heat transfer towards a stretching sheet in porous medium. [Dzulkiffi et al. \(2022\)](#) studied numerically unsteady stagnation-point flow and heat transfer over a stretching/shrinking sheet with the slip velocity effect in nanofluids.

Moreover, the inclusion of magnetic nanofluid in convective heat transfer and cooling problems has great importance, as explained by [Gupta \(2016b\)](#). For instance, biomedical applications, detection of ammonia, rotating seals, display devices, heat transfer, environmental and energy applications (cleaning of crude oil), etc. ([Mody et al., 2014](#); [Scherer and Figueiredo Neto, 2005](#); [Blums, 2002](#); [Kuzubov and Ivanova, 1994](#)). Taking into consideration this fact, [Jamaludin et al. \(2020\)](#) explored a two-dimensional hydromagnetic stagnation point flow of  $\text{Fe}_3\text{O}_4$ -water ferrofluid flow past a permeable non-linearly stretching/shrinking surface by considering the thermal radiation effect. They found that dual solutions exist in certain ranges of mixed convection parameters and thermal radiation diminishes the rate of heat transfer from the sheet surface. Besides all these, some researchers have investigated heat transfer enhancement processes by considering hybridized nanoparticles. For instance, [Waini et al. \(2020\)](#) numerically examined buoyancy effects on stagnation point flow of hybrid nanofluid towards an exponentially stretching/shrinking vertical sheet and found that the heat transfer rate is greater for  $\text{Al}_2\text{O}_3$ -Cu/water hybrid nanofluid compared to Cu/water nanofluid.

## 2.3 Boundary Layer Flow in a Porous Medium

Problems of boundary layer flow in porous media with the applications of magnetic fields have been extensively studied by many researchers owing to their many industrial applications, such as MHD generators, pumps, cooling of nuclear reactors, cooling of electronic components, combustion modeling, fire engineering, geo-thermal energy extractors, thermal insulators, nuclear waste disposal, heat exchangers, petroleum and polymer technology, and heat transfers involving metallurgical processes ([Hayat et al., 2016, 2017](#); [Seth and Mandal, 2018](#)).

Keeping in view of the importance of such studies, a number of researchers are working on hydromagnetic natural, forced, and mixed convection flows in Darcian and non-Darcian porous media. [Makinde and Egunjobi \(2016\)](#) studied unsteady MHD chemically reacting and radiating mixed convection slip flow past a stretching surface in a porous medium. They found that buoyancy forces increment enhance both heat and mass transfer rate while thermal and concentration boundary layer denseness diminished. [Eid and Makinde \(2018\)](#) studied the combined effect of solar radiation, chemical reaction, joule heating, viscous dissipation and magnetic field on flow of an electrically conducting nanofluid over a convectively heated stretching sheet embedded in a saturated porous media.

[Jagadha and Amrutha \(2019\)](#) analyzed the steady laminar viscous incompressible nanofluid flow of mixed convection and mass transfer about an isothermal vertical flat plate embedded in a Darcy porous medium in the presence of magnetic field and viscous dissipation. [Khashi'ie et al. \(2020\)](#) examined MHD mixed convective stagnation point flow over a shrinking/stretching surface saturated in a porous medium. In their study, they obtained dual solutions within the specific range of buoyancy parameter and velocity ratio parameter. Furthermore, the skin friction coefficient, heat transfer, and mass transfer rates for both stretching and shrinking surfaces are boosted as the porous parameter inflates.

[Mondal et al. \(2020\)](#) examined mixed convection in a nanofluid flow in a porous medium along a vertical plate subjected to magnetic effects and nonlinear thermal radiation. The study further assumes the effects of heat generation within the boundary layer flow. The numerical solution was done through the Runge-Kutta-Fehlberg scheme

with a shooting technique. From the numerical results obtained, it is observed, among other findings, that an increase in the Darcy number leads to an increase in the velocity profiles. [Sulochana et al. \(2021\)](#) numerically examined MHD Darcy-Forchheimer hybrid nanofluid flow past a nonlinear stretching surface and obtained that the heat transfer rate is greater in the silver-iron oxide combination as compared to silver-molybdenum disulfide. [Obalalu et al. \(2022\)](#) numerically studied magneto-convective non-Newtonian nanofluid slip flow over a stretching/shrinking sheet embedded in a porous medium and remarked that the account for the velocity slip in the boundary conditions increases the velocity component. Also, the liquid acts as a Newtonian fluid when the Casson parameter increases. Consequently, some of those parameters contribute to the cooling plate, while others have the opposite effect.

## **2.4 Stagnation Point flow of Magnetic Nanofluid Flow in a Porous Medium**

Problems of fluid flow and heat transfer in a porous medium have a wide range of applications in various engineering systems. These problems occur in the storage of radioactive nuclear waste; transpiration cooling; separation processes in chemical industries; filtration processes; transport processes in aquifers; groundwater pollution; geothermal extraction; and fiber insulation, as reported by [Menni et al. \(2019\)](#). Using nanofluid is a potential technique to improve the problem of heat transfer in high technology industries, as mentioned by [Kakaç and Pramuanjaroenkij \(2009\)](#). [Choi and Eastman \(1995\)](#) are the leading persons to specify engineered colloids consisting of nanoparticles dispersed in a base fluid like water, ethylene glycol, engine oil, or others as a nanofluid. On the other hand, using porous media is an effective method for heat transfer enhancement in industrial systems, as described by [Toosi and Siavashi \(2017\)](#). Following these facts, a lot of work has been done on fluid flow and heat transfer problems in a porous medium with nanofluid. Accordingly, [Mahdi et al. \(2015\)](#) pointed out that an alternative method for improving heat transfer characteristics in various thermal devices is using porous media and nanofluids together. [Kasaeian et al. \(2017\)](#) conducted a wide-ranging review of the simultaneous application of nanofluids and porous media for heat transfer enhancement cases in thermal systems with diverse

conditions. Different aspects of this problem have been explored by many investigators, such as [Chamkha and Ismael \(2013\)](#); [Mahdi et al. \(2013\)](#); [Sun and Pop \(2014\)](#); [Motlagh et al. \(2016\)](#); [Sheikholeslami and Ganji \(2017\)](#).

Nanofluid is produced by mixing nanosized metallic or nonmetallic particles or nanofiber particles into conventional fluids in order to increase the thermal properties [Gupta et al. \(2018\)](#). Among different research on nanofluids, some work has been focused on a new kind of nanofluid called ferrofluids [Bahiraei and Hangi \(2015\)](#). Ferrofluids (Magnetic nanofluids) are a special class of nanofluids exhibiting both magnetic and fluid properties [Bahiraei and Hangi \(2015\)](#). Ferrofluids are defined as solutions comprising colloidal mixtures of super-paramagnetic nanoparticles (Magnetite, Hematite, Cobalt Ferrite, or some other compounds containing iron) and a nonmagnetic base fluid. In the occurrence of the magnetic field, the thermal conductivity of the magnetic nanofluid is affected by the orientation and the intensity of the applied magnetic field [Odenbach \(2004\)](#). Furthermore, ferrofluids and magnetic fields can also be used for fluid flow control and for improving the heat transfer process taking place in the case of natural, forced, and mixed convection [Gupta \(2016b\)](#).

Using magnetic fluids has various uses in different engineering processes and biomedical applications such as removing particles and contamination from drinking/wastewater streams, removing radioactive chemicals, MRI, drug delivery in cancer treatment, low-friction seals, dampening and cooling agents in loudspeakers, recovery of hazardous wastes, heat transfer, computer hardware, dynamic sealing, electronic packaging, aerospace, power electric transformers, solar collectors and magnetically controlled thermosyphons as mentioned by [Mody et al. \(2014\)](#); [Scherer and Figueiredo Neto \(2005\)](#); [Blums \(2002\)](#); [Kuzubov and Ivanova \(1994\)](#). Following these facts, several studies have been done experimentally and numerically to determine the fluid flow characteristics and heat transfer enhancement of a magnetic nanofluid by considering several aspects of the problem. For instance, [Lajvardi et al. \(2010\)](#) experimentally examined the convective heat transfer characteristics of the magnetic nanofluids with a magnetic field effect and obtained that the heat transfer rate upsurges with the magnetic nanoparticle concentration and the applied magnetic field. [Sivakumar et al. \(2017\)](#) numerically scrutinized the cumulative effects of viscous dissipation, thermal radiation, convective heating, and slip effect on the MHD ferrofluid flow past a per-

meable nonlinear stretching sheet and concluded that the heat transfer rate increases with the convective heating and the viscous dissipation while thermal radiation acts on the contrary.

Fluid flow caused by a stretching/shrinking sheet has many practical applications in the fields of metallurgy, polymer technology, chemical engineering, industrial processes, etc [Lok et al. \(2011\)](#); [Soid et al. \(2018\)](#); [Waini et al. \(2019\)](#). Fluid flow towards a shrinking case is possible whenever sufficient mass suction is imposed on the boundary [Miklavčič and Wang \(2006\)](#) or with the consideration of stagnation point flow [Wang \(2008\)](#). Due to the unconfined fluid flow occurring in the boundary layer of the shrinking case, no possible solution is found. However, the application of the adequate value of wall mass suction [Miklavčič and Wang \(2006\)](#) or with an added stagnation flow [Wang \(2008\)](#), a non-unique solution may exist. The governing system of differential equations may have a non-unique solution. Temporal stability analysis is a mathematical technique that is conducted to test the temporal stability of non-unique solutions. Though the lower branch solution cannot be produced experimentally, this solution is a part of the solution of the differential equations and therefore should be considered. Different works on stability analysis are documented in the literature [Merkin \(1986\)](#); [Weidman et al. \(2006\)](#); [Harris et al. \(2009\)](#); [Roşca and Pop \(2013\)](#); [Ishak \(2014\)](#). Recently, such fluid flow problems have been extensively investigated by considering different aspects of the problem. For instance, [Khashi'ie et al. \(2020\)](#) numerically examined the combined effects of the controlling parameters such as magnetic field, suction, and Joule heating on fluid flow and heat transfer characteristics of a hybrid nanofluid past a permeable stretching/shrinking sheet. From the temporal stability analysis, they verified that only the upper branch solution is stable and physically realizable.

Investigations into the stagnation point flow of nanofluid or ferrofluid have gained more attention due to their immense applications in many industrial manufacturing processes such as aerodynamics, extrusion of plastic sheet, and the cooling and drying of paper, as reported by [Kamal et al. \(2018\)](#). Owing to this importance, such fluid flow problems have been extended in various ways. For example, [Abbas and Sheikh \(2017\)](#) studied the stagnation point flow of a magnetic nanofluid past a flat sheet with the consideration of non-linear slip boundary conditions and homogeneous-heterogeneous reactions and concluded that the skin friction obtained for water-based ferrofluid exceeds

that for kerosene-based ferrofluid. [Makinde \(2018\)](#) numerically investigated hydrodynamic stagnation point flow of  $\text{Fe}_3\text{O}_4$ -water ferrofluid towards a permeable stretching or shrinking sheet with the effects of applied magnetic field. They perform hydrodynamic stability analysis to identify stable solutions among those solutions that exist within the specific range of stretching/shrinking parameter. [Mohamed et al. \(2019\)](#) numerically examined the combined effects of the magnetic field, velocity slip, nanoparticles volume fraction, stretching, and conjugate parameter on the boundary layer flow of a water-based magnetite ferrofluid. They reported that the heat transfer rate rises with the magnetite nanoparticle volume fraction, whereas the velocity slip diminishes the skin friction coefficient. Moreover, [Jamaludin et al. \(2020\)](#) explored a two-dimensional hydromagnetic stagnation point flow of  $\text{Fe}_3\text{O}_4$ -water ferrofluid flow past a permeable non-linearly stretching/shrinking surface by considering the thermal radiation effect. They found that dual solutions exist in certain ranges of mixed convection parameters, and thermal radiation diminishes the rate of heat transfer from the sheet surface.

For fluid flows in a porous medium, the inclusion of porous dissipation in the model equation modifies the viscous dissipation term in the energy equation [Kausar et al. \(2019\)](#). From the literature survey and to the best of our knowledge, more attention is required to problems of fluid flow and heat transfer past a stretching/shrinking sheet embedded in a Darcy or Darcy-Forchheimer porous medium in the presence of porous dissipation.

# Chapter 3

## Research Methodology

This chapter is devoted to see about the derivations of the general governing equations of fluid flow and the computational techniques/methods of solution used in the analysis of the fluid flow problems.

### 3.1 Governing Equations

The analysis of convection momentum, heat, and mass transfer relies on the applications of the basic laws: conservation of mass, momentum, and energy. Since the objective of this dissertation is the determination of velocity, temperature, and species concentration distribution, the basic laws must be formulated in an appropriate form.

The fundamental equations of the flow of viscous incompressible fluids are the equations of continuity (conservation of total mass), motions(conservation of momentum), energy equation (conservation of energy) and species conservation equation (conservation of species). These fundamental physical principles can be expressed in terms of basic mathematical equations, which in their most general form are either integral equations or partial differential equations.

#### 3.1.1 The Continuity Equation

Consider a fixed and non-deforming control volume  $V$  surrounded by a surface  $S$ . Let  $\rho$  and  $\vec{q}$  be the mass density and velocity of a given fluid at point  $(x, y, z)$  and time  $t$ . The net mass contained within  $V$  is

$$M = \int_V \rho dV, \quad (3.1.1)$$

where  $dV$  is an element of  $V$ . Furthermore, the mass flux across  $S$ , and out of  $V$ , is

$$\Phi_M = \int_S \rho \vec{q} \cdot \vec{n} dS, \quad (3.1.2)$$

where  $dS$  is surface element and  $\vec{n}$  is the outward normal vector. Mass conservation requires that the rate of increase of the mass contained within  $V$ , plus the net mass

flux out of  $V$ , should equal zero: that is,

$$\frac{dM}{dt} + \Phi_M = 0, \quad (3.1.3)$$

$$\frac{d}{dt} \int_V \rho dV + \int_S \rho \vec{q} \cdot \vec{n} dS = 0. \quad (3.1.4)$$

Here, we are assuming that there is no mass generation (or destruction) within  $V$  (because individual molecules are effectively indestructible). It follows that

$$\int_V \frac{\partial \rho}{\partial t} dV + \int_S \rho \vec{q} \cdot \vec{n} dS = 0, \quad (3.1.5)$$

because  $V$  is non-time-varying and  $\rho$  is a function of space and time. Making use of the divergence theorem, equation (3.1.1) becomes

$$\int_V \left[ \frac{\partial \rho}{\partial t} + \nabla \cdot (\rho \mathbf{q}) \right] dV = 0. \quad (3.1.6)$$

However, this result is true irrespective of the size, shape, or location of volume  $V$ , which is only possible if

$$\frac{\partial \rho}{\partial t} + \nabla \cdot (\rho \mathbf{q}) = 0, \quad (3.1.7)$$

throughout the fluid.

In index notation,

$$\frac{\partial \rho}{\partial t} + \frac{\partial (\rho u_j)}{\partial x_j} = 0. \quad (3.1.8)$$

### 3.1.2 The Momentum Equation (Navier-Stokes Equation)

The Navier-Stokes equations, describe the momentum balance in the fluid flow. Therefore, these equations are sometimes known as momentum equation or simply the equation of motion for the flow. It is derived based on Newton's second law of motion i.e.  $\mathbf{F} = m\mathbf{a}$ .

Consider a fixed volume  $V$  surrounded by a surface  $S$ . Let  $\rho$  and  $\vec{q}$  be the density and velocity of a given fluid at point  $(x, y, z)$  and time  $t$ .

From Newton's second law of motion i.e.,  $\mathbf{F} = m\mathbf{a}$ ,

$$\text{The rate of change of momentum} = \frac{d}{dt} \int_V \rho \mathbf{q} dV = F_{\text{applied}} = F_{\text{surface}} + F_{\text{body}}. \quad (3.1.9)$$

Now applying the Reynold's transport theorem for a control mass(system)

$$\frac{dN}{dt} \Big|_{system} = \frac{\partial}{\partial t} \int_{cv} \rho n dV + \int_{cs} \rho n (\vec{q}_r \cdot \vec{n}) dS, \quad (3.1.10)$$

where  $N$  refers to an extensive properties of the fluid,  $n$  refers to an intensive properties of the fluid and  $\vec{q}_r$  is the velocity of the fluid relative to the control surface. Now taking  $N = m\vec{q} =$  momentum of the system,  $n = \vec{q} =$  the fluid velocity and  $\vec{q}_r = \vec{q}$  for fixed and non deforming control volume.

$$\frac{d}{dt} \left( \int_V \rho \vec{q} dV \right) = \frac{\partial}{\partial t} \int_{cv} \rho \vec{q} dV + \int_S \rho \vec{q} (\vec{q} \cdot \vec{n}) dS = F_{surface} + F_{body}, \quad (3.1.11)$$

where  $\vec{n}$  is the unit vector in the outward normal direction. Making use of the divergence theorem, equation (3.1.11) becomes

$$\int_V \frac{\partial(\rho \vec{q})}{\partial t} dV + \int_V \nabla \cdot (\rho \vec{q}) \vec{q} dV = F_{surface} + F_{body}. \quad (3.1.12)$$

The  $i^{th}$  component of the total surface force due to stresses and the body force on the control volume is given by

$$\begin{aligned} F_{surface} &= \int_{cs} \vec{T}_i^n dS = \int_{cs} \vec{\tau}_i \cdot \hat{n} dS = \int_V \nabla \cdot \vec{\tau}_i, \\ F_{body} &= \int_V \rho F_m dV. \end{aligned} \quad (3.1.13)$$

Using Cauchy's theorem, we can rewrite the force per unit area (traction vector)  $T_i^n$  as a dot product of the stress vector  $\vec{\tau}_i = \tau_{i1}i + \tau_{i2}j + \tau_{i3}k$  and the orientation of the normal to the particular surface on which the traction vector is calculated  $\hat{n} = n_1i + n_2j + n_3k$  and  $F_m$  is a body force per unit mass acting on the flow.

Hence the Navier momentum balance equation becomes

$$\begin{aligned} \int_V \frac{\partial(\rho \vec{q})}{\partial t} dV + \int_V \nabla \cdot (\rho \vec{q}) \vec{q} dV &= \int_V \nabla \cdot \vec{\tau}_i dV + \int_V \rho F_m dV, \\ \int_V \left( \frac{\partial(\rho \vec{q})}{\partial t} dV + \nabla \cdot (\rho \vec{q}) \vec{q} \right) dV &= \int_V (\nabla \cdot \vec{\tau}_i dV + \rho F_m) dV, \end{aligned} \quad (3.1.14)$$

$$\int_V \left[ \frac{\partial(\rho \vec{q})}{\partial t} + \nabla \cdot (\rho \vec{q}) \vec{q} - \nabla \cdot \vec{\tau}_i - \rho F_m \right] dV = 0. \quad (3.1.15)$$

For any arbitrary control volume, equation (3.1.15) becomes

$$\frac{\partial(\rho\vec{q})}{\partial t} + \nabla \cdot (\rho\vec{q})\vec{q} - \nabla \cdot \vec{\tau}_i - \rho F_{mi} = 0. \quad (3.1.16)$$

Taking the  $i^{th}$  component of equation (3.1.16), we obtained the Navier equation of equilibrium in index notation as shown below

$$\frac{\partial(\rho u_i)}{\partial t} + \frac{\partial(\rho u_i u_j)}{\partial x_j} = \frac{\partial \tau_{ij}}{\partial x_j} + \rho F_i. \quad (3.1.17)$$

Assuming homogeneous, isotropic, Newtonian and Stokesian fluid, we can determine  $\tau_{ij}$  as

$$\begin{aligned} \tau_{ij} &= -P\delta_{ij} + \lambda \frac{\partial u_k}{\partial x_k} \delta_{ij} + \mu \left[ \frac{\partial u_i}{\partial x_j} + \frac{\partial u_j}{\partial x_i} \right], \\ \frac{\partial \tau_{ij}}{\partial x_j} &= -\frac{\partial P}{\partial x_i} + \frac{\partial}{\partial x_i} \left( \lambda \frac{\partial u_k}{\partial x_k} \right) + \frac{\partial}{\partial x_j} \left( \mu \frac{\partial u_i}{\partial x_j} \right) + \frac{\partial}{\partial x_i} \left( \mu \frac{\partial u_j}{\partial x_i} \right), \end{aligned} \quad (3.1.18)$$

$$\frac{\partial \tau_{ij}}{\partial x_j} = -\frac{\partial P}{\partial x_i} + \frac{\partial}{\partial x_j} \left( \mu \frac{\partial u_i}{\partial x_j} \right) + \frac{\partial}{\partial x_i} \left( (\mu + \lambda) \frac{\partial u_k}{\partial x_k} \right) \quad (3.1.19)$$

where  $P$  is the pressure force,  $\mu$  is the dynamic viscosity and  $\lambda$  is the bulk viscosity coefficient. For a Newtonian fluid, the shear stress is proportional to the rate of deformation (the change in velocity in the directions of the stress). Making use of the Stoke's hypothesis i.e.,  $\lambda = -\frac{2}{3}\mu$  in equation (3.1.19), we get the Navier- Stokes equation

$$\frac{\partial(\rho u_i)}{\partial t} + \frac{\partial(\rho u_i u_j)}{\partial x_j} = -\frac{\partial P}{\partial x_i} + \frac{\partial}{\partial x_j} \left( \mu \frac{\partial u_i}{\partial x_j} \right) + \frac{\partial}{\partial x_i} \left( \frac{\mu}{3} \frac{\partial u_k}{\partial x_k} \right) + \rho F_i. \quad (3.1.20)$$

The non conservative form of the Navier-Stokes can be obtained by considering the continuity equations

$$LHS = \rho \left[ \frac{\partial u_i}{\partial t} + u_j \frac{\partial u_i}{\partial x_j} \right] + u_i \left[ \frac{\partial \rho}{\partial t} + \frac{\partial(\rho u_j)}{\partial x_j} \right] = \rho \left[ \frac{\partial u_i}{\partial t} + u_j \frac{\partial u_i}{\partial x_j} \right] = \rho \frac{Du_i}{Dt}, \quad (3.1.21)$$

$$\rho \frac{Du_i}{Dt} = -\frac{\partial P}{\partial x_i} + \frac{\partial}{\partial x_j} \left( \mu \frac{\partial u_i}{\partial x_j} \right) + \frac{\partial}{\partial x_i} \left( \frac{\mu}{3} \frac{\partial u_k}{\partial x_k} \right) + \rho F_i. \quad (3.1.22)$$

For incompressible fluids, there is no rate of volumetric deformation, i.e.,  $\frac{\partial u_k}{\partial x_k} = 0$ ,

then equation (3.1.22) is simplified as

$$\begin{aligned}\rho \left[ \frac{\partial u_i}{\partial t} + u_j \frac{\partial u_i}{\partial x_j} \right] &= -\frac{\partial P}{\partial x_i} + \frac{\partial}{\partial x_j} \left( \mu \frac{\partial u_i}{\partial x_j} \right) + \rho F_i, \\ \rho \frac{Du_i}{Dt} &= -\frac{\partial P}{\partial x_i} + \frac{\partial}{\partial x_j} \left( \mu \frac{\partial u_i}{\partial x_j} \right) + \rho F_i.\end{aligned}\tag{3.1.23}$$

Now taking  $(u_1, u_2, u_3) = (u, v, w)$  and  $(x_1, x_2, x_3) = (x, y, z)$ .

The vector form of the Navier- Stokes equation will be

$$\begin{aligned}\rho \left[ \frac{\partial u}{\partial t} + u \frac{\partial u}{\partial x} + v \frac{\partial u}{\partial y} + w \frac{\partial u}{\partial z} \right] &= -\frac{\partial P}{\partial x} + \frac{\partial}{\partial x} \left( \mu \frac{\partial u}{\partial x} \right) + \frac{\partial}{\partial y} \left( \mu \frac{\partial u}{\partial y} \right) \\ &+ \frac{\partial}{\partial z} \left( \mu \frac{\partial u}{\partial z} \right) + \rho F_x.\end{aligned}\tag{3.1.24}$$

Making  $\mu$  constant, we get

$$\rho \left[ \frac{\partial u}{\partial t} + u \frac{\partial u}{\partial x} + v \frac{\partial u}{\partial y} + w \frac{\partial u}{\partial z} \right] = -\frac{\partial P}{\partial x} + \mu \left[ \frac{\partial^2 u}{\partial x^2} + \frac{\partial^2 u}{\partial y^2} + \frac{\partial^2 u}{\partial z^2} \right] + \rho F_x.\tag{3.1.25}$$

Generalizing the above results for other components, we get the general form of Navier-Stokes equation for Newtonian incompressible fluid

$$\rho \left[ \frac{\partial q}{\partial t} + (q \cdot \nabla) q \right] = -\nabla P + \mu \nabla^2 q + \rho F_b.\tag{3.1.26}$$

### 3.1.3 The Energy Equation

The energy equation is derived from the first law of thermodynamics which states that the amount of heat added to a system  $dQ$  is equal to change in internal energy  $dE$  of the control mass(system) plus the amount of energy lost due to work done  $dW$  on the system, that is  $dQ = dE + dW$ . In other words if a net energy transfer to a system occurs, the energy contained/stored in the system must increase by an amount equal to the energy transferred. This implies that energy can neither be created nor destroyed, it can only change in form. The first law of thermodynamics can be mathematically written as,

$$\frac{dQ}{dt} = \frac{dE}{dt} \Big|_{system} + \frac{dW}{dt},\tag{3.1.27}$$

$$\left. \frac{dE}{dt} \right|_{system} = \dot{Q}_{cv} - \dot{W}_{cv}. \quad (3.1.28)$$

First let us write the expression for the heat transfer by considering the surface heat transfer and volumetric heat transfer.

$$\dot{Q}_{cv} = \int_{cv} Q''' dV + \int_{cs} (-\vec{q}'') \cdot n dS, \quad (3.1.29)$$

where  $Q'''$  is the rate of heat generation (heat generation per unit volume),  $\vec{q}''$  is the heat flux,  $n$  is the unit vector in the outward normal direction to the surface  $S$ .

Making use of the divergence theorem, equation (3.1.29) becomes

$$\dot{Q}_{cv} = \int_{cv} Q''' dV - \int_{cv} \nabla \cdot \vec{q}'' dV = \int_{cv} (Q''' - \nabla \cdot \vec{q}'') dV. \quad (3.1.30)$$

Expression for the work done due to surface force and body force will be

$$-\dot{W}_{cv} = \dot{W}_{\text{surface force}} + \dot{W}_{\text{Body force}} = \int_{cs} \vec{T}^n \cdot \vec{q} dS + \int_{cv} F_{\text{Body force}} \cdot \vec{q} dV, \quad (3.1.31)$$

where  $\vec{T}^n$  is a force per unit area (traction vector) and  $F_{\text{Body force}}$  is the body force per unit volume.

Using the Cartesian index notation, the  $i^{\text{th}}$  component of equation (3.1.31) will be

$$-\dot{W}_{cv} = \int_{cs} T_i^n u_i dS + \int_{cv} F_i u_i dV, \quad (3.1.32)$$

where  $u_i, F_i, T_i^n$  is the  $i^{\text{th}}$  component of the fluid velocity  $\vec{q}$ , the body force per unit volume  $F$  and the traction vector  $\vec{T}^n$ , respectively.  $\vec{n}$  is orientation of the normal to the surface on which the traction vector is calculated. Using Cauchy's theorem, we can rewrite  $T_i^n$  as a dot product of two vectors as shown below

$$\begin{aligned} T_i^n &= \tau_{i1}n_1 + \tau_{i2}n_2 + \tau_{i3}n_3 = (\tau_{i1}i + \tau_{i2}j + \tau_{i3}k) \cdot (n_1i + n_2j + n_3k) \\ &= \vec{\tau}_i \cdot \vec{n}. \end{aligned} \quad (3.1.33)$$

Making use of equation (3.1.33) and Gauss divergence theorem, equation (3.1.32) can be rewritten as

$$\begin{aligned}
-\dot{W}_{cv} &= \int_{cs} \vec{\tau}_i \cdot \vec{n} u_i dS + \int_{cv} F_i u_i dV, \\
&= \int_{cs} \vec{\tau}_i u_i \cdot \vec{n} dS + \int_{cv} F_i u_i dV, \\
&= \int_{cv} \nabla \cdot (\vec{\tau}_i u_i) dV + \int_{cv} F_i u_i dV, \\
&= \int_{cv} \frac{\partial}{\partial x_j} (\tau_{ij} u_i) dV + \int_{cv} F_i u_i dV.
\end{aligned} \tag{3.1.34}$$

Substituting equation (3.1.30) and equation (3.1.34) into equation (3.1.28), we obtain the following equation

$$\begin{aligned}
\frac{dE}{dt} \Big|_{system} &= \int_{cv} Q''' dV - \int_{cv} \frac{\partial q_j''}{\partial x_j} dV + \int_{cv} \frac{\partial}{\partial x_j} (\tau_{ij} u_i) dV + \int_{cv} F_i u_i dV, \\
&= \int_{cv} \left( Q''' - \frac{\partial q_j''}{\partial x_j} + \frac{\partial}{\partial x_j} (\tau_{ij} u_i) + F_i u_i \right) dV.
\end{aligned} \tag{3.1.35}$$

Now applying the Reynold's transport theorem for a control mass(system)

$$\frac{dN}{dt} \Big|_{system} = \frac{\partial}{\partial t} \int_{cv} \rho n dV + \int_{cs} \rho n (\vec{q}_r \cdot \vec{n}) dS. \tag{3.1.36}$$

where  $N$  refers to an extensive properties of the fluid and  $n$  refers to an intensive properties of the fluid. Now taking  $N = E =$  total energy of the system(sum of internal, kinetic and potential energies) and  $n = e =$  specific energy(total energy per unit mass).

$$\frac{dE}{dt} \Big|_{system} = \frac{\partial}{\partial t} \int_{cv} \rho e dV + \int_{cs} \rho e (\vec{v}_r \cdot \vec{n}) dS. \tag{3.1.37}$$

Assuming the control volume is stationary(i.e.,  $\vec{v}_r = \vec{v}$ ) and non deformable (i.e., the time derivative can be taken inside of the integral), we have

$$\frac{dE}{dt} \Big|_{system} = \int_{cv} \frac{\partial}{\partial t} (\rho e) dV + \int_{cs} \rho e (\vec{v} \cdot \vec{n}) dS. \tag{3.1.38}$$

Making use of Einestien index notation and Gauss divergence theorem, we have

$$\begin{aligned}
\left. \frac{dE}{dt} \right|_{system} &= \int_{cv} \frac{\partial}{\partial t} (\rho e) dV + \int_{cv} \nabla \cdot (\rho e \vec{v}) dV, \\
&= \int_{cv} \frac{\partial}{\partial t} (\rho e) dV + \int_{cv} \frac{\partial}{\partial x_j} (\rho e u_j) dV, \\
&= \int_{cv} \left( \frac{\partial}{\partial t} (\rho e) + \frac{\partial}{\partial x_j} (\rho e u_j) \right) dV,
\end{aligned} \tag{3.1.39}$$

$$\begin{aligned}
\left. \frac{dE}{dt} \right|_{system} &= \int_{cv} \left( \rho \frac{\partial e}{\partial t} + e \frac{\partial \rho}{\partial t} + \rho u_j \frac{\partial e}{\partial x_j} + e \frac{\partial (\rho u_j)}{\partial x_j} \right) dV, \\
&= \int_{cv} \left[ \rho \left( \frac{\partial e}{\partial t} + u_j \frac{\partial e}{\partial x_j} \right) + e \left( \frac{\partial \rho}{\partial t} + \frac{\partial (\rho u_j)}{\partial x_j} \right) \right] dV.
\end{aligned} \tag{3.1.40}$$

Applying the continuity equation,  $\frac{\partial \rho}{\partial t} + \frac{\partial (\rho u_j)}{\partial x_j} = 0$ , equation (3.1.40) becomes,

$$\left. \frac{dE}{dt} \right|_{system} = \int_{cv} \rho \left( \frac{\partial e}{\partial t} + u_j \frac{\partial e}{\partial x_j} \right) dV = \int_{cv} \rho \frac{De}{Dt}. \tag{3.1.41}$$

For any arbitrary control volume, combining equation (3.1.35) and (3.1.41), we obtain the following equation.

$$\begin{aligned}
\rho \left[ \frac{\partial e}{\partial t} + u_j \frac{\partial e}{\partial x_j} \right] &= Q''' - \frac{\partial q_j''}{\partial x_j} + \frac{\partial (\tau_{ij} u_i)}{\partial x_j} + F_i u_i, \\
\rho \left[ \frac{\partial e}{\partial t} + u_j \frac{\partial e}{\partial x_j} \right] &= Q''' - \frac{\partial q_j''}{\partial x_j} + \tau_{ij} \frac{\partial u_i}{\partial x_j} + u_i \frac{\partial \tau_{ij}}{\partial x_j} + F_i u_i.
\end{aligned} \tag{3.1.42}$$

Above is the equation of total energy (the sum mechanical energy and thermal energy) conservation, however we are interested in thermal energy only and hence we would subtract the mechanical energy (sum of kinetic and potential energy) from the above equation.

Multiplying the Navier equation of momentum balance by  $u_i$ , we obtain equation for mechanical energy (the sum of kinetic and potential energy)

$$\begin{aligned}
u_i \left[ \rho \frac{\partial u_i}{\partial t} + \rho u_j \frac{\partial u_i}{\partial x_j} \right] &= u_i \frac{\partial \tau_{ij}}{\partial x_j} + F_i u_i, \\
\rho \left[ \frac{\partial}{\partial t} \left( \frac{u_i^2}{2} \right) + u_j \frac{\partial}{\partial x_j} \left( \frac{u_i^2}{2} \right) \right] &= u_i \frac{\partial \tau_{ij}}{\partial x_j} + F_i u_i.
\end{aligned} \tag{3.1.43}$$

Subtracting equation (3.1.42) from equation (3.1.43), we obtain the conservation equation for the internal energy ( $i$ ) only

$$\frac{\partial(\rho i)}{\partial t} + \frac{\partial(\rho u_j i)}{\partial x_j} = Q''' - \frac{\partial q_j''}{\partial x_j} + \tau_{ij} \frac{\partial u_i}{\partial x_j}, \quad (3.1.44)$$

$$\left[ \rho \left( \frac{\partial i}{\partial t} + u_j \frac{\partial i}{\partial x_j} \right) + i \left( \frac{\partial \rho}{\partial t} + \frac{\partial(\rho u_j)}{\partial x_j} \right) \right] = Q''' - \frac{\partial q_j''}{\partial x_j} + \tau_{ij} \frac{\partial u_i}{\partial x_j}, \quad (3.1.45)$$

$$\rho \frac{Di}{Dt} = Q''' - \frac{\partial q_j''}{\partial x_j} + \tau_{ij} \frac{\partial u_i}{\partial x_j}.$$

We need to determine the viscous heating because of the energy dissipation due to work gone against viscous shear i.e.,  $\tau_{ij} \frac{\partial u_i}{\partial x_j}$ .

Assuming homogeneous, isotropic, Newtonian and Stokesian fluid, we can determine the stress tensor as

$$\tau_{ij} = -P\delta_{ij} + \lambda \frac{\partial u_k}{\partial x_k} \delta_{ij} + \mu \left( \frac{\partial u_i}{\partial x_j} + \frac{\partial u_j}{\partial x_i} \right), \quad (3.1.46)$$

$$\tau_{ij} \frac{\partial u_i}{\partial x_j} = -P \frac{\partial u_i}{\partial x_i} + \mu \Phi, \quad (3.1.47)$$

where  $\Phi$  is the viscous dissipation function and given by

$$\Phi = 2 \left[ \left( \frac{\partial u}{\partial x} \right)^2 + \left( \frac{\partial v}{\partial y} \right)^2 + \left( \frac{\partial w}{\partial z} \right)^2 \right] + \left[ \left( \frac{\partial u}{\partial y} + \frac{\partial v}{\partial x} \right)^2 + \left( \frac{\partial v}{\partial z} + \frac{\partial w}{\partial y} \right)^2 + \left( \frac{\partial w}{\partial x} + \frac{\partial u}{\partial z} \right)^2 \right]$$

Now defining enthalpy  $h = i + \frac{P}{\rho} \implies \rho i = \rho h - P$  and substituting this and equation (3.1.47) in to equation (3.1.45), we have

$$\begin{aligned} \frac{\partial(\rho i)}{\partial t} + \frac{\partial(\rho u_j i)}{\partial x_j} &= Q''' - \frac{\partial q_j''}{\partial x_j} - P \frac{\partial u_k}{\partial x_k} + \mu \Phi \\ \frac{\partial(\rho h)}{\partial t} - \frac{\partial P}{\partial t} + \frac{\partial(\rho u_j h)}{\partial x_j} - \frac{\partial(P u_j)}{\partial x_j} &= Q''' - \frac{\partial q_j''}{\partial x_j} - P \frac{\partial u_k}{\partial x_k} + \mu \Phi \\ \rho \left[ \frac{\partial h}{\partial t} + u_j \frac{\partial h}{\partial x_j} \right] - \frac{\partial P}{\partial t} - u_j \frac{\partial P}{\partial x_j} - P \frac{\partial u_j}{\partial x_j} &= Q''' - \frac{\partial q_j''}{\partial x_j} - P \frac{\partial u_k}{\partial x_k} + \mu \Phi \\ \rho \frac{Dh}{Dt} - \frac{DP}{Dt} - P \frac{\partial u_k}{\partial x_k} &= Q''' - \frac{\partial q_j''}{\partial x_j} - P \frac{\partial u_k}{\partial x_k} + \mu \Phi \\ \rho \frac{Dh}{Dt} &= Q''' - \frac{\partial q_j''}{\partial x_j} + \mu \Phi + \frac{DP}{Dt} \end{aligned} \quad (3.1.48)$$

For simple compressible pure substance with no phase change, enthalpy is a function of temperature and pressure i.e.,  $h = h(T, P)$  then  $dh = \frac{\partial h}{\partial T} \Big|_P dT + \frac{\partial h}{\partial P} \Big|_T dP$  and in terms of entropy ( $s$ ) it can be defined as  $dh = Tds + v dP$ . Since entropy is a function of temperature and pressure,  $s = s(T, P)$ , and  $dh = T \left( \frac{\partial s}{\partial T} \Big|_P dT + \frac{\partial s}{\partial P} \Big|_T dP \right) + v dP$ . Comparing this two expression we obtain  $\frac{\partial h}{\partial P} \Big|_T = T \frac{\partial s}{\partial P} + v$ . By one of the Maxwell's equation we can redefine  $\frac{\partial h}{\partial P} \Big|_T = v - T \frac{\partial v}{\partial P} \Big|_T$ . By the definition of volumetric expansion coefficient  $\beta = \frac{1}{v} \frac{\partial v}{\partial P} \Big|_T$  then  $\frac{\partial h}{\partial P} \Big|_T = v - \beta v T = v(1 - \beta T)$ . Combining all this things together we obtain,

$$\begin{aligned} dh &= C_P dT + v(1 - \beta T) dP \\ \rho \frac{Dh}{Dt} &= \rho C_P \frac{DT}{Dt} + \rho v(1 - \beta T) \frac{DP}{Dt} \end{aligned} \quad (3.1.49)$$

substituting equation (3.1.49) in to equation (3.1.48), we obtain

$$\begin{aligned} \rho C_P \frac{DT}{Dt} + \rho v(1 - \beta T) \frac{DP}{Dt} &= Q''' - \frac{\partial q_j''}{\partial x_j} + \mu \Phi + \frac{DP}{Dt} \\ \rho C_P \frac{DT}{Dt} &= Q''' - \frac{\partial q_j''}{\partial x_j} + \mu \Phi + \beta T \frac{DP}{Dt} \end{aligned} \quad (3.1.50)$$

From Fourier's law,  $q_j'' = -k_j \frac{\partial T}{\partial x_j} \implies -\frac{\partial q_j''}{\partial x_j} = \frac{\partial}{\partial x_j} \left( k_j \frac{\partial T}{\partial x_j} \right)$ .

Finally we obtain the energy equation in index notation

$$\rho C_P \left[ \frac{\partial T}{\partial t} + u_j \frac{\partial T}{\partial x_j} \right] = Q''' - \frac{\partial}{\partial x_j} \left( k_j \frac{\partial T}{\partial x_j} \right) + \mu \Phi + \beta T \frac{DP}{Dt}. \quad (3.1.51)$$

In vector form, energy equation is given as

$$\rho C_p \left[ \frac{\partial T}{\partial t} + (\mathbf{q} \cdot \nabla) T \right] = Q''' - \nabla \cdot \mathbf{k} \nabla T + \mu \Phi + \beta T \frac{DP}{Dt}. \quad (3.1.52)$$

Where the last term is the pressure work and it is not important when compressibility is negligible.

### 3.1.4 The Species Concentration Equation

The species concentration equation is derived based on the law of mass balance.

Rate of increase of mass of species  $i$  within the control volume = rate of inflow of species  $i$  – rate of outflow of species  $i$  + rate of diffusion of species  $i$  into the control volume + rate of generation of species  $i$  due to chemical reaction.

This principle can be applied to a differential control volume in a manner very similar to the continuity relation. The only new consideration is that mass of species  $i$  can be created or destroyed via chemical reactions so that

$$\frac{\partial \rho_i}{\partial t} + \nabla \cdot \rho_i \bar{U}_i = r_i, \quad (3.1.53)$$

where  $r_i$  is the generation rate of species  $i$  per unit volume,  $\bar{U}_i$  is the species velocity (this velocity is a continuum average that includes the effects of bulk flow and diffusion) and  $\rho = \sum_{i=1}^N \rho_i$  for multi component mixture. The mass averaged velocity of the mixture is  $\bar{U} = \frac{\sum_{i=1}^N \bar{U}_i \rho_i}{\rho}$  then the local rate at which mass passes through a unit cross sectional area perpendicular to  $\bar{U} = \rho \bar{U} = \sum_{i=1}^N \bar{U}_i \rho_i$ .

The drift velocity of species  $i$  causes a flux  $\vec{J}$  which can be expressed by  $\vec{J} = \rho_i(\bar{U}_i - \bar{U})$ . Therefore,  $\rho_i \bar{U}_i = \vec{J} + \rho_i \bar{U}$ . Substituting this into the expression for species conservation, we obtain

$$\frac{\partial \rho_i}{\partial t} + \nabla \cdot (\vec{J} + \rho_i \bar{U}) = r_i. \quad (3.1.54)$$

From Fick's law of binary system where the drift velocity is due to diffusion, we can write  $\vec{J}_i = -D \nabla \rho_i$ . Noting the mass fraction that  $C_i = \frac{\rho_i}{\rho}$ , we obtain the species concentration equation as

$$\frac{\partial \rho C_i}{\partial t} + \nabla \cdot (\rho \bar{U} C_i) = \nabla \cdot (\rho D \nabla C_i) + r_i, \quad (3.1.55)$$

If the species flows with the fluid flow velocity then  $\bar{U}$  = flow velocity  $u$ .

## Maxwell's Equations

A set of partial differential equations that, together with the Lorentz force law, form the foundation of classical electrodynamics and electric circuits are known as Maxwell's equations. Maxwell's equations, named after the Scottish physicist and mathematician James Clerk Maxwell, describe how magnetic and electric fields are generated and their interaction with charges. The following are Maxwell's equations.

$$\begin{aligned}\nabla \cdot \mathbf{E} &= \frac{\rho_v}{\epsilon} && \text{(Gauss law)} \\ \nabla \cdot \mathbf{B} &= 0 && \text{(Gauss law for magnetism)} \\ -\frac{\partial \mathbf{B}}{\partial t} &= \nabla \times \mathbf{E} && \text{(Faraday's law)} \\ \nabla \times \mathbf{B} &= \mu_e \mathbf{j} && \text{(Ampere's law)} \\ \mathbf{j} &= \sigma(\mathbf{E} + \mathbf{q} \times \mathbf{B}) && \text{(Ohm's law)}\end{aligned}\tag{3.1.56}$$

Where  $\rho_v$  is the volume charge density,  $\epsilon$  is the permittivity of the material,  $\mu_e$  is magnetic permeability,  $\mathbf{B}$  is Magnetic field,  $\mathbf{j}$  is electric current density,  $\mathbf{E}$  is electric field and  $\sigma$  is electrical conductivity.

## 3.2 Methods of Solution

In this research, some mathematical techniques were employed to tackle the resulting non-linear boundary value problems. For some simple cases of flows through tubes, channels and parallel plates, the resulting systems of differential equations may have exact solutions, but in general, most of the fluid mechanics problems have no exact solutions because of the nonlinearity of the problems.

In this section the methods of solution that are the numerical computations used in this study are described. The entire computational algorithms evolved from this work were implemented using MAPLE symbolic package.

### 3.2.1 Computational Techniques for Solving BVPs

#### The Shooting Method

Many important real world physical problems lead to boundary value problems(BVPs). The shooting method is one among the commonly used powerful numerical methods for solving boundary value problems for ordinary differential equations. The shooting method is an iterative algorithm that reformulates the original boundary value problem (BVPs) to a related initial value problem (IVPs) with its appropriate initial conditions. The new problem requires the solution of the IVP with the initial conditions arbitrary chosen to approximate the boundary conditions at the end points. If these boundary conditions are not satisfied to the required accuracy, the procedure is repeated again with a new set of initial conditions until the required accuracy is acquired or a limit to the iteration is reached. The resultant IVP is solved numerically using any appropriate methods of solving IVPs.

For illustrations, consider the two point boundary value problem

$$y'''(x) = f(x, y, y', y'') \quad \text{with} \quad y(a) = \alpha \quad y(b) = \beta, \quad y'(b) = \gamma, \quad x \in [a, b]. \quad (3.2.1)$$

To solve this problem by shooting method, it needs to be reduced to the equivalent system of first order ODEs.

Defining new variables:  $y = f_1$ ,  $y' = f_2$ ,  $y'' = f_3$  and assuming the missing initial conditions as  $f_2(a) = p$ ,  $f_3(a) = q$ , we obtain the following system of IVPs

$$\begin{aligned} f_1' &= f_2, & f_1(a) &= \alpha, \\ f_2' &= f_3, & f_2(a) &= p, \\ f_3' &= f(x, f_1, f_2, f_3), & f_3(a) &= q, \end{aligned} \quad (3.2.2)$$

with two shooting parameters  $p$  and  $q$ . The solution of this IVP fulfills the following two requirements,

$$\begin{aligned} F_1(p, q) &= f_1(b; p, q) - \beta = 0, \\ F_2(p, q) &= f_2(b; p, q) - \gamma = 0. \end{aligned} \quad (3.2.3)$$

The zeros  $(p, q)$  of this system of non-linear algebraic equations can be found with any standard root-finding techniques such as Newton-Raphson method.

The solution  $f_1(x; p, q)$  of the IVP Equation (3.2.2) can be obtained using any standard IVP solving techniques such as Runge-Kutta-Fehlberg method and will coincide with the solution  $y(x)$  of the BVP Equation (3.2.1), as long as the values for  $p$  and  $q$  are found and satisfy the requirements mentioned above.

### Multidimensional Newton Raphson Method

In numerical analysis, the Newton-Raphson Method is a method for finding successively better approximations to the roots (or zeros) of a real-valued function.

Consider a system of  $n$  nonlinear equations with  $n$  unknowns, as the one described below:

$$\begin{bmatrix} f_1(x_1, x_2, \dots, x_n) \\ f_2(x_1, x_2, \dots, x_n) \\ \cdot \\ \cdot \\ \cdot \\ f_n(x_1, x_2, \dots, x_n) \end{bmatrix} = \begin{bmatrix} 0 \\ 0 \\ \cdot \\ \cdot \\ \cdot \\ 0 \end{bmatrix}, \quad (3.2.4)$$

where  $f_i(x_1, x_2, \dots, x_n) : \mathbb{R}^n \rightarrow \mathbb{R}, i = 1, \dots, n$ , are nonlinear functions. The system of equations (3.2.4) can be rewritten in compact form as:

$$\mathbf{f}(\mathbf{x}) = \mathbf{0}, \quad (3.2.5)$$

where  $\mathbf{f} = [f_1(\mathbf{x}), f_2(\mathbf{x}), \dots, f_n(\mathbf{x})]^T = \mathbf{0} : \mathbb{R}^n \rightarrow \mathbb{R}^n, \mathbf{x} = [x_1, x_2, \dots, x_n]^T \in \mathbb{R}^n, \mathbf{0} = [0, 0, \dots, 0]^T$

Given an initial value for vector  $\mathbf{x}$ , i.e.,  $\mathbf{x}^{(0)}$ , we have, in general, that  $\mathbf{f}(\mathbf{x}^{(0)}) \neq \mathbf{0}$ . Thus, we need to find  $\Delta \mathbf{x}^{(0)}$  so that  $\mathbf{f}(\mathbf{x}^{(0)} + \Delta \mathbf{x}^{(0)}) = \mathbf{0}$ . Using the first-order Taylor series  $\mathbf{f}(\mathbf{x}^{(0)} + \Delta \mathbf{x}^{(0)})$  can be approximately expressed as:

$$\mathbf{f}(\mathbf{x}^{(0)} + \Delta \mathbf{x}^{(0)}) \approx \mathbf{f}(\mathbf{x}^{(0)}) + \mathbf{J}^{(0)} \Delta \mathbf{x}^{(0)}, \quad (3.2.6)$$

where  $\mathbf{J}$  is  $n \times n$  Jacobian:

$$\mathbf{J} = \begin{bmatrix} \frac{\partial f_1(\mathbf{x})}{\partial x_1} & \frac{\partial f_1(\mathbf{x})}{\partial x_2} & \dots & \frac{\partial f_1(\mathbf{x})}{\partial x_n} \\ \frac{\partial f_2(\mathbf{x})}{\partial x_1} & \frac{\partial f_2(\mathbf{x})}{\partial x_2} & \dots & \frac{\partial f_2(\mathbf{x})}{\partial x_n} \\ \vdots & \vdots & \ddots & \vdots \\ \frac{\partial f_n(\mathbf{x})}{\partial x_1} & \frac{\partial f_n(\mathbf{x})}{\partial x_2} & \dots & \frac{\partial f_n(\mathbf{x})}{\partial x_n} \end{bmatrix} \quad (3.2.7)$$

Since we seek  $\mathbf{f}(\mathbf{x}^{(0)} + \Delta\mathbf{x}^{(0)}) = \mathbf{0}$ , from Equation(3.2.6) we can compute  $\Delta\mathbf{x}^{(0)}$  as

$$\Delta\mathbf{x}^{(0)} \approx -[\mathbf{J}^{(0)}]^{-1}\mathbf{f}(\mathbf{x}^{(0)}) \quad (3.2.8)$$

Then, we can update vector  $\mathbf{x}$  as:

$$\mathbf{x}^{(1)} = \mathbf{x}^{(0)} + \Delta\mathbf{x}^{(0)} \quad (3.2.9)$$

$$\mathbf{x}^{(\nu+1)} = \mathbf{x}^{(\nu)} - [\mathbf{J}^{(\nu)}]^{-1}\mathbf{f}(\mathbf{x}^{(\nu)}), \quad (3.2.10)$$

where  $\nu$  is the iteration counter.

### Runge-Kutta-Fehlberg Method

One way to guarantee accuracy in the solution of an IVP is to solve the problem twice using step sizes  $h$  and  $\frac{h}{2}$  and compare answers at the mesh points corresponding to the larger step size. But this requires a significant amount of computation for the smaller step size and must be repeated if it is determined that the agreement is not good enough.

The Runge-Kutta-Fehlberg method (denoted RKF45) is one way to try to resolve this problem. It has a procedure to determine if the proper step size  $h$  is being used. At each step, two different approximations for the solution are made and compared. If the two answers are in close agreement, the approximation is accepted. If the two answers do not agree to a specified accuracy, the step size is reduced. If the answers agree to more significant digits than required, the step size is increased ([Faires and](#)

Burden, 2012). Each step requires the use of the following six values:

$$\begin{aligned}
k_1 &= hf(t_k, y_k), \\
k_2 &= hf\left(t_k + \frac{1}{4}h, y_k + \frac{1}{4}k_1\right), \\
k_3 &= hf\left(t_k + \frac{3}{8}h, y_k + \frac{3}{32}k_1 + \frac{9}{32}k_2\right), \\
k_4 &= hf\left(t_k + \frac{12}{13}h, y_k + \frac{1932}{2197}k_1 - \frac{7200}{2197}k_2 + \frac{7296}{2197}k_3\right), \\
k_5 &= hf\left(t_k + h, y_k + \frac{439}{216}k_1 - 8k_2 + \frac{3680}{513}k_3 - \frac{845}{4104}k_4\right), \\
k_6 &= hf\left(t_k + \frac{1}{2}h, y_k - \frac{8}{27}k_1 + 2k_2 - \frac{3544}{2565}k_3 + \frac{1859}{4104}k_4 - \frac{11}{40}k_5\right),
\end{aligned} \tag{3.2.11}$$

An approximation to the solution of the IVP is made using a Runge-Kutta method of order 4:

$$y_{k+1} = y_k + \frac{25}{216}k_1 - \frac{1408}{2565}k_3 + \frac{2197}{4104}k_4 - \frac{1}{5}k_5, \tag{3.2.12}$$

A better value for the solution is determined using a Runge-Kutta method of order 5:

$$Z_{k+1} = y_k + \frac{16}{135}k_1 + \frac{6656}{12825}k_3 + \frac{28561}{56430}k_4 - \frac{9}{50}k_5 + \frac{2}{55}k_6, \tag{3.2.13}$$

An estimate of the error can be obtained by subtracting the two values obtained. If the error exceeds a specific threshold, the results can be recalculated using a smaller step size. The approach to estimating the new step size is given below:

$$h_{new} = h_{old} \left( \frac{\epsilon h_{old}}{2|Z_{k+1} - y_{k+1}|} \right)^{\frac{1}{4}} \tag{3.2.14}$$

Where  $\epsilon$  is the prescribed tolerance.

The following chapters deal with the formulation of different problems of boundary layer flow of nanofluid.

## Chapter 4

# Mixed Convection Flow of a Radiating Magnetic Nanofluid Past a Heated Permeable Stretching/Shrinking Sheet in a Porous Medium

### 4.1 Introduction

Mixed convection in heat and mass transfer has different applications in heat exchanges, solar collectors, nuclear reactors, atmospheric boundary layer flow, nanotechnology, and electronic apparatus, as reported by [Jamaludin et al. \(2019\)](#). Besides being used as a convective heat transfer mechanism, thermal radiation plays a key role in managing heat transfer processes. Controlling the effects of radiation on fluid flow and heat transfer problems has vigorous significance in engineering processes, nuclear plants, space vehicles, gas turbines, and satellites involving high temperatures needed in designing specific equipment, as reported by [Jamil et al. \(2020\)](#) and [Prasad et al. \(2006\)](#).

Taking this fact into account, various researchers have investigated radiation effects on mixed convection flow problems in view of different aspects of the problem. [Makinde \(2012\)](#) numerically investigated hydromagnetic mixed convection stagnation point flow past a vertical plate embedded in a highly porous medium with the effects of radiation and internal heat generation. Their results revealed that the local skin friction, local Nusselt number, and local Sherwood number intensify as magnetic field strength and radiation parameters increase. [Yasin et al. \(2016\)](#) investigated steady two-dimensional magnetohydrodynamic (MHD) flow past a permeable stretching or shrinking sheet with radiation effects. According to their results, dual solutions exist for shrinking surfaces, and the solution is unique for the stretching case. [Pal \(2009\)](#) analyzed the heat and mass transfer characteristics in a two-dimensional stagnation-point flow over a stretching vertical sheet under the effects of buoyancy force and thermal radiation using the implicit finite-difference method. Extending the idea, [Rashidi et al. \(2014\)](#) numerically investigated the buoyancy and thermal radiation effects on heat transfer of water-based nanofluid flow over a stretching sheet. Their results showed that the skin friction coefficient upturns with the intensification of the magnetic field and the radiation effect and declines with buoyancy parameter and nanoparticle volume fraction

parameter.

Despite the fact that several works on fluid flow and heat transfer problems with nanofluid have been testified, there appear to be no efforts in the literature to consider the combined effects of buoyancy force, thermal radiation, viscous and porous dissipation, and porous medium on the hydromagnetic stagnation point flow of nanofluid flowing past a permeable stretching/shrinking sheet with convective boundary conditions.

Thus, in this chapter, mixed convection stagnation point flow of a radiating magnetic nanofluid over a permeable stretching/shrinking sheet in a porous medium with convective conditions is investigated. Moreover, the inclusion of viscous and porous dissipation terms in the energy equation enables us to examine their effects on fluid flow and heat transfer. Such magnetohydrodynamic (MHD) boundary layer fluid flows of an electrically conducting fluid past a stretching/shrinking sheet have various applications in modern metallurgical and metal-working processes such as drawing of continuous filaments through quiescent fluids, and annealing and tinning of copper wires as mentioned in [Pal and Mondal \(2012\)](#) and [Chu et al. \(2020\)](#).

## 4.2 Mathematical Model Formulation

Considering a steady, laminar, viscous, and incompressible two dimensional stagnation point flow of a magnetic nanofluid past a heated permeable stretching/shrinking sheet which is embedded in a porous medium along the  $x$ -direction. It is assumed that a constant magnetic field of strength  $B_0$  is applied in the positive  $y$ -direction normal to the surface. The induced magnetic field is assumed to be small compared to the applied magnetic field. The ambient temperature of the fluid and the ambient concentration are taken as  $T_\infty$  and  $C_\infty$ , respectively. While the surface below the stretching/shrinking sheet is heated by convection from a hot fluid having initial temperature  $T_f$  with nanoparticles concentration  $C_f$  which provides a heat transfer coefficient  $h_1$  and mass transfer coefficient  $h_2$ . It is assumed that the porous medium is homogeneous and isotropic, and saturated with a nanofluid which is in local thermal equilibrium with the solid matrix. Further, the flow is assumed to be slow so that a Forchheimer quadratic drag term do not appear in the momentum equation.

The effects of thermal radiation is incorporated through energy equation. The fluid is considered to be a gray, absorbing emitting radiation but non-scattering medium and the Rosseland's approximation is used to describe the radiative heat flux in the energy equation. We choose the coordinate system so that the  $x$ -axis is along the stretching/shrinking sheet and the  $y$ -axis is normal to the sheet surface. A sketch of the physical model and the coordinates are given in Figure 4.2.1.

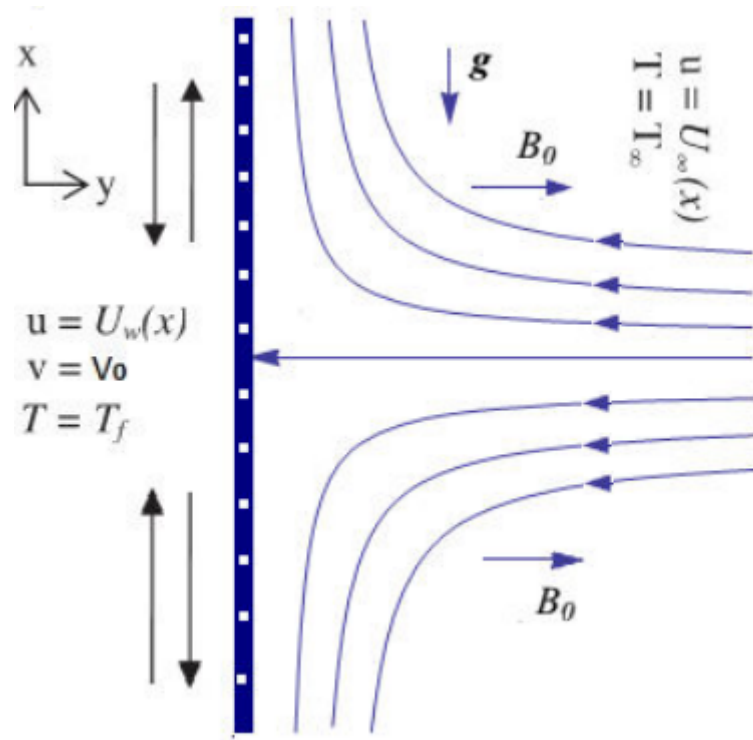


Figure 4.2.1: Flow diagram of the model

Based on the general fluid flow governing equations derived in chapter 3, the Buongiorno convective transport model equations and the above stated physical assumptions, the governing equation of total mass, momentum, temperature and species concentration in the presence of a transverse magnetic field past a convectively heated stretching/shrinking sheet embedded in a Darcian porous medium takes the following form:

$$\begin{aligned}
\frac{\partial u}{\partial x} + \frac{\partial v}{\partial y} &= 0, \\
u \frac{\partial u}{\partial x} + v \frac{\partial u}{\partial y} &= -\frac{1}{\rho_f} \frac{\partial p}{\partial x} + \frac{\mu_f}{\rho_f} \left( \frac{\partial^2 u}{\partial x^2} + \frac{\partial^2 u}{\partial y^2} \right) + \frac{J \times B}{\rho_f} - \frac{1}{\rho_f} (\rho \mathbf{g}) - \frac{\mu}{\rho_f K} u, \\
u \frac{\partial v}{\partial x} + v \frac{\partial v}{\partial y} &= -\frac{1}{\rho_f} \frac{\partial p}{\partial y} + \frac{\mu_f}{\rho_f} \left( \frac{\partial^2 v}{\partial x^2} + \frac{\partial^2 v}{\partial y^2} \right), \\
u \frac{\partial T}{\partial x} + v \frac{\partial T}{\partial y} &= \alpha_f \left( \frac{\partial^2 T}{\partial x^2} + \frac{\partial^2 T}{\partial y^2} \right) + \tau \left[ D_B \left( \frac{\partial C}{\partial x} \frac{\partial T}{\partial x} + \frac{\partial C}{\partial y} \frac{\partial T}{\partial y} \right) + \frac{D_T}{T_\infty} \left[ \left( \frac{\partial T}{\partial x} \right)^2 + \left( \frac{\partial T}{\partial y} \right)^2 \right] \right] \\
&\quad + \frac{\alpha_f \mu_f}{k} \left( \frac{\partial u}{\partial y} \right)^2 + \frac{J.J}{(\rho c_p)_f \sigma} + \frac{\mu u^2}{(\rho c_p)_f K} - \frac{1}{(\rho c_p)_f} \frac{\partial q_r}{\partial y}, \\
u \frac{\partial C}{\partial x} + v \frac{\partial C}{\partial y} &= D_B \left( \frac{\partial^2 C}{\partial x^2} + \frac{\partial^2 C}{\partial y^2} \right) + \left( \frac{D_T}{T_\infty} \right) \left( \frac{\partial^2 T}{\partial x^2} + \frac{\partial^2 T}{\partial y^2} \right).
\end{aligned}$$

Now making the standard boundary-layer approximation based on scale analysis, we obtained that variations along the y-axis within the boundary layer is much faster than the variations along the x-axis. i.e,

$$\frac{\partial u}{\partial x} \ll \frac{\partial u}{\partial y}, \quad \frac{\partial v}{\partial x} \ll \frac{\partial v}{\partial y}, \quad \frac{\partial T}{\partial x} \ll \frac{\partial T}{\partial y} \quad \text{and} \quad \frac{\partial C}{\partial x} \ll \frac{\partial C}{\partial y}.$$

Following the above discussion, the governing equations are simplified as

$$\frac{\partial u}{\partial x} + \frac{\partial v}{\partial y} = 0, \tag{4.2.1}$$

$$u \frac{\partial u}{\partial x} + v \frac{\partial u}{\partial y} = -\frac{1}{\rho_f} \frac{\partial p}{\partial x} + \frac{\mu_f}{\rho_f} \left( \frac{\partial^2 u}{\partial y^2} \right) + \frac{J \times B}{\rho_f} - \frac{1}{\rho_f} (\rho \mathbf{g}) - \frac{\mu}{\rho_f K} u, \tag{4.2.2}$$

$$\frac{\partial p}{\partial y} = 0, \tag{4.2.3}$$

$$\begin{aligned}
u \frac{\partial T}{\partial x} + v \frac{\partial T}{\partial y} &= \alpha_f \left( \frac{\partial^2 T}{\partial y^2} \right) + \tau \left[ D_B \left( \frac{\partial C}{\partial y} \frac{\partial T}{\partial y} \right) + \frac{D_T}{T_\infty} \left( \frac{\partial T}{\partial y} \right)^2 \right] \\
&\quad + \frac{\alpha_f \mu_f}{k} \left( \frac{\partial u}{\partial y} \right)^2 + \frac{J.J}{(\rho c_p)_f \sigma} + \frac{\mu u^2}{(\rho c_p)_f K} - \frac{1}{(\rho c_p)_f} \frac{\partial q_r}{\partial y},
\end{aligned} \tag{4.2.4}$$

$$u \frac{\partial C}{\partial x} + v \frac{\partial C}{\partial y} = D_B \left( \frac{\partial^2 C}{\partial y^2} \right) + \left( \frac{D_T}{T_\infty} \right) \left( \frac{\partial^2 T}{\partial y^2} \right). \tag{4.2.5}$$

The nanofluid density  $\rho$  can be approximated by the the base fluid density  $\rho_f$  when  $C$  is small, i. e.  $\rho = C\rho_p + (1 - C)\rho_f$ .

By using the Oberbeck-Boussinesq approximation, body force term in the momentum equation can be linearized by neglecting a term proportional to the product of  $C$  and  $T$ . This assumption is likely to be valid in the case of small temperature gradients in a dilute suspension of nano particles. Thus, we can approximate the body force term as

$$\rho_f = \rho_{f\infty} + \frac{\partial \rho}{\partial T}(T - T_\infty) + \text{Higher order terms} \quad (4.2.6)$$

where,

$$\beta = -\frac{1}{\rho_{f\infty}} \frac{\partial \rho}{\partial T} \implies \frac{\partial \rho}{\partial T} = -\beta \rho_{f\infty}.$$

Neglecting the higher order terms and making a substitution, we get

$$\rho_f = \rho_{f\infty} - \beta \rho_{f\infty}(T - T_\infty). \quad (4.2.7)$$

By substituting 4.2.7 into the momentum equation, we get

$$\begin{aligned} u \frac{\partial u}{\partial x} + v \frac{\partial u}{\partial y} = & -\frac{1}{\rho_f} \frac{\partial p}{\partial x} + \frac{\mu_f}{\rho_f} \left( \frac{\partial^2 u}{\partial y^2} \right) + \frac{J \times B}{\rho_f} - \frac{\mu}{\rho_f K} u \\ & - \frac{1}{\rho_f} [C \rho_p + (1-C) \rho_{f\infty} - (1-C) \rho_{f\infty} \beta (T - T_\infty)] \mathbf{g}. \end{aligned} \quad (4.2.8)$$

The Lorenzean force,  $J \times B$ , is obtained as

$$J = \sigma(E + q \times B). \quad (4.2.9)$$

Where  $J$  is current density,  $B = (0, B_0, 0)$  is magnetic field normal to the flow,  $q = (u, v, 0)$  is velocity,  $\sigma$  is electrical conductivity and  $E = 0$  is the electric field.

$$J = \sigma(E + q \times B) = \sigma \begin{vmatrix} i & j & k \\ u & v & 0 \\ 0 & B_0 & 0 \end{vmatrix} = \sigma(0, 0, uB_0). \quad (4.2.10)$$

Then

$$J \times B = \begin{vmatrix} i & j & k \\ 0 & 0 & \sigma u B_0 \\ 0 & B_0(x) & 0 \end{vmatrix} = -\sigma u B_0^2 i \quad (4.2.11)$$

$$\frac{J.J}{\sigma} = \frac{\sigma^2 B_0^2 u^2}{\sigma} = \sigma B_0^2 u^2 \quad (4.2.12)$$

Substituting the Lorenzean force term 4.2.11 into equation 4.2.8, then the momentum equation will be

$$\begin{aligned} \rho_f \left( u \frac{\partial u}{\partial x} + v \frac{\partial u}{\partial y} \right) &= -\frac{\partial p}{\partial x} + \mu_f \left( \frac{\partial^2 u}{\partial y^2} \right) - \sigma B_0^2 u - \frac{\mu}{\rho_f K} u \\ &\quad - [C \rho_p + (1 - C) \rho_{f\infty} - (1 - C) \rho_{f\infty} \beta (T - T_\infty)] \mathbf{g}. \end{aligned} \quad (4.2.13)$$

At free stream, i.e.  $y \rightarrow \infty$

$$-\frac{\partial p}{\partial x} = \rho_f U_\infty \frac{\partial U_\infty}{\partial x} + \sigma B_0^2 U_\infty + \frac{\mu}{\rho_f K} U_\infty + [\rho_p C_\infty + \rho_{f\infty} - C_\infty \rho_{f\infty}] \mathbf{g}. \quad (4.2.14)$$

Now substituting for the  $-\frac{\partial p}{\partial x}$  term into the momentum equation, the momentum equation becomes

$$\begin{aligned} u \frac{\partial u}{\partial x} + v \frac{\partial u}{\partial y} &= U_\infty \frac{\partial U_\infty}{\partial x} + \frac{\mu_f}{\rho_f} \frac{\partial^2 u}{\partial y^2} - \frac{\sigma B_0^2}{\rho_f} (u - U_\infty) - \frac{\mu_f}{\rho_f K} (u - U_\infty) \\ &\quad + \frac{1}{\rho_f} \left[ (1 - C_\infty) \rho_{f\infty} \beta \mathbf{g} (T - T_\infty) - (\rho_p - \rho_\infty) \mathbf{g} (C - C_\infty) \right]. \end{aligned} \quad (4.2.15)$$

Considering equation 4.2.12, the energy equation is redefined as

$$\begin{aligned} u \frac{\partial T}{\partial x} + v \frac{\partial T}{\partial y} &= \alpha_f \left( \frac{\partial^2 T}{\partial y^2} \right) + \tau \left[ D_B \frac{\partial C}{\partial y} \frac{\partial T}{\partial y} + \frac{D_T}{T_\infty} \left( \frac{\partial T}{\partial y} \right)^2 \right] + \frac{\alpha_f \mu_f}{k} \left( \frac{\partial u}{\partial y} \right)^2 + \frac{\sigma_f B_0^2 u^2}{(\rho c_p)_f} \\ &\quad + \frac{\mu u^2}{(\rho c_p)_f K} - \frac{1}{(\rho c_p)_f} \frac{\partial q_r}{\partial y}. \end{aligned} \quad (4.2.16)$$

By using the Rosseland diffusion approximation, the radiative heat flux,  $q_r$  is given by:

$$q_r = \frac{-4\sigma^* T_\infty^3}{3k^*} \frac{\partial T^4}{\partial y} \quad (4.2.17)$$

where  $\sigma^*$  and  $k^*$  are the Stefan-Boltzman constant and the Rosseland mean absorption coefficient, respectively. We assume that the temperature differences within the flow are sufficiently small so that  $T^4$  may be expressed as a linear function of temperature  $T$ .

$$T^4 = 4T_\infty^3 T - 3T_\infty^4 \quad (4.2.18)$$

Then the radiative flux in energy equation is determined as

$$\frac{\partial q_r}{\partial y} = \frac{16\sigma^*T_\infty^3}{3kk^*} \frac{\partial^2 T}{\partial y^2} \quad (4.2.19)$$

Then substituting equation 4.2.19 into the energy equation, we get

$$\begin{aligned} u \frac{\partial T}{\partial x} + v \frac{\partial T}{\partial y} = \alpha_f \left( 1 + \frac{16\sigma^*T_\infty^3}{3kk^*} \right) \left( \frac{\partial^2 T}{\partial y^2} \right) + \tau \left[ D_B \frac{\partial C}{\partial y} \frac{\partial T}{\partial y} + \frac{D_T}{T_\infty} \left( \frac{\partial T}{\partial y} \right)^2 \right] \\ + \frac{\alpha_f \mu_f}{k} \left( \frac{\partial u}{\partial y} \right)^2 + \left( \frac{\alpha_f \sigma B_0^2 u^2}{k} + \frac{\alpha_f \mu_f u^2}{kK} \right). \end{aligned} \quad (4.2.20)$$

In order to have a balanced equation at the free stream condition, the energy equation is redefined as

$$\begin{aligned} u \frac{\partial T}{\partial x} + v \frac{\partial T}{\partial y} = \alpha_f \left( 1 + \frac{16\sigma^*T_\infty^3}{3kk^*} \right) \left( \frac{\partial^2 T}{\partial y^2} \right) + \tau \left[ D_B \frac{\partial C}{\partial y} \frac{\partial T}{\partial y} + \frac{D_T}{T_\infty} \left( \frac{\partial T}{\partial y} \right)^2 \right] + \\ \frac{\alpha_f \mu_f}{k} \left( \frac{\partial u}{\partial y} \right)^2 + \left( \frac{\alpha_f \sigma B_0^2}{k} + \frac{\alpha_f \mu_f}{kK} \right) (u - U_\infty)^2. \end{aligned} \quad (4.2.21)$$

After performing the Oberbeck-Boussinesq approximation and boundary layer approximations for mass, momentum, thermal energy and solid volume fraction of nanofluid in the presence of magnetic field, the governing equations for the nanofluid flow past a stretching/shrinking sheet is expressed as:

$$\frac{\partial u}{\partial x} + \frac{\partial v}{\partial y} = 0, \quad (4.2.22)$$

$$\begin{aligned} u \frac{\partial u}{\partial x} + v \frac{\partial u}{\partial y} = U_\infty \frac{\partial U_\infty}{\partial x} + \frac{\mu_f}{\rho_f} \frac{\partial^2 u}{\partial y^2} - \frac{\sigma B_0^2}{\rho_f} (u - U_\infty) - \frac{\mu_f}{\rho_f K} (u - U_\infty) + \\ \frac{1}{\rho_f} \left[ (1 - C_\infty) \rho_{f\infty} \beta g (T - T_\infty) - (\rho_p - \rho_{f\infty}) g (C - C_\infty) \right], \end{aligned} \quad (4.2.23)$$

$$\begin{aligned} u \frac{\partial T}{\partial x} + v \frac{\partial T}{\partial y} = \alpha_f \left( 1 + \frac{16\sigma^*T_\infty^3}{3kk^*} \right) \left( \frac{\partial^2 T}{\partial y^2} \right) + \tau \left( D_B \frac{\partial C}{\partial y} \frac{\partial T}{\partial y} + \frac{D_T}{T_\infty} \left( \frac{\partial T}{\partial y} \right)^2 \right) + \\ \frac{\alpha_f \mu_f}{k} \left( \frac{\partial u}{\partial y} \right)^2 + \left( \frac{\alpha_f \sigma B_0^2}{k} + \frac{\alpha_f \mu_f}{kK} \right) (u - U_\infty)^2, \end{aligned} \quad (4.2.24)$$

$$u \frac{\partial C}{\partial x} + v \frac{\partial C}{\partial y} = D_B \frac{\partial^2 C}{\partial y^2} + \left( \frac{D_T}{T_\infty} \right) \left( \frac{\partial^2 T}{\partial y^2} \right), \quad (4.2.25)$$

where the velocity components along the  $x$  and  $y$  directions are given by  $u$  and  $v$ , respectively. The nanoparticle density, the density of base fluid, the absolute viscosity of

the base fluid, the thermal diffusivity of the base fluid, the Stefan-Boltzman constant, the mean absorption coefficient are denoted by  $\rho_p$ ,  $\rho_f$ ,  $\mu_f$ ,  $\alpha_f$ ,  $\sigma^*$ ,  $k^*$ , respectively. Furthermore,  $\tau = \frac{(\rho c)_p}{(\rho c)_f}$  is the ratio of nanoparticle heat capacity and the base fluid heat capacity,  $K$  is the porous medium permeability,  $T$  is the local temperature,  $C$  is the local solid volume fraction of the nanofluid,  $\beta$  is volumetric thermal expansion coefficient of the base fluid,  $D_B$  is the Brownian diffusion coefficient,  $D_T$  is the thermophoretic diffusion coefficient and  $g$  is the acceleration due to gravity. The subscript  $\infty$  denotes the values at large values of  $y$  where the fluid is quiescent.

The boundary conditions are written as:

$$y = 0 : u = U_w(x) = ax, \quad v = V_0, \quad -k \frac{\partial T}{\partial y} = h_1(T_f - T), \quad -D_B \frac{\partial C}{\partial y} = h_2(C_f - C), \quad (4.2.26)$$

$$y \rightarrow \infty : u \rightarrow U_\infty(x), \quad T \rightarrow T_\infty, \quad C \rightarrow C_\infty, \quad (4.2.27)$$

where  $U_\infty(x) = \frac{\alpha_f}{x} Ra_x^{1/2}$  is the external velocity,  $Ra_x = \frac{(1 - C_\infty) g \beta (T_f - T_\infty) x^3}{\nu \alpha_f}$  is the local Rayleigh number,  $U_w(x) = ax$  is the stretching/shrinking velocity of the sheet,  $a$  is a constant and  $V_0$  is the wall mass transfer velocity.

### 4.3 Similarity Transformation

Introducing the following non-dimensional similarity variables, the governing equations (4.2.22) - (4.2.24) and the boundary equations (4.2.26) - (4.2.27) are transformed into a non-dimensional form (Makinde et al., 2013):

$$\eta = \frac{y}{x} Ra_x^{1/4}, \quad \psi(x, y) = \alpha_f Ra_x^{1/4} f(\eta), \quad \theta(\eta) = \frac{T - T_\infty}{T_f - T_\infty}, \quad \phi(\eta) = \frac{C - C_\infty}{C_f - C_\infty}. \quad (4.3.1)$$

Now using the similarity transformation quantities given above, the similarity transformation processes to ordinary differential equations are as shown below,

$$u = \frac{\partial \psi}{\partial y} = \frac{\alpha_f}{x} Ra_x^{1/4} f'(\eta) Ra_x^{1/4} \Rightarrow u = \frac{\alpha_f}{x} Ra_x^{1/2} f'(\eta), \quad (4.3.2)$$

$$v = -\frac{\partial \psi}{\partial x} = -\frac{\partial}{\partial x} \left( \alpha_f Ra_x^{1/4} f(\eta) \right) = -\alpha_f \left[ Ra_x^{1/4} f'(\eta) \frac{\partial \eta}{\partial x} + f(\eta) \frac{\partial Ra_x^{1/4}}{\partial x} \right]$$

$$\begin{aligned}
v = -\frac{\partial\psi}{\partial x} &= -\frac{\partial}{\partial x} \left( \alpha_f Ra_x^{\frac{1}{4}} f(\eta) \right) = -\alpha_f \left[ \frac{-y}{4x^2} Ra_x^{\frac{1}{2}} f'(\eta) + \frac{3}{4x} Ra_x^{\frac{1}{4}} f(\eta) \right], \\
&= \frac{\alpha_f Ra_x^{\frac{1}{4}}}{4x} \left( \eta f'(\eta) - 3f(\eta) \right) \tag{4.3.3}
\end{aligned}$$

$$T = T_\infty + (T_f - T_\infty)\theta(\eta) \Rightarrow \frac{\partial T}{\partial y} = (T_f - T_\infty)\theta'(\eta) \frac{Ra_x^{\frac{1}{4}}}{x}, \tag{4.3.4}$$

$$\Rightarrow \frac{\partial^2 T}{\partial y^2} = \frac{(T_f - T_\infty)}{x^2} \theta''(\eta) Ra_x^{\frac{1}{2}}, \tag{4.3.5}$$

and

$$\frac{\partial T}{\partial x} = (T_f - T_\infty)\theta'(\eta) \frac{d\eta}{dx} \Rightarrow \frac{\partial T}{\partial x} = -\frac{y}{4x^2} (T_f - T_\infty)\theta'(\eta) Ra_x^{\frac{1}{4}}, \tag{4.3.6}$$

$$C = C_\infty + (C_f - C_\infty)\phi(\eta) \Rightarrow \frac{\partial C}{\partial y} = \frac{(C_f - C_\infty)}{x} \phi'(\eta) Ra_x^{\frac{1}{4}}, \tag{4.3.7}$$

$$\Rightarrow \frac{\partial^2 C}{\partial y^2} = \frac{(C_f - C_\infty)}{x^2} \phi''(\eta) Ra_x^{\frac{1}{2}}, \tag{4.3.8}$$

and

$$\frac{\partial C}{\partial x} = (C_f - C_\infty)\phi'(\eta) \frac{d\eta}{dx} = -\frac{y}{4x^2} (C_f - C_\infty)\phi'(\eta) Ra_x^{\frac{1}{4}}. \tag{4.3.9}$$

### The Continuity equation

$$\begin{aligned}
\frac{\partial u}{\partial x} + \frac{\partial v}{\partial y} &= \frac{\partial}{\partial x} \left( \frac{\alpha_f}{x} Ra_x^{\frac{1}{2}} f'(\eta) \right) + \frac{\partial}{\partial y} \left( -\alpha_f \left[ \frac{-y}{4x^2} Ra_x^{\frac{1}{2}} f'(\eta) + \frac{3}{4x} Ra_x^{\frac{1}{4}} f(\eta) \right] \right) \\
&= 0. \tag{4.3.10}
\end{aligned}$$

### The Momentum equation

Substituting equations (4.3.2)- (4.3.9) into the x-momentum equation (4.2.23), we obtain

$$\begin{aligned}
&\frac{-1}{x^3} \alpha_f^2 Ra_x f'(\eta)^2 + \frac{3}{2x^3} \alpha_f^2 Ra_x f'(\eta)^2 - \frac{y}{4x^4} \alpha_f^2 Ra_x^{\frac{5}{4}} f'(\eta) f''(\eta) - \frac{3}{4x^3} \alpha_f^2 Ra_x f(\eta) f''(\eta) + \\
&\frac{y}{4x^4} \alpha_f^2 Ra_x^{\frac{5}{4}} f'(\eta) f''(\eta) = \frac{1}{x} \alpha_f Ra_x^{\frac{1}{2}} \left( -\frac{\alpha_f}{x^2} Ra_x^{\frac{1}{2}} + \frac{3\alpha_f}{2x^2} Ra_x^{\frac{1}{2}} \right) + \frac{\mu_f}{\rho_f} \frac{\partial}{\partial y} \left( \frac{\alpha_f}{x} Ra_x^{\frac{1}{2}} f''(\eta) \frac{1}{x} Ra_x^{\frac{1}{4}} \right) - \\
&\frac{\sigma_f B_0^2}{\rho_f} \left( \frac{\alpha_f}{x} Ra_x^{\frac{1}{2}} f'(\eta) - \frac{\alpha_f}{x} Ra_x^{\frac{1}{2}} \right) - \frac{\mu_f}{\rho_f K} \left( \frac{\alpha_f}{x} Ra_x^{\frac{1}{2}} f'(\eta) - \frac{\alpha_f}{x} Ra_x^{\frac{1}{2}} \right) + \\
&\frac{1}{\rho_f} \left[ (1 - C_\infty) \rho_{f\infty} \beta g (T - T_\infty) - (\rho_p - \rho_{f\infty}) g (C - C_\infty) \right], \tag{4.3.11}
\end{aligned}$$

After some simplifications of equation (4.3.11), we obtain

$$\begin{aligned} \frac{1}{2x^3}\alpha_f^2 Ra_x (f'(\eta))^2 - \frac{3}{4x^3}\alpha_f^2 Ra_x f(\eta) f''(\eta) &= \frac{1}{2x^3}\alpha_f^2 Ra_x + \frac{\alpha_f \mu_f}{x^3 \rho_f} f'''(\eta) Ra_x - \frac{\sigma_f B_0^2}{\rho_f x} \alpha_f Ra_x^{\frac{1}{2}} (f'(\eta) - 1) \\ - \frac{\mu_f}{\rho_f K} \frac{\alpha_f}{x} Ra_x^{\frac{1}{2}} (f'(\eta) - 1) + \frac{1}{\rho_f} &[(1 - C_\infty) \rho_{f\infty} \beta g(T - T_\infty) - (\rho_p - \rho_\infty) \mathbf{g}(C - C_\infty)]. \end{aligned} \quad (4.3.12)$$

Dividing each term by  $Ra$ , we get

$$\begin{aligned} \frac{1}{2x^3}\alpha_f^2 (f'(\eta))^2 - \frac{3}{4x^3}\alpha_f^2 f(\eta) f''(\eta) &= \frac{\alpha_f^2}{2x^3} + \frac{\alpha_f \mu_f}{x^3 \rho_f} f'''(\eta) - \frac{\sigma_f B_0^2}{\rho_f x} \alpha_f Ra_x^{-\frac{1}{2}} (f'(\eta) - 1) - \\ \frac{\mu_f}{\rho_f K} \frac{\alpha_f}{x} Ra_x^{\frac{1}{2}} (f'(\eta) - 1) + \frac{1}{Ra_x \rho_f} &[(1 - \phi_\infty) \rho_{f\infty} \beta g(T - T_\infty) - (\rho_p - \rho_\infty) \mathbf{g}(\phi - \phi_\infty)]. \end{aligned} \quad (4.3.13)$$

Multiplying each term by  $\frac{x^3 \rho_f}{\mu_f \alpha_f}$ , we get

$$\begin{aligned} f'''(\eta) - \frac{\alpha_f \rho_f}{2\mu_f} (f'(\eta))^2 + \frac{3\alpha_f \rho_f}{4\mu_f} f(\eta) f''(\eta) + \frac{1}{2Pr} - \frac{\sigma_f B_0^2 x^2}{\mu_f} Ra_x^{-\frac{1}{2}} (f'(\eta) - 1) - \\ \frac{x^2}{K} Ra_x^{\frac{1}{2}} (f'(\eta) - 1) + \frac{x^3}{Ra_x \mu_f \alpha_f} [(1 - C_\infty) \rho_{f\infty} \beta g(T - T_\infty) - (\rho_p - \rho_\infty) \mathbf{g}(C - C_\infty)] = 0. \end{aligned} \quad (4.3.14)$$

After some simplifications and substitution of the parameters, we obtain

$$\begin{aligned} f'''(\eta) - (M + \frac{1}{Da}) (f'(\eta) - 1) - \frac{1}{2Pr} (f'(\eta))^2 + \frac{3}{4Pr} f(\eta) f''(\eta) + \frac{1}{2Pr} + \frac{T - T_\infty}{T_f - T_\infty} - \\ \frac{(\rho_p - \rho_f)(C_w - C_\infty)}{\rho_f \beta (1 - C_w)(T_f - T_\infty)} \frac{(C - C_\infty)}{(C_w - C_\infty)} = 0. \end{aligned} \quad (4.3.15)$$

Finally, we obtain

$$f''' - (M + \frac{1}{Da}) (f' - 1) + \frac{1}{4Pr} [3ff'' - 2f'^2 + 2] + \theta - Nrf = 0. \quad (4.3.16)$$

## The Energy equation

Substituting equations (4.3.2)- (4.3.9) into the energy equation (4.2.24), we obtain

$$\begin{aligned} \frac{\alpha_f}{x} Ra_x^{\frac{1}{2}} f'(\eta) \left( -\frac{y}{4x^2} (T_f - T_\infty) \theta'(\eta) Ra_x^{\frac{1}{4}} \right) + \left( \frac{y \alpha_f}{4x^2} f'(\eta) Ra_x^{\frac{1}{2}} - \frac{3\alpha_f}{4x} f(\eta) Ra_x^{\frac{1}{4}} \right) \\ \frac{(T_f - T_\infty)}{x} \theta'(\eta) Ra_x^{\frac{1}{4}} = \left[ 1 + \frac{16\sigma^* T_\infty^3}{3kk^*} \right] \frac{\alpha_f}{x^2} (T_f - T_\infty) \theta''(\eta) Ra_x^{\frac{1}{2}} + \tau \left( \frac{D_T}{T_\infty} \right) \left[ \frac{(T_f - T_\infty)}{x} \theta'(\eta) Ra_x^{\frac{1}{4}} \right]^2 + \\ \tau \left[ D_B \frac{(C_w - C_\infty)}{x} \phi'(\eta) Ra_x^{\frac{1}{4}} \frac{(T_f - T_\infty)}{x} \theta'(\eta) Ra_x^{\frac{1}{4}} \right] \frac{\alpha_f \mu_f}{k} \left( \frac{\alpha_f}{x^2} f''(\eta) Ra_x^{\frac{3}{4}} \right)^2 + \frac{\sigma B_0^2 \alpha_f^3}{kx^2} Ra_x (f'(\eta) - 1)^2 \\ + \frac{\alpha_f^3 \mu_f}{kKx^2} Ra_x (f'(\eta) - 1)^2, \end{aligned} \quad (4.3.17)$$

$$\begin{aligned}
& -\frac{3\alpha_f}{4x^2}(T_f - T_\infty)f(\eta)\theta'(\eta)Ra_x^{\frac{1}{2}} = \left(1 + \frac{4}{3}R\right)\frac{\alpha_f}{x^2}(T_f - T_\infty)\theta''(\eta)Ra_x^{\frac{1}{2}} + \\
& \tau \left[ D_B \frac{(C_w - C_\infty)(T_f - T_\infty)}{x^2} \phi'(\eta)\theta'(\eta)Ra_x^{\frac{1}{2}} \right] + \tau \left( \frac{D_T}{T_\infty} \right) \left[ \frac{(T_f - T_\infty)}{x} \theta'(\eta)Ra_x^{\frac{1}{4}} \right]^2 + \\
& \frac{\alpha_f \mu_f}{k} \left( \frac{\alpha_f}{x^2} f''(\eta) Ra_x^{\frac{3}{4}} \right)^2 + \frac{\sigma B_0^2 \alpha_f^3}{kx^2} Ra_x (f'(\eta) - 1)^2 + \frac{\alpha_f^3 \mu_f}{kKx^2} Ra_x (f'(\eta) - 1)^2. \quad (4.3.18)
\end{aligned}$$

Multiplying each term of equation (4.3.18) by the term  $\frac{x^2}{\alpha_f(T_f - T_\infty)Ra_x^{\frac{1}{2}}}$ , we obtain

$$\begin{aligned}
& \left(1 + \frac{4}{3}R\right)\theta''(\eta) + \frac{3}{4}f(\eta)\theta'(\eta) + \frac{\tau D_B(\phi_w - \phi_\infty)}{\alpha_f} \phi'(\eta)\theta'(\eta) + \frac{\tau D_T(T_f - T_\infty)}{T_\infty \alpha_f} \theta'(\eta)^2 \\
& + \frac{\alpha_f^2 \mu_f}{x^2 k (T_f - T_\infty)} Ra_x f''(\eta)^2 + \frac{\sigma B_0^2(x) \alpha_f^2}{k(T_f - T_\infty)} Ra_x^{\frac{1}{2}} (f'(\eta) - 1)^2 \\
& + \frac{\alpha_f^2 \mu_f}{kK(T_f - T_\infty)} Ra_x^{\frac{1}{2}} (f'(\eta) - 1)^2 = 0. \quad (4.3.19)
\end{aligned}$$

After some simplification, we obtain

$$\left(1 + \frac{4}{3}R\right)\theta'' + \frac{3}{4}f\theta' + EcPr \left[ f'^2 + \left(M + \frac{1}{Da}\right)(f' - 1)^2 \right] + Nb\phi'\theta' + Nt\theta'^2 = 0. \quad (4.3.20)$$

### The concentration equation

Substituting equation (4.3.2)- (4.3.9) into the concentration equation (4.2.25), we obtain

$$\begin{aligned}
& \frac{\alpha_f}{x} Ra_x^{\frac{1}{2}} f'(\eta) \left[ -\frac{y}{4x^2} (C_w - C_\infty) \phi'(\eta) Ra_x^{\frac{1}{4}} \right] + \frac{(C_w - C_\infty)}{x} \phi'(\eta) Ra_x^{\frac{1}{4}} \left[ \frac{y}{4x^2} \alpha_f f'(\eta) Ra_x^{\frac{1}{2}} - \frac{3}{4x} \alpha_f f(\eta) Ra_x^{\frac{1}{4}} \right] \\
& = D_B \frac{(C_w - C_\infty)}{x^2} \phi''(\eta) Ra_x^{\frac{1}{2}} + \left( \frac{D_T}{T_\infty} \right) \frac{(T_f - T_\infty)}{x^2} \theta''(\eta) Ra_x^{\frac{1}{2}}, \quad (4.3.21)
\end{aligned}$$

$$\begin{aligned}
& -\frac{y\alpha_f}{4x^3} (C_w - C_\infty) Ra_x^{\frac{3}{4}} f'(\eta) \phi'(\eta) + \frac{y\alpha_f}{4x^3} (C_w - C_\infty) Ra_x^{\frac{3}{4}} f'(\eta) \phi'(\eta) - \frac{3}{4x^2} \alpha_f \phi'(\eta) f(\eta) Ra_x^{\frac{1}{2}} \\
& = D_B \frac{(C_w - C_\infty)}{x^2} \phi''(\eta) Ra_x^{\frac{1}{2}} + \left( \frac{D_T}{T_\infty} \right) \frac{(T_f - T_\infty)}{x^2} \theta''(\eta) Ra_x^{\frac{1}{2}}. \quad (4.3.22)
\end{aligned}$$

Multiplying each terms of equation (4.3.22) by the term  $\frac{x^2}{D_B(C_w - C_\infty)Ra_x^{\frac{1}{2}}}$ , we obtain

$$\begin{aligned} & \left[ \frac{x^2}{D_B(C_w - C_\infty)Ra_x^{\frac{1}{2}}} \right] \frac{-3}{4x^2} \alpha_f \phi'(\eta) f(\eta) Ra_x^{\frac{1}{2}} = D_B \frac{(C_w - C_\infty)}{x^2} \phi''(\eta) Ra_x^{\frac{1}{2}} \left[ \frac{x^2}{D_B(C_w - C_\infty)Ra_x^{\frac{1}{2}}} \right] \\ & + \left[ \frac{x^2}{D_B(C_w - C_\infty)Ra_x^{\frac{1}{2}}} \right] \left( \frac{D_T}{T_\infty} \right) \frac{(T_f - T_\infty)}{x^2} \theta''(\eta) Ra_x^{\frac{1}{2}}, \end{aligned} \quad (4.3.23)$$

$$\phi'' + \frac{Nt}{Nb} \theta'' + \frac{3}{4} Le \phi' f = 0. \quad (4.3.24)$$

The boundary conditions will be

As  $\eta \rightarrow 0$

$$u(x, 0) = ax = \frac{\alpha_f}{x} Ra_x^{\frac{1}{2}} f'(0) \Rightarrow f'(0) = \frac{ax^2}{\alpha_f \sqrt{Ra_x}} = \lambda$$

$$v(x, 0) = V_0 = -\alpha_f \left[ -\frac{y}{4x^2} Ra_x^{\frac{1}{2}} f'(0) + \frac{3}{4x} Ra_x^{\frac{1}{4}} f(0) \right] \Rightarrow f(0) = \frac{-4x}{3\alpha_f Ra_x^{1/4}} V_0 = S$$

Substituting equation (4.3.4) in the convective boundary equation (4.2.26), we obtain

$$\theta'(0) = \frac{x}{-k(T_f - T_\infty)Ra_x^{\frac{1}{4}}} h_f(x)(T_f - T) \Rightarrow \theta'(0) = -Nc(1 - \theta(0))$$

Substituting equation (4.3.7) in the convective boundary equation (4.2.26), we obtain

$$\phi'(0) = \frac{x}{-D_B(C_f - C_\infty)Ra_x^{\frac{1}{4}}} h_f(x)(C_f - C) \Rightarrow \phi'(0) = -Nc^*(1 - \phi(0))$$

As  $\eta \rightarrow \infty$

$$u(x, \infty) = U_\infty(x) = \frac{\alpha_f}{x} Ra_x^{\frac{1}{2}} f'(\infty) \Rightarrow \frac{\alpha_f}{x} Ra_x^{\frac{1}{2}} = \frac{\alpha_f}{x} Ra_x^{\frac{1}{2}} s'(\infty) \Rightarrow f'(\infty) = 1$$

$$\theta(\infty) = \frac{T(x, \infty) - T_\infty}{T_f - T_\infty} = \frac{T_\infty - T_\infty}{T_f - T_\infty} \Rightarrow \theta(\infty) = 0$$

$$\phi(\infty) = \frac{C(x, \infty) - C_\infty}{C_w - C_\infty} = \frac{C_\infty - C_\infty}{C_w - C_\infty} \Rightarrow \phi(\infty) = 0$$

Finally, we obtained the following nonlinear ordinary differential equations as shown below:

$$f''' - \left(M + \frac{1}{Da}\right) (f' - 1) + \frac{1}{4Pr} [3ff'' - 2f'^2 + 2] + \theta - Nr\phi = 0, \quad (4.3.25)$$

$$\left(1 + \frac{4}{3}R\right) \theta'' + \frac{3}{4}f\theta' + EcPr \left[f''^2 + \left(M + \frac{1}{Da}\right) (f' - 1)^2\right] + Nb\phi'\theta' + Nt\theta'^2 = 0, \quad (4.3.26)$$

$$\phi'' + \frac{Nt}{Nb}\theta'' + \frac{3}{4}Le\phi'f = 0, \quad (4.3.27)$$

and the boundary equations become:

$$\eta = 0: \quad f(0) = S, \quad f'(0) = \lambda, \quad \theta'(0) = -Nc[1 - \theta(0)], \quad \phi'(0) = -Nc^*[1 - \phi(0)]. \quad (4.3.28)$$

$$\eta \rightarrow \infty: \quad f'(\infty) = 1, \quad \theta(\infty) = 0, \quad \phi(\infty) = 0. \quad (4.3.29)$$

Here  $f', \theta, \phi$  and  $\eta$  are the dimensionless velocity, temperature, particle concentration and similarity variable, respectively. The variables  $Nr, Pr, Le, Nb, Nt, R, M, Ec, Da, S$ , and  $\lambda$  denotes the nanofluid buoyancy ratio parameter, Prandtl number, the Lewis number, the Brownian motion parameter, the thermophoresis diffusion parameter, the radiation parameter, magnetic field parameter, Eckert number, the porous media parameter, suction/injection parameter and stretching/shrinking parameter, respectively. The parameters and dimensionless numbers are defined as follows:

$$\begin{aligned} Nr &= \frac{(\rho_p - \rho_f)(C_f - C_\infty)}{\rho_f \beta (1 - C_f)(T_f - T_\infty)}, & Nb &= \frac{\tau D_B (C_f - C_\infty)}{\alpha_f}, & Nt &= \frac{\tau D_T (T_f - T_\infty)}{\alpha_f T_\infty} \\ M &= \frac{\sigma_f B_0^2 x^2}{\mu_f Ra_x^{1/2}}, & Ec &= \frac{U_\infty^2}{C_{pf}(T_f - T_\infty)}, & Nc &= \frac{h_1 x}{k Ra_x^{1/4}}, & Nc^* &= \frac{h_2 x}{D_B Ra_x^{1/4}}, \\ R &= \frac{4\sigma^* T_\infty^3}{k^* k}, & Da &= \frac{K Ra_x^{1/2}}{x^2}, & \lambda &= \frac{ax^2}{\alpha_f \sqrt{Ra_x}}, & S &= \frac{-4x}{3\alpha_f Ra_x^{1/4}} V_0, & Pr &= \frac{\nu}{\alpha_f}. \\ Le &= \frac{\alpha_f}{D_B}. \end{aligned} \quad (4.3.30)$$

Where  $Nc$  and  $Nc^*$  are the heat transfer convective parameter and the mass transfer convective parameter, respectively. When  $Nc \rightarrow \infty$  and  $Nc^* \rightarrow \infty$ , the convective boundary conditions reduce to a uniform surface temperature and nanoparticle concentration.

## 4.4 Important Engineering Parameters

The important physical quantities of interest, in this problem, are the dimensionless skin friction coefficient, the local Nusselt number, and the local Sherwood number. Skin friction coefficient measures the friction that occurs at the boundary, Nusselt number helps to determine the wall heat flux and Sherwood number is used to determine the wall mass flux as explained by [Anwar \(2020\)](#). These important engineering parameters are defined as:

$$C_f = \frac{\tau_w}{\rho U_\infty^2} \implies f''(0) = \frac{C_f x^2}{\mu \alpha_f Ra_x^{3/4}}, \quad Nu_x = \frac{x q_w''}{k(T_f - T_\infty)}, \quad \text{and} \quad Sh_x = \frac{x q_m''}{D_B(C_f - C_\infty)}, \quad (4.4.1)$$

where  $\tau_w$  is the wall shear stress,  $q_w''$  is the wall heat flux due to the temperature gradient and  $q_m''$  is the wall mass flux due to the Brownian motion force at  $y = 0$  and given by

$$\tau_w = \mu \left( \frac{\partial u}{\partial y} \right) \Big|_{\eta=0}, \quad q_w'' = - \left[ \left( k + \frac{16\sigma^* T_\infty^3}{3k^*} \right) \frac{\partial T}{\partial y} \Big|_{\eta=0} \right], \quad \text{and} \quad q_m'' = -D_B \left( \frac{\partial C}{\partial y} \right) \Big|_{\eta=0}.$$

The dimensionless form of the wall shear stress, local Nusselt number and the local Sherwood number are derived as

$$C_f = \frac{\mu \left( \frac{\partial u}{\partial y} \right) \Big|_{\eta=0}}{\rho U_\infty^2} = \frac{\mu \frac{\partial}{\partial y} \left( \frac{\alpha_f}{x} Ra_x^{1/2} f'(\eta) \right) \Big|_{\eta=0}}{\rho U_\infty^2} = \frac{\mu \alpha_f Ra_x^{1/2} f''(0)}{x^2 \rho U_\infty^2}, \quad (4.4.2)$$

$$\implies C_f = \frac{\mu \alpha_f Ra_x^{1/2}}{x^2 \rho U_\infty^2} \implies C_f Ra_x^{1/4} = Pr f''(0)$$

$$Nu_x = \frac{-x \left[ \left( k + \frac{16\sigma^* T_\infty^3}{3k^*} \right) \frac{\partial T}{\partial y} \Big|_{\eta=0} \right]}{k(T_f - T_\infty)} = \frac{-xk \left( 1 + \frac{16\sigma^* T_\infty^3}{3kk^*} \right) (T_f - T_\infty) \theta'(0) Ra_x^{1/4}}{xk(T_f - T_\infty)} \quad (4.4.3)$$

$$\implies Nu_x = - \left( 1 + \frac{4}{3} R \right) \theta'(0) Ra_x^{1/4}$$

$$\implies Nu = Nu_x Ra_x^{-1/4} = - \left( 1 + \frac{4}{3} R \right) \theta'(0)$$

$$Sh_x = \frac{-xD_B \left( \frac{\partial C}{\partial y} \right) \Big|_{\eta=0}}{D_B(C_f - C_\infty)} = \frac{-xD_B(C_f - C_\infty) \phi'(0) Ra_x^{1/4}}{xD_B(C_f - C_\infty)} = -Ra_x^{1/4} \phi'(0)$$

$$\begin{aligned}\Rightarrow Sh_x &= -Ra_x^{1/4} \phi'(0) \\ \Rightarrow Sh &= Sh_x Ra_x^{-1/4} = -\phi'(0)\end{aligned}$$

where  $Ra_x, Nu_x, Sh_x$  are local Rayleigh number, local Nusselt number and local Sherwood number, respectively.

## 4.5 Numerical Procedures

The fourth-fifth order Runge-Kutta-Fehlberg method along with the shooting technique is implemented to analyze the flow model for the above coupled nonlinear ordinary differential equations (4.3.25)- (4.3.27) subject to the boundary conditions. Equations (4.3.28) and (4.3.29) for various values of the governing parameters. The solution procedure is an efficient, adaptive, and accurate method of order 4 with an error estimator of order 5. This method has been used by several researchers for solving problems of convective boundary layer flows, for instance papers by [Bohra et al. \(2017\)](#). To solve numerically using the Runge-Kutta-Fehlberg method, first, we need to reduce the coupled boundary value problem into a set of first-order ODEs to obtain a system of seven simultaneous equations of the first order.

Defining new variables, we obtain the following system

$$f = f_1, \quad f' = f_2, \quad f'' = f_3, \quad \theta = f_4, \quad \theta' = f_5, \quad \phi = f_6, \quad \phi' = f_7, \quad (4.5.1)$$

$$\begin{aligned}f_1' &= f_2, \\ f_2' &= f_3, \\ f_3' &= \left(M + \frac{1}{Da}\right)(f_2 - 1) - \frac{1}{4Pr} [3f_1 f_3 - 2f_2^2 + 2] - f_4 + Nr f_6, \\ f_4' &= f_5, \\ f_5' &= \frac{1}{\left(1 + \frac{4}{3}R\right)} \left[ \frac{-3}{4} f_1 f_5 - EcPr \left( f_3^2 + \left(M + \frac{1}{Da}\right)(f_2 - 1)^2 \right) - Nb f_7 f_5 - Nt f_5^2 \right], \\ f_6' &= f_7, \\ f_7' &= \frac{-Nt}{Nb\left(1 + \frac{4}{3}R\right)} \left[ \frac{-3}{4} f_1 f_5 - EcPr \left( f_3^2 + \left(M + \frac{1}{Da}\right)(f_2 - 1)^2 \right) - Nb f_7 f_5 - Nt f_5^2 \right] \\ &\quad - \frac{3}{4} Le f_7 f_1.\end{aligned} \quad (4.5.2)$$

Here prime denotes the differentiation with respect to  $\eta$  and the corresponding initial conditions are:

$$\begin{bmatrix} f_1(0) \\ f_2(0) \\ f_3(0) \\ f_4(0) \\ f_5(0) \\ f_6(0) \\ f_7(0) \end{bmatrix} = \begin{bmatrix} S \\ \lambda \\ u_1 \\ u_2 \\ -Nc(1-u_2) \\ u_3 \\ -Nc^*(1-u_3) \end{bmatrix} \quad (4.5.3)$$

Here we require seven initial conditions but one initial condition in each of  $f$ ,  $\theta$  and  $\phi$  are unknown. Thus, the values of the missing initial conditions  $u_1, u_2$  and  $u_3$  are approximated by using Newton-Raphson method until the boundary conditions at  $\eta \rightarrow \infty$  are satisfied.

To estimate the value of  $\eta_\infty$ , we start with some initial guess value and solve the problem consisting of equations (4.3.25)- (4.3.27). The process of finding a solution is repeated with another larger value of  $\eta_\infty$  until two consecutive values of the missing boundary conditions at  $\eta = 0$  differ only after desired significant digits. The last value  $\eta_\infty$  is taken as the finite value of the limit  $\eta_\infty$  for the particular set of parameters. For our case we choose  $\eta_\infty = 12$  so that the boundary conditions given by equation (4.3.29) become  $f'(12) = 1, \theta(12) = 0$  and  $\phi(12) = 0$ . The choice of  $\eta_\infty = 12$  ensures that all numerical solutions approached the asymptotic values correctly. MAPLE software is used to generate the numerical solutions of the transformed equations and boundary conditions.

## 4.6 Results and Discussion

The combined effects of buoyancy force, thermal radiation, porous medium, convective heating, viscous dissipation, magnetic field and nanofluid parameters on the dimensionless velocity, temperature, rescaled nanoparticle volume fraction, skin friction, heat and mass transfer rates from a permeable stretching/shrinking sheet are investigated numerically and presented. The range of parameters used in this study are  $0.1 \leq M \leq 0.5, 0 \leq Nr \leq 3.5, 0.1 \leq Ec \leq 1, 0.2 \leq Da \leq 10, 0.1 \leq Nb \leq 1.5, 0.1 \leq Nt \leq$

$0.5, -0.5 \leq S \leq 0.6, 0.1 \leq R \leq 1.5, 0 \leq Nc \leq 5, 0.1 \leq Nc^* \leq 1.5, 0.1 \leq Le \leq 1.5$ , and  $Pr = 6.2$  is used to signify the pure water as the base fluid.

### 4.6.1 Velocity Profiles with Parameter Variations

The alteration of the dimensionless velocity profile with the magnetic field and nanofluid buoyancy ratio parameters is depicted in Figure 4.6.1a. Due to the growing applications of the magnetic field normal to the stretching sheet surface, the velocity boundary layer thickness diminutions. It is further noted that the parameter ratio of buoyancy forces due to the thermal expansion of the base fluid and difference in densities of the nanoparticles and the base fluid (water) amplifies the dimensionless velocity profile drops. We thus deduce that the flow in the upward direction decelerates as the nanofluid buoyancy force due to the difference in densities of the nanoparticles and the base fluid (water) toughens. The role of porous media and mass suction/injection parameters on the dimensionless velocity profile is portrayed through Figure 4.6.1b. The dimensionless velocity profile drops with an increment in porous media parameter and the hydrodynamic boundary layer gets thickens as the porosity of the media increases. According to the numerical result obtained in Figure 4.6.1b, an increase in the mass suction/injection parameter reduces the dimensionless velocity profile within the hydrodynamic boundary layer. Causes for the deceleration of the fluid flow are that suction carries on the distance fluid into the region adjacent to the sheet thereby enhancing the viscosity which in turn opposes the fluid motion.

Figure 4.6.2a shows the dimensionless velocity profile for different values of the stretching/shrinking parameter while other parameters are assumed to be constant. As shown in this figure, when the stretching velocity increases, the dimensionless velocity profile decreases just after the transition point  $\eta = 0.56$  but very near the sheet surface a reverse phenomenon is observed. The momentum boundary layer thickness has also dependent on the stretching/shrinking parameter. For the stretching sheet, the momentum boundary layer thickness is larger than the shrinking case for layers of the fluid far from the sheet surface starting at  $\eta = 0.56$ . For highly shrinking surfaces, exaggerated change in dimensionless velocity and boundary layer thickness is observed which is contrary to a stretching surface. These kinds of changes in dimensionless velocity and momentum boundary layer thickness can occur until the shrinking surface

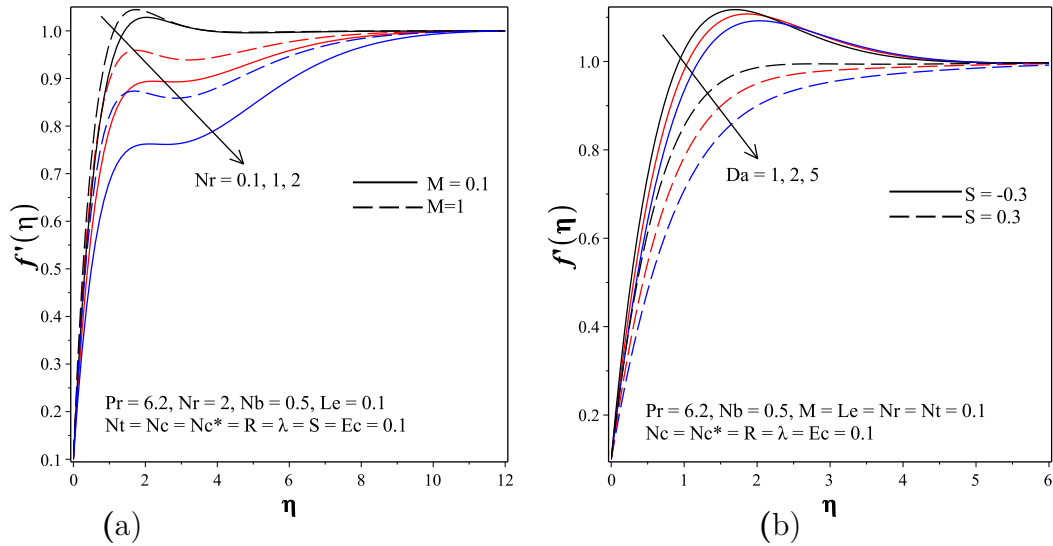


Figure 4.6.1: (a) Influence of  $Nr$  and  $M$  on the velocity profile (b) Influence of  $Da$  and  $S$  on the velocity profile.

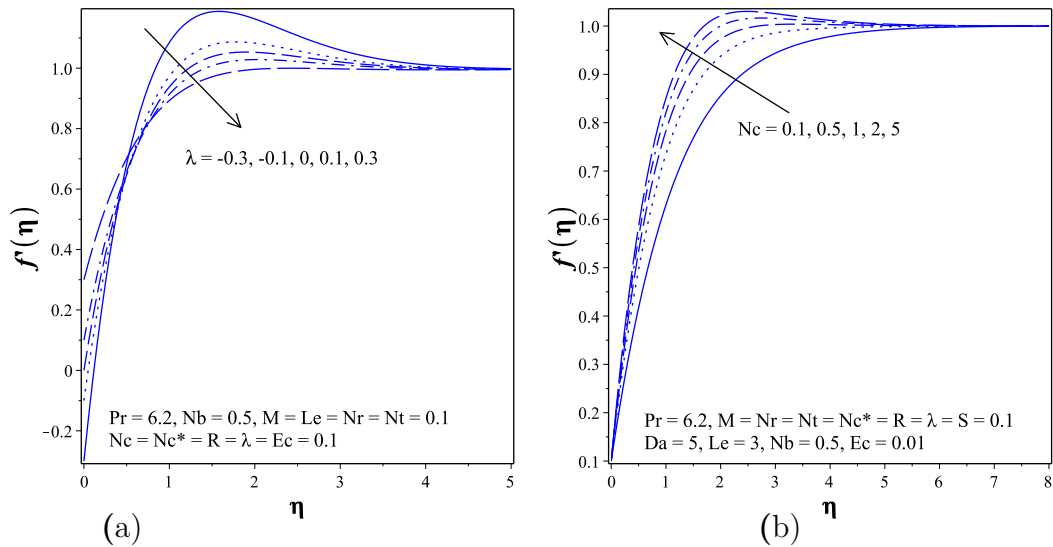


Figure 4.6.2: (a) Influence of  $\lambda$  on the velocity profile (b) Influence of  $Nc$  on the velocity profile.

reaches the critical stretching/shrinking parameter ( $\lambda_c$ ) value. The convective parameter,  $Nc$ , measures the ratio of conduction resistance to convection resistance within the body. When  $Nc = 0$ , no convection takes place at the surface. As shown in Figure 4.6.2b, the increment in convective parameter results in an increment in dimensionless velocity profile, and at the same time, the momentum boundary layer thickness goes in a reverse manner.

## 4.6.2 Temperature Profiles with Parameter Variations

The variation of the dimensionless temperature profile with transverse distance is shown in Figure 4.6.3 and 4.6.4 for different values of the flow governing parameters. The effects of stretching/shrinking and magnetic field parameters on the dimensionless temperature profile within the thermal boundary layer are shown in Figure 4.6.3a. In the absence of a magnetic field parameter, the dimensionless surface temperature is found to be lower and increases with an increase in magnetic field. This is because of the fact that a higher magnetic field produces a force called the Lorentz force which acts in the opposite direction of motion and hence overwhelms the velocity field. Simultaneously, it generates some thermal energy in the fluid motion, which causes a rise in the fluid temperature and its layer thickness. It is also important to note that the thermal boundary layer thickness decreases with increasing values of the stretching/shrinking parameter.

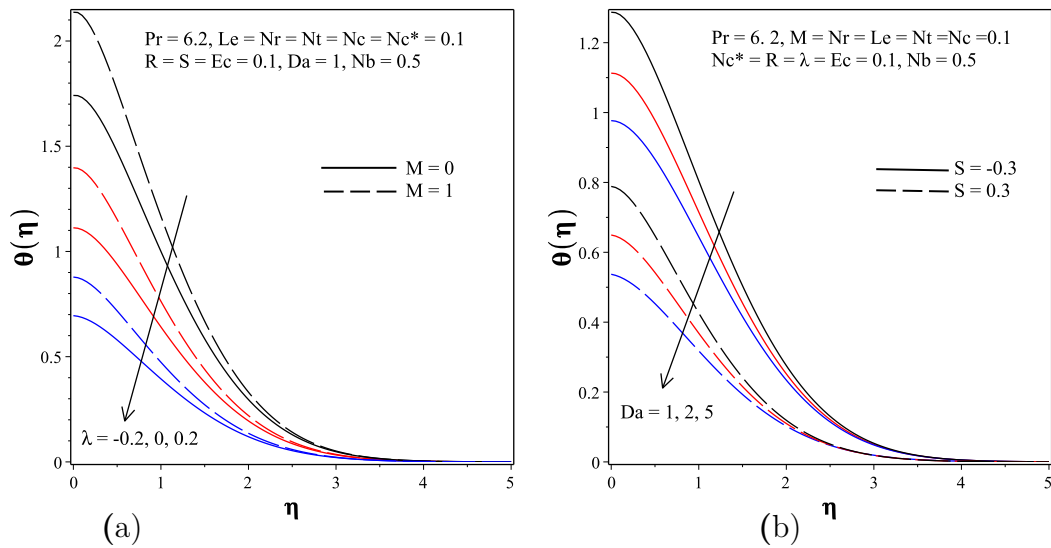


Figure 4.6.3: (a) Influence of  $\lambda$  and  $M$  on the temperature profile (b) Influence of  $Da$  and  $\delta$  on the temperature profile.

Figure 4.6.3b illustrates the influence of the mass transfer and porous media parameters on the dimensionless temperature profiles. For a stretching problem, solutions exist for both mass suction and injection. For specified values of other parameters, the dimensionless temperature profile decreases with increasing mass suction/injection parameter. As a result, the thermal boundary layer thickness becomes thicker into the fluid. The dimensionless surface temperature decreases as the porous media parameter

increases. It is also noted that the thermal boundary layer thickness formed through injection exceeds thermal boundary layer thickness formed through suction for any porous medium.

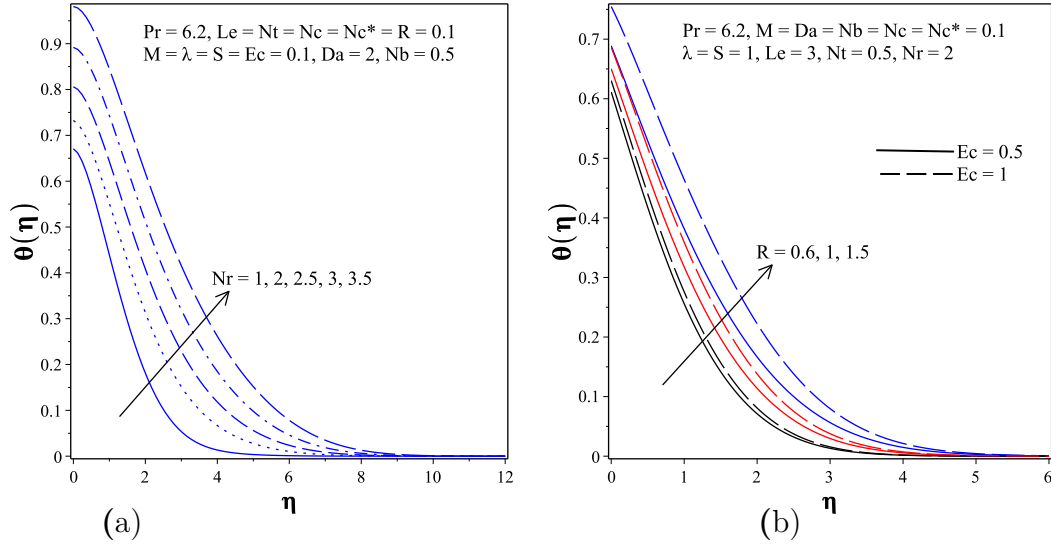


Figure 4.6.4: (a) Influence of  $Nr$  on the temperature profile (b) Influence of  $R$  and  $Ec$  on the temperature profile.

As per the illustration in Figure 4.6.4a, the dimensionless temperature profile increases as the nanofluid buoyancy ratio parameter increases. This is from the reality that higher values of nanofluid buoyancy ratio parameter enhance the temperature of the fluid so that the thermal boundary layer thickness is increased. The effects of viscous dissipation on the dimensionless temperature profile for different values of thermal radiation parameter are depicted in Figure 4.6.4b. In Figure 4.6.4b, the intensification of viscous dissipation increases the temperature of the fluid. In viscous fluid flow, the viscosity of the fluid takes kinetic energy from the motion of the fluid and transforms it into internal that heats the fluid. Furthermore, it can be observed that radiation enhances the dimensionless temperature leading to the development of an ascending thermal boundary layer. Higher fluid temperature contributes to a reduction in heat transfer from the plate. Hence, it is expected that thermal radiation must be kept low to attain more cooling from the plate.

### 4.6.3 Nanoparticle Volume Fraction Profiles with Parameter Variations

The effects on nanoparticle volume fraction with emerging parameters are presented in Figure 4.6.5a. From Figure 4.6.5a, one can see that as the stretching/shrinking parameter increases, the nanoparticle volume fraction enhances up to the region of fluid  $\eta = 2$ , then followed by transition there and it gets diminution with the same condition of  $\lambda$  whereas, an increase in magnetic field parameter resulted in decreasing nanoparticle volume fraction within a few layers of the fluid from the plate which is up to  $\eta = 2$  and just after the transition the effect is negligible.

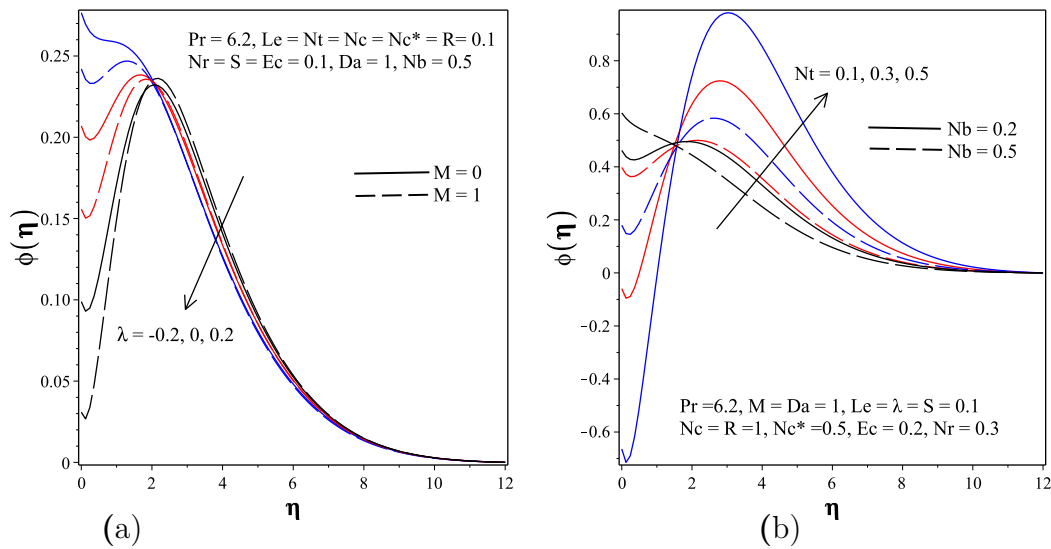


Figure 4.6.5: (a) Influence of  $\lambda$  and  $M$  on the concentration profile (b) Influence of  $Nt$  and  $Nb$  on the concentration profile.

The combined effects of the nanofluid parameters (Brownian and thermophoresis parameters) are shown in Figure 4.6.5b. We can see that an increase in  $Nt$  shows decreasing effects on nanoparticle volume fraction within a few layers of the fluid from the plate which is up to  $\eta = 1.6$ . Afterwards, that is in the region  $\eta = 1.6$  to  $\eta = 10$ , the nanoparticle volume fraction undergoes the reverse impact due to increase in  $Nt$  followed by transition at  $\eta = 1.6$ . This is because a rising of  $Nt$  indicating a strong thermophoretic force leading to larger diffusion of nanoparticles from the hot plate to the ambient fluid. Furthermore, an increase in  $Nb$  shows increasing effects on nanoparticle volume fraction within a few layers of the fluid from the plate which is up to  $\eta = 1.6$  and follows a reverse trend just after the transition.

#### 4.6.4 Skin Friction, Reduced Nusselt and Reduced Sherwood Number

The skin friction variation with different parameters is shown in Figure 4.6.6a. As presented in Figure 4.6.6a, the skin friction is less for higher values of the radiation parameter. The effect of the magnetic field parameter is to increase skin friction due to viscous effects. Furthermore, the increase in the nanofluid buoyancy ratio parameter helps in decreasing skin friction. Figure 4.6.6b characterizes the skin friction for increasing values of the convective parameter and Brownian motion parameters for the cases of permeable and impermeable sheets. As we can see from the graph, with an intensification in the convective parameter, the skin friction increases for the Brownian motion parameter and decreases for the suction/injection parameter.

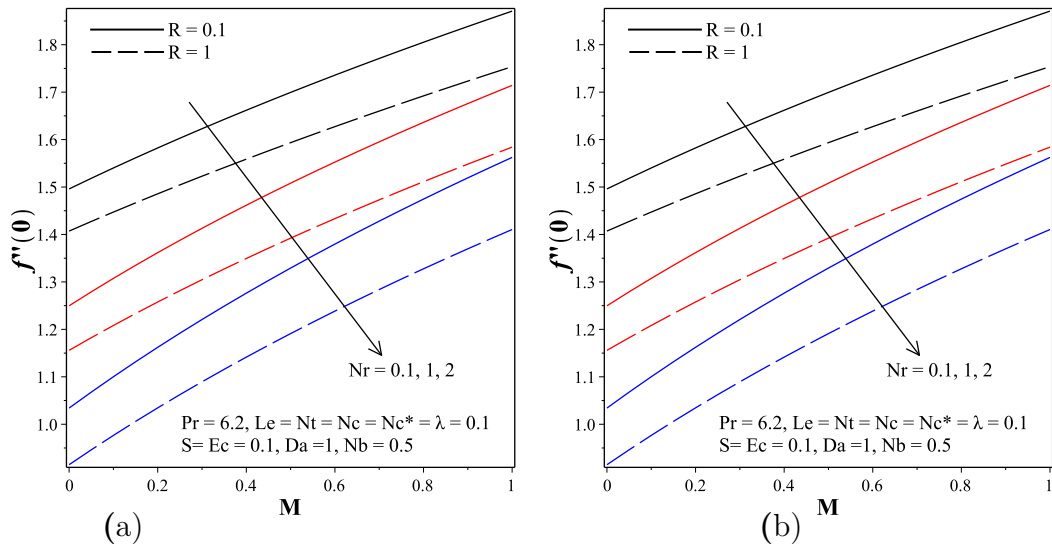


Figure 4.6.6: (a) Variation of skin friction with  $M$  for different values of  $Nr$  and  $R$  (b) Variation of skin friction with  $Nc$  for different values of  $Nb$  and  $S$ .

Combined effects of nanofluid buoyancy parameter, magnetic field parameter, and stretching/shrinking parameter on reduced Nusselt number (a measure of heat transfer rate from the plate ) is plotted in Figure 4.6.7a. We can see that with an increased magnetic field parameter the reduced Nusselt number decreases and with an increase in nanofluid buoyancy parameter the reduced Nusselt number increases. Also, the reduced Nusselt number is larger for the stretching sheet than the shrinking sheet. It is found in Figure 4.6.7b that a difference is appearing in the reduced Nusselt number for the convective parameter and the Brownian motion parameter for permeable and

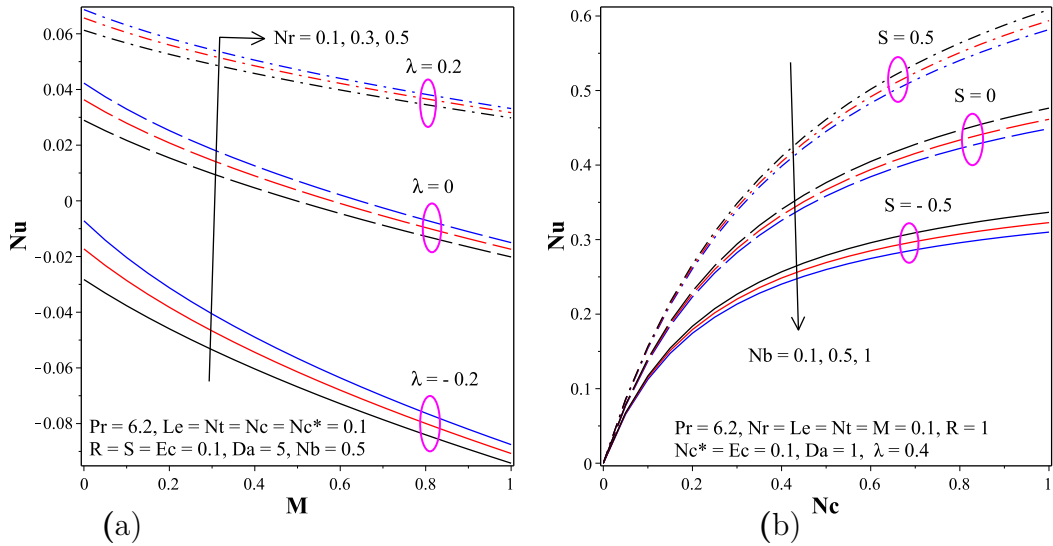


Figure 4.6.7: (a) Variation of reduced Nusselt number with  $M$  for different values of  $Nr$  and  $\lambda$  (b) Variation of reduced Nusselt number with  $Nc$  for different values of  $Nb$  and  $S$ .

impermeable sheets. An increase in convective parameter increases the reduced Nusselt number while opposite behavior is obtained on reduced Nusselt number for increasing values of the Brownian motion parameter for both permeable and impermeable sheets. As illustrated in this figure, suction assists the movement of heated fluid particles towards the wall and subsequently, increases heat transfer rates compared to injection.

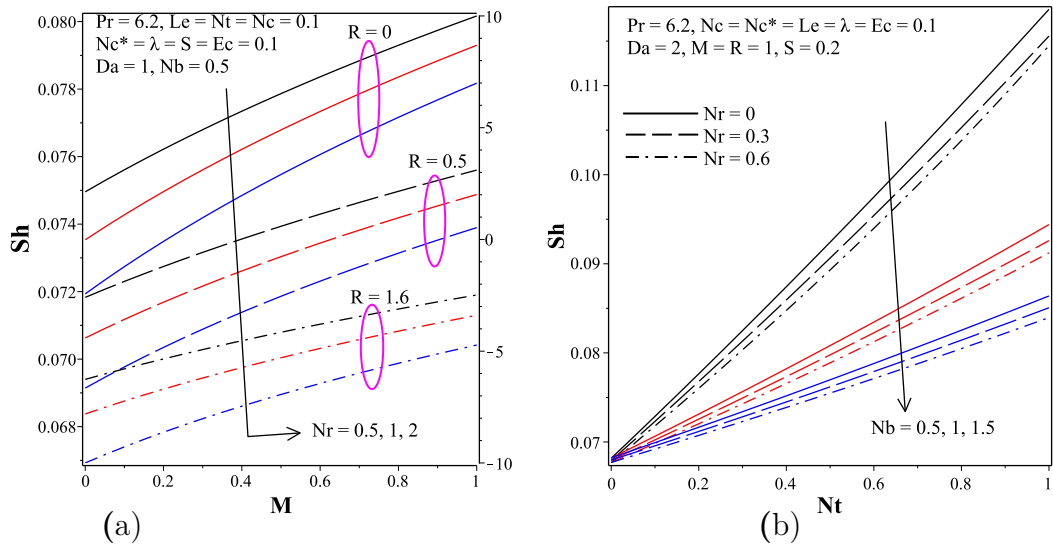


Figure 4.6.8: (a) Variation of  $Sh$  with  $M$  for different values of  $Nr$  and  $R$  (b) Variation of  $Sh$  with  $Nt$  for different values of  $Nb$  and  $Nr$ .

The effects of the magnetic field parameter and nanofluid buoyancy parameter in

Table 4.6.1: Computations showing the effects of buoyancy, magnetic, viscous dissipation, convective heating and stretching/shrinking parameters on dimensionless temperature, shear stress, heat and mass transfer rates when  $Pr = 6.2, Le = 3, Nb = Nt = 0.3, Nc^* = 0.1, R = 0.1, Da = 1, S = 0.1$

	$f''(0)$	$-(1 + \frac{4}{3}R)\theta'(0)$	$-\phi'(0)$
$\lambda$	$M = 0.1, Ec = 0.1, Nc = 0.1, Nr = 1$		
-0.3	3.72216	-0.24874	0.20268
0	1.96888	-0.02765	0.12925
0.5	0.73428	0.07519	0.09572
$Nr$	$M = 0.1, Ec = 0.1, Nc = 0.1, \lambda = -0.1$		
0	2.20195	-0.06593	0.14275
0.3	2.25119	-0.06742	0.14326
0.5	2.28448	-0.06847	0.14362
1	2.36960	-0.07134	0.14457
$M$	$\lambda = -0.1, Ec = 0.1, Nc = 0.1, Nr = 1$		
0	2.31130	-0.06600	0.14281
0.5	2.57923	-0.09083	0.15090
1	2.80403	-0.11221	0.15768
10	5.03698	-0.35215	0.22592
$Ec$	$M = 0.1, \lambda = -0.1, Nc = 0.1, Nr = 1$		
0	1.25636	0.09333	0.08686
0.5	2.36960	-0.07134	0.14457
$Nc$	$M = 0.1, Ec = 0.1, \lambda = -0.1, Nr = 1$		
0.1	2.36960	-0.07134	0.14457
1	2.12912	-0.21083	0.14229
10	2.04461	-0.26926	0.14203

the presence of thermal radiation are depicted in Figure 4.6.8a. The Sherwood number (mass transfer rate) increases with the magnetic field parameter and decreases with the nanofluid buoyancy parameter for the case of both occurrence and nonoccurrence of the thermal radiation parameter. Moreover, the Sherwood number has an inverse relationship with the thermal radiation parameter. Figure 4.6.8b indicates that the influence of the change of nanofluid parameters on the Sherwood number for different values of the buoyancy parameter. The Sherwood number upsurges with the thermophoresis parameter but falls with the Brownian motion parameter for all values of nanofluid buoyancy parameters.

The combined effects of buoyancy force, convective heating, viscous dissipation, and magnetic field parameters on skin friction, and heat and mass transfer from a permeable stretching/shrinking sheet in a porous medium are investigated numerically and obtained results are presented in Table 4.6.1 and Table 4.6.2.

Table 4.6.2: Computations showing the effects of Brownian, suction/injection, thermophoresis, convective mass transfer, radiation and the porous media parameters on dimensionless temperature, shear stress, heat and mass transfer rates when  $Pr = 6.2, Le = 0.1, Nr = 1, M = 1, Ec = Nc = \lambda = 0.1$

	$f''(0)$	$-(1 + \frac{4}{3}R)\theta'(0)$	$-\phi'(0)$
S	$Nb = 0.3, Nt = 0.3, Nc^* = 0.1, R = 0.1, Da = 0.1$		
-0.5	10.21855	-1.68520	1.23498
0	3.98653	-0.16588	0.23885
0.5	3.64907	-0.08893	0.17686
Nb	$Nt = 0.3, S = 0.2, Nc^* = 0.1, R = 0.1, Da = 0.1$		
0.3	3.82272	-0.12910	0.20910
0.6	3.64867	-0.12656	0.13818
Nt	$Nb = 0.3, S = 0.2, Nc^* = 0.1, R = 0.1, Da = 0.1$		
0.1	3.56831	-0.11859	0.11336
0.3	3.82272	-0.12910	0.20910
Nc*	$Nb = 0.3, Nt = 0.3, S = 0.2, R = 0.1, Da = 0.1$		
0.1	3.82272	-0.12910	0.20910
1	3.44429	-0.14380	0.55853
10	3.33633	-0.15366	0.67566
R	$Nb = 0.3, Nt = 0.3, Nc^* = 0.1, S = 0.2, Da = 0.1$		
0	3.88340	-0.12863	0.22256
1	3.53589	-0.11228	0.14951
2	3.40631	-0.07428	0.12457
Da	$Nb = 0.3, Nt = 0.3, Nc^* = 0.1, R = 0.1, S = 0.2$		
0.5	2.22301	-0.02740	0.13541
2	1.62546	0.00655	0.10917
5	1.45769	0.01531	0.10201

#### 4.6.5 Dual Solutions

Two real solutions exist within the valid range of shrinking parameter  $\lambda < 0$ . These dual solutions exist in the range  $\lambda_c < \lambda$  and no solution exists for  $\lambda < \lambda_c$ , where  $\lambda_c$  is the critical value of shrinking parameter for which unique solution exists. It is well documented in the literature that only the upper solution branch for shrinking sheet is stable and physically realistic (Makinde et al., 2013), (Bhatti et al., 2017) while the other one diverge when subjected to disturbances. Therefore, only one valid solution exist within the range of shrinking parameter values.

As shown in Figure 4.6.9a the value of  $f''(0)$  for the upper branch solution was observed to increase as  $M$  increases. This shows that the increase in magnetic field parameters caused the wall shear stress to increase. Likewise, the value of  $|\lambda_c|$  increased

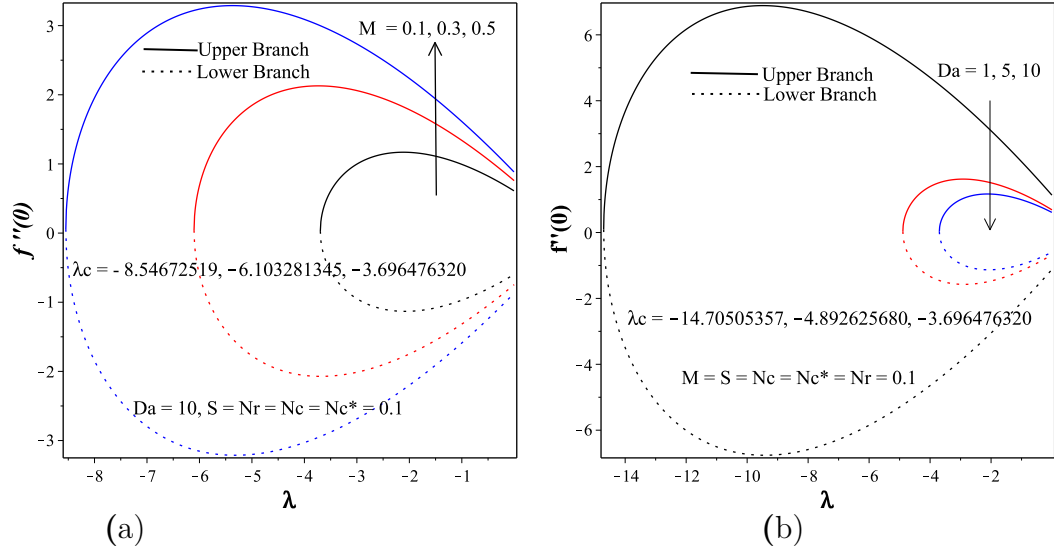


Figure 4.6.9: (a) Impact of  $M$  on  $\lambda_c$  and skin friction. (b) Impact of  $Da$  on  $\lambda_c$  and skin friction.

Table 4.6.3: Computation showing critical shrinking parameter( $\lambda_c$ ) when  $Pr = 6.2$

<b>M</b>	<b>Da</b>	<b>S</b>	<b>Nr</b>	<b>Nc</b>	<b>Nc*</b>	<b><math>\lambda_c</math></b>
0.1	10	0.1	0.1	0.1	0.1	-3.696
0.3	10	0.1	0.1	0.1	0.1	-6.103
0.5	10	0.1	0.1	0.1	0.1	-8.546
0.1	5	0.1	0.1	0.1	0.1	-4.892
0.1	3	0.1	0.1	0.1	0.1	-6.508
0.1	1	0.1	0.1	0.1	0.1	-14.705
0.1	1	1.0	0.1	0.1	0.1	-14.705
0.1	1	0.1	0.5	0.1	0.1	-14.676
0.1	1	0.1	1.0	0.1	0.1	-14.640
0.1	1	0.1	0.1	0.5	0.1	-14.893
0.1	1	0.1	0.1	1.0	0.1	-15.020
0.1	1	0.1	0.1	1.0	0.5	-14.686
0.1	1	0.1	0.1	0.1	1.0	-14.672

as  $M$  increased. Furthermore, the effects of the porosity parameter on the critical value of the shrinking parameter ( $\lambda_c$ ) and wall shear stress is depicted in Figure 4.6.9b. For the upper branch solution, the value of  $f''(0)$  decreased as the porosity parameter ( $Da$ ) increased and the value of  $|\lambda_c|$  decreased as  $Da$  increased.

As shown in Figure 4.6.9a and Figure 4.6.9b, the model exhibits a critical value for shrinking parameter values below which no solution exists. This implies that the sheet will stop shrinking when the critical value of the shrinking parameter is attained. This critical value also varies depending on the values of other emerging parameters.

Moreover, it is important to note that for shrinking sheets, the convergence of the solution is limited with the critical parameter value ( $\lambda_c$ ). The solution only converges for a range of parameter values  $\lambda_c < \lambda < 0$  and the value of ( $\lambda_c$ ) depends on the values of other embedded thermophysical parameters in the governing model. The effects of those emerging parameters on critical value of the shrinking parameter ( $\lambda_c$ ) are presented in Table 4.6.3.

The convergence and validity of the solutions obtained are displayed in Table 4.6.4. The special case of our numerical results was validated with the one already in the literature [Makinde et al. \(2013\)](#) and excellent agreement is achieved.

Table 4.6.4: Comparison of values for skin friction and Nusselt number for different values of  $\lambda$  and  $Nr$  with  $M = 1, Ec = 0.1, Nc = 1$  for the case of  $Da = Nc^* = \infty, R = 0, S = 0$

$\lambda$	$Nr$	$f''(0)$		Nu	
		<a href="#">Makinde et al. (2013)</a>	Present result	<a href="#">Makinde et al. (2013)</a>	Present result
-0.5	0	2.35476	2.3547617880	0.13379	0.13379056427
	0.3	2.21267	2.2126690902	0.13425	0.13424984870
	0.5	2.11589	2.1158915121	0.13409	0.13408574710
0	0	1.73177	1.7317739823	0.25999	0.25999218413
	0.3	1.60462	1.6046181450	0.26005	0.26005145639
	0.5	1.51848	1.5184779144	0.25979	0.25978597088
0.5	0	1.03430	1.0343034653	0.34415	0.34415369544
	0.3	0.92053	0.92053122986	0.34357	0.34356698719
	0.5	0.84380	0.84379568546	0.34297	0.34296800192

## Chapter 5

# Magnetite Ferrofluid flow Past a Convectively Heated Permeable Stretching/Shrinking Sheet in a Darcy-Forchheimer Porous Medium

### 5.1 Introduction

Fluid flow and transport processes in porous media have many applications in hydrology, agriculture, civil, petroleum engineering, environmental and industrial systems such as heat exchange design, catalytic reactors, geothermal energy systems, fermentation processes, grain storage, groundwater pollution, groundwater systems, movement of water in reservoirs, crude oil production and recovery systems as explained by [Hayat et al. \(2016, 2017\)](#); [Seth and Mandal \(2018\)](#). Because of its significance, Darcy's law has inspired a number of works. However, in many practical applications, porous media with relatively high porosity and permeability are used, especially to reduce the pressure drop. Hence, the Reynolds number based on the pore size may be greater than unity and there is an impermeable boundary, making Darcy's law inapplicable [Muhammad et al. \(2017\)](#). For these reasons, it is important to incorporate the velocity-squared term in addition to Darcian velocity in the momentum equation in order to include the effect of inertia porous media resistance [Eid and Makinde \(2018\)](#); [Makinde and Egunjobi \(2016\)](#).

Following this fact, an important analysis is done on the convective transport process in a porous medium with an inertial effect. To mention some, [Bakar et al. \(2016\)](#) numerically examined effects of velocity and thermal slip on stagnation point flow towards a shrinking sheet embedded in Darcy-Forchheimer porous medium. They obtained the existence of dual solutions in certain ranges of the velocity ratio parameter. [Ali Lund et al. \(2019\)](#) examined Darcy-Forchheimer's flow of Casson type nanofluid past a non-linearly shrinking sheet to identify the effects of slip condition and viscous dissipation. They identified the existence of a dual solution.

Motivated by the above cited works of literature, the main goal of this chapter is to examine carefully the characteristics of the magnetohydrodynamic stagnation point flow of a magnetite ferrofluid past a permeable stretching/shrinking sheet in a

Darcy-Forchheimer porous medium with viscous and porous dissipation and convective heating. For such fluid flow problems, the existence of a dual solution is possible, and stability analysis is performed to identify stable and physically reliable solutions. To the best of our knowledge, no work has been done to analyze the combined effects of these parameters on the ferrofluid flow and heat transfer characteristics. The dimensionless velocity, temperature, skin friction coefficient, and Nusselt number are obtained numerically and presented in graphs and tables.

## 5.2 Mathematical Model Formulation

Consider a steady, laminar, viscous, and incompressible stagnation point flow of  $\text{Fe}_3\text{O}_4$ - $\text{H}_2\text{O}$  nanofluid towards a convectively heated permeable stretching/shrinking sheet which is kept in a two dimensional Darcy-Forchheimer porous medium. The flow is subjected to a constant magnetic field of strength  $B_0$  which is applied in the positive  $y$ -direction normal to the surface. The induced magnetic field is assumed to be small compared to the applied magnetic field. The ambient temperature of the fluid is taken as  $T_\infty$  while the surface below the stretching/shrinking sheet is heated by convection from a hot fluid having initial temperature  $T_f$  which provides a heat transfer coefficient  $h_f$ . It is assumed that the porous medium is homogeneous and isotropic, and saturated with a nanofluid which is in local thermal equilibrium with the solid matrix. We choose the coordinate system so that  $x$ -axis along the permeable stretching/shrinking sheet and  $y$ -axis is normal to the sheet surface. Figure 5.2.1 shows the physical model and the coordinate systems.

Based on the general fluid flow governing equations derived in chapter 3, the Tawari-Das convective transport model equations, the Darcy-Forchheimer flow model and the above assumptions, the governing equation of total mass, momentum and temperature in the presence of a transverse magnetic field past a convectively heated stretching/shrinking sheet embedded in a Non-Darcian porous medium takes the following form:

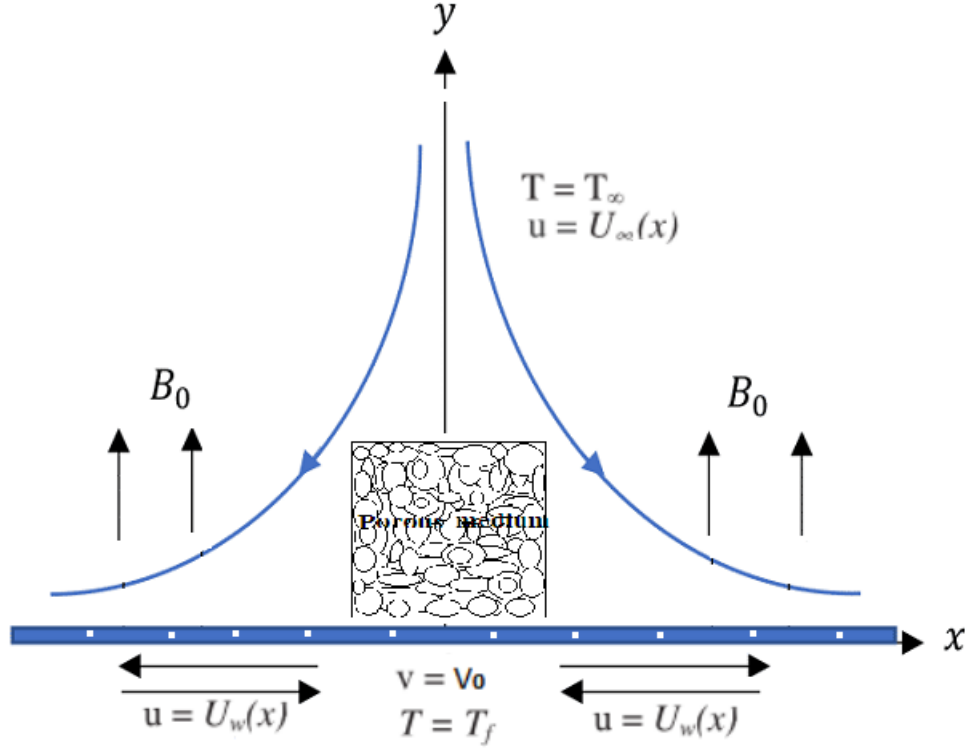


Figure 5.2.1: Flow diagram of the model.

$$\begin{aligned}
\frac{\partial u}{\partial x} + \frac{\partial v}{\partial y} &= 0, \\
u \frac{\partial u}{\partial x} + v \frac{\partial u}{\partial y} &= -\frac{1}{\rho_{nf}} \frac{\partial p}{\partial x} + \frac{\mu_{nf}}{\rho_{nf}} \left( \frac{\partial^2 u}{\partial x^2} + \frac{\partial^2 u}{\partial y^2} \right) + \frac{J \times B}{\rho_{nf}} - \frac{\mu_{nf}}{\rho_{nf} K} u - \frac{\rho_f C_F}{\rho_{nf} \sqrt{K}} u^2, \\
u \frac{\partial v}{\partial x} + v \frac{\partial v}{\partial y} &= -\frac{1}{\rho_{nf}} \frac{\partial p}{\partial y} + \frac{\mu_{nf}}{\rho_f} \left( \frac{\partial^2 v}{\partial x^2} + \frac{\partial^2 v}{\partial y^2} \right), \\
u \frac{\partial T}{\partial x} + v \frac{\partial T}{\partial y} &= \alpha_f \left( \frac{\partial^2 T}{\partial x^2} + \frac{\partial^2 T}{\partial y^2} \right) + \frac{\alpha_{nf} \mu_{nf}}{k} \left( \frac{\partial u}{\partial y} \right)^2 + \frac{J \cdot J}{(\rho c_p)_{nf} \sigma} + \frac{\mu u^2}{(\rho c_p)_{nf} K} + \\
&\quad \frac{\rho_{nf} C_F u^3}{(\rho c_p)_{nf} \sqrt{K}}.
\end{aligned} \tag{5.2.1}$$

Now making the standard boundary-layer approximation based on scale analysis, we obtained that variations along y-axis within the boundary layer is much faster than the variations along x-axis. i.e,

$$\frac{\partial u}{\partial x} \ll \frac{\partial u}{\partial y}, \quad \frac{\partial v}{\partial x} \ll \frac{\partial v}{\partial y}, \quad \text{and} \quad \frac{\partial T}{\partial x} \ll \frac{\partial T}{\partial y}.$$

Following the above discussion, the governing equations are simplified as

$$\begin{aligned}
\frac{\partial u}{\partial x} + \frac{\partial v}{\partial y} &= 0, \\
u \frac{\partial u}{\partial x} + v \frac{\partial u}{\partial y} &= -\frac{1}{\rho_{nf}} \frac{\partial p}{\partial x} + \frac{\mu_{nf}}{\rho_{nf}} \left( \frac{\partial^2 u}{\partial y^2} \right) + \frac{J \times B}{\rho_{nf}} - \frac{\mu_{nf}}{\rho_{nf} K} u - \frac{\rho_{nf} C_F}{\rho_{nf} \sqrt{K}} u^2, \\
\frac{\partial p}{\partial y} &= 0, \\
u \frac{\partial T}{\partial x} + v \frac{\partial T}{\partial y} &= \alpha_f \left( \frac{\partial^2 T}{\partial y^2} \right) + \frac{\alpha_{nf} \mu_{nf}}{k} \left( \frac{\partial u}{\partial y} \right)^2 + \frac{J \cdot J}{(\rho c_p)_{nf} \sigma} + \frac{\mu_{nf} u^2}{(\rho c_p)_{nf} K} + \frac{\rho_{nf} C_F u^3}{(\rho c_p)_{nf} \sqrt{K}}.
\end{aligned} \tag{5.2.2}$$

Substituting the Lorenzean Force term which is obtained in equation 4.2.11 into the  $x$ - momentum equation, we obtained that

$$u \frac{\partial u}{\partial x} + v \frac{\partial u}{\partial y} = -\frac{1}{\rho_{nf}} \frac{\partial p}{\partial x} + \frac{\mu_{nf}}{\rho_{nf}} \left( \frac{\partial^2 u}{\partial y^2} \right) - \frac{\sigma_{nf} B_0^2 u}{\rho_{nf}} - \frac{\mu_{nf}}{\rho_{nf} K} u - \frac{\rho_{nf} C_F}{\rho_{nf} \sqrt{K}} u^2. \tag{5.2.3}$$

In order to balance the momentum equation at the free stream, the momentum equation is redefined as

$$u \frac{\partial u}{\partial x} + v \frac{\partial u}{\partial y} = U_\infty \frac{\partial U_\infty}{\partial x} + \frac{\mu_{nf}}{\rho_{nf}} \frac{\partial^2 u}{\partial y^2} - \left( \frac{\sigma_{nf} B_0^2}{\rho_{nf}} + \frac{\mu_{nf}}{\rho_{nf} K} \right) (u - U_\infty) + \frac{F}{\rho_{nf} \sqrt{K}} (u - U_\infty)^2. \tag{5.2.4}$$

Considering the joule heating term given in equation 4.2.12, the energy equation becomes

$$\begin{aligned}
u \frac{\partial T}{\partial x} + v \frac{\partial T}{\partial y} &= \frac{k_{nf}}{(\rho C_p)_{nf}} \frac{\partial^2 T}{\partial y^2} + \frac{\mu_{nf}}{(\rho C_p)_{nf}} \left( \frac{\partial u}{\partial y} \right)^2 + \left( \frac{\sigma_{nf} B_0^2}{(\rho C_p)_{nf}} + \frac{\mu_{nf}}{(\rho C_p)_{nf} K_1} \right) u^2 \\
&\quad + \frac{F}{(\rho C_p)_{nf} \sqrt{K}} u^3.
\end{aligned} \tag{5.2.5}$$

Similarly, in order to have a balanced equation at the free stream condition, the energy equation is redefined as

$$\begin{aligned}
u \frac{\partial T}{\partial x} + v \frac{\partial T}{\partial y} &= \frac{k_{nf}}{(\rho C_p)_{nf}} \frac{\partial^2 T}{\partial y^2} + \frac{\mu_{nf}}{(\rho C_p)_{nf}} \left( \frac{\partial u}{\partial y} \right)^2 + \left( \frac{\sigma_{nf} B_0^2}{(\rho C_p)_{nf}} + \frac{\mu_{nf}}{(\rho C_p)_{nf} K_1} \right) (u - U_\infty)^2 \\
&\quad + \frac{F}{(\rho C_p)_{nf} \sqrt{K}} (u - U_\infty)^3.
\end{aligned} \tag{5.2.6}$$

After performing the boundary layer approximations for momentum and thermal energy, the flow equations for continuity, conservation of momentum and energy for

the magnetic nanofluid flow past a stretching/shrinking sheet is defined as:

$$\frac{\partial u}{\partial x} + \frac{\partial v}{\partial y} = 0, \quad (5.2.7)$$

$$u \frac{\partial u}{\partial x} + v \frac{\partial u}{\partial y} = U_\infty \frac{\partial U_\infty}{\partial x} + \frac{\mu_{nf}}{\rho_{nf}} \frac{\partial^2 u}{\partial y^2} - \left( \frac{\sigma_{nf} B_0^2}{\rho_{nf}} + \frac{\mu_{nf}}{\rho_{nf} K_1} \right) (u - U_\infty) + \frac{F}{\rho_{nf} \sqrt{K}} (u - U_\infty)^2, \quad (5.2.8)$$

$$u \frac{\partial T}{\partial x} + v \frac{\partial T}{\partial y} = \frac{k_{nf}}{(\rho C_p)_{nf}} \frac{\partial^2 T}{\partial y^2} + \frac{\mu_{nf}}{(\rho C_p)_{nf}} \left( \frac{\partial u}{\partial y} \right)^2 + \left( \frac{\sigma_{nf} B_0^2}{(\rho C_p)_{nf}} + \frac{\mu_{nf}}{(\rho C_p)_{nf} K_1} \right) (u - U_\infty)^2 + \frac{F}{(\rho C_p)_{nf} \sqrt{K}} (u - U_\infty)^3, \quad (5.2.9)$$

with the boundary conditions:

$$u(x, 0) = U_w(x), \quad v(x, 0) = V_0, \quad -k_f \frac{\partial T}{\partial y}(x, 0) = h_f (T_f - T(x, 0)), \quad (5.2.10)$$

$$u(x, \infty) \rightarrow U_\infty(x), \quad T(x, \infty) \rightarrow T_\infty, \quad (5.2.11)$$

where  $u$  and  $v$  are the velocity components along the  $x$  and  $y$  directions, respectively. The expressions  $U_w(x) = bx$  is the stretching/shrinking velocity of the sheet where  $b > 0$  is for stretching case and  $b < 0$  for shrinking case,  $U_\infty(x) = ax$  is the free stream velocity where  $a > 0$  is the strength of stagnation flow, and  $T_f = T_\infty + nx^2$  is the temperature of the hot fluid below the sheet. The terms  $V_0$  is the sheet suction/injection velocity,  $K$  is the permeability of the porous medium,  $F = \rho_{nf} C_F$  is the non-uniform inertial coefficient of porous medium,  $\rho_{nf}$  is the nanofluid density,  $\mu_{nf}$  is the nanofluid dynamic viscosity,  $k_{nf}$  is the nanofluid thermal conductivity,  $(\rho C_p)_{nf}$  is heat capacity of the nanofluid at constant pressure and  $\sigma_{nf}$  is the nanofluid electrical conductivity are defined as follows (Makinde, 2018):

$$\begin{aligned} \rho_{nf} &= (1 - \phi)\rho_f + \phi\rho_s, & (\rho C_p)_{nf} &= (1 - \phi)(\rho C_p)_f + \phi(\rho C_p)_s, \\ \mu_{nf} &= \frac{\mu_f}{(1 - \phi)^{2.5}}, & \frac{k_{nf}}{k_f} &= \frac{k_s + 2k_f - 2\phi(k_f - k_s)}{k_s + 2k_f + \phi(k_f - k_s)}, & r &= \frac{\sigma_s}{\sigma_f}, \\ \frac{\sigma_{nf}}{\sigma_f} &= 1 + \frac{3(r - 1)\phi}{(r + 2) - (r - 1)\phi}, \end{aligned} \quad (5.2.12)$$

where  $\rho_f$  is the density of the base fluid,  $\rho_s$  is the density of the solid nanoparticle,  $k_f$  is the base fluid thermal conductivity,  $k_s$  is the nanoparticles thermal conductivity,  $\sigma_f$

is the base fluid electrical conductivity,  $\sigma_s$  is the nanoparticles electrical conductivity,  $\phi$  is the nanoparticles volume fraction,  $\mu_f$  is the base fluid dynamic viscosity  $C_{pf}$  is the base fluid specific heat capacity and  $C_{ps}$  is the nanoparticles specific heat capacity. The thermo-physical properties of  $Fe_3O_4$  nanoparticles and  $H_2O$  are listed in Table 5.2.1 below (Makinde, 2018);

Table 5.2.1: Nanoparticle and base fluid thermophysical properties

Physical properties	$\rho(\text{kg}/\text{m}^3)$	$C_p(\text{J}/\text{kgK})$	$k(\text{W}/\text{mK})$	$\sigma(\text{S}/\text{m})$
$H_2O$	997.1	4179	0.613	$5 \times 10^{-6}$
$Fe_3O_4$	5180	670	9.7	$2.5 \times 10^6$

### 5.3 Similarity Transformation

Introducing the following non-dimensional similarity variables, the governing equations (5.2.8) - (5.2.9) and the boundary equations (5.2.10) - (5.2.11) are transformed into a non-dimensionless form (Makinde, 2018):

$$\eta = y\sqrt{\frac{a}{\nu_f}}, \quad \psi(x, y) = x\sqrt{a\nu_f}f(\eta), \quad \theta(\eta) = \frac{T - T_\infty}{T_f - T_\infty}. \quad (5.3.1)$$

Now using the similarity transformation quantities given above, the similarity transformation processes to ordinary differential equations are as shown below,

$$u = \frac{\partial\psi}{\partial y} = \frac{\partial}{\partial y}(f(\eta)x\sqrt{a\nu_f}) \Rightarrow u = axf'(\eta), \quad (5.3.2)$$

$$v = -\frac{\partial\psi}{\partial x} = -\frac{\partial}{\partial x}(f(\eta)x\sqrt{a\nu_f}) \Rightarrow v = -\sqrt{a\nu_f}f(\eta), \quad (5.3.3)$$

$$T = T_\infty + (T_f - T_\infty)\theta(\eta) \Rightarrow \frac{\partial T}{\partial y} = (T_f - T_\infty)\theta'(\eta)\sqrt{\frac{a}{\nu_f}}, \quad (5.3.4)$$

$$\Rightarrow \frac{\partial^2 T}{\partial y^2} = \frac{a(T_f - T_\infty)}{\nu_f}\theta''(\eta). \quad (5.3.5)$$

## The Continuity equation

The equation of continuity is satisfied for the chosen stream function  $\psi(x, y)$ .

$$\frac{\partial u}{\partial x} + \frac{\partial v}{\partial y} = \frac{\partial}{\partial x} (axf'(\eta)) + \frac{\partial}{\partial y} (-\sqrt{a\nu}f(\eta)) = 0. \quad (\text{Which is satisfied})(5.3.6)$$

## The Momentum equation

Substituting equation (5.3.2)- (5.3.5) into equation (5.2.8), we get

$$axf'(\eta) \frac{\partial}{\partial x} (axf'(\eta)) - \sqrt{a\nu}f(\eta) \frac{\partial}{\partial y} (-\sqrt{a\nu}f(\eta)) = ax \frac{d}{dx} (ax) + \quad (5.3.7)$$

$$\begin{aligned} & \frac{\mu_{nf}}{\rho_{nf}} \frac{\partial}{\partial y} \left( \frac{\partial}{\partial y} (axf'(\eta)) \right) - ax \left( \frac{\sigma_{nf} B_0^2}{\rho_{nf}} + \frac{\mu_{nf}}{\rho_{nf} K} \right) (f'(\eta) - 1) + \frac{a^2 x^2 F}{\rho_{nf} \sqrt{K_1}} (f'(\eta) - 1)^2, \\ a^2 x \left[ (f'(\eta))^2 - f(\eta) f''(\eta) \right] &= a^2 x + \frac{\mu_{nf}}{\rho_{nf}} \frac{a^2 x}{\nu} f'''(\eta) - ax \left( \frac{\sigma_{nf} B_0^2}{\rho_{nf}} + \frac{\mu_{nf}}{\rho_{nf} K} \right) (f'(\eta) - 1) \\ &+ \frac{a^2 x^2 F}{\rho_{nf} \sqrt{K}} (f'(\eta) - 1)^2. \end{aligned} \quad (5.3.8)$$

Multiplying each term of equation (5.3.8) by the term  $\frac{\nu \rho_{nf}}{a^2 x \mu_{nf}}$ , we get

$$\begin{aligned} \nu \frac{\rho_{nf}}{\mu_{nf}} \left[ (f'(\eta))^2 - f(\eta) f''(\eta) \right] &= \nu \frac{\rho_{nf}}{\mu_{nf}} + f'''(\eta) - \frac{\nu}{a} \frac{\rho_{nf}}{\mu_{nf}} \left( \frac{\sigma_{nf} B_0^2}{\rho_{nf}} + \frac{\mu_{nf}}{\rho_{nf} K} \right) (f'(\eta) - 1) \\ &+ \frac{\nu \rho_{nf}}{a^2 x \mu_{nf}} \frac{a^2 x^2 F}{\rho_{nf} \sqrt{K}} (f'(\eta) - 1)^2, \end{aligned}$$

$$\begin{aligned} \frac{\mu_f \rho_{nf}}{\rho_f \mu_{nf}} \left[ (f'(\eta))^2 - f(\eta) f''(\eta) \right] &= \frac{\mu_f \rho_{nf}}{\rho_f \mu_{nf}} + f'''(\eta) - \frac{\mu_f \rho_{nf}}{a \rho_f \mu_{nf}} \left( \frac{\sigma_{nf} B_0^2}{\rho_{nf}} + \frac{\mu_{nf}}{\rho_{nf} K} \right) (f'(\eta) - 1) \\ &+ \frac{\mu_f}{\mu_{nf}} \frac{F x}{\rho_f \sqrt{K}} (f'(\eta) - 1)^2. \end{aligned}$$

Now using equation (5.2.12), we simplify

$$\begin{aligned} \left[ (1 - \phi) + \phi \rho_s / \rho_f \right] (1 - \phi)^{2.5} \left[ (f'(\eta))^2 - f(\eta) f''(\eta) \right] &= \left[ (1 - \phi) + \phi \rho_s / \rho_f \right] (1 - \phi)^{2.5} + f'''(\eta) \\ - \left( \frac{\sigma_f B_0^2}{a \rho_f} \frac{\sigma_{nf} (1 - \phi)^{2.5}}{\sigma_f} + \frac{\nu_f}{a K} \right) (f'(\eta) - 1) &+ (1 - \phi)^{2.5} \frac{F x}{\rho_f \sqrt{K}} (f'(\eta) - 1)^2. \end{aligned} \quad (5.3.9)$$

Finally, we obtain

$$A_1 \left[ (f'(\eta))^2 - f(\eta) f''(\eta) \right] = A_1 + f'''(\eta) - \left( MA_2 + \frac{1}{Da} \right) (f'(\eta) - 1) + A_3 F_n (f'(\eta) - 1)^2.$$

where,

$$M = \frac{\sigma_f B_0^2}{a \rho_f}, \quad Pr = \frac{\mu_f C_{pf}}{k_f}, \quad Da = \frac{aK}{\nu_f}, \quad Fn = \frac{Fx}{\rho_f \sqrt{K}},$$

$$A_1 = (1 - \phi + \frac{\phi \rho_s}{\rho_f})(1 - \phi)^{2.5}, \quad A_2 = \frac{(1 - \phi)^{2.5}}{\sigma_f} \sigma_{nf}, \quad A_3 = (1 - \phi)^{2.5}. \quad (5.3.10)$$

### The Energy equation

Substituting equations (5.3.2)- (5.3.5) into the energy equation (5.2.9), we obtain

$$(\rho C_p)_{nf} a n x [\theta(\eta) f'(\eta) - f(\eta) \theta'(\eta)] = \frac{a n x}{\nu} k_{nf} \theta''(\eta) + \frac{\mu_{nf} a^3 x^2}{\nu} (f''(\eta))^2$$

$$- a^2 x^2 \left( \sigma_{nf} B_0^2 + \frac{\mu_{nf}}{K} \right) (f'(\eta) - 1)^2 + \frac{a^3 x^3 F}{\sqrt{K}} (f'(\eta) - 1)^3. \quad (5.3.11)$$

Multiplying each term of equation (5.2.10) by  $\frac{\nu}{a n x k_{nf}}$ , we obtain

$$\frac{\nu (\rho C_p)_{nf}}{k_{nf}} [\theta(\eta) f'(\eta) - f(\eta) \theta'(\eta)] = \theta''(\eta) + \frac{a^2 x \mu_{nf}}{n k_{nf}} (f''(\eta))^2 -$$

$$\frac{\nu a x}{n k_{nf}} \left( \sigma_{nf} B_0^2 + \frac{\mu_{nf}}{K} \right) (f'(\eta) - 1)^2 + \frac{\nu a^2 x^2 F}{n k_{nf} \sqrt{K}} (f'(\eta) - 1)^3. \quad (5.3.12)$$

Now using equation (5.2.12), we simplify

$$\frac{k_f}{k_{nf}} \left[ 1 - \phi + \frac{\phi (\rho C_p)_s}{(\rho C_p)_f} \right] \frac{\mu_f (C_p)_f}{k_f} [\theta(\eta) f'(\eta) - f(\eta) \theta'(\eta)] = \theta''(\eta) + \frac{a^2 x \mu_f}{n k_{nf} (1 - \phi)^{2.5}} (f''(\eta))^2$$

$$- \left( \frac{a x}{n k_{nf} \rho_f} \mu_f \sigma_{nf} B_0^2 + \frac{a x}{n k_{nf} \rho_f} \frac{\mu_f \mu_{nf}}{K} \right) (f'(\eta) - 1)^2 + \frac{\mu_f a^2 x^2 F}{\rho_f n k_{nf} \sqrt{K}} (f'(\eta) - 1)^3, \quad (5.3.13)$$

$$A_4 Pr [\theta(\eta) f'(\eta) - f(\eta) \theta'(\eta)] = \theta''(\eta) + \frac{k_f}{k_{nf} (1 - \phi)^{2.5}} \frac{\mu_f C_{pf}}{k_f} \frac{a^2 x}{n C_{pf}} (f''(\eta))^2 -$$

$$\left[ \frac{a^2 x}{n C_{pf}} \frac{\mu_f C_{pf}}{k_f} \frac{k_f \sigma_{nf}}{k_{nf} \rho_f} \frac{\sigma_f B_0^2}{a \rho_f} + \frac{a^2 x}{n C_{pf}} \frac{\mu_f C_{pf}}{k_f} \frac{k_f}{k_{nf} (1 - \phi)^{2.5}} \frac{\nu}{a K} \right] (f'(\eta) - 1)^2 +$$

$$\frac{a^2 x}{n C_{pf}} \frac{\mu_f C_{pf}}{k_f} \frac{\mu_f k_f}{\rho_f k_{nf} \rho_f \sqrt{K}} \frac{F x}{\rho_f \sqrt{K}} (f'(\eta) - 1)^3, \quad (5.3.14)$$

$$A_4 Pr [\theta(\eta) f'(\eta) - f(\eta) \theta'(\eta)] = \theta''(\eta) + A_5 Pr Ec (f''(\eta))^2 + Ec Pr \left[ A_6 M + A_5 \frac{1}{Da} \right]$$

$$(f'(\eta) - 1)^2 + A_7 Ec Pr Fn (f'(\eta) - 1)^3. \quad (5.3.15)$$

Where,

$$\begin{aligned}
M &= \frac{\sigma_f B_0^2}{a \rho_f}, & Pr &= \frac{\mu_f C_{pf}}{k_f}, & Ec &= \frac{a^2}{n C_{pf}}, & Da &= \frac{a K_1}{\nu_f}, & F_n &= \frac{F x}{\rho_f \sqrt{K}}, \\
A_4 &= \frac{k_f}{k_{nf}} \left( 1 - \phi + \frac{\phi (\rho C_p)_s}{(\rho C_p)_f} \right), & A_5 &= \frac{k_f}{k_{nf} (1 - \phi)^{2.5}}, & A_6 &= \frac{\sigma_{nf} k_f}{\sigma_f k_{nf}}, \\
A_7 &= \frac{k_f}{k_{nf}}.
\end{aligned} \tag{5.3.16}$$

The boundary conditions will be

As  $\eta \rightarrow 0$

$$u(x, 0) = u_w(x) = bx \Rightarrow ax f'(0) = bx \Rightarrow f'(0) = \frac{b}{a} = \lambda$$

$$v(x, 0) = V_0 = -\sqrt{a \nu_f} f(0) \Rightarrow f(0) = \frac{V_0}{-\sqrt{a \nu_f}} = S$$

Substituting equation (5.3.4) in the convective boundary equation (5.2.11), we obtain

$$\theta'(\eta = 0) = \sqrt{\frac{a}{\nu}} \frac{h_f [T_f - T_\infty - (T_f - T_\infty) \theta(0)]}{-k_f (T_f - T_\infty)} \Rightarrow \theta'(0) = -Bi(1 - \theta(0))$$

As  $\eta \rightarrow \infty$ ,

$$u(x, \infty) = U_\infty(x) = ax \Rightarrow ax f'(\eta = \infty) = ax \Rightarrow f'(\infty) = 1$$

$$\theta(\infty) = \frac{T(x, \infty) - T_\infty}{T_f - T_\infty} = \frac{T_\infty - T_\infty}{T_f - T_\infty} \Rightarrow \theta(\infty) = 0$$

Finally, the following nonlinear ordinary differential equations has been obtained:

$$f''' - A_1((f')^2 - f f'' - 1) - \left( M A_2 + \frac{1}{Da} \right) (f' - 1) - F_n A_3 (f' - 1)^2 = 0, \tag{5.3.17}$$

$$\begin{aligned}
\theta'' - A_4 Pr (2\theta f' - f \theta') + A_5 Pr Ec (f'')^2 + Ec Pr (A_6 M + A_5 \frac{1}{Da}) (f' - 1)^2 \\
+ A_7 Ec Pr F_n (f' - 1)^3 = 0.
\end{aligned} \tag{5.3.18}$$

and the boundary conditions in terms of the new variables:

$$\eta = 0: \quad f(0) = S, \quad f'(0) = \lambda, \quad \theta'(0) = -Bi[1 - \theta(0)], \tag{5.3.19}$$

$$\eta \rightarrow \infty: \quad f'(\infty) = 1, \quad \theta(\infty) = 0. \tag{5.3.20}$$

Here a prime symbol denotes differentiation with respect to  $\eta$  and  $f', \theta$  and  $\eta$  are the dimensionless velocity, temperature and similarity variable, respectively. The parameters, the dimensionless numbers and the variables defined are as follows:

$$\begin{aligned}
M &= \frac{\sigma_f B_0^2}{a \rho_f}, & Pr &= \frac{\mu_f C_{pf}}{k_f}, & Ec &= \frac{a^2}{n C_{pf}}, & Da &= \frac{aK}{\nu_f}, & F_n &= \frac{Fx}{\rho_f \sqrt{K}}, \\
\lambda &= \frac{b}{a}, & S &= \frac{-V_0}{\sqrt{a\nu_f}}, & Bi &= \frac{h_f}{k_f} \sqrt{\frac{a}{\nu_f}}, & A_1 &= (1 - \phi + \frac{\phi \rho_s}{\rho_f})(1 - \phi)^{2.5}, \\
A_2 &= \frac{(1 - \phi)^{2.5}}{\sigma_f} \sigma_{nf}, & A_3 &= (1 - \phi)^{2.5}, & A_4 &= \frac{k_f}{k_{nf}} \left[ 1 - \phi + \frac{\phi(\rho C_p)_s}{(\rho C_p)_f} \right], \\
A_5 &= \frac{k_f}{k_{nf}(1 - \phi)^{2.5}}, & A_6 &= \frac{\sigma_{nf} k_f}{\sigma_f k_{nf}}, & A_7 &= \frac{k_f}{k_{nf}}.
\end{aligned} \tag{5.3.21}$$

Where  $M, Pr, Ec, Da, F_n, S, \lambda$  and  $Bi$  denote the magnetic field parameter, Prandtl number, Eckert number, the porous media parameter, porous medium inertia parameter, the constant mass flux parameter (where  $S > 0$  for suction and  $S < 0$  for injection or withdrawal of the fluid), stretching/shrinking parameter (where  $\lambda > 0$  for a stretching sheet), and  $\lambda < 0$  for a shrinking sheet, and Biot number, respectively. It is important to note that the porous medium inertia parameter ( $F_n$ ) is a local similarity parameter. Nonetheless, the parameter  $F_n$  may become a similarity parameter if the non-uniform inertial coefficient of porous medium is defined as  $F = \frac{C_d}{x}$ , where  $C_d$  is drag coefficient. In this case, the expression for  $F_n = \frac{C_d}{\rho_f \sqrt{K}}$  is a similarity parameter since it is independent of  $x$  (Hayat et al. (2016); Das et al. (2020b); Upreti et al. (2020)).

## 5.4 Important Engineering Parameters

The important physical quantities of interest, in this problem, are the skin friction coefficient  $C_f$  and the Nusselt number  $Nu$  are defined as:

$$C_f = \frac{\tau_w}{\rho_f U_\infty^2}, \quad Nu = \frac{x q_w''}{k_f (T_f - T_\infty)}, \tag{5.4.1}$$

where  $\tau_w$  is the skin friction and  $q_w''$  is heat flux from the sheet surface are given by

$$\begin{aligned}
\tau_w &= \mu_{nf} \left. \frac{\partial u}{\partial y} \right|_{\eta=0} = \mu_{nf} \left. \frac{\partial}{\partial y} (ax f'(\eta)) \right|_{\eta=0} = \frac{\mu_f}{(1-\phi)^{2.5}} ax \sqrt{\frac{a}{\nu_f}} f''(0), \\
q_w'' &= -k_{nf} \left. \frac{\partial T}{\partial y} \right|_{\eta=0} = -k_{nf} (T_f - T_\infty) \sqrt{\frac{a}{\nu_f}} \theta'(0).
\end{aligned} \tag{5.4.2}$$

Substituting equation(5.4.2) into equation (5.4.1), we obtain

$$\begin{aligned}
C_f &= \frac{\tau_w}{\rho_f U_\infty^2} = \frac{ax \mu_f}{\rho_f (1-\phi)^{2.5} a^2 x^2} \sqrt{\frac{a}{\nu_f}} f''(0) = \sqrt{\frac{\nu_f}{ax^2}} \frac{f''(0)}{(1-\phi)^{2.5}}, \\
\Rightarrow C_f Re_x^{1/2} &= \frac{f''(0)}{(1-\phi)^{2.5}},
\end{aligned} \tag{5.4.3}$$

$$\begin{aligned}
Nu &= \frac{-x k_{nf} (T_f - T_\infty) \sqrt{\frac{a}{\nu_f}} \theta'(0)}{k_f (T_f - T_\infty)} = \frac{-x k_{nf} \sqrt{\frac{a}{\nu_f}} \theta'(0)}{k_f} = -\sqrt{\frac{ax^2}{\nu_f}} \frac{k_{nf}}{k_f} \theta'(0), \\
\Rightarrow Nu &= Nu_x Re_x^{-1/2} = -\frac{k_{nf}}{k_f} \theta'(0).
\end{aligned} \tag{5.4.4}$$

In dimensionless form, the skin friction coefficient and reduced Nusselt number are rewritten as:

$$C_f Re_x^{1/2} = \frac{f''(0)}{(1-\phi)^{2.5}}, \quad Nu Re_x^{-1/2} = -\frac{k_{nf}}{k_f} \theta'(0). \tag{5.4.5}$$

The heat transfer enhancement (HTE) of the nanoparticles can be determined as

$$HTE = \frac{Nu Re_x^{-1/2}(\phi \neq 0) - Nu Re_x^{-1/2}(\phi = 0)}{Nu Re_x^{-1/2}(\phi = 0)} * 100\%. \tag{5.4.6}$$

Where  $Re_x = \frac{U_\infty x}{\nu_f}$  is the local Reynold number.

## 5.5 Stability Analysis

The stability analysis is important to test the reliability of the non-unique similarity solutions. In general, depending on the assumptions of physical model, a boundary layer problem may produce zero, unique or multiple solutions. For such cases, it is substantial to perform stability analysis in order to examine which of the solutions is physically practicable and stable. The execution of the stability analysis is mathematically performed to validate the real solution among all the solutions. It is implemented

by considering an unsteady (time dependent) problem Merkin (1986). Hence, for the present analysis, an unsteady form of equations (5.2.8) and (5.2.9) have to be inspected:

$$\begin{aligned} \frac{\partial u}{\partial t} + u \frac{\partial u}{\partial x} + v \frac{\partial u}{\partial y} = U_\infty \frac{\partial U_\infty}{\partial x} + \frac{\mu_{nf}}{\rho_{nf}} \frac{\partial^2 u}{\partial y^2} - \left( \frac{\sigma_{nf} B_0^2}{\rho_{nf}} + \frac{\mu_{nf}}{\rho_{nf} K} \right) (u - U_\infty) \\ + \frac{F}{\rho_{nf} \sqrt{K}} (u - U_\infty)^2, \end{aligned} \quad (5.5.1)$$

$$\begin{aligned} \frac{\partial T}{\partial t} + u \frac{\partial T}{\partial x} + v \frac{\partial T}{\partial y} = \frac{k_{nf}}{(\rho C_p)_{nf}} \frac{\partial^2 T}{\partial y^2} + \left[ \frac{\sigma_{nf} B_0^2}{(\rho C_p)_{nf}} + \frac{\mu_{nf}}{(\rho C_p)_{nf} K} \right] (u - U_\infty)^2 + \\ \frac{\mu_{nf}}{(\rho C_p)_{nf}} \left( \frac{\partial u}{\partial y} \right)^2 + \frac{F}{(\rho C_p)_{nf} \sqrt{K}} (u - U_\infty)^3. \end{aligned} \quad (5.5.2)$$

Following Makinde (2018), new transformations are applied to the unsteady equations (5.5.1) and (5.5.2) where  $\tau$  is the non-dimensional time variable:

$$\begin{aligned} \eta = y \sqrt{\frac{a}{\nu_f}}, \quad u = ax \frac{\partial f}{\partial \eta}(\eta, \tau), \quad v = -\sqrt{a \nu_f} f(\eta, \tau), \quad \psi = f(\eta, \tau) x \sqrt{a \nu_f}, \\ \theta(\eta, \tau) = \frac{T - T_\infty}{T_f - T_\infty}, \quad \tau = bt. \end{aligned} \quad (5.5.3)$$

Now using equation (5.5.3), equation (5.5.1) and (5.5.2) become

$$\begin{aligned} \frac{\partial^3 f}{\partial \eta^3} - A_1 \left( \frac{\partial^2 f}{\partial \tau \partial \eta} + \left( \frac{\partial f}{\partial \eta} \right)^2 - f \frac{\partial^2 f}{\partial \eta^2} \right) - \left( MA_2 + \frac{1}{Da} \right) \left( \frac{\partial f}{\partial \eta} - 1 \right) \\ - F_n A_3 \left( \frac{\partial f}{\partial \eta} - 1 \right)^2 + A_1 = 0, \end{aligned} \quad (5.5.4)$$

$$\begin{aligned} \frac{\partial^2 \theta}{\partial \eta^2} - A_4 Pr \left( \frac{\partial \theta}{\partial \tau} + 2\theta \frac{\partial f}{\partial \eta} - f \frac{\partial \theta}{\partial \eta} \right) + A_5 Pr Ec \left( \frac{\partial^2 f}{\partial \eta^2} \right)^2 \\ + Ec Pr \left( A_6 M + \frac{A_5}{Da} \right) \left( \frac{\partial f}{\partial \eta} - 1 \right)^2 + A_7 Ec Pr F_n \left( \frac{\partial f}{\partial \eta} - 1 \right)^3 = 0, \end{aligned} \quad (5.5.5)$$

and the boundary conditions become:

$$\begin{aligned} f(0, \tau) = S, \quad \frac{\partial f}{\partial \eta}(0, \tau) = \lambda, \quad \frac{\partial \theta}{\partial \eta}(0, \tau) = -Bi[1 - \theta(0, \tau)], \\ \frac{\partial f}{\partial \eta}(\infty, \tau) \rightarrow 1, \quad \theta(\infty, \tau) \rightarrow 0. \end{aligned} \quad (5.5.6)$$

Based on [Harris et al. \(2009\)](#), we test the stability of the steady flow solution  $f(\eta) = f_0(\eta)$  and  $\theta(\eta) = \theta_0(\eta)$  satisfying the set of boundary-value problem equation (5.3.17)-(5.3.20) by writing

$$\begin{aligned} f(\eta, \tau) &= f_0(\eta) + e^{-\beta\tau} F(\eta, \tau) \\ \theta(\eta, \tau) &= \theta_0(\eta) + e^{-\beta\tau} G(\eta, \tau) \end{aligned} \quad (5.5.7)$$

where  $\beta$  is an unknown eigenvalue parameter (a small disturbance of growth or decay) and  $F(\eta, \tau)$  and  $G(\eta, \tau)$  are small relative to  $f_0(\eta)$  and  $\theta_0(\eta)$ , respectively. The following equations are obtained by substituting (5.5.7) into (5.5.4)- (5.5.6)

$$\begin{aligned} \frac{\partial^3 F}{\partial \eta^3} + A_1 f_0 \frac{\partial^2 F}{\partial \eta^2} + A_1 F \frac{\partial^2 f_0}{\partial \eta^2} + \frac{\partial F}{\partial \eta} \left[ \beta A_1 - 2A_1 \frac{\partial f_0}{\partial \eta} - A_2 M - \frac{1}{Da} \right. \\ \left. - 2A_3 F_n \left( \frac{\partial f_0}{\partial \eta} - 1 \right) \right] - A_1 \frac{\partial^2 F}{\partial \eta \partial \tau} = 0, \end{aligned} \quad (5.5.8)$$

$$\begin{aligned} \frac{\partial^2 G}{\partial \eta^2} + \frac{\partial F}{\partial \eta} \left[ 2EcPr \left( A_6 M + A_5 \frac{1}{Da} \right) \left( \frac{\partial f_0}{\partial \eta} - 1 \right) + 3A_7 EcPr F_n \left( \frac{\partial f_0}{\partial \eta} - 1 \right)^2 \right. \\ \left. - A_4 Pr \theta_0 \right] + 2A_5 Pr Ec f_0 \frac{\partial^2 \theta_0}{\partial \eta^2} \frac{\partial^2 G}{\partial \eta^2} + A_4 Pr f_0 \frac{\partial G}{\partial \eta} + A_4 Pr G \left( \beta - 2 \frac{\partial f_0}{\partial \eta} \right) \\ + A_4 Pr F \frac{\partial \theta_0}{\partial \eta} - A_4 Pr \frac{\partial G}{\partial \tau} = 0, \end{aligned} \quad (5.5.9)$$

subjected to the boundary conditions:

$$\begin{aligned} F(0, \tau) = 0, \quad \frac{\partial F}{\partial \eta}(0, \tau) = 0, \quad \frac{\partial G}{\partial \eta}(0, \tau) = BiG(0, \tau), \\ \frac{\partial F}{\partial \eta}(\infty, \tau) \rightarrow 0, \quad G(\infty, \tau) \rightarrow 0. \end{aligned} \quad (5.5.10)$$

Following [Weidman et al. \(2006\)](#), the initial growth or decay of the solution (5.5.7) can be identified by setting  $\tau = 0$  so that  $F = F_0(\eta)$  and  $G = G_0(\eta)$  in Equations (5.5.8)- (5.5.10). Solutions of the eigenvalue problem give an infinite set of eigenvalues  $\beta_1 < \beta_2 < \beta_3 \dots$ ; if  $\beta_1$  is negative, there is an initial growth of disturbances and the flow is unstable but when  $\beta_1$  is positive, there is an initial decay and the flow is stable. The linearized Eigenvalue problem are given by

$$F_0''' + A_1 f_0 F_0'' + A_1 F_0 f_0'' + F_0' \left[ \beta A_1 - 2A_1 f_0' - A_2 M - \frac{1}{Da} - 2A_3 F_n \left( f_0' - 1 \right) \right] = 0, \quad (5.5.11)$$

$$\begin{aligned}
& G_0'' + F_0' \left[ 2EcPr \left( A_6M + A_5 \frac{1}{Da} \right) (f_0' - 1) + 3A_7EcPrF_n (f_0' - 1)^2 - A_4Pr\theta_0 \right] \\
& + 2A_5PrEc f_0 \theta_0'' G_0'' + A_4Pr f_0 G_0' + A_4Pr G_0 (\beta - 2f_0') + A_4Pr F_0 \theta_0' = 0,
\end{aligned} \tag{5.5.12}$$

with the new boundary conditions:

$$F_0(0) = 0, \quad F_0'(0) = 0, \quad G_0'(0) = BiG_0(0), \quad F_0'(\infty) \rightarrow 0, \quad G_0(\infty) \rightarrow 0. \tag{5.5.13}$$

As suggested by [Harris et al. \(2009\)](#), the range of possible eigenvalues can be obtained by relaxing one of the boundary conditions given in equation (5.5.13),  $F_0'(\infty) \rightarrow 0$  or  $G_0(\infty) \rightarrow 0$ . Thus, the boundary condition  $F_0'(\infty) \rightarrow 0$  is relaxed and replaced with the normalizing boundary condition  $F_0''(0) = 1$ , and the boundary conditions become:

$$F_0(0) = 0, \quad F_0'(0) = 0, \quad G_0'(0) = BiG_0(0), \quad F_0''(0) = 1, \quad G_0(\infty) \rightarrow 0. \tag{5.5.14}$$

Finally, equations (5.5.11) and (5.5.12) are solved along the new boundary conditions (5.5.14).

## 5.6 Numerical Procedures

The non-linear system of equations (5.3.17) and (5.3.18) along with the boundary conditions (5.3.19) and (5.3.20) are solved numerically using the fourth-fifth order Runge-Kutta-Fehlberg method and the shooting method with the help of Maple software. However, this system needs to be reduced to the equivalent system of first order ODEs as follows:

$$\begin{aligned}
f' &= g, \\
g' &= h, \\
h' &= A_1((g)^2 - fh - 1) + \left( MA_2 - \frac{1}{Da} \right) (g - 1) + F_n A_3 (g - 1)^2, \\
\theta' &= p, \\
p' &= A_4Pr(2\theta g - fp) - A_5PrEc(h)^2 - EcPr \left( A_6M + A_5 \frac{1}{Da} \right) (g - 1)^2 \\
&\quad + A_7EcPrF_n(g - 1)^3,
\end{aligned} \tag{5.6.1}$$

with boundary conditions

$$f(0) = S, \quad g(0) = \lambda, \quad h(0) = \alpha_1, \quad \theta(0) = \alpha_2, \quad p(0) = -Bi[1 - \alpha_2], \quad (5.6.2)$$

Here,  $\alpha_1$  and  $\alpha_2$  are unknown initial conditions. We have to shoot these initial conditions with some arbitrary slope such that the solution of the ODE system satisfies the given far-field boundary conditions. Thereafter, the resultant system of first-order ODEs is solved by employing the fourth-fifth order Runge-Kutta-Fehlberg method, and the accuracy of missing initial conditions is then checked by comparing calculated values with the given terminal points. The dual solutions are obtained by taking different initial guesses for the values of  $\alpha_1$  and  $\alpha_2$ , where the far-field boundary conditions might be satisfied by all profiles asymptotically.

## 5.7 Results and Discussion

In this study, the effects of shrinking/stretching parameter  $\lambda$ , magnetic field parameter  $M$ , the porous medium parameter  $Da$ , porous medium inertia parameter  $F_n$ , the constant mass flux parameter  $S$ , viscous dissipation and convective heating on the magnetite ferrofluid velocity and temperature are demonstrated in graphs. The range of parameters used in this study are  $0.1 \leq M \leq 1.1, 0 \leq \phi \leq 0.1, 0.1 \leq Ec \leq 0.3, 0.2 \leq Da \leq 2, 0.1 \leq F_n \leq 1.5, -1 \leq S \leq 2$  and  $Pr = 6.2$  is used to signify the pure water as the base fluid. The existence of dual solutions for certain ranges of parameter variations are shown for the skin friction coefficient in the form of graphs and tables and also the variations of Nusselt number are illustrated in graphs for different values of the parameters change.

Equation (5.3.17) and equation (5.3.18) together with the boundary conditions (5.3.19) and (5.3.20) are solved numerically using the shooting method in Maple2018. Validation of the numerical method used in this study is checked by comparing the results obtained in the present study with the results from the previous study for different parameters, as shown in Table 5.7.1. As presented in a below table, it was found that the present results are in a good agreement with the solution obtained by Nazar et al. (2011) for a regular fluid case. This is our guarantee that the method used to tackle our problem is accurate and valid. In this study, the computations are

Table 5.7.1: The computation showing  $Re_x^{1/2}C_f$  and  $Re_x^{-1/2}Nu$  for different stretching/shrinking parameter value with  $Pr = 1$  for  $\phi = 0$  (Regular fluid),  $M = 0, S = 0, Da = \infty, F_n = 0, Bi = \infty, Ec = 0$

$\lambda$	$Re_x^{1/2}C_f$		$Re_x^{-1/2}Nu$	
	Present result	(Nazar et al., 2011)	Present result	(Nazar et al., 2011)
1	0	0	1.253314	1.25331
0.5	0.713295	0.71329	1.051458	1.05146
0.2	1.051130	1.05113	0.913303	0.91330
0	1.232588	1.232588	0.811301	0.811301
-0.25	1.402241	1.40224	0.668573	0.66857
-0.5	1.495670	1.49567	0.501448	0.50145
-0.75	1.489298	1.48930	0.293763	0.29378
-1	1.328817	1.32882	0	0

done for different values of parameters involved in the governing flow equations. The velocity profiles, temperature profiles, the graph of skin friction and Nusselt number are plotted.

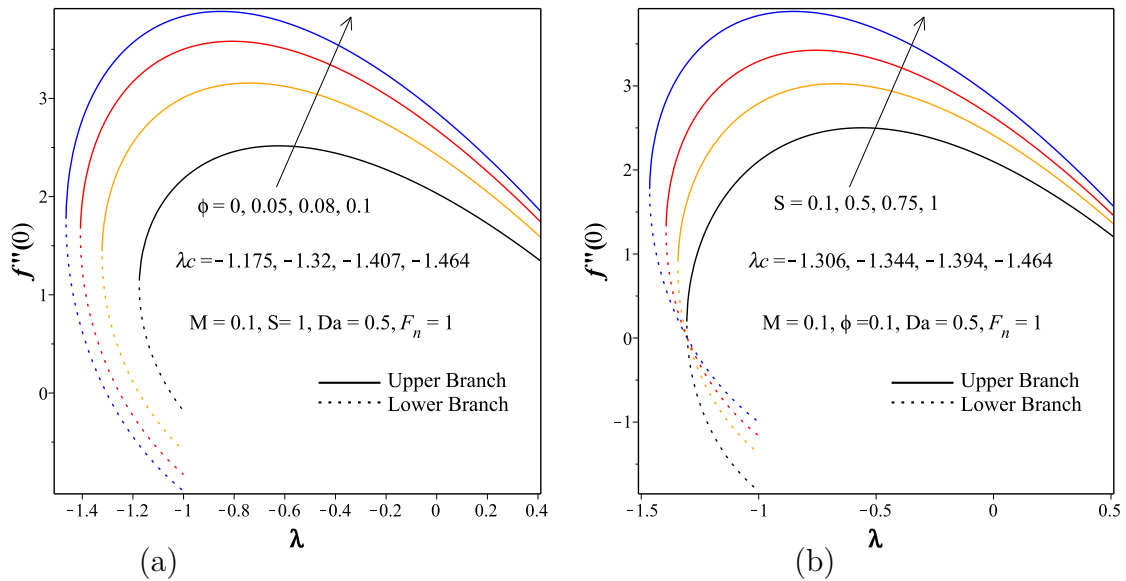


Figure 5.7.1: (a) Variation of skin friction for different values of magnetite nanoparticle volume fraction,  $\phi$  (b) Variation of skin friction for different values of suction parameter,  $S$ .

The variations of the skin friction for various values of the governing parameters are presented in Figure 5.7.1 - 5.7.3. From these figures, we observe that dual solutions with upper and lower branch solutions exist when  $\lambda > \lambda_c$ , while no real solution is obtained when  $\lambda < \lambda_c$ . The critical value  $\lambda_c$  is the value where the upper branch solution meets the lower branch solution. These figures also show that the magnitude

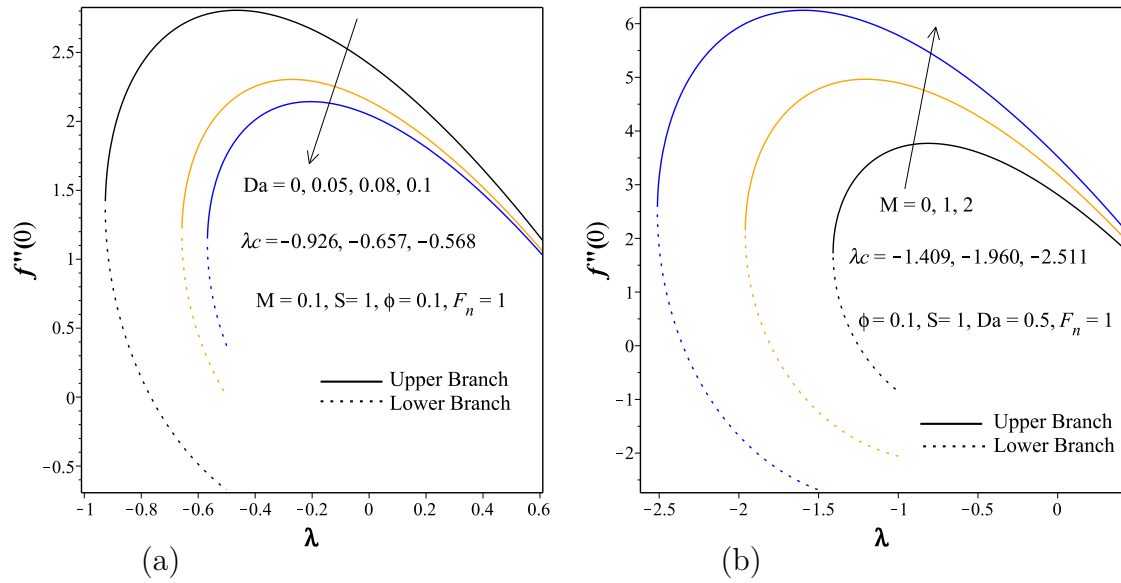


Figure 5.7.2: (a) Variation of skin friction for different values of porous media parameter,  $Da$  (b) Variation of skin friction for different values of magnetic field parameter,  $M$

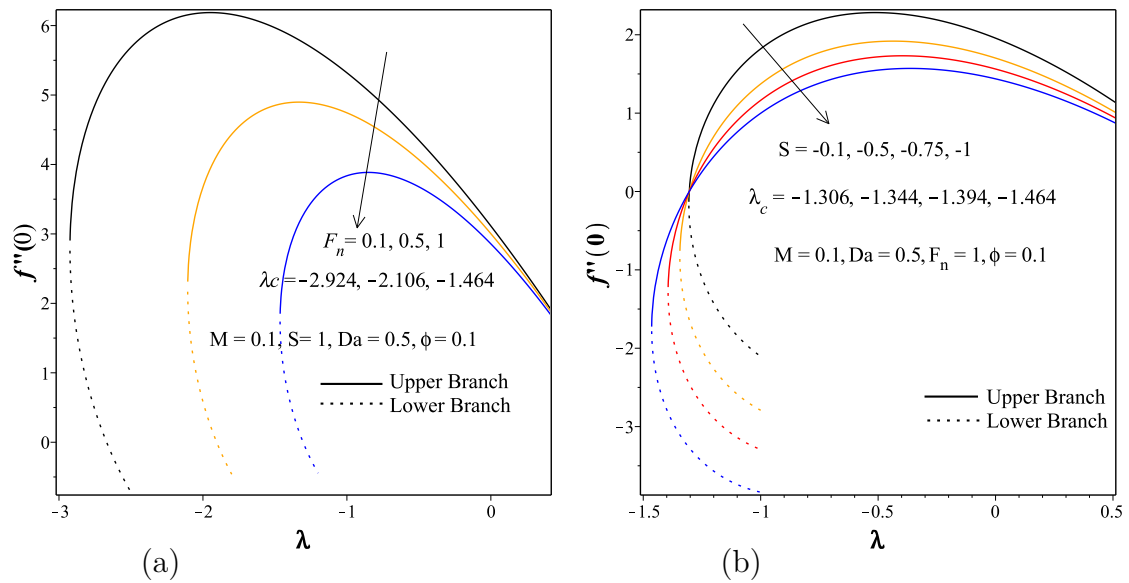


Figure 5.7.3: (a) Variation of skin friction for different values of second-order porous resistance parameter,  $F_n$  (b) Variation of skin friction for different values of injection parameter,  $S$

of  $\lambda_c$  increases with each parameter  $\phi, S, M$  and acts in opposite fashion with the porous resistance parameters,  $Da$  and  $F_n$ . Hence, the intensification of the nanoparticle volume fraction, suction, injection, and the magnetic field parameter widen the range of  $\lambda$  for which the solution exists and narrow for the increment of the porous medium parameter and porous medium inertia parameter. There is no similarity solutions exist beyond this critical value due to the boundary layer separation from the surface

and the solution based upon the boundary layer approximations are not possible.

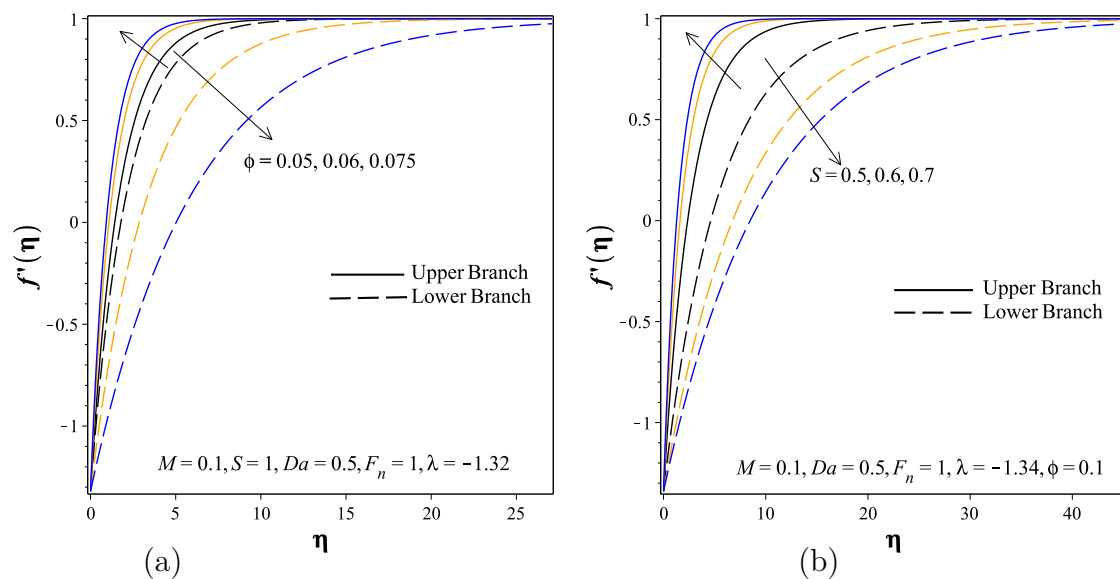


Figure 5.7.4: (a) Dual solution for velocity profiles with nanoparticles concentration,  $\phi$ . (b) Dual solution for velocity profiles with suction parameter,  $S$ .

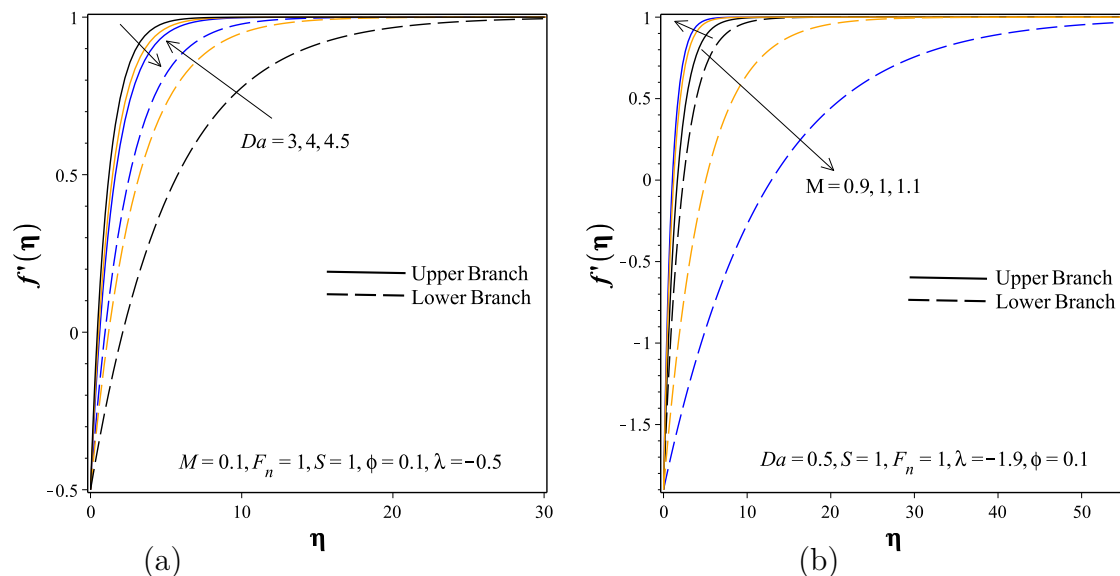


Figure 5.7.5: (a) Dual solution for velocity profiles with porous media parameter,  $Da$ . (b) Dual solution for velocity profiles with magnetic field parameter,  $M$ .

Figure 5.7.1a illustrates that the value of the skin friction coefficient is intensified with the quantity of magnetite nanoparticle volume fraction for the upper branch solution, which come to an agreement with the results obtained in Table 5.7.2. This indicates that an increase in nanoparticle volume fraction resulted in a stronger wall shear stress. Furthermore, it is noted that no skin friction is achieved when  $\lambda = 1$  for all values of

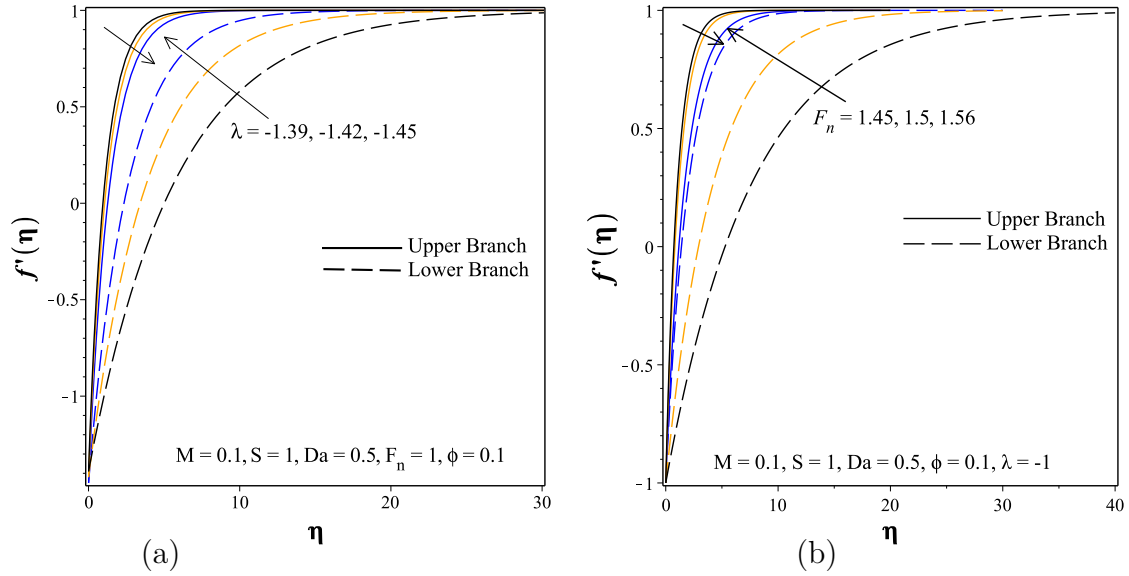


Figure 5.7.6: (a) Dual solution for velocity profiles with shrinking parameter,  $\lambda$ . (b) Dual solution for velocity profiles with second-order porous resistance parameter,  $F_n$ .

nanoparticles volume fraction. This is due to the fact that the fluid velocity is equal to the stretching/shrinking sheet velocity.

Table 5.7.2: The computation showing skin friction and critical shrinking parameter for various values of  $\phi$  and  $\lambda$  when  $M = 0.1, S = 1, Da = 0.5, F_n = 1$

$\phi$	$\lambda_c$	$\lambda$	$Re_x^{1/2} C_f$	
			Lower Branch	Upper Branch
0	-1.175	-1.139	0.495546	1.643453
	-1.175	-1.140	0.503809	1.636190
	-1.175	-1.170	0.868000	1.302000
0.05	-1.322	-1.240	0.339038	2.370809
	-1.322	-1.260	0.475999	2.258044
	-1.322	-1.290	0.737148	2.033187
0.08	-1.407	-1.340	0.531744	2.593573
	-1.407	-1.350	0.613821	2.524851
	-1.407	-1.360	0.703912	2.448116
0.1	-1.464	-1.400	0.624384	2.782431
	-1.464	-1.420	0.814838	2.620368
	-1.464	-1.430	0.927322	2.522079

As seen in Figure 5.7.1b that for the upper branch solution, the skin friction coefficient rises with an increase in suction. This is because suction at the boundary slows down the fluid motion and hence increases the velocity gradient at the surface. Similar behavior of the skin friction coefficient is observed with an intensification of the magnetic field parameter as presented in Figure 5.7.2b. An increase in the porous media parameter, porous medium inertia parameter, and injection parameter drops the skin

friction coefficient as shown in Figures 5.7.2a, 5.7.3a, and 5.7.3b, respectively. All the results obtained graphically agreed with the results mentioned in Table 5.7.3.

Table 5.7.3: The computation showing impact of parameters variation on skin friction and critical shrinking parameter for  $\text{Fe}_3\text{O}_4/\text{H}_2\text{O}$  when  $\phi = 0.1$

S	Da	M	$F_n$	$\lambda_c$	$\lambda$	$Re_x^{1/2} C_f$	
						Lower Branch	Upper Branch
1	0.5	0.1	1	-1.464	-1.319	0.07793708	3.2138980
1.5	0.5	0.1	1	-1.664	-1.660	2.52654336	3.1372878
2	0.5	0.1	1	-1.944	-1.940	3.83650193	4.5101975
1	1	0.1	1	-0.926	-0.920	1.09144325	1.6340093
1	1.5	0.1	1	-0.746	-0.740	0.97564168	1.4942997
1	2	0.1	1	-0.657	-0.650	0.91902959	1.4231562
1	0.5	0.5	1	-1.680	-1.680	1.57861803	2.2256596
1	0.5	1	1	-1.960	-1.950	1.56597395	2.6215704
1	0.5	0.1	1.5	-1.041	-1.011	0.73522094	2.1194067
1	0.5	0.1	2	-0.743	-0.740	1.01571989	1.4542215

The effects of various values of the governing parameters on fluid velocity are shown in Figures 5.7.4 - 5.7.6. In these figures, we noted that the existence of dual solutions with the upper and lower branches for certain values of the parameter variations and the far end boundary conditions are satisfied asymptotically. Furthermore, it is noted that the hydrodynamic boundary layer thickness for the upper branch solution is less than that of the lower branch solution. As displayed in Figure 5.7.4a, the intensification of the quantity of the magnetite nanoparticle volume fraction leads to an increment in the fluid velocity for the upper branch solution and a decrement in the lower branch solution. It is also noticed that the hydrodynamic boundary layer thickness goes in the reverse pattern for the upper branch solution and the same pattern for the lower branch solution.

The effects of the suction parameter on ferrofluid velocity for the shrinking sheet are observed in Figure 5.7.4b. This profile shows that the increment in the suction parameter resulted in an increment in fluid velocity for the upper branch solution and decrement for the lower branch solution. Further, we noted that the hydrodynamic boundary layer thickness decrease for the upper branch solution and, thus, increases the flow near the surface as the suction parameter intensifies. This is because of the reason that suction is one of the mechanisms used to reduce drag on bodies to control

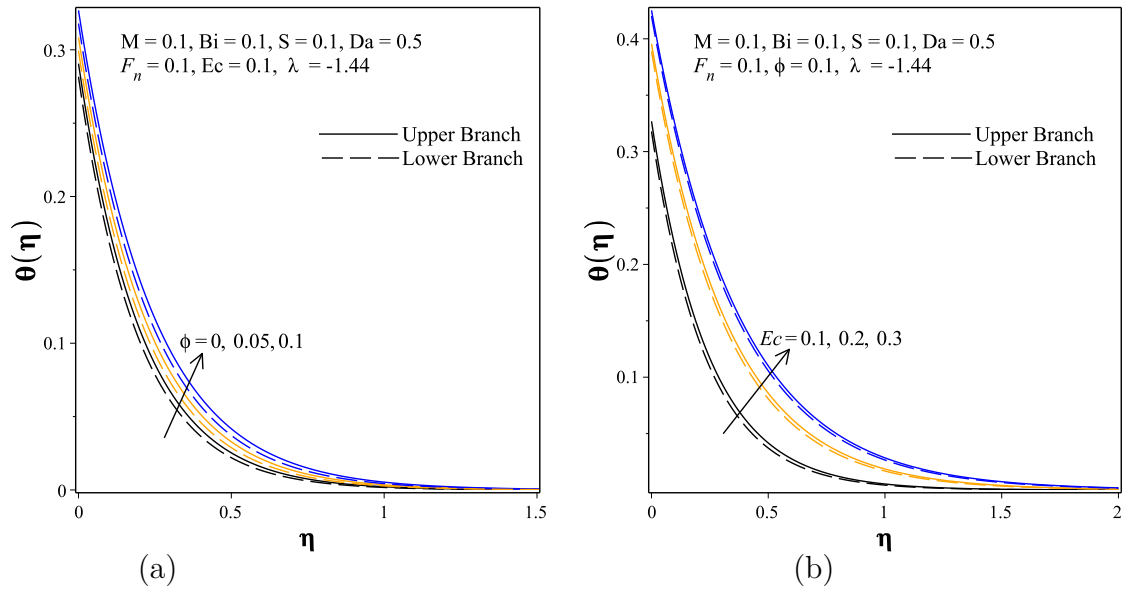


Figure 5.7.7: (a) Dual solution for temperature profiles with nanoparticles concentration,  $\phi$  (b) Dual solution for temperature profiles with viscous dissipation,  $Ec$ .

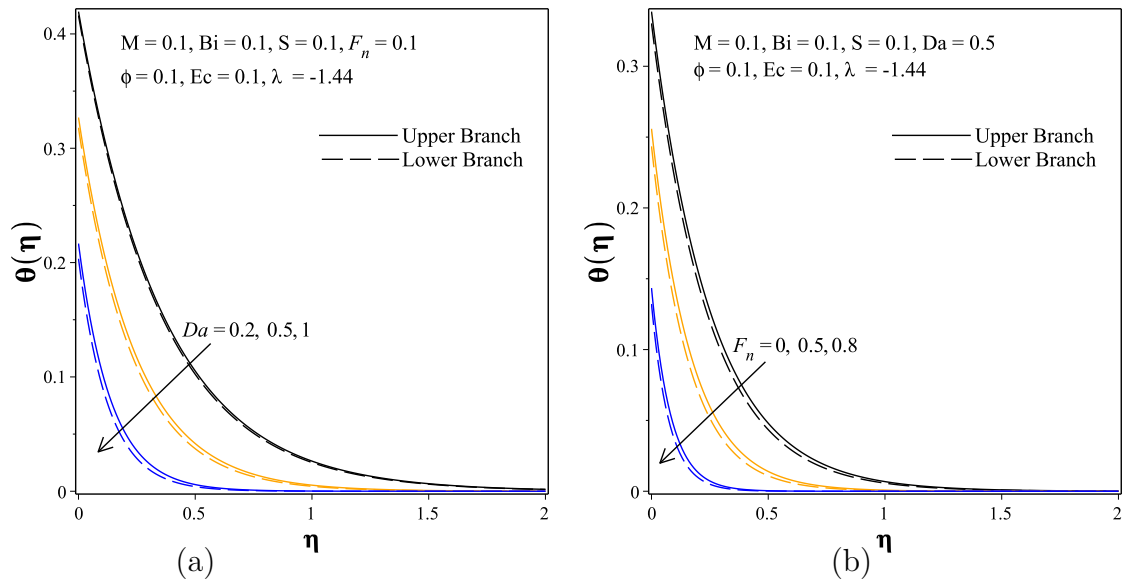


Figure 5.7.8: (a) Dual solution for temperature profiles with porous medium parameter,  $Da$  (b) Dual solution for temperature profiles with second-order porous resistance parameter,  $F_n$ .

the boundary layer separation.

The variation of fluid velocity profile with the variation of the porous medium parameter is illustrated in Figure 5.7.5a. It can be noted that the higher the value of the porous medium parameter, the lower the fluid velocity in the upper branch solution. However, a different result is obtained for the lower branch solution that the intensification in the value of porous media parameter initiated the velocity to upsurge. Moreover, the hydrodynamic boundary layer thickness gets diminished for lower values

of the porous medium parameter for the stable solution meanwhile goes in the same pattern for the lower solution.

As illustrated in Figure 5.7.5b, the magnetite ferrofluid is derived to the sheet surface due to the increment in the magnetic field in the porous medium for the upper branch solution. Further resistance to the flow and the magnetite nanoparticles are resulted due to the Lorentz force associated with the applied magnetic field. This resulting force leads to the thinning of the hydrodynamic boundary layer; however, the boundary layer thickens with the magnetic field parameter for the lower branch solution. Furthermore, it is found that the higher values of the magnetic field applied lead to the increment of the fluid velocity for the upper branch solution and the decrement of the fluid velocity for the lower branch solution.

Figure 5.7.6a displays the effects of the shrinking parameter on the fluid velocity. The graph exhibits that the existence of dual solution for increasing values of  $|\lambda|$  for some fixed parameters. We noted that the fluid velocity decreases as the magnitude of the stretching/shrinking parameter  $|\lambda|$  increases for the upper branch solution and it increases as  $|\lambda|$  increases for the lower branch solution. Figure 5.7.6b deals about effects of the porous medium inertia parameter on the fluid velocity. In many practical applications the non-Darcy behavior is important for characterizing fluid flow problems in a porous medium. To see the effect of this parameter, the velocity squared term is included in the momentum equation which is known as the Forchheimer's extension of Darcy's law. As we can see from the graph, for the upper branch solution the porous medium inertia parameter affects the the fluid velocity in opposite manner compared to the lower branch solution. It is also noted that the hydrodynamic boundary layer thickness increases with the porous medium inertia parameter for the upper branch solution.

The dual natures of the temperature profile with sensible numerical values to the governing parameters  $\phi, Ec, Da$  and  $F_n$  variations are illustrated in Figure 5.7.7 and Figure 5.7.8. For the chosen parameter in these figures, it seems that the difference between the upper branch and lower branch solutions is very small and dual solutions almost do not exist in the temperature profile.

As shown in Figure 5.7.7a, the effects of the ferrofluid particle concentration on the fluids temperature profile for other fixed parameters are manifested. It is obtained that

an increase in magnetite nanoparticle volume fraction, increased fluid temperature, and also the thermal boundary layer increased with the magnetite nanoparticle concentration. This is because the enhanced thermal conductivity property of the magnetite nanoparticles promotes the thermal enhancement of the ferrofluid past the permeable shrinking surface. From this graph, we also noted that the value  $\phi = 0$  (regular fluids) implies that no magnetite nanoparticles in the base fluid which in turn tells us that the surface temperature obtained for the base fluid(water) is lower than that of the surface temperature provided by magnetite ferrofluid  $\phi > 0$ . Figure 5.7.7b conveys the consequences of the viscous dissipation parameter on the fluid temperature. An escalation in this parameter gives rise to an increment in the fluid temperature. Since Eckert number has a major role in cooling the stretching or shrinking surface which in turn the heat acquired from this stretching/shrinking surface increased the fluid temperature. Additionally, the thermal boundary layer thickness gets thickens with the Eckert number because an increase in dissipation boosts the thermal conductivity of the flow which leads to an increase in the thermal boundary layer.

As we see from Figure 5.7.8a, the effects of the porous medium parameter on the fluid temperature for the shrinking sheet are verified. This profile shows that the thermal boundary layer thickness decreases for increasing values of the porous medium parameter. Figure 5.7.8b displays the effects of the nonlinear porous medium inertia parameter on the variation of fluids temperature for other fixed parameters. It is obtained that an increase in porous medium inertia parameter increases the fluid temperature and also the thermal boundary layer decreases with the increment of this parameter.

The nature of dual solution occurrence is explicated by local Nusselt number graphs, Figure 5.7.9 and Figure 5.7.10, by taking sensible numerical values to the governing parameters to exploit their effects on the heat transfer processes and the intervals of the existence of the dual solution. Figure 5.7.9a shows the variation of the reduced local Nusselt number with  $\lambda$  for different values of the magnetite nanoparticles volume fraction. It can be seen that the reduced local Nusselt number upsurges with magnetite nanoparticles volume fraction which physically means that the heat transfer rate at the surface increases as  $\phi$  increases. The application of the magnetite nanoparticles volume fraction causes an increase in temperature gradient at the sheet surface

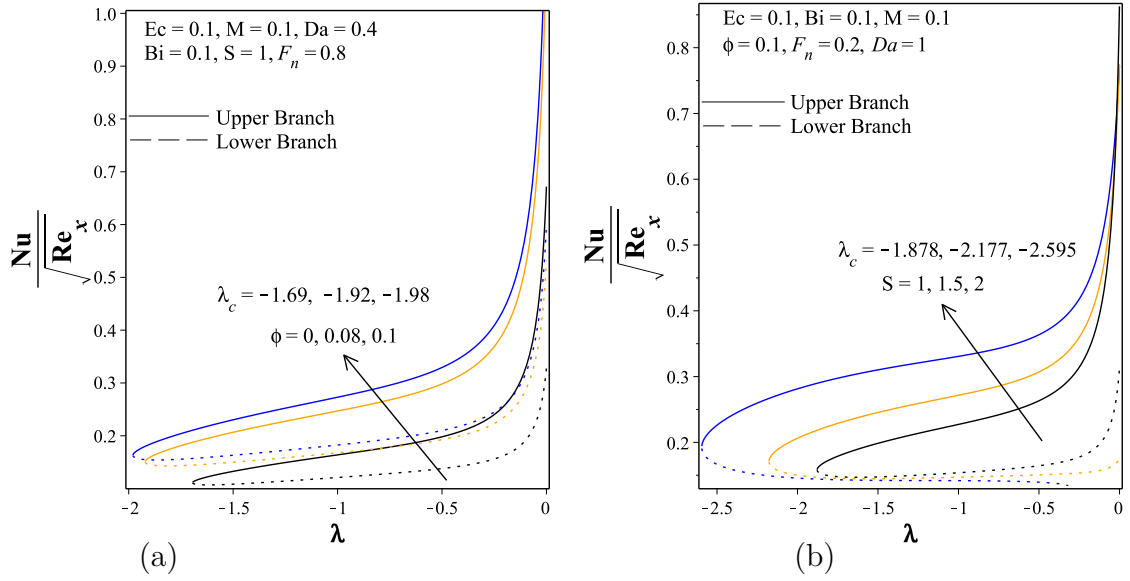


Figure 5.7.9: (a) Variation of local Nusselt number for different values of magnetite nanoparticle volume fraction,  $\phi$  (b) Variation of local Nusselt number for different values of suction parameter,  $S$ .

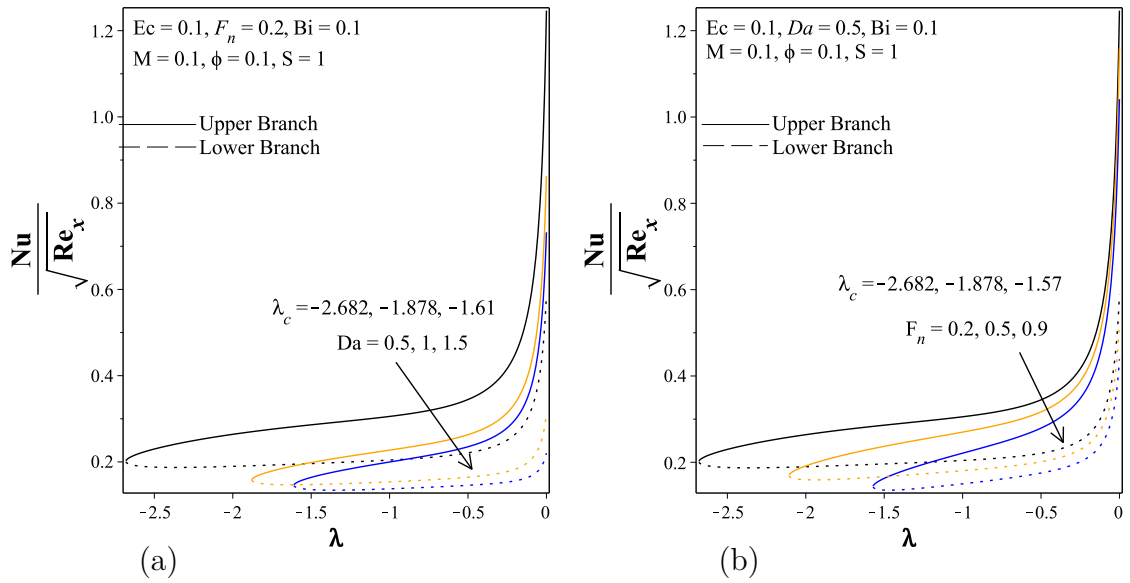


Figure 5.7.10: (a) Variation of local Nusselt number for different values of porous media parameter,  $Da$  (b) Variation of local Nusselt number for different values of second-order porous resistance parameter,  $F_n$ .

and hence enhances the rate of heat transfer from the surface to the fluid. It is also noted that the heat transfer characteristics of the base fluid (water) are improved due to the application of the magnetite nanoparticles. It is also observed that the solution domain increases with the intensification of the magnetite nanoparticles volume fraction. The combined effects of the suction parameter and the shrinking sheet are presented in Figure 5.7.9b. For flows past a shrinking sheet, dual solutions are found

Table 5.7.4: The computation of smallest eigenvalue ( $\beta$ ) for both lower and upper branch solutions for  $\text{Fe}_3\text{O}_4 / \text{H}_2\text{O}$

$\phi$	Da	S	M	$F_n$	$\lambda_c$	$\lambda$	$\beta$	
							Lower Branch	Upper Branch
0.00	0.5	1	0.1	1	-1.175	-1.139	-1.84658908	1.110213025
0.00	0.5	1	0.1	1	-1.175	-1.140	-1.822189105	1.092015814
0.00	0.5	1	0.1	1	-1.175	-1.170	-0.818609230	0.266895080
0.05	0.5	1	0.1	1	-1.321	-1.190	-3.28358197	2.078299080
0.05	0.5	1	0.1	1	-1.321	-1.200	-3.13104704	1.994941488
0.05	0.5	1	0.1	1	-1.321	-1.300	-1.33509522	0.743335278
0.08	0.5	1	0.1	1	-1.405	-1.300	-2.764296237	1.7836607793
0.08	0.5	1	0.1	1	-1.405	-1.350	-2.006142312	1.2585794567
0.08	0.5	1	0.1	1	-1.405	-1.390	-1.184362485	0.5938153589
0.1	0.5	1	0.1	1	-1.4641	-1.400	-2.07935102	1.2944575652
0.1	0.5	1	0.1	1	-1.4641	-1.420	-1.746482488	1.0368550235
0.1	0.5	1	0.1	1	-1.4641	-1.440	-1.34409043	0.7045052433

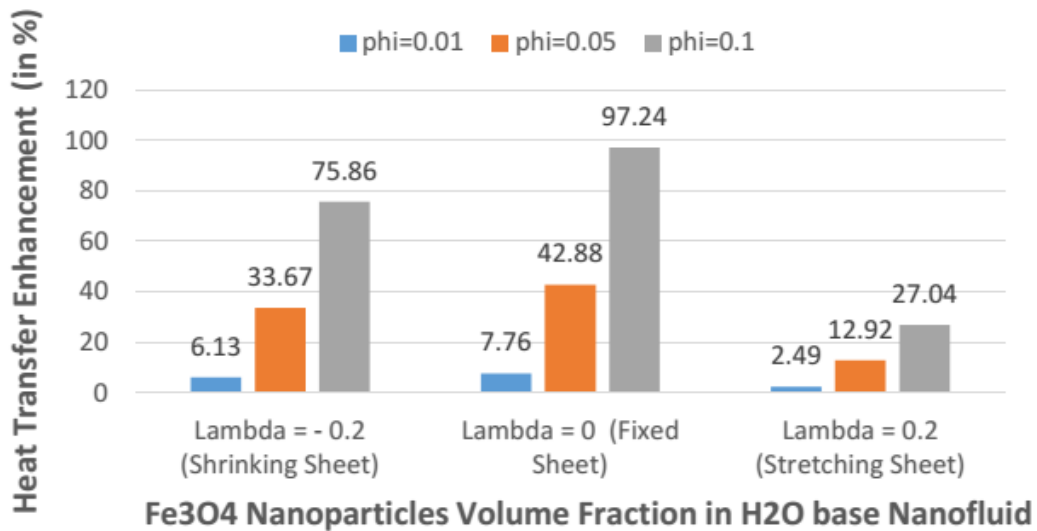


Figure 5.7.11: Heat transfer enhancement rate with nanoparticles concentration when  $S = F_n = 1, Bi = Ec = M = 0.1, Da = 0.5$ .

for up to some critical value  $\lambda_c$  beyond which the boundary layer separates from the surface and no solution is excepted in this region. For the upper branch solution, the intensification of suction assists the heat transfer processes from the shrinking sheet surface. This is because a rise in the rate of suction increases the ferrofluid particles on the shrinking surface which leads to an increase in the rate of heat transfer. It is also noted that the interval of existence of dual solution increases with the suction parameter. Figure 5.7.10a shows that opposite behavior is observed for local Nusselt

numbers for varying values of the porous medium parameter. It is also observed that the solution domain decreases with the intensification of the porous medium parameter. Figure 5.7.10b shows the variability of the reduced local Nusselt number concerning the shrinking surface parameter for different values of second-order porous resistance parameter. From this graph, we observed that an inverse relationship exists between the local Nusselt number and the second-order porous resistance parameter. It is also noted that the interval of existence of dual solution diminishes with the slight increment of this parameter.

Moreover, the heat transfer enhancement (HTE) of the  $\text{Fe}_3\text{O}_4$  nanoparticle for the cases of shrinking, fixed and stretching sheet are presented in figure 5.7.11. As we can see from the bar chart given, for the magnetite nanoparticles volume fraction  $\phi = 0.1$ , a maximum heat transfer enhancement with values of 75.86%, 97.24%, and 27.04% are obtained for shrinking sheet with  $\lambda = -0.2$ , fixed sheet with  $\lambda = 0$  and stretching sheet with  $\lambda = 0.2$ , respectively.

The numerical results obtained in this problem show the existence of a dual solution for certain ranges of the stretching/shrinking parameter  $\lambda$ . To identify stable solutions stability analysis is done for the solutions. The smallest eigenvalue,  $\beta$ , for the temporal development of small disturbances with respect to the basic steady flow is obtained for various values of  $\phi$  and  $\lambda$  when  $M = 0.1, S = 1, Da = 0.5, F_n = 1$  as shown in Table 5.7.4. we noted that the eigenvalues,  $\beta$ , obtained for the upper branch solution are positive while those of lower branch solutions are negative. This confirms that the upper branch solution is hydrodynamically stable and the solution is physically achievable whereas the lower branch solution is unstable and physically unrealistic.

## Chapter 6

# Temporal Stability Analysis of Unsteady Slip Flow of Magnetic Nanofluid Past a Heated Permeable Stretching/Shrinking Sheet in a Non-Darcian Porous Medium

### 6.1 Introduction

A boundary layer flow of incompressible fluid past a shrinking sheet has received much attention in fluid dynamics research due to its increasing applications in polymeric materials processing [Gupta et al. \(2014\)](#). Unlike the fluid flow past a stretching sheet, the flow towards a shrinking sheet is distracted away from the sheet due to the unconfined vorticity [Khashi'ie et al. \(2019\)](#). Hence, the application of enough wall mass suction and stagnation flow, which contains the vorticity, can effectively be used to stabilize the vorticity within the boundary layer and, subsequently, delay the boundary layer separation [Miklavčič and Wang \(2006\)](#) and [Wang \(2008\)](#). In addition, [Miklavčič and Wang \(2006\)](#) proved that the similarity dual solutions were attainable for higher magnitude of the suction parameter  $S > 2$  while zero solution for  $S < 2$ . Such fluid flows past a shrinking sheet and may have a non-unique solution. Due to the non-uniqueness of the solutions of the governing systems of differential equations of such a fluid flow problem, a mathematical technique called stability analysis is required to test the reliability of the non-unique similarity solutions.

Following these facts, [Sharma et al. \(2014\)](#) numerically examined the MHD stagnation point flow of a viscous, incompressible and electrically conducting fluid over a stretching and shrinking permeable semi-infinite flat plate and obtained that the range of the stretching/shrinking parameter increases with an increase in suction, pressure gradient as well as the magnetic parameter and the smallest eigenvalues for several values of suction and stretching/shrinking parameters are determined. Furthermore, [Mustafa et al. \(2020\)](#) numerically investigated the problem of hydromagnetic flow due to shrinking sheet and calculated dual solutions against velocity ratio parameter in case of shrinking sheet. A stability analysis is performed for the purpose of checking

which solution is stable.

In boundary layer flow and heat transfer analyses, it is customary for the flow to be assumed as steady. Nevertheless, in many engineering applications, unsteadiness becomes an integral part of the problem where the flow becomes time-dependent, and there are many situations where the flow and heat transfer are unsteady due to sudden stretching and shrinking of a sheet [Mansur and Ishak \(2016\)](#). Many researchers have investigated the unsteady flow over a stretching or shrinking sheet. [Rosali et al. \(2020\)](#) numerically analyzed the combined effects of velocity and thermal slip on the unsteady boundary layer stagnation point flow and heat transfer towards a stretching sheet in porous medium. [Dzulkiffi et al. \(2022\)](#) studied numerically unsteady stagnation-point flow and heat transfer over stretching/shrinking sheet with the slip velocity effect in nanofluids using the Tiwari and Das model. Further investigations into the combined effects of unsteadiness parameter, chemically reacting and radiating magnetic nanofluid, suction/injection and Porous medium resistance on boundary layer flow past a convectively heated stretching/shrinking sheet embedded in a Darcy-Forchheimer porous medium is required.

## 6.2 Mathematical Model Formulation

Consider unsteady, laminar, viscous, and incompressible stagnation point flow of chemically reacting and radiating magnetic nanofluid towards a convectively heated permeable stretching/shrinking sheet which is kept in a two dimensional Darcy-Forchheimer porous medium. The flow is subjected to a magnetic field of strength  $B = B_0/\sqrt{1-ct}$  which is applied normal to the flow field, such that the magnetic Reynolds number is selected small. The induced magnetic field is assumed to be small compared to the applied magnetic field. The ambient temperature of the fluid and the ambient concentration are taken as  $T_\infty$  and  $C_\infty$ , respectively while the surface below the stretching/shrinking sheet is heated by convection from a hot fluid having initial temperature  $T_f(x, t)$  which provides a heat transfer coefficient  $h_f$ . The effects of thermal radiation is incorporated through energy equation. The fluid is considered to be a gray, absorbing emitting radiation but non-scattering medium and the Rosseland's approximation is used to describe the radiative heat flux in the energy equation.

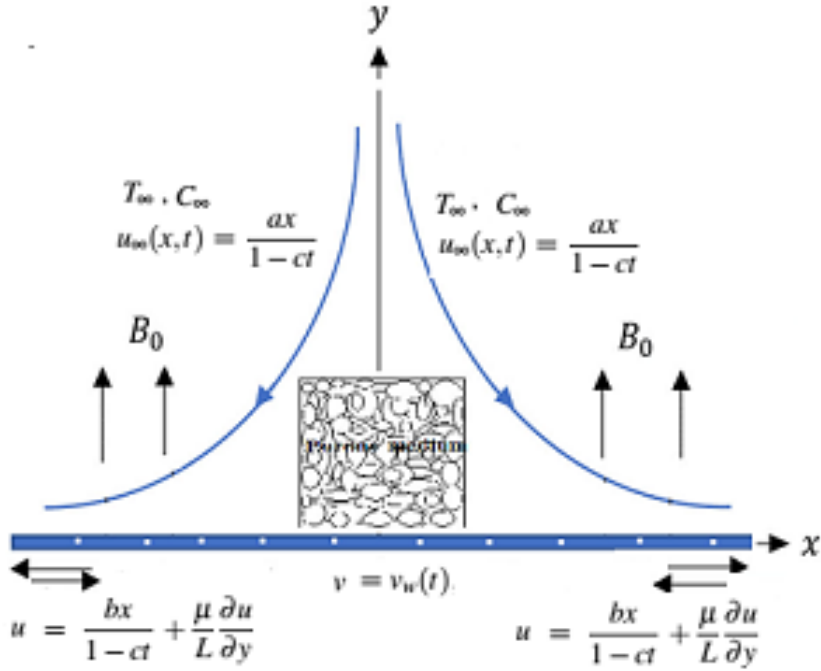


Figure 6.2.1: Flow diagram of the model.

Furthermore, it is assumed that the porous medium is homogeneous and isotropic, and saturated with a nanofluid which is in local thermal equilibrium with the solid matrix. We choose the coordinate system so that x-axis along the permeable stretching/shrinking sheet and y-axis is normal to the sheet surface. The physical model and the coordinate system are shown in Figure 6.2.1.

The governing equation of this problem has similarity with the model equations derived in chapter 4 and chapter 5. However, the problem considered here is unsteady, and the concentration equation is amended to incorporate the reaction term. Furthermore, the boundary condition for velocity assumed here is that there is no slip condition. Therefore, by considering the above assumptions and using the Darcy-Forchheimer flow model, the governing equations of the conservation of total mass, momentum, energy and nanoparticles volume fraction in the presence of magnetic field past a permeable stretching/shrinking sheet take the following form.

$$\frac{\partial u}{\partial x} + \frac{\partial v}{\partial y} = 0, \quad (6.2.1)$$

$$\frac{\partial u}{\partial t} + u \frac{\partial u}{\partial x} + v \frac{\partial u}{\partial y} = \frac{\partial U_\infty}{\partial t} + U_\infty \frac{\partial U_\infty}{\partial x} + \nu \frac{\partial^2 u}{\partial y^2} - \left( \frac{\sigma B^2}{\rho} + \frac{\nu}{K} \right) (u - U_\infty) - \frac{F}{\rho \sqrt{K}} (u - U_\infty)^2, \quad (6.2.2)$$

$$\begin{aligned} \frac{\partial T}{\partial t} + u \frac{\partial T}{\partial x} + v \frac{\partial T}{\partial y} &= \alpha \left( 1 + \frac{16\sigma^* T_\infty^3}{3kk^*} \right) \left( \frac{\partial^2 T}{\partial y^2} \right) + \tau \left( D_B \frac{\partial C}{\partial y} \frac{\partial T}{\partial y} + \frac{D_T}{T_\infty} \left( \frac{\partial T}{\partial y} \right)^2 \right) \\ &+ \frac{\mu}{(\rho c)_f} \left( \frac{\partial u}{\partial y} \right)^2 + \left( \frac{\sigma B^2}{(\rho c)_f} + \frac{\mu}{(\rho c)_f K_1} \right) (u - U_\infty)^2 + \frac{F}{(\rho c)_f \sqrt{K}} (u - U_\infty)^3, \end{aligned} \quad (6.2.3)$$

$$\frac{\partial C}{\partial t} + u \frac{\partial C}{\partial x} + v \frac{\partial C}{\partial y} = D_B \frac{\partial^2 C}{\partial y^2} + \left( \frac{D_T}{T_\infty} \right) \left( \frac{\partial^2 T}{\partial y^2} \right) - r(C - C_\infty), \quad (6.2.4)$$

with initial conditions for  $t < 0$

$$u(x, y, t) = v(x, y, t) = 0, \quad T(x, y, t) = T_\infty, \quad C(x, y, t) = C_\infty \quad \text{for any } x \text{ and } y \quad (6.2.5)$$

and the boundary conditions for  $t \geq 0$

$$\begin{aligned} u(x, 0, t) &= u_w(x, t) + \frac{\mu}{L} \frac{\partial u}{\partial y}, \quad v(x, 0, t) = v_w(t), \quad -k \frac{\partial T}{\partial y} = h_f(T_f - T), \\ D_B \frac{\partial C}{\partial y} &= -\frac{D_T}{T_\infty} \frac{\partial T}{\partial y}, \end{aligned} \quad (6.2.6)$$

$$u(x, \infty, t) = u_\infty(x, t), \quad T(x, \infty, t) = T_\infty, \quad C(x, \infty, t) = C_\infty \quad (6.2.7)$$

Here,  $u_w(x, t) = \frac{bx}{1-ct}$  denotes the velocity of the linearly stretching/shrinking sheet, in which  $b$  is a stretching/shrinking rate and  $u_\infty(x, t) = \frac{ax}{1-ct}$  defines the ambient velocity.  $v_w(t) = \frac{v_0}{\sqrt{1-ct}}$  defines the wall mass flux velocity with  $v_w > 0$  denotes injection and  $v_w < 0$  indicates suction.  $T_f(x, t) = T_\infty + \frac{nx^2}{(1-ct)^2}$  denotes the temperature of the hot fluid. Where  $a$  and  $c$  are constants (with  $a > 0, c \geq 0$ , where  $ct < 1$ ) and both have dimensions  $\text{time}^{-1}$ . We also have  $L = \frac{L_0}{\sqrt{1-ct}}$  and  $r = \frac{r_0}{1-ct}$  which represents the velocity slip factor and rate of chemical reaction where  $L_0$  and  $r_0$  are the initial value of the velocity slip factor and rate of chemical reaction, respectively.  $u$  and  $v$  are the velocity components of the fluid in the  $x$  and  $y$  -directions, respectively. The nanoparticle density, the density of base fluid, the absolute viscosity, the thermal diffusivity, the Stefan-Boltzman constant, the mean absorption coefficient are denoted by  $\rho_p, \rho_f, \mu, \alpha, \sigma^*, k^*$ , respectively. Furthermore,  $\tau = \frac{(\rho c)_p}{(\rho c)_f}$  is the ratio of the nanoparticle heat capacity and the fluid heat capacity,  $K$  is the porous medium permeability,  $T$  is the local temperature,  $C$  is the local solid volume fraction of the nanofluid,  $D_B$  is the Brownian diffusion coefficient,  $D_T$  is the thermophoretic diffusion coefficient and  $g$  is the acceleration due to gravity. The subscript  $\infty$  denotes the values at large values of

$y$  where the fluid is quiescent.

### 6.3 Similarity Transformation

The mathematical analysis of the problem is simplified by using the following transformations, as in [Abdullah et al. \(2018\)](#) and [Abdullah et al. \(2015\)](#):

$$\eta = y\sqrt{\frac{a}{\nu(1-ct)}}, \quad \psi(t, x, y) = \sqrt{\frac{a\nu}{1-ct}}xf(\eta), \quad \theta(\eta) = \frac{T-T_\infty}{T_f-T_\infty}, \quad \phi(\eta) = \frac{C-C_\infty}{C_\infty}. \quad (6.3.1)$$

Now using the similarity transformation quantities given above, the similarity transformation processes on equation (6.2.2) - (6.2.4) and the boundary equations (6.2.6) - (6.2.7) to ordinary differential equations are as shown below,

$$u = \frac{\partial\psi}{\partial y} = \frac{\partial}{\partial y} \left( xf(\eta)\sqrt{\frac{a\nu}{1-ct}} \right) \Rightarrow u = \frac{ax}{1-ct}f'(\eta), \quad (6.3.2)$$

$$v = -\frac{\partial\psi}{\partial x} = -\frac{\partial}{\partial x} \left( xf(\eta)\sqrt{\frac{a\nu}{1-ct}} \right) \Rightarrow v = -\sqrt{\frac{a\nu}{1-ct}}f(\eta), \quad (6.3.3)$$

$$T = T_\infty + (T_f - T_\infty)\theta(\eta) \quad \text{and} \quad C = C_\infty + \phi(\eta)C_\infty. \quad (6.3.4)$$

#### The Continuity equation

The equation of continuity is satisfied for the chosen stream function  $\psi(x, y)$ .

$$\frac{\partial u}{\partial x} + \frac{\partial v}{\partial y} = \frac{\partial}{\partial x} \left( \frac{ax}{1-ct}f'(\eta) \right) + \frac{\partial}{\partial y} \left( -\sqrt{\frac{a\nu}{1-ct}}f(\eta) \right) = 0. \quad (\text{satisfied}) \quad (6.3.5)$$

#### The Momentum equation

$$\frac{\partial u}{\partial t} + u\frac{\partial u}{\partial x} + v\frac{\partial u}{\partial y} = \frac{\partial U_\infty}{\partial t} + U_\infty\frac{\partial U_\infty}{\partial x} + \nu\frac{\partial^2 u}{\partial y^2} - \left(\frac{\sigma B^2}{\rho} + \frac{\nu}{K}\right)(u - U_\infty) - \frac{F}{\rho\sqrt{K}}(u - U_\infty)^2.$$

Substituting equation (6.3.1)- (6.3.4) into the momentum equation (6.2.2), we get

$$\begin{aligned} & \frac{\partial}{\partial t} \left( \frac{ax}{1-ct}f'(\eta) \right) + \frac{ax}{1-ct}f'(\eta)\frac{\partial}{\partial x} \left( \frac{ax}{1-ct}f'(\eta) \right) - \sqrt{\frac{a\nu}{1-ct}}f(\eta)\frac{\partial}{\partial y} \left( \frac{ax}{1-ct}f'(\eta) \right) \\ & = \frac{\partial}{\partial t} \left( \frac{ax}{(1-ct)^2} \right) + \frac{ax}{(1-ct)}\frac{\partial}{\partial x} \left( \frac{ax}{(1-ct)} \right) + \nu\frac{\partial}{\partial y} \left( \frac{\partial}{\partial y} \left( \frac{ax}{1-ct}f'(\eta) \right) \right) - \\ & \frac{ax}{1-ct} \left( \frac{\sigma B_0^2}{\rho} + \frac{\nu}{K_1} \right) (f'(\eta) - 1) - \frac{a^2x^2F}{\rho\sqrt{K_1}}(f'(\eta) - 1)^2, \end{aligned}$$

$$\begin{aligned}
& \frac{axc}{(1-ct)^2} f'(\eta) + \frac{acx}{(1-ct)^2} \left(\frac{\eta}{2}\right) f''(\eta) + \frac{a^2x}{(1-ct)^2} (f'(\eta))^2 - \frac{a^2x}{(1-ct)^2} (f(\eta)f''(\eta)) \\
&= \frac{axc}{(1-ct)^2} + \frac{a^2x}{(1-ct)^2} + \frac{a^2x}{(1-ct)^2} f'''(\eta) - \frac{ax}{(1-ct)} \left(\frac{\sigma B_0^2}{\rho} + \frac{\nu}{K_1}\right) (f'(\eta) - 1) \\
&- \frac{ax^2 Fx}{(1-ct)^2 \rho \sqrt{K_1}} (f'(\eta) - 1)^2.
\end{aligned} \tag{6.3.6}$$

Multiplying each term of equation (6.3.6) by  $\frac{(1-ct)^2}{a^2x}$ , we get

$$\begin{aligned}
\frac{c}{a} f'(\eta) + \frac{c\eta}{a^2} f''(\eta) + (f'(\eta))^2 - f(\eta)f''(\eta) &= \frac{c}{a} + 1 + f'''(\eta) - (1-ct) \left(\frac{\sigma B_0^2}{a\rho} + \frac{\nu}{aK_1}\right) (f'(\eta) - 1) \\
- \frac{Fx}{\rho \sqrt{K_1}} (f'(\eta) - 1)^2.
\end{aligned} \tag{6.3.7}$$

After some simplifications and rearrangements (6.3.7) becomes,

$$\begin{aligned}
A f'(\eta) + A \frac{\eta}{2} f''(\eta) + (f'(\eta))^2 - f(\eta)f''(\eta) &= A + 1 + f'''(\eta) - \left(\frac{\sigma B_0^2 x^2}{\rho Re_x} + \frac{x^2}{K_1 Re_x}\right) \\
(f'(\eta) - 1) - F_n (f'(\eta) - 1)^2.
\end{aligned} \tag{6.3.8}$$

Finally, we obtain

$$\begin{aligned}
A f'(\eta) + A \frac{\eta}{2} f''(\eta) + (f'(\eta))^2 - f(\eta)f''(\eta) &= A + 1 + f'''(\eta) - \left(M A_2 + \frac{1}{Da}\right) (f'(\eta) - 1) \\
- F_n (f'(\eta) - 1)^2.
\end{aligned} \tag{6.3.9}$$

where,

$$A = \frac{c}{a}, \quad M = \frac{\sigma B_0^2 x^2}{\mu Re_x}, \quad Da = \frac{K}{x^2} Re_x, \quad F_n = \frac{Fx}{\rho_f \sqrt{K}} \tag{6.3.10}$$

### The Energy equation

$$\begin{aligned}
\frac{\partial T}{\partial t} + u \frac{\partial T}{\partial x} + v \frac{\partial T}{\partial y} &= \alpha \left[1 + \frac{16\sigma^* T_\infty^3}{3kk^*}\right] \left(\frac{\partial^2 T}{\partial y^2}\right) + \tau \left[D_B \frac{\partial C}{\partial y} \frac{\partial T}{\partial y} + \frac{D_T}{T_\infty} \left(\frac{\partial T}{\partial y}\right)^2\right] \\
+ \frac{\mu}{(\rho c)_f} \left(\frac{\partial u}{\partial y}\right)^2 &+ \left[\frac{\sigma B^2}{(\rho c)_f} + \frac{\mu}{(\rho c)_f K_1}\right] (u - U_\infty)^2 + \frac{F}{(\rho c)_f \sqrt{K}} (u - U_\infty)^3,
\end{aligned} \tag{6.3.11}$$

Substituting equations (6.3.2)- (6.3.4) into the energy equation (6.2.3), we obtain

$$\begin{aligned}
& \frac{\partial}{\partial t} \left( T_\infty + (T_f - T_\infty)\theta(\eta) \right) + \frac{ax}{1-ct} f'(\eta) \frac{\partial}{\partial x} \left( T_\infty + (T_f - T_\infty)\theta(\eta) \right) - \sqrt{\frac{a\nu}{1-ct}} f(\eta) \\
& \frac{\partial}{\partial y} \left( T_\infty + (T_f - T_\infty)\theta(\eta) \right) = \alpha \left[ 1 + \frac{16\sigma^* T_\infty^3}{3kk^*} \right] \frac{\partial}{\partial y} \left( \frac{\partial}{\partial y} \left( T_\infty + (T_f - T_\infty)\theta(\eta) \right) \right) + \\
& \tau \left[ D_B \frac{\partial}{\partial y} \left( C_\infty + \phi(\eta)C_\infty \right) \frac{\partial}{\partial y} \left( T_\infty + (T_f - T_\infty)\theta(\eta) \right) + \frac{D_T}{T_\infty} \left( \frac{\partial}{\partial y} \left( T_\infty + (T_f - T_\infty)\theta(\eta) \right) \right)^2 \right] \\
& + \frac{\mu}{(\rho C)_p} \left( \frac{\partial}{\partial y} \left( \frac{ax}{1-ct} f'(\eta) \right) \right)^2 + \left( \frac{ax}{1-ct} \right)^2 \left[ \frac{\sigma B^2}{(\rho C)_p} + \frac{\mu}{(\rho C)_p K_1} \right] (f'(\eta) - 1)^2 + \\
& \left( \frac{ax}{1-ct} \right)^3 \frac{F}{(\rho C)_p \sqrt{K_1}} (f'(\eta) - 1)^3, \\
& (T_f - T_\infty)\theta'(\eta) \frac{\eta}{2} \left( \frac{c}{1-ct} \right) + \frac{2nx^2c}{(1-ct)^3} \theta(\eta) + \frac{2nax^2}{(1-ct)^3} f'(\eta)\theta(\eta) - \frac{a}{1-ct} (T_f - T_\infty) f(\eta)\theta'(\eta) \\
& = \alpha \left[ 1 + \frac{16\sigma^* T_\infty^3}{3kk^*} \right] \frac{a(T_f - T_\infty)}{\nu(1-ct)} \theta''(\eta) + \tau \left[ D_B C_\infty \phi'(\eta)\theta'(\eta) \frac{a(T_f - T_\infty)}{\nu(1-ct)} + \frac{D_T}{T_\infty} (T_f - T_\infty)^2 \right. \\
& \left. \theta'(\eta)^2 \frac{a}{\nu(1-ct)} \right] + \frac{\nu}{(C)_p} \left( \frac{a}{(1-ct)} \sqrt{\frac{a}{\nu(1-ct)}} f''(\eta) \right)^2 + \frac{a^2 x^2}{(1-ct)^2} \left[ \frac{\sigma B^2}{\rho C_p} + \frac{\nu}{C_p K_1} \right] \\
& (f'(\eta) - 1)^2 + \frac{a^3 x^2}{(1-ct)^3} \frac{F x}{\rho C_p \sqrt{K_1}} (f'(\eta) - 1)^3. \tag{6.3.12}
\end{aligned}$$

Multiplying each term of equation (6.3.12) by  $\frac{\nu(1-ct)}{\alpha a(T_f - T_\infty)}$ , we obtain

$$\begin{aligned}
& \frac{\nu}{\alpha} \frac{c}{a} \frac{\eta}{2} \theta'(\eta) + 2 \frac{\nu}{\alpha} \frac{c}{a} \theta(\eta) + 2 \frac{\nu}{\alpha} f'(\eta)\theta(\eta) - \frac{\nu}{\alpha} f(\eta)\theta'(\eta) = \left[ 1 + \frac{16\sigma^* T_\infty^3}{3kk^*} \right] \theta''(\eta) \\
& + \frac{\tau}{\alpha} D_B C_\infty \phi'(\eta)\theta'(\eta) + \frac{\tau}{\alpha} \frac{D_T}{T_\infty} (T_f - T_\infty) (\theta'(\eta))^2 + \frac{\nu}{\alpha} \frac{U_\infty^2}{C_p (T_f - T_\infty)} (f''(\eta))^2 + \\
& \frac{\nu}{\alpha} \frac{U_\infty^2}{C_p (T_f - T_\infty)} \left[ \frac{\sigma B^2}{\rho C_p} + \frac{\nu}{C_p K_1} \right] (f'(\eta) - 1)^2 + \frac{\nu}{\alpha} \frac{U_\infty^2}{C_p (T_f - T_\infty)} \frac{F x}{\rho \sqrt{K_1}} (f'(\eta) - 1)^3. \tag{6.3.13}
\end{aligned}$$

Further simplification gives us

$$\begin{aligned}
& Pr A \frac{\eta}{2} \theta'(\eta) + 2 Pr A \theta(\eta) + 2 Pr f'(\eta)\theta(\eta) - Pr f(\eta)\theta'(\eta) = \left( 1 + \frac{4}{3} R \right) \theta''(\eta) \\
& + Pr Nb \phi'(\eta)\theta'(\eta) + Pr Nt (\theta'(\eta))^2 + Pr Ec (f''(\eta))^2 + Pr Ec \left( M + \frac{1}{Da} \right) \\
& (f'(\eta) - 1)^2 + Pr Ec F_n (f'(\eta) - 1)^3. \tag{6.3.14}
\end{aligned}$$

Where,

$$A = \frac{c}{a}, \quad M = \frac{\sigma B_0^2}{\rho a}, \quad Da = \frac{K}{x^2} Re_x, \quad F_n = \frac{Fx}{\rho_f \sqrt{K}}, \quad R = \frac{4\sigma^* T_\infty^3}{k^* k},$$

$$Pr = \frac{\nu}{\alpha}, \quad Nb = \frac{\tau D_B C_\infty}{\nu}, \quad Nt = \frac{\tau D_T (T_f - T_\infty)}{\nu T_\infty}, \quad Ec = \frac{a^2}{nC_p}. \quad (6.3.15)$$

### The Concentration equation

$$\frac{\partial C}{\partial t} + u \frac{\partial C}{\partial x} + v \frac{\partial C}{\partial y} = D_B \frac{\partial^2 C}{\partial y^2} + \left( \frac{D_T}{T_\infty} \right) \left( \frac{\partial^2 T}{\partial y^2} \right) - r(C - C_\infty), \quad (6.3.16)$$

Substituting equations (6.3.2)- (6.3.4) into the energy equation (6.2.4), we obtain

$$\begin{aligned} & \frac{\partial}{\partial t} \left( C_\infty + C_\infty \phi(\eta) \right) + \frac{ax}{1-ct} f'(\eta) \frac{\partial}{\partial x} \left( C_\infty + C_\infty \phi(\eta) \right) - \sqrt{\frac{a\nu}{1-ct}} f(\eta) C_\infty \sqrt{\frac{a}{\nu(1-ct)}} \phi'(\eta) \\ & = D_B \frac{\partial}{\partial y} \left( \frac{\partial}{\partial y} \left( C_\infty + C_\infty \phi(\eta) \right) \right) + \frac{D_T}{T_\infty} \frac{\partial}{\partial y} \left( C_\infty \sqrt{\frac{a}{\nu(1-ct)}} \phi'(\eta) \right) - r\phi(\eta) C_\infty, \quad (6.3.17) \\ & \frac{c}{1-ct} C_\infty \frac{\eta}{2} \phi'(\eta) + 0 - \frac{a}{1-ct} C_\infty f(\eta) \phi'(\eta) = D_B C_\infty \frac{a}{\nu(1-ct)} \phi''(\eta) + \\ & \frac{D_T}{T_\infty} (T_f - T_\infty) \frac{a}{\nu(1-ct)} \theta''(\eta) - r\phi(\eta) C_\infty. \end{aligned}$$

Multiplying each term of equation (6.3.17) by  $\frac{\nu(1-ct)}{D_B C_\infty a}$ , we obtain

$$\frac{\nu}{D_B} \frac{c}{a} \frac{\eta}{2} \phi'(\eta) - \frac{\nu}{D_B} f(\eta) \phi'(\eta) = \phi''(\eta) + \frac{1}{D_B} \frac{D_T}{T_\infty} \frac{(T_f - T_\infty)}{C_\infty} \theta''(\eta) - \frac{r\nu(1-ct)}{D_B a} \phi(\eta). \quad (6.3.18)$$

Further simplification gives us

$$ScA \frac{\eta}{2} \phi'(\eta) - Scf(\eta) \phi'(\eta) = \phi''(\eta) + \frac{Nt}{Nb} \theta''(\eta) - Sc \frac{r(1-ct)}{a} \phi(\eta). \quad (6.3.19)$$

Where,

$$A = \frac{c}{a}, \quad Pr = \frac{\nu}{\alpha}, \quad Nb = \frac{\tau D_B C_\infty}{\nu}, \quad Nt = \frac{\tau D_T (T_f - T_\infty)}{\nu T_\infty}, \quad Sc = \frac{\nu}{D_B}, \quad \delta = \frac{r_0}{b},$$

$$r = \frac{\mu}{L_0} \sqrt{\frac{a}{\nu}}.$$

The boundary conditions will be

As  $\eta = 0$ ,

$$\begin{aligned}
u(x, 0, t) &= u_w(x, t) + \frac{\mu}{L} \frac{\partial u}{\partial y} \Rightarrow \frac{ax}{1-ct} f'(\eta=0) = \frac{bx}{1-ct} + \frac{\mu}{L} \frac{\partial}{\partial y} \left( \frac{ax}{1-ct} f'(\eta) \right) \\
&\Rightarrow f'(0) = \frac{b}{a} + \frac{\mu}{L} \sqrt{\frac{a}{\nu(1-ct)}} f''(0) \Rightarrow f'(0) = \lambda + \gamma f''(0). \\
v(x, 0, t) &= v_w(t) \Rightarrow -\sqrt{\frac{a\nu}{1-ct}} f(\eta=0) = v_w(t), \\
&\Rightarrow f(0) = -\sqrt{\frac{1-ct}{a\nu}} v_w(t) = S.
\end{aligned} \tag{6.3.20}$$

$$\begin{aligned}
-k_f \frac{\partial T}{\partial y} &= h_f(T_f - T) \Rightarrow -k_f(T_f - T)\theta'(0) \sqrt{\frac{a}{\nu(1-ct)}} = h_f(T_f - T), \\
&\Rightarrow \theta'(0) = \frac{-h_f}{k_f} \sqrt{\frac{\nu(1-ct)}{a}} (1 - \theta(0)) \Rightarrow \theta'(0) = -Bi(1 - \theta(0)). \\
D_B \frac{\partial C}{\partial y} &= -\frac{D_T}{T_\infty} \frac{\partial T}{\partial y} \Rightarrow D_B C_\infty \phi'(0) = -\frac{D_T}{T_\infty} (T_f - T_\infty) \theta'(0), \\
&\Rightarrow \phi'(0) = -\frac{D_T(T_f - T_\infty)}{T_\infty D_\infty C_\infty} \theta'(0) = -\frac{Nt}{Nb} \theta'(0) \\
&\Rightarrow Nb\phi'(0) + Nt\theta'(0) = 0.
\end{aligned} \tag{6.3.21}$$

As  $\eta \rightarrow \infty$ ,

$$\begin{aligned}
u(x, \infty, t) &= u_\infty(x, t) = \frac{ax}{1-ct} \Rightarrow \frac{ax}{1-ct} f'(\eta = \infty) = \frac{ax}{1-ct} \Rightarrow f'(\infty) = 1, \\
T(x, \infty, t) &= T_\infty \Rightarrow \theta(\infty) = \frac{T(x, \infty, t) - T_\infty}{T_f - T_\infty} = \frac{T_\infty - T_\infty}{T_f - T_\infty} \Rightarrow \theta(\infty) = 0, \\
C(x, \infty, t) &= C_\infty \Rightarrow C(\infty) = \frac{C(x, \infty, t) - C_\infty}{C_\infty} = \frac{C_\infty - C_\infty}{C_\infty} \Rightarrow C(\infty) = 0.
\end{aligned} \tag{6.3.22}$$

Finally, we obtained the following nonlinear ordinary differential equations as shown below:

$$f''' + ff'' - (f')^2 + A \left( 1 - f' - \frac{\eta}{2} f'' \right) + 1 - \left( M + \frac{1}{Da} \right) (f' - 1) - F_n (f' - 1)^2 = 0, \tag{6.3.23}$$

$$\begin{aligned}
\left( 1 + \frac{4}{3} R \right) \theta'' - PrA(2\theta + \frac{\eta}{2} \theta') + Pr(\theta' f - 2\theta f') + PrNb\theta' \phi' + PrNt\theta'^2 \\
+ PrEc(f'')^2 + PrEc \left( M + \frac{1}{Da} \right) (f' - 1)^2 + PrEcF_n(f' - 1)^3 = 0,
\end{aligned} \tag{6.3.24}$$

$$\phi'' + Sc \left( f\phi' - \frac{\eta}{2} A\phi' - \delta\phi \right) + \frac{Nt}{Nb} \theta'' = 0. \tag{6.3.25}$$

With boundary conditions

$$\begin{aligned} \text{At } \eta = 0: \quad f(0) = S, \quad f'(0) = \lambda + \gamma f''(0), \quad \theta'(0) = -Bi[1 - \theta(0)], \\ Nb\phi'(0) + Nt\theta'(0) = 0. \end{aligned} \quad (6.3.26)$$

$$\text{As } \eta \rightarrow \infty: \quad f'(\eta) \rightarrow 1, \quad \theta(\eta) \rightarrow 0, \quad \phi(\eta) \rightarrow 0. \quad (6.3.27)$$

Where  $f'$ ,  $\theta$  and  $\phi$  are the dimensionless velocity, temperature, and particle volume fraction, respectively. The prime denotes differentiation with respect to the similarity variable  $\eta$ . The variables  $A, M, Da, F_n, \lambda, R, Pr, Nb, Nt, Ec, Sc, \delta, S, \gamma$  and  $Bi$  denotes the unsteadiness parameter with  $A > 0$  shows the accelerating flow while  $A < 0$  implies the decelerating flow, magnetic field parameter, Darcy number, second order porous resistance parameter (Forchheimer number), thermal radiation parameter, Prandtl number, the Brownian motion parameter, the thermophoresis diffusion parameter, Eckert number, schmidt number, chemical reaction parameter in which  $\delta > 0$  associates with destructive chemical reaction while  $\delta < 0$  corresponds to generative chemical reaction, suction ( $S > 0$ ) or injection ( $S < 0$ ) parameter, stretching ( $\lambda > 0$ ) or shrinking ( $\lambda < 0$ ) parameter, velocity slip parameter and Biot number, respectively. The parameters and dimensionless numbers are defined as follows:

$$\begin{aligned} A = \frac{c}{a}, \quad \lambda = \frac{b}{a}, \quad M = \frac{\sigma B_0^2}{\rho a}, \quad Da = \frac{K}{x^2} Re_x, \quad F_n = \frac{Fx}{\rho_f \sqrt{K}}, \quad R = \frac{4\sigma^* T_\infty^3}{k^* k}, \\ Pr = \frac{\nu}{\alpha}, \quad Nb = \frac{\tau D_B C_\infty}{\nu}, \quad Nt = \frac{\tau D_T (T_f - T_\infty)}{\nu T_\infty}, \quad Ec = \frac{a^2}{nc_p}, \quad Sc = \frac{\nu}{D_B}, \quad (6.3.28) \\ \delta = \frac{r_0}{b}, \quad S = \frac{-v_0}{\sqrt{\nu a}}, \quad \gamma = \frac{\mu}{L_0} \sqrt{\frac{a}{\nu}}, \quad Bi = \frac{h_f x}{k_f Re_x^{1/2}}. \end{aligned}$$

It is important to note that the porous medium inertia parameter ( $F_n$ ) is a local similarity parameter. Nonetheless, the parameter  $F_n$  may become a similarity parameter if the non-uniform inertial coefficient of porous medium is defined as  $F = \frac{C_d}{x}$  where  $C_d$  is drag coefficient. In this case, the expression for  $F_n = \frac{C_d}{\rho_f \sqrt{K_1}}$  is a similarity parameter since it is independent of  $x$  (Hayat et al., 2016; Das et al., 2020b; Upreti et al., 2020). Similarly, in order to have a similarity solution define  $h_f = \frac{h_1}{\sqrt{1-ct}}$  where  $h_1$  is constant (Das et al., 2020a), then  $Bi = h_1 \sqrt{\frac{\nu}{a}}$  becomes a similarity parameter.

## 6.4 Important Engineering Parameters

The important physical quantities of interest, in this problem, are the dimensionless skin friction coefficient, the local Nusselt number, and the local Sherwood number. Skin friction coefficient measures the friction that occurs at the boundary, Nusselt number helps to determine the wall heat flux and Sherwood number is used to determine the wall mass flux. These important engineering parameters are defined as:

$$C_f = \frac{\tau_w}{\rho U_\infty^2}, \quad Nu_x = \frac{xq_w''}{k(T_f - T_\infty)}, \quad \text{and} \quad Sh_x = \frac{xq_m''}{D_B C_\infty}, \quad (6.4.1)$$

where  $\tau_w$  is the wall shear stress,  $q_w''$  is the wall heat flux due to the temperature gradient and  $q_m''$  is the wall mass flux due to the Brownian motion force at  $y = 0$  and given by

$$\tau_w = \mu \left( \frac{\partial u}{\partial y} \right) \Big|_{\eta=0}, \quad q_w'' = - \left[ \left( k + \frac{16\sigma^* T_\infty^3}{3k^*} \right) \frac{\partial T}{\partial y} \Big|_{\eta=0} \right], \quad \text{and} \quad q_m'' = -D_B \left( \frac{\partial C}{\partial y} \right) \Big|_{\eta=0}.$$

The dimensionless form of the wall shear stress, local Nusselt number and the local Sherwood number are derived as

$$\begin{aligned} C_f &= \frac{\mu \left( \frac{\partial u}{\partial y} \right) \Big|_{\eta=0}}{\rho U_\infty^2} = \frac{\mu \frac{\partial}{\partial y} \left( \frac{ax}{1-ct} f'(\eta) \right) \Big|_{\eta=0}}{\rho \left( \frac{ax}{1-ct} \right)^2} = \frac{\mu}{\rho} \frac{ax}{(1-ct)} \sqrt{\frac{a}{\nu(1-ct)}} \frac{(1-ct)^2}{a^2 x^2}, \\ &\Rightarrow C_f = \sqrt{\frac{\nu(1-ct)}{ax^2}} f''(0) = f''(0) Re_x^{-1/2}, \Rightarrow f''(0) = C_f Re_x^{1/2}. \\ Nu_x &= \frac{-x \left[ \left( k + \frac{16\sigma^* T_\infty^3}{3k^*} \right) \frac{\partial T}{\partial y} \Big|_{\eta=0} \right]}{k(T_f - T_\infty)} = \frac{-xk \left( 1 + \frac{16\sigma^* T_\infty^3}{3kk^*} \right) (T_f - T_\infty) \theta'(0) \sqrt{\frac{a}{\nu(1-ct)}}}{k(T_f - T_\infty)}, \\ &\Rightarrow Nu_x = -x \sqrt{\frac{a}{\nu(1-ct)}} \left( 1 + \frac{4}{3} R \right) \theta'(0), \\ &\Rightarrow Nu = Nu_x Re_x^{-1/2} = - \left( 1 + \frac{4}{3} R \right) \theta'(0). \\ Sh_x &= \frac{-xD_B \left( \frac{\partial C}{\partial y} \right) \Big|_{\eta=0}}{D_B C_\infty} = \frac{-xC_\infty \phi'(0)}{C_\infty} \sqrt{\frac{a}{\nu(1-ct)}} = - \sqrt{\frac{ax^2}{\nu(1-ct)}} \phi'(0), \\ &\Rightarrow Sh_x = -Re_x^{1/2} \phi'(0) \Rightarrow Sh = Sh_x Re_x^{-1/2} = -\phi'(0). \end{aligned} \quad (6.4.2)$$

where  $Re_x, Nu_x, Sh_x$  are local Reynolds number, local Nusselt number and local Sherwood number, respectively.

## 6.5 Stability Analysis

From the numerical result obtained, such a boundary layer problem may produce zero, unique, dual or multiple solutions depending on the physical parameters under consideration. For such cases, it is important to identify all the possible solutions that may arise in such fluid flow problem to avoid misinterpretation of the fluid flow characteristics. Generally, for non-unique solutions, the first solution which satisfies the boundary condition is denoted as the physically realistic or real solution as compared to the other solutions. In some cases, the second solution may exhibit the same pattern of the real flow characteristics based on the velocity, temperature or concentration profiles. Hence, it is necessary to validate the real solution through a proper analysis called stability analysis. The execution of the stability analysis is mathematically performed to verify the physical or real solution among all the solutions. Stability analysis requires the introduction of new similarity transformations as mentioned in [Safwa Khashi'ie et al. \(2019\)](#)

$$\begin{aligned} \eta &= y \sqrt{\frac{a}{\nu(1-ct)}}, \quad u = \frac{ax}{(1-ct)} \frac{\partial f}{\partial \eta}(\eta, \tau), \quad v = -\sqrt{\frac{a\nu}{(1-ct)}} f(\eta, \tau), \\ \psi &= f(\eta, \tau) x \sqrt{\frac{a\nu}{(1-ct)}}, \quad \theta(\eta, \tau) = \frac{T - T_\infty}{T_f - T_\infty}, \quad \phi(\eta, \tau) = \frac{C - C_\infty}{C_\infty}, \quad \tau = \frac{at}{1-ct}. \end{aligned} \quad (6.5.1)$$

Where  $\tau$  is the dimensionless time variable. Substitute (6.5.1) into equations (6.2.2) - (6.2.4) and the following equations are obtained

$$\begin{aligned} \frac{\partial^3 f}{\partial \eta^3} + f \frac{\partial^2 f}{\partial \eta^2} + \left( \frac{\partial f}{\partial \eta} \right)^2 + A \left( 1 - \frac{\partial f}{\partial \eta} - \frac{\eta}{2} \frac{\partial^2 f}{\partial \eta^2} \right) + 1 - (1 + A\tau) \frac{\partial^2 f}{\partial \eta \partial \tau} \\ \left( M + \frac{1}{Da} \right) \left( \frac{\partial f}{\partial \eta} - 1 \right) - F_n \left( \frac{\partial f}{\partial \eta} - 1 \right)^2 = 0, \end{aligned} \quad (6.5.2)$$

$$\begin{aligned} \left( 1 + \frac{4}{3}R \right) \frac{\partial^2 \theta}{\partial \eta^2} - Pr \left( 2\theta \frac{\partial f}{\partial \eta} - f \frac{\partial \theta}{\partial \eta} \right) - PrA \left( \theta + \frac{\eta}{2} \frac{\partial \theta}{\partial \eta} \right) - Pr(1 + A\tau) \frac{\partial \theta}{\partial \tau} \\ + PrNb \frac{\partial \theta}{\partial \eta} \frac{\partial \phi}{\partial \eta} + PrNt \left( \frac{\partial \theta}{\partial \eta} \right)^2 + EcPr \left( \frac{\partial^2 f}{\partial \eta^2} \right)^2 + EcPr \left( M + \frac{1}{Da} \right) \left( \frac{\partial f}{\partial \eta} - 1 \right)^2 \\ + EcPrF_n \left( \frac{\partial f}{\partial \eta} - 1 \right)^3 = 0, \end{aligned} \quad (6.5.3)$$

$$\frac{\partial^2 \phi}{\partial \eta^2} - ASc \frac{\eta}{2} \frac{\partial \phi}{\partial \eta} + Scf \frac{\partial \phi}{\partial \eta} - Sc(1 + A\tau) \frac{\partial \phi}{\partial \tau} + \frac{Nt}{Nb} \frac{\partial^2 \theta}{\partial \eta^2} - Sc\delta\phi = 0, \quad (6.5.4)$$

and the boundary conditions become

$$\begin{aligned} f(0, \tau) = s, \quad \frac{\partial f}{\partial \eta}(0, \tau) = \xi + \beta \frac{\partial^2 f}{\partial \eta^2}(0, \tau), \quad \frac{\partial \theta}{\partial \eta}(0, \tau) = -Bi[1 - \theta(0, \tau)], \\ Nb \frac{\partial \phi}{\partial \eta}(0, \tau) + Nt \frac{\partial \theta}{\partial \eta}(0, \tau), \quad \frac{\partial f}{\partial \eta}(\infty, \tau) \rightarrow 1, \quad \theta(\infty, \tau) \rightarrow 0, \quad \phi(\infty, \tau) \rightarrow 0. \end{aligned} \quad (6.5.5)$$

To test the stability of the steady flow solution  $f(\eta) = f_0(\eta)$ ,  $\theta(\eta) = \theta_0(\eta)$  and  $\phi(\eta) = \phi_0(\eta)$  satisfying the set of boundary-value problem equation (6.3.26)- (6.3.27), we write

$$\begin{aligned} f(\eta, \tau) &= f_0(\eta) + e^{-\beta\tau} F(\eta, \tau), \\ \theta(\eta, \tau) &= \theta_0(\eta) + e^{-\beta\tau} G(\eta, \tau), \\ \phi(\eta, \tau) &= \phi_0(\eta) + e^{-\beta\tau} H(\eta, \tau), \end{aligned} \quad (6.5.6)$$

where  $\beta$  is an unknown eigenvalue parameter (growth rate of disturbance) and  $F(\eta, \tau)$ ,  $G(\eta, \tau)$  and  $H(\eta, \tau)$  are small relative to  $f_0(\eta)$ ,  $\theta_0(\eta)$  and  $\phi_0(\eta)$ , respectively. The following linearized problem will be obtained by substituting (6.5.6) into (6.3.23)- (6.3.25)

$$\begin{aligned} \frac{\partial^3 F}{\partial \eta^3} + (f_0 - A \frac{\eta}{2}) \frac{\partial^2 F}{\partial \eta^2} + \frac{\partial F}{\partial \eta} \left[ A + 2 \frac{\partial f_0}{\partial \eta} + (1 + A\tau)\beta - M - \frac{1}{Da} - 2F_n \left( \frac{\partial f_0}{\partial \eta} - 1 \right) \right] \\ + F \frac{\partial^2 f_0}{\partial \eta^2} - (1 + A\tau) \frac{\partial^2 F}{\partial \tau \partial \eta} = 0, \end{aligned} \quad (6.5.7)$$

$$\begin{aligned} \left( 1 + \frac{4}{3}R \right) \frac{\partial^2 G}{\partial \eta^2} + Pr \left( f_0 - A \frac{\eta}{2} + 2Nt \frac{\partial \theta_0}{\partial \eta} + Nb \frac{\partial \phi_0}{\partial \eta} \right) \frac{\partial G}{\partial \eta} - Pr \left( A + 2 \frac{\partial f_0}{\partial \eta} \right) G \\ + Pr(1 + A\tau)\beta G + Pr \frac{\partial F}{\partial \eta} \left[ 2Ec \left( M + \frac{1}{Da} \right) \left( \frac{\partial f_0}{\partial \eta} - 1 \right) + 3EcF_n \left( \frac{\partial f_0}{\partial \eta} - 1 \right)^2 - 2\theta_0 \right] \\ + Pr \left( F + Nb \frac{\partial H}{\partial \eta} \right) \frac{\partial \theta_0}{\partial \eta} - Pr(1 + A\tau) \frac{\partial G}{\partial \tau} = 0, \end{aligned} \quad (6.5.8)$$

$$\begin{aligned} \frac{\partial^2 H}{\partial \eta^2} + \frac{\partial H}{\partial \eta} \left[ Scf_0 - ASc \frac{\eta}{2} \right] + Sc(1 + A\tau)\beta H + ScF \frac{\partial \phi_0}{\partial \eta} - Sc(1 + A\tau) \frac{\partial H}{\partial \tau} + \frac{Nt}{Nb} \frac{\partial^2 G}{\partial \eta^2} \\ - Sc\delta H = 0, \end{aligned} \quad (6.5.9)$$

subjected to the boundary conditions:

$$\begin{aligned}
F(0, \tau) = 0, \quad \frac{\partial F}{\partial \eta}(0, \tau) = \beta \frac{\partial^2 F}{\partial \eta^2}(0, \tau), \quad \frac{\partial G}{\partial \eta}(0, \tau) = BiG(0, \tau), \\
Nb \frac{\partial H}{\partial \eta}(0, \tau) + Nt \frac{\partial G}{\partial \eta}(0, \tau), \quad \frac{\partial F}{\partial \eta}(\infty, \tau) \rightarrow 0, \quad G(\infty, \tau) \rightarrow 0, \quad H(\infty, \tau) \rightarrow 0.
\end{aligned} \tag{6.5.10}$$

Following [Weidman et al. \(2006\)](#), the initial growth or decay of the solution (6.5.6) can be identified by setting  $\tau = 0$  so that  $F = F_0(\eta)$ ,  $G = G_0(\eta)$  and  $H = H_0(\eta)$  in equations (6.5.7)- (6.5.10). Solutions of the eigenvalue problem give an infinite set of eigenvalues  $\beta_1 < \beta_2 < \beta_3 \dots$ ; if  $\beta_1$  is negative, there is an initial growth of disturbances and the flow is unstable but when  $\beta_1$  is positive, there is an initial decay and the flow is stable. The linearized Eigenvalue problem are given by

$$F_0''' + (f_0 - A \frac{\eta}{2}) F_0'' + f_0' F_0 + F_0' \left[ \beta - 2f_0' - A - (M + \frac{1}{Da}) - 2F_n (f_0' - 1) \right] = 0, \tag{6.5.11}$$

$$\begin{aligned}
(1 + \frac{4}{3}R) G_0'' + Pr \left[ f_0 - A \frac{\eta}{2} + 2Nt\theta_0' + Nb\phi_0' \right] G_0' - Pr (A + 2f_0' - \beta) G_0 + \\
Pr \left[ 2Ec (M + \frac{1}{Da}) (f_0' - 1) + 3EcF_n (f_0' - 1)^2 - 2\theta_0 \right] F_0' + Pr (F_0 + NbH_0') \theta_0' = 0,
\end{aligned} \tag{6.5.12}$$

$$H_0'' + Sc \left[ f_0 - A \frac{\eta}{2} \right] H_0' + Sc (\beta - \delta) H_0 + Sc \phi_0' F_0 + \frac{Nt}{Nb} G_0'' = 0, \tag{6.5.13}$$

with the new boundary conditions:

$$\begin{aligned}
F_0(0) = 0, \quad F_0'(0) = \beta F_0''(0), \quad G_0'(0) = BiG_0(0), \quad NbH_0'(0) + NtG_0(0) = 0, \\
F_0'(\infty) \rightarrow 0, \quad G_0(\infty) \rightarrow 0, \quad H_0(\infty) \rightarrow 0.
\end{aligned} \tag{6.5.14}$$

As suggested by [Harris et al. \(2009\)](#), the range of possible eigenvalues can be obtained by relaxing one of the boundary conditions,  $F_0'(\infty) \rightarrow 0$  or  $G_0(\infty) \rightarrow 0$ . Thus, the boundary condition  $F_0'(\infty) \rightarrow 0$  is relaxed and replaced with the normalizing boundary condition  $F_0''(0) = 1$ , and the boundary conditions become:

$$F_0(0) = 0, \quad F_0'(0) = 0, \quad G_0'(0) = BiG_0(0), \quad F_0''(0) = 1, \quad G_0(\infty) \rightarrow 0. \tag{6.5.15}$$

Finally, equations (6.5.11) - (6.5.13) are solved along the new boundary conditions (6.5.15).

## 6.6 Numerical Procedures

In this problem, shooting method with fourth- fifth order Runge-Kutta-Fehlberg integration procedure has been applied for solving the set of nonlinear ordinary differential equation (6.3.23) - equation (6.3.25) under the boundary conditions equation (6.3.26) and equation(6.3.27) with the help of Maple software. Runge-Kutta-Fehlberg fourth-fifth method (Fehlberg method) is an algorithm in numerical analysis for the numerical solution of ordinary differential equations and is a method of order 4 with an error estimator of order 5, the algorithm is as follow:

- Convert the boundary value problem into initial value problem.
- Choose the suitable finite value of eta .
- Shooting technique is used to guess missing initial conditions by an iterative process until boundary conditions are satisfied.
- Solve the reduced system of the initial value equations by Runge-Kutta-Fehlberg method by taking step size h.
- This process was repeated until we obtained results correct up to the desired accuracy.

Dual solutions are obtained using two different initial guesses for the unknown values of  $f''(0)$ ,  $-\theta(0)$  and  $\phi(0)$  for the same value of parameter, which produce two different velocities, temperature and concentration profiles where both of them reach the far field boundary conditions given in equation(6.3.27) asymptotically.

## 6.7 Results and Discussion

In this study, the effects of unsteadiness parameter  $A$ , velocity slip parameter  $\gamma$ , shrinking/stretching parameter  $\lambda$ , magnetic field parameter  $M$ , the porous medium parameter  $Da$ , porous medium inertia parameter  $F_n$ , the mass flux parameter  $S$ , viscous dissipation , thermal radiation, chemical reaction and convective heating on the magnetic nanofluid velocity, temperature and species concentration are demonstrated in graphs.

The existence of dual solutions for certain ranges of parameter variations are shown for the skin friction coefficient in the form of graphs and tables and also the variations of Nusselt number are illustrated in graphs for different values of the parameters change.

Equation (6.3.23) - equation (6.3.25) together with the boundary conditions equation (6.3.26) and equation(6.3.27) are solved numerically using the shooting method with fourth-fifth order Runge-Kutta-Fehlberg integration procedure in Maple2018. This method has been used by several researchers for solving problems of convective boundary layer flows. For instance, papers by Bohra et al. (2017). In this study, the computational analysis was done to investigate the effects of those embedded parameters involved in the fluid flow equations on the velocity profiles, temperature profiles and the concentration profile. The graphs depicting these effects are plotted. In addition to these, graphs showing the skin friction, heat transfer and the mass transfer rate are plotted.

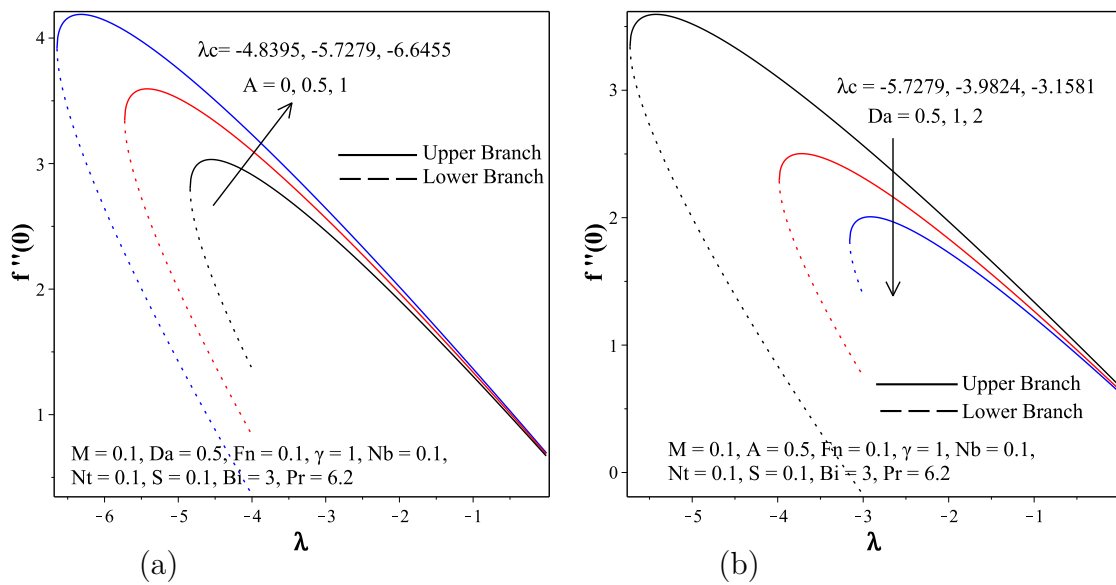


Figure 6.7.1: (a) Variation of skin friction for different values of unsteadiness parameter,  $A$  (b) Variation of skin friction for different values of porous medium parameter,  $Da$

The effects of different parameters on skin friction are presented in Figures 6.7.1-6.7.15. From the graphs obtained, the existence of a dual solution is witnessed. The range of existence of dual solution, upper branch and lower branch solutions, increases with the intensification of the unsteadiness, Magnetic field, and suction/injection parameters, whereas it decreases with the porous resistance and velocity slip parameters. Beyond the declared lambda critical values, no similar solution is expected due to the boundary layer separation from the surface and the inapplicability of the boundary

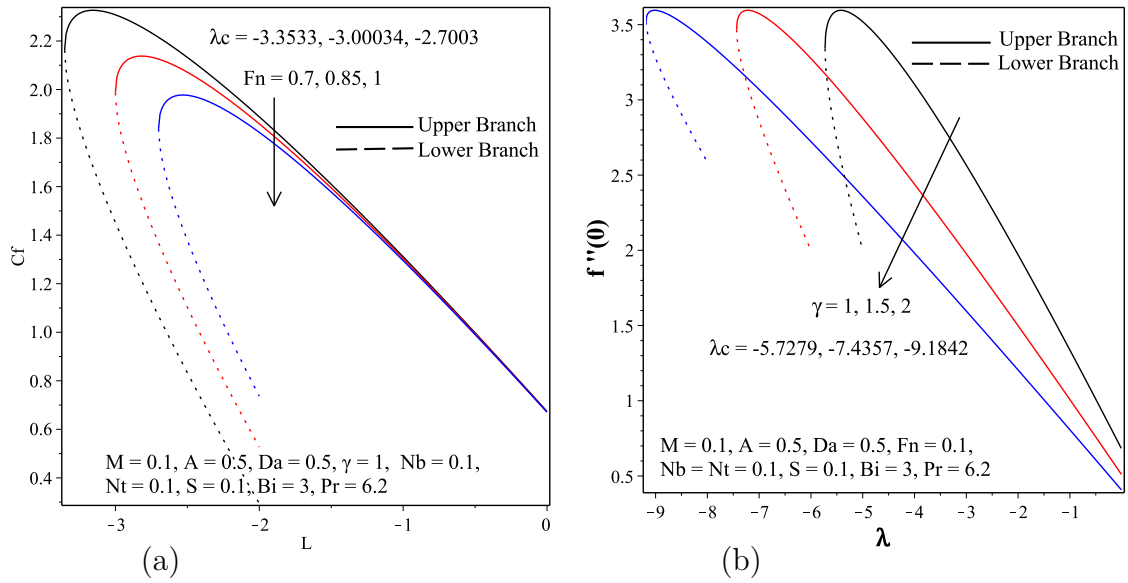


Figure 6.7.2: (a) Variation of skin friction for different values of second-order porous resistance parameter,  $F_n$  (b) Variation of skin friction for different values of slip parameter,  $\gamma$

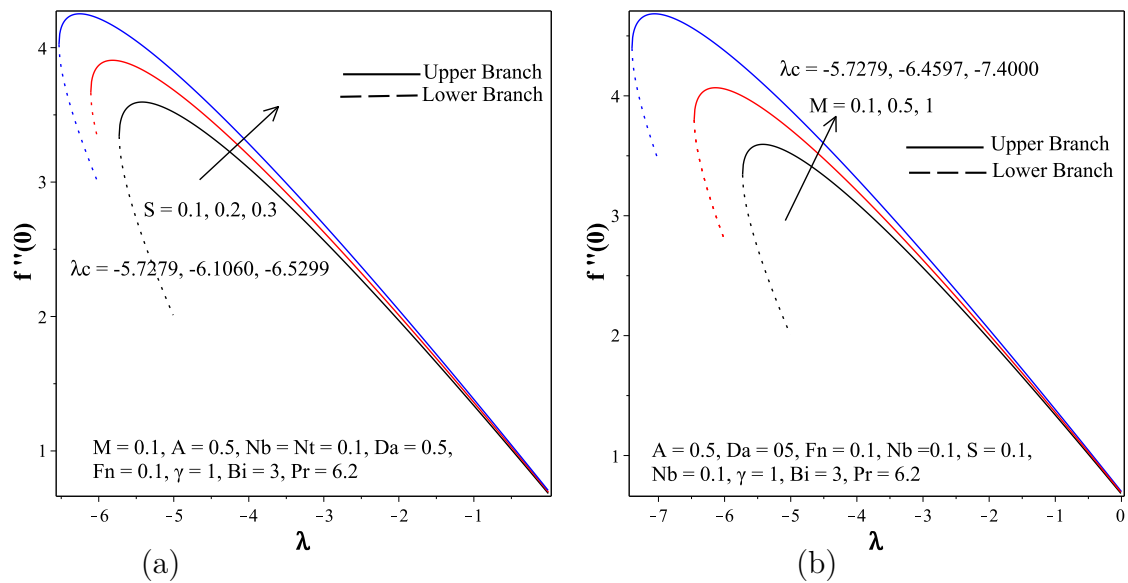


Figure 6.7.3: (a) Variation of skin friction for different values of suction parameter,  $S$  (b) Variation of skin friction for different values of Magnetic field parameter,  $M$

layer approximations.

As revealed in Figure 6.7.1, the appreciation of the unsteadiness parameter appreciates the skin friction for the upper branch solution and widens the interval of lambda for which a dual solution exists. From Figure 6.7.1b - 6.7.3b, it is observed that due to the decrement of the porous resistance parameters, Darcy porous and porous medium inertia parameters, decrease the skin friction for the upper branch solutions and up

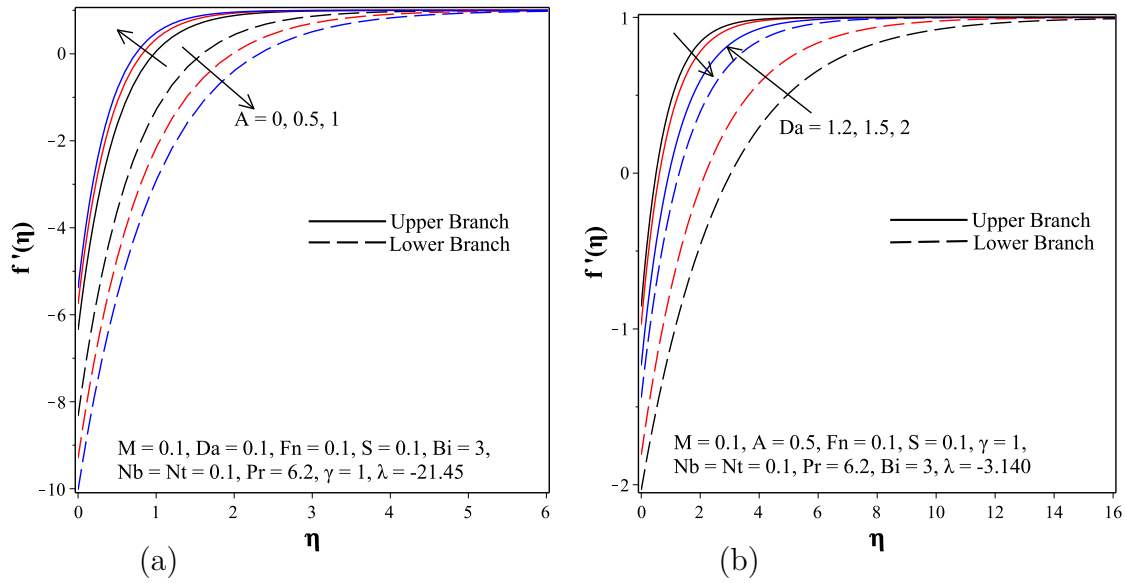


Figure 6.7.4: (a) Dual solution for velocity profiles with unsteadiness parameter,  $A$ . (b) Dual solution for velocity profiles with porous medium parameter,  $Da$ .

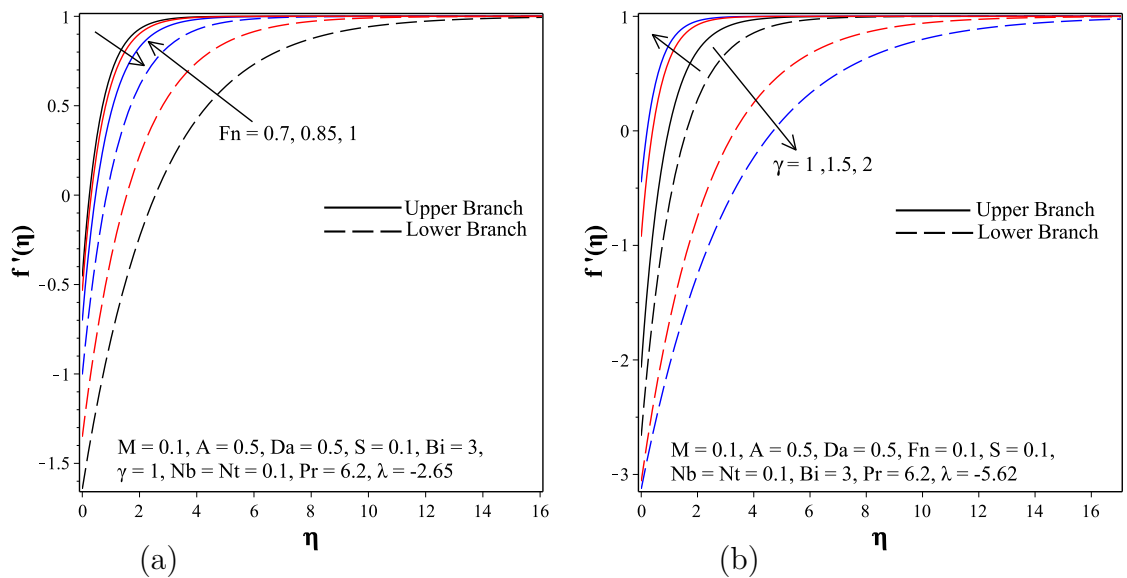


Figure 6.7.5: (a) Dual solution for velocity profiles with second-order porous resistance parameter,  $F_n$ . (b) Dual solution for velocity profiles with velocity slip parameter,  $\gamma$ .

to some shrinking parameter value, a similar character is observed for velocity slip parameter variation. Furthermore, the increment of the porous resistance parameters diminishes the possible lambda value for which the dual solution exists, but an opposite trend is observed for the velocity slip parameter. The effects of magnetic field and suction parameters are depicted in Figure 6.7.3. For the upper branch solutions, the increment of these parameters increases skin friction. The manifestation of more suction at the boundary surface slows down the fluid motion and this results in an

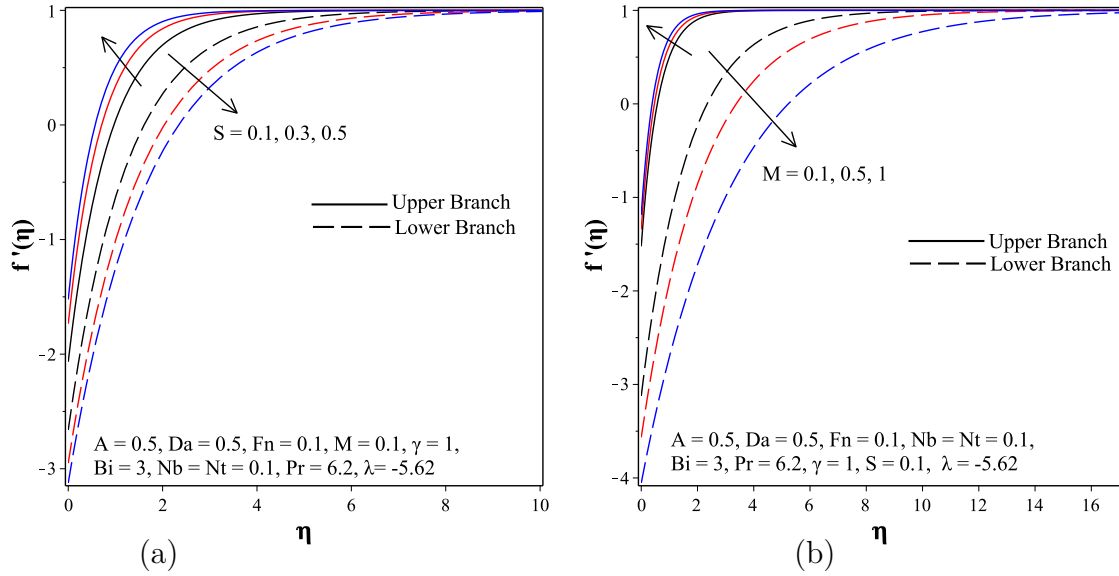


Figure 6.7.6: (a) Dual solution for velocity profiles with suction/injection parameter,  $S$ . (b) Dual solution for velocity profiles with Magnetic field parameter,  $M$ .

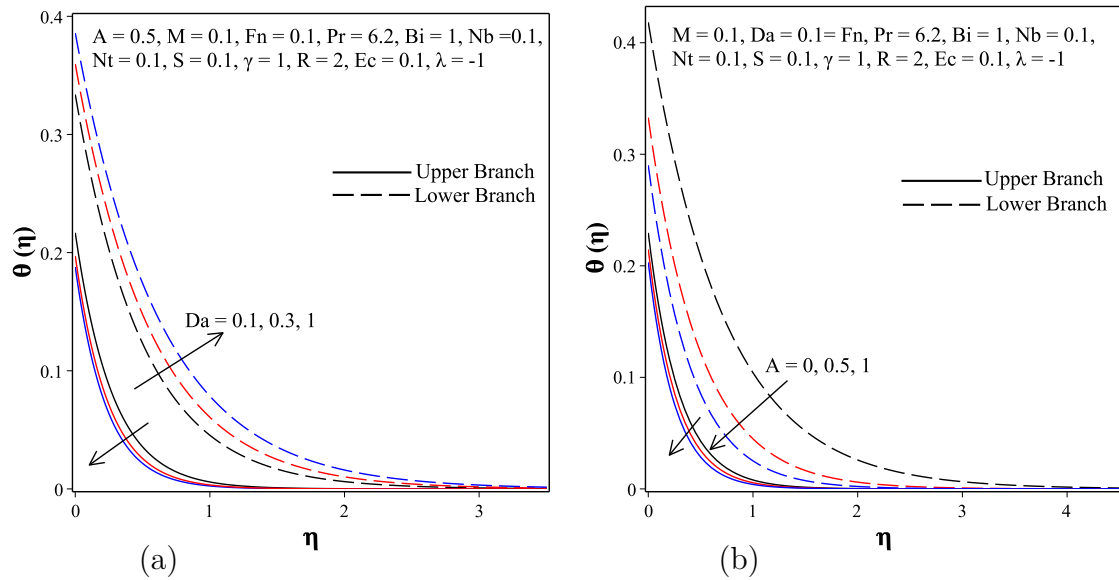


Figure 6.7.7: (a) Dual solution for temperature profiles with porous medium parameter,  $Da$  (b) Dual solution for temperature profiles with unsteadiness parameter,  $A$ .

increment in velocity gradient at the sheet surface. All the results obtained graphically come to an excellent agreement with the results shown in Table 6.7.1.

The dual nature of the real solution for velocity profile with a variety of different parameter values is illustrated in Figures 6.7.4-6.7.6. From the graphs obtained, it is observed that the hydrodynamic boundary layer thickness for the upper branch solutions is smaller than that of the lower branch solution. As well, it is noted that both the upper branch and lower branch solutions satisfy the far end condition asymptotically.

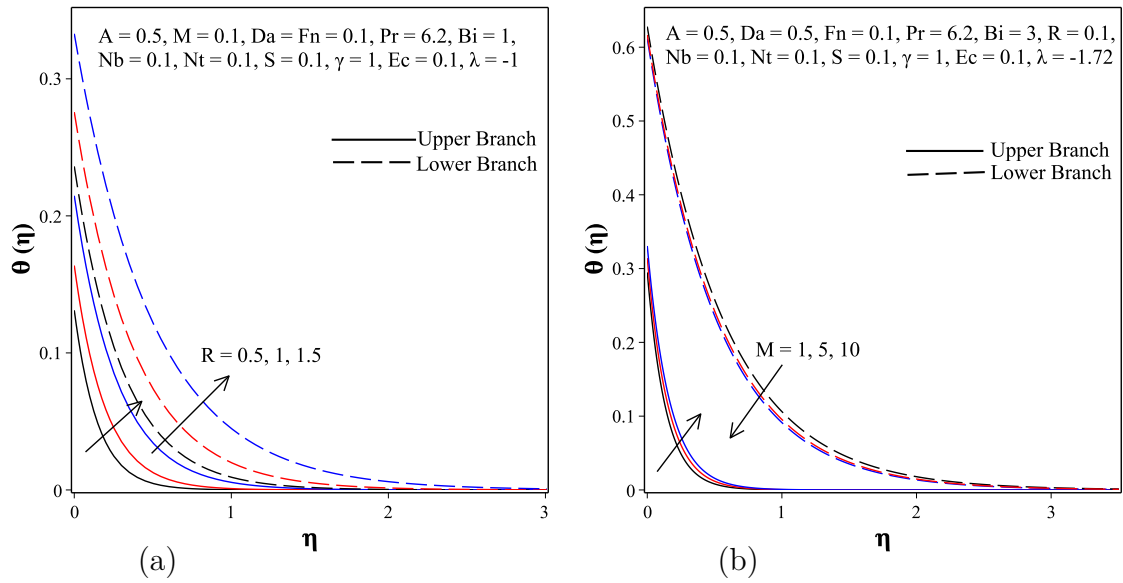


Figure 6.7.8: (a) Dual solution for temperature profiles with radiation parameter,  $R$   
(b) Dual solution for temperature profiles with Magnetic field,  $M$ .

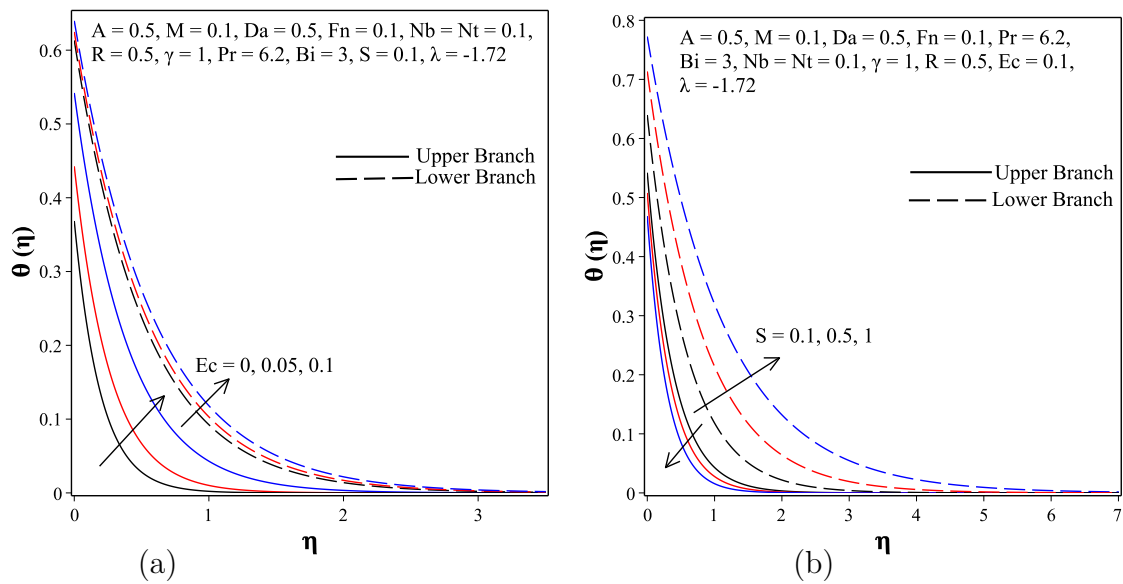


Figure 6.7.9: (a) Dual solution for temperature profiles with viscous dissipation,  $Ec$   
(b) Dual solution for temperature profiles with suction/injection parameter,  $S$ .

Figure 6.7.4a depicts the effects of the unsteadiness parameter on the velocity profile, an increase in the unsteadiness parameter enhances the fluid velocity for the upper branch solution, and a reverse trend is seen in the case of lower branch solutions. The amplification of the porous resistance parameters diminishes the fluid velocity for the upper branch solutions as revealed in Figures 6.7.4b and 6.7.5a. The effects of the velocity slip parameter on the velocity profile are established in Figure 6.7.5b. For the upper branch solution, as the velocity slip parameter increases the fluid velocity also in-

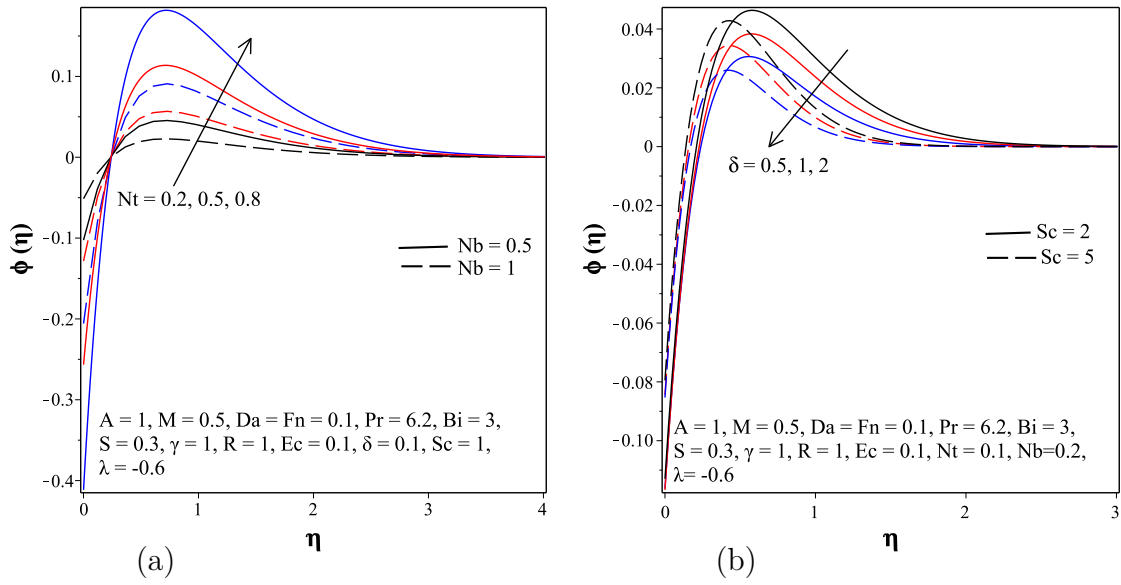


Figure 6.7.10: (a) Influence of  $Nt$  and  $Nb$  on the concentration profile (b) Influence of  $\delta$  and  $Sc$  on the concentration profile.

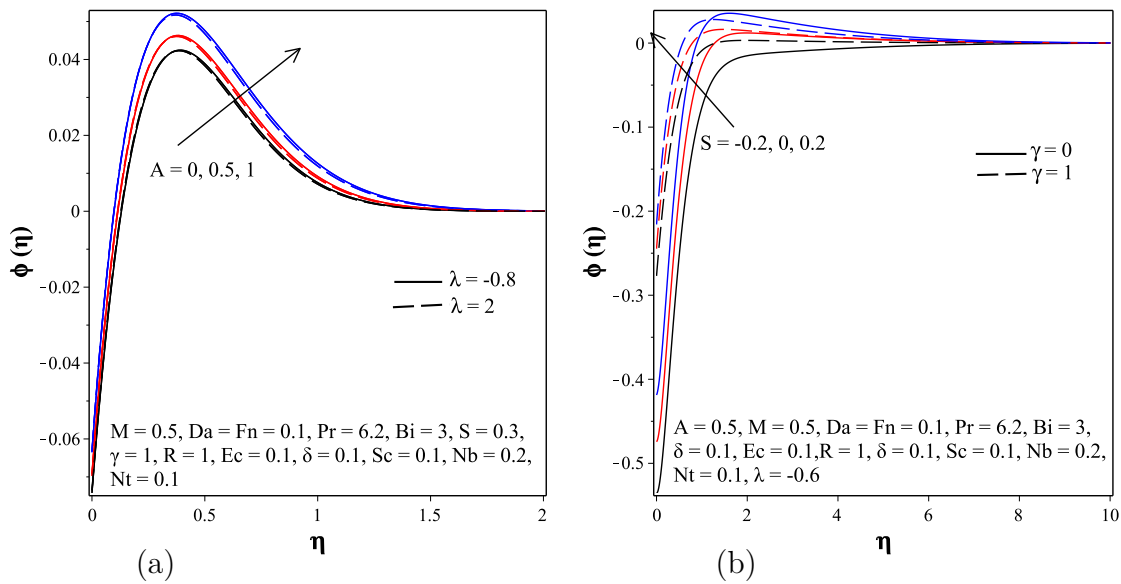


Figure 6.7.11: (a) Influence of  $A$  and  $\lambda$  on the concentration profile (b) Influence of  $S$  and  $\gamma$  on the concentration profile.

creases but an opposite character is seen in the lower branch solution. Furthermore, the hydrodynamic boundary layer thickness is getting thicker for the lower branch solution than the upper branch solution with increasing effects of the velocity slip parameter. Comparatively speaking, its effects are more pronounced in the lower branch solution than that in upper branch solutions. Figure 6.7.6a and 6.7.6b exposed effects of suction and magnetic field parameters variation on a dimensionless fluid velocity profile. For the upper branch solution, it is noted that as suction parameters increase the fluid

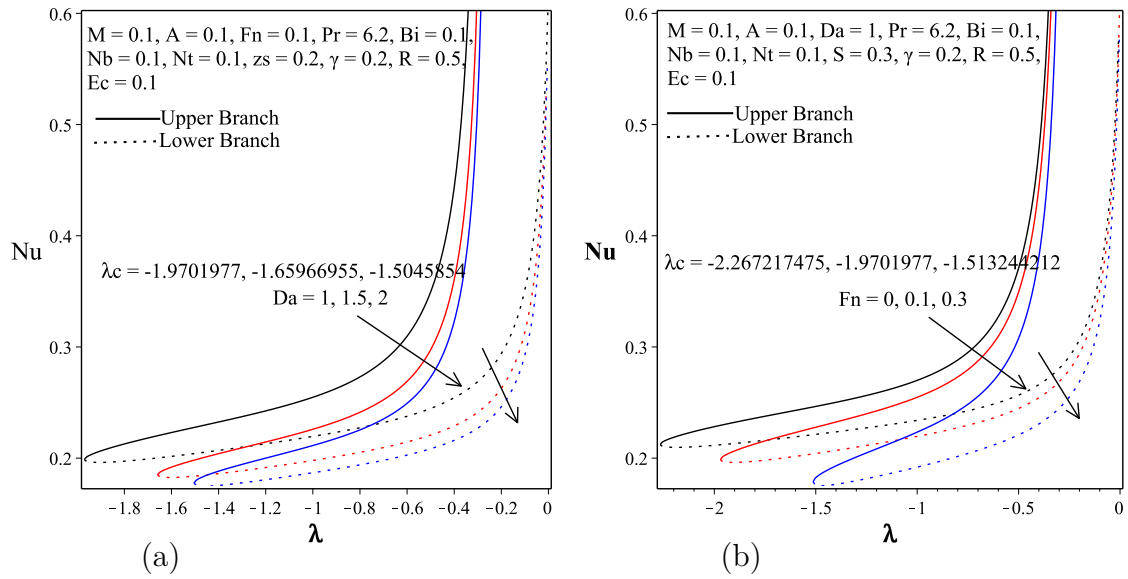


Figure 6.7.12: (a) Variation of local Nusselt number for different values of porous medium parameter,  $Da$  (b) Variation of local Nusselt number for different second-order porous resistance parameter,  $F_n$

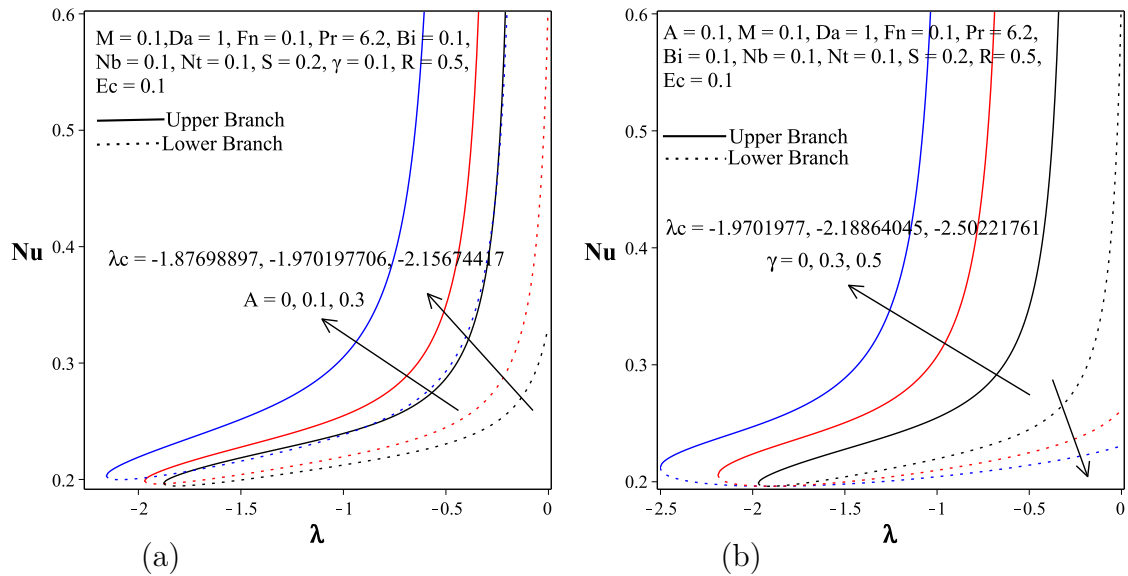


Figure 6.7.13: (a) Variation of local Nusselt number for different values of unsteadiness parameter,  $A$  (b) Variation of local Nusselt number for different values of velocity slip parameter,  $\gamma$ .

velocity increases, and the hydrodynamic boundary layer thickness gets diminished but a reverse arrangement is observed in the lower branch solutions. Similarly, as the magnetic field parameter increases, the fluid velocity shows an increment for the upper branch solution decrement for the lower branch solutions. Associated with the applied magnetic field, there is a Lorentz force that causes the thinning of the hydrodynamic boundary layer thickness; conversely, an opposite pattern is observed for the lower

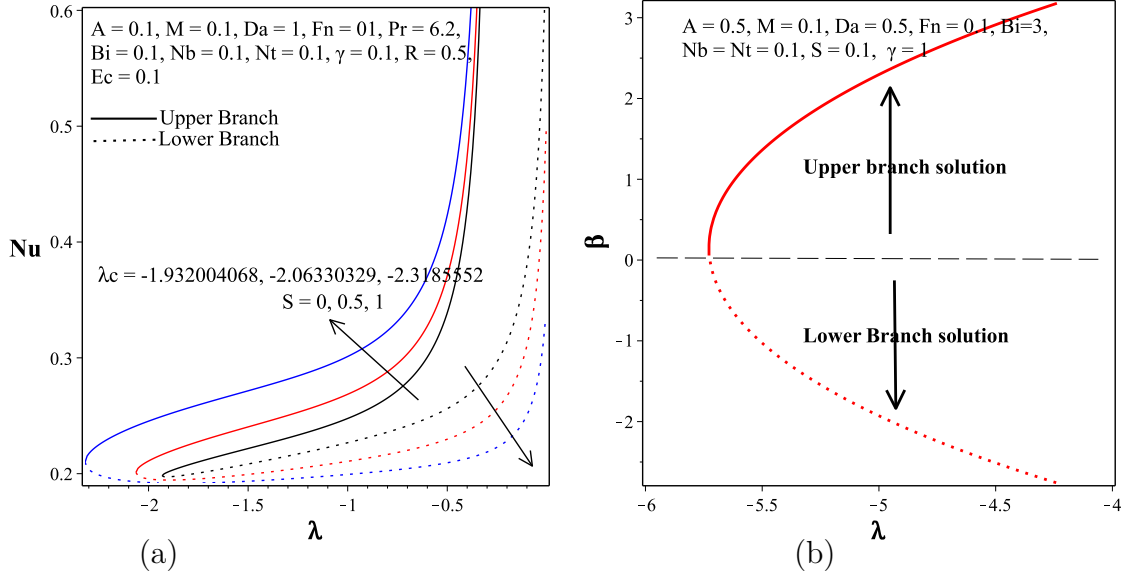


Figure 6.7.14: (a) Variation of local Nusselt number for different values of suction/injection,  $S$  (b) Smallest eigen value  $\beta$  for various values of,  $\lambda$ .

Table 6.7.1: The computation showing impact of parameters variation on the skin friction and the critical shrinking parameter

$A$	$Da$	$\gamma$	$F_n$	$S$	$M$	$\lambda_c$	$\lambda$	$Re_x^{1/2} C_f$	
								Upper Branch	Lower Branch
0	0.5	1	0.1	0.1	0.1	4.839594	-4.73	2.998643484	2.426298287
0.5	0.5	1	0.1	0.1	0.1	-5.727857	-5.62	3.553247865	2.957696409
1	0.5	1	0.1	0.1	0.1	-6.645569	-6.54	4.137864730	3.523509229
0.5	1	1	0.1	0.1	0.1	-3.982387	-3.95	2.412216802	2.116906748
0.5	2	1	0.1	0.1	0.1	-3.158140	-3.14	1.906020856	1.698752449
0.5	0.5	2	0.1	0.1	0.1	-9.184214	-9.17	3.557168316	3.468533005
0.5	0.5	3	0.1	0.1	0.1	-12.72701	-12.62	3.595345499	3.456468789
0.5	0.5	1	0.5	0.1	0.1	-3.933762	-3.92	2.531135973	2.348512447
0.5	0.5	1	1	0.1	0.1	-2.700322	-2.65	1.948646164	1.646824738
0.5	0.5	1	0.1	0.3	0.1	-6.105996	-6.00	3.868198032	3.293908286
0.5	0.5	1	0.1	0.5	0.1	-6.529904	-6.42	4.220608360	3.650765637
0.5	0.5	1	0.1	0.1	0.5	-6.459739	-6.42	4.634272193	2.978576650
0.5	0.5	1	0.1	0.1	1	-7.400005	-7.30	5.277204053	3.431150547

branch solution. Furthermore, the effects of the magnetic field parameter are more noticeable in the lower branch solution than that in the upper branch solution.

The effects of the Darcy porous medium parameter on the fluid temperature are well-thought-out in Figure 6.7.7a. From the results obtained, it is noted that the porosity of the medium drops the fluid temperature and decreases the thermal boundary layer in the case of upper branch solutions, whereas the thermal boundary layer get

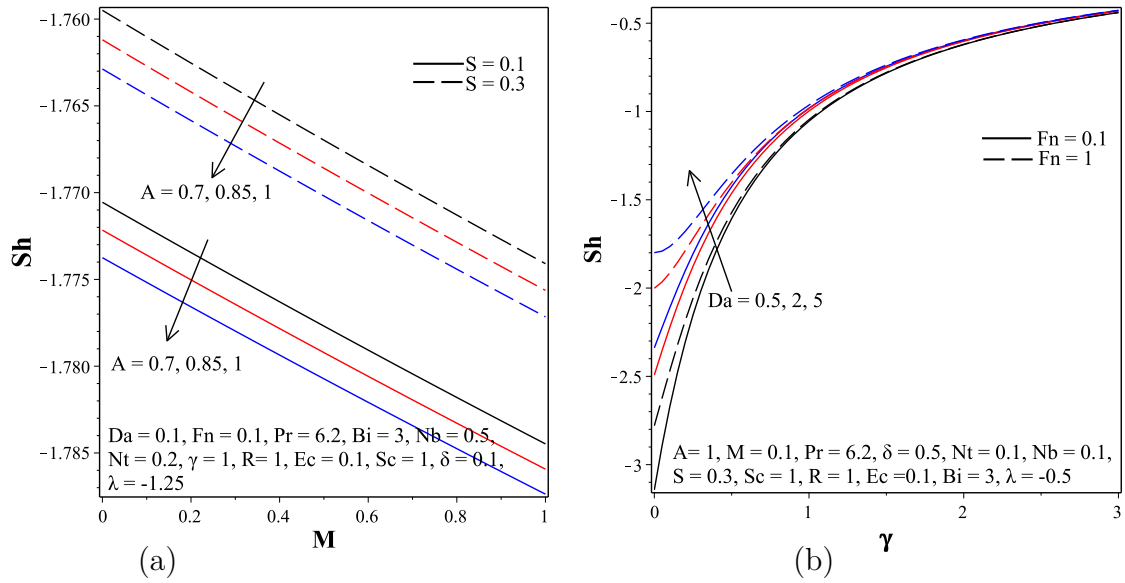


Figure 6.7.15: (a) Variation of local Sherwood number for different values of  $S$  and  $A$  (b) Variation of local Sherwood number for different values of  $Da$  and  $Fn$

Table 6.7.2: The computation of smallest eigenvalue ( $\beta$ ) for both lower and upper branch solutions

$A$	$Da$	$\gamma$	$F_n$	$S$	$M$	$\lambda_c$	$\lambda$	$\beta$	
								Upper Branch	Lower Branch
0	0.5	1	0.1	0.1	0.1	-4.839594	-4.73	1.01196247439228	-0.632791854277556
0.5	0.5	1	0.1	0.1	0.1	-5.727857	-5.62	0.98709657943535	-0.661201898715320
1	0.5	1	0.1	0.1	0.1	-6.645569	-6.54	0.97442908349414	-0.681766753482524
0.5	1	1	0.1	0.1	0.1	-3.982387	-3.95	0.55607501612195	-0.291416767856250
0.5	2	1	0.1	0.1	0.1	-3.158140	-3.14	0.42408093843914	-0.187383984353734
0.5	0.5	2	0.1	0.1	0.1	-9.184214	-8.17	2.16269986254263	-1.645186712452700
0.5	0.5	3	0.1	0.1	0.1	-12.72701	-12.62	0.79306583008564	-0.255717432035400
0.5	0.5	1	0.5	0.1	0.1	-3.933762	-3.75	1.75535332558558	-0.795901111523959
0.5	0.5	1	1	0.1	0.1	-2.700322	-2.65	1.54241693712506	-0.001559288563474
0.5	0.5	1	0.1	0.3	0.1	-6.105996	-6.00	1.01113535137353	-0.596085869794046
0.5	0.5	1	0.1	0.5	0.1	-6.529904	-6.42	1.06014158150795	-0.551519597522842
0.5	0.5	1	0.1	0.1	0.5	-6.459739	-6.42	2.53037842055148	-1.974599829881230
0.5	0.5	1	0.1	0.1	1	-7.400005	-7.30	2.77454723677370	-2.196082522905320

thickens as the porous medium parameter increases. As publicized in Figure 6.7.7b, the unsteadiness parameter reduces the fluid temperature and diminishes the thermal boundary layer for the upper branch solutions. Effects of this parameter are more apparent in the lower branch solutions than in the upper branch solutions.

As shown in Figure 6.7.8a, the thermal radiation parameter enhances the fluid temperature for both the upper and lower branch solutions and which leads to the

development of the thermal boundary layer. The intensification of thermal radiation reduces the heat transfer process from the sheet surface. Hence, more cooling from the surface is achieved through less application of thermal radiation. From Figure 6.7.8b, it is noted that the magnetic field parameter enriches the fluid temperature but a reverse configuration is realized in the lower branch solution. A considerable change in the thermal boundary layer thickness is not observed due to the amplification of the applied magnetic field.

The effects of viscous dissipation on fluid temperature profile are well elucidated in Figure 6.7.9a. As the viscous dissipation parameter increases, the fluid temperature and the thermal boundary layer thickness increase. This is due to the fact that in viscous fluid flow the viscosity of the fluid takes kinetic energy from the fluid and transforms it into internal energy that heats the fluid. As defined in Figure 6.7.9b, the suction parameter lessens the fluid temperature for the upper branch solutions and improves for the lower branch solutions. The thermal boundary layer thickness gets thinner as the suction parameter increases for the upper branch solution and goes in the opposite fashion for the lower branch solutions.

The joint effects of the nanofluid parameters on the species concentration profiles are exposed in Figure 6.7.10a. Thermophoretic forces coming from increasing values of the thermophoresis diffusion parameter lead to more diffusion of nanoparticles from the hot plate to the ambient fluid which in turn enhances the species concentration profiles, but a reverse arrangement is realized within a few layers of the fluid from the plate. Moreover, the Brownian motion parameter has an increasing effect on the species concentration profiles within a few layers of the fluid from the plate and an opposite pattern is observed after the transition point. This is due to the fact that the existence of high random motions of the nanoparticles in the fluid regions leads to lesser nanoparticle volume fraction in the fluid layers.

The effect of increasing the reaction parameter on the species concentration profiles for a generative chemical reaction is shown in Figure 6.7.10b. It is noticed from this graph that there is a marked effect of increasing the value of the chemical reaction rate parameter on species concentration distribution at the middle of the solutes boundary layer compared to the region closer to the stretching/shrinking surface.

It is clearly observed from this figure that the value of the species concentration at

the middle of the boundary layer decreases till it attains the minimum value of zero at the end of the boundary layer and this trend is seen for all the values of reaction rate parameter. Further, it is observed that increasing the value of the chemical reaction rate parameter decreases the concentration of species in the boundary layer, this is due to the fact that the solutes boundary layer decreases with the chemical reaction rate parameter. Similar facts are seen in the case when the value of the Schmidt number is increased as noted in Figure 6.7.10b. As expected, the mass transfer decreases as the Schmidt parameter increases by keeping all other physical parameters fixed, i.e. an increase in the value of the Schmidt number is associated with the reduction in the concentration profiles.

Figure 6.7.11a demonstrates the combined effects of the unsteadiness parameter and stretching/ shrinking parameter on species concentration profile. It is observed that the effects of increasing the value of the unsteadiness parameter enhance the species concentration profile till it attains the far end condition for both stretching and shrinking parameters. Furthermore, the effects of the stretching/shrinking parameter on the species concentration profile are not too substantial. The effects of suction and injection on the species concentration profile with and without the effects of velocity slip parameters are exploited in Figure 6.7.11b. As we can see from this graph, a larger species concentration profile is seen in the presence of suction than injection through the permeable surface in both cases.

The variations of local Nusselt number for different values of the governing parameters are justified in Figure 6.7.12a- Figure 6.7.14a. Moreover, the possible ranges of shrinking parameter values where the dual solution exists are pointed out. Figure 6.7.12a displays the effects of the porous medium parameter (Darcy number) on the wall heat transfer rate from the shrinking surface and the interval of existence of a dual solution. It is witnessed that the intensifications of the porous medium parameter decrease the surface heat transfer rate and weakens the intervals where a dual solution exists. Similarly, as shown in Figure 6.7.12b, increasing the second-order porous resistance parameter decreases the local Nusselt number and narrows the intervals of dual solution.

The increasing effects of the unsteadiness parameter are seen in Figure 6.7.13a. From this graph, it is noted that the unsteadiness parameter boosts the heat transfer

rate from the permeable shrinking surface and also widens the solution domain of occurrence of dual solutions. As indicated in Figure 6.7.13b, a remarked change in heat transfer rate from the surface is observed. The velocity slip parameter increases the heat transfer and widens the intervals of occurrence of dual solutions. In Figure 6.7.14a, the combined effects of the suction parameter and shrinking sheet are explicated. The application of more suction enhances the heat transfer process from the shrinking surface. This is due to the fact that increasing the suction rate increases the nanofluid particles which in turn increases the rate of heat transfer from the surface. Additionally, the interval of existence of dual solution increases with the suction parameter. Figure 6.7.14b depicts the smallest eigenvalue for different values of the shrinking parameter. For the upper branch solutions, a positive eigenvalue is obtained and negative values are obtained for the lower branch solutions which have strong support for the values given in Table 6.7.2. In Figure 6.7.15, the effects of different parameters on the wall mass transfer rate is disclosed. As the magnetic field parameter and unsteadiness parameter increases, the wall mass transfer rate decreases but it increases for the appreciation of suction/injection, velocity slip and porous medium parameters.

# Chapter 7

## Summary, Conclusion and Recommendation

### 7.1 Summary

Due to the wide applications of the boundary layer theory in numerous problems of fluid dynamics, this dissertation aims to develop and analyze a mathematical model of magnetic nanofluid flows to study the heat and mass transfer behavior of the working fluid in a boundary layer. The general objective was achieved through the following specific objectives which are: to develop nonlinear mathematical models of boundary layer flow of magnetic nanofluid with heat and mass transfer problems under various physical parameters; to apply numerical algorithms that will tackle the resulting nonlinear models and implement them using appropriate software; to analyze effects of embedded parameters on velocity, temperature, nanoparticle volume fraction, skin friction, heat transfer and mass transfer characteristics; to investigate the existence of dual solutions for some governing parameters; to analyze and establish the temporal stability analysis of the basic flows. The models are mainly based on continuity, Navier-Stokes, energy, mass concentration and Maxwell equations which were solved numerically and the results were compared for consistency. The results were obtained and presented graphically as well as in tabular form and discussed quantitatively.

Chapter 1 consists of a general introduction and an overview of the research including basic definitions of physical properties in fluid flow, motivation of the study, statement of the problem, objectives, significance, scope of the study and organization of the dissertation. Then, chapter 2 deals with previous studies regarding boundary layer theory in general and specifically about boundary layer flow past a stretching/shrinking sheet and boundary layer flow in a Darcian and non-Darcian porous medium. In chapter 3, derivations of fluid flow governing equations based on the conservation laws and the computational techniques (Techniques of solving boundary value problems) used are explicated.

Mixed convection of a radiating magnetic nanofluid past a heated permeable stretching/shrinking sheet in a Darcian porous medium is studied in chapter 4. The effects of some pertinent embedded parameters on fluid velocity profile, temperature profile, species concentration profile, wall skin friction, wall heat transfer and wall mass trans-

fer are demonstrated in graphic representation and the existence of two real solutions for a specific range of shrinking parameters  $\lambda$  is observed. Moreover, in addition to the effects of thermal radiation and viscous dissipation, the effects of porous dissipation are considered.

Hydromagnetic stagnation point flow of  $\text{Fe}_3\text{O}_4$ -water ferrofluid flow past a permeable convectively heated stretching/shrinking surface in a Darcy-Forchheimer porous Medium is investigated in chapter 5. The effects of flow governing parameters on ferrofluid flow and heat transfer characteristics are investigated by using a single-phase flow model. Furthermore, hydrodynamic stability analysis is done to identify solutions that are hydrodynamically stable and physically achievable.

Using Buongiorno convective transport equations, the collective effects of various parameters: the unsteady flow, slip condition, viscous dissipation and porous dissipation, magnetic field, chemical reaction, suction/injection, porous medium, porous medium inertia parameter, and convective heating on the dimensionless fluid velocity profile, temperature profile, species concentration profile, wall skin friction, the wall heat transfer and wall mass transfer characteristics are studied in chapter 6. In addition to this, temporal stability analysis of unsteady slip flow of a magnetic nanofluid past a convectively heated permeable stretching/shrinking sheet in a non-Darcian porous medium is carried out numerically to identify intervals of occurrence of stable and physically reliable solutions. The effects of some governing parameters' variation on the intervals of occurrence of dual solutions are presented in graphs and tables.

This study has examined the numerical solutions and the occurrence of dual solutions under the effects of some parameters change. All problems are studied theoretically, and the solutions are obtained numerically using the fourth-fifth order Runge-Kutta-Fehlberg method along with the shooting technique and MAPLE software is used to generate the numerical solutions.

## 7.2 Conclusion

In this study, a problem of two-dimensional boundary layer flow of magnetic nanofluid with heat and mass transfer characteristics in Darcian and non-Darcian porous medium is studied. The mathematical formulation of these problems is developed based on the

two flow models such as the Buongiorno convective transport flow model, and Tiwari and Das nanofluids flow model. From the flow model analysis and the numerical results obtained in chapter 4, 5 and 6, significant findings are mentioned below:

- The dimensionless velocity and temperature profiles decrease with porous medium parameter and mass suction/injection parameter, whereas an increase in radiation increases the temperature.
- The skin friction increases with both convective and Brownian motion parameters but decreases with increasing mass suction/injection which is also lower for higher values of radiation parameter and shows intensification with magnetic field parameter.
- The reduced Nusselt numbers are higher for stretching sheets than shrinking sheets and also decrease with magnetic field parameter and Brownian motion parameter but upsurges with nanofluid buoyancy ratio, heat convective parameter, and thermophoresis parameter.
- The Sherwood numbers increase with the magnetic field and thermophoresis parameter but decrease with nanofluid buoyancy ratio, thermal radiation parameter, and Brownian motion parameter.
- Two real solutions exist within a specific range of shrinking parameter; however, only one of the two solutions is physically realistic and the other one diverges when subjected to disturbances.
- The value of  $|\lambda_c|$  increases with increasing values of the magnetic field parameter  $M$ , whereas the value of  $|\lambda_c|$  decreases with increasing value of the porosity parameter  $Da$ .
- The upper branch solution is hydrodynamically stable and is physically achievable, whereas the lower branch solution is unstable and physically unrealistic.
- The intensification of the magnetite nanoparticle volume fraction, suction/injection, and the magnetic field parameter widen the range of  $\lambda$  for which the solution exists and narrow for the increment of the porous media parameter and the porous medium inertia parameter.

- The skin friction coefficient for the upper branch solution is intensified with an increase in the quantity of magnetite nanoparticle volume fraction, suction, and the magnetic field parameters but drops for the porous medium parameter, porous medium inertia parameter, and the injection parameter.
- For the upper branch solution, the ferrofluid velocity increases with the quantity of magnetite nanoparticle volume fraction, suction, and the magnetic field parameters, whereas decreases with an increase in the shrinking parameter and porous medium parameter.
- The momentum boundary layer thickness increases with the shrinking parameter and porous medium parameter but decreases with an increase in the magnetite nanoparticle volume fraction, suction, and magnetic field parameters.
- The ferrofluid temperature and thermal boundary layer thickness are enhanced with an increase in the magnetite nanoparticle volume fraction and Eckert number but diminished with an increase in porous media parameter and porous medium inertia parameter.
- The heat transfer rate increases with the magnetite nanoparticle volume fraction and suction parameters, whereas decreases with the porous media parameter and porous medium inertia parameter.
- Non-unique solutions exist for a particular range of the shrinking parameter.
- Stability analysis demonstrated a positive smallest eigenvalue in the upper branch solutions.
- The interval of occurrence of dual solutions widen with the intensification of the unsteadiness, suction, and the magnetic field parameters and weakens for the increment of the porous media parameter and the porous medium inertia parameter.
- In the upper branch solutions, the skin friction coefficient and the fluid velocity are intensified with an intensification of the unsteadiness parameter, suction, and the magnetic field parameters but drops for the porous medium parameter and porous medium inertia parameter

- The fluid temperature and the thermal boundary layer thickness are enhanced with an increase in the thermal radiation parameter, suction parameter and Eckert number but diminished with an increase in porous media parameter and the slip velocity parameter.
- Through the intensification of the thermophoresis diffusion parameter, unsteadiness parameter and suction/injection parameter, the species concentration profile increases but a reverse phenomena is seen for chemical reaction and Brownian motion parameters.
- The wall heat transfer rate increases with the velocity slip, unsteadiness and suction parameters, whereas decreases with the porous media parameter and porous medium inertia parameter.
- The wall mass transfer rate intensifies with magnetic field, suction and unsteadiness parameters, whereas diminishes with the velocity slip, the porous media parameter and porous medium inertia parameter.

## **7.3 Recommendation and Suggestions for Future Research**

### **7.3.1 Recommendation**

The results obtained in this dissertation have a lot of applications in various engineering systems, especially in the process of cooling electronic devices and heat transfer enhancement in many industrial manufacturing processes. The results obtained in such a mathematical investigation of fluid flow problems can be used as a platform for experimental investigation of practical problems occurring in different thermal management of heat-generating electronic devices for optimal performance.

### **7.3.2 Suggestions for Future Research**

Due to the importance of such fluid flow problems in Engineering and industrial processing applications, the work presented in this dissertation can be extended in different ways as given below:

- Hybrid nanofluid with different nanoparticles and base fluid model can be incorporated in the same geometry.
- Different non-Newtonian fluids can be considered such as Casson fluid, Williamson nanofluid, Jeffrey nanofluids, etc.
- The flow geometry can be changed into cylindrical, wedges, disc and cone.
- Various nanoparticles (silver, gold, carbon nanotubes, etc.) can be considered in three dimensional stagnation point flows.

## References

- Abbas, Z. and Sheikh, M. (2017). Numerical study of homogeneous–heterogeneous reactions on stagnation point flow of ferrofluid with non-linear slip condition. *Chinese Journal of Chemical Engineering*, 25(1):11–17.
- Abdullah, A., Ibrahim, F., Gawad, A., and Batyyb, A. (2015). Investigation of unsteady mixed convection flow near the stagnation point of a heated vertical plate embedded in a nanofluid-saturated porous medium by self-similar. *Am. J. Energy Eng*, 3:42–51.
- Abdullah, A. A., Ibrahim, F. S., and Chamkha, A. J. (2018). Nonsimilar solution of unsteady mixed convection flow near the stagnation point of a heated vertical plate in a porous medium saturated with a nanofluid. *Journal of Porous Media*, 21(4).
- Ali Lund, L., Omar, Z., Khan, I., Raza, J., Bakouri, M., and Tlili, I. (2019). Stability analysis of darcy-forchheimer flow of casson type nanofluid over an exponential sheet: Investigation of critical points. *Symmetry*, 11(3):412.
- Anwar, M. S. (2020). Numerical study of transport phenomena in a nanofluid using fractional relaxation times in buongiorno model. *Physica Scripta*, 95(3):035211.
- Arulmurugan, R., Vaidyanathan, G., Sendhilnathan, S., and Jeyadevan, B. (2006). Mn–zn ferrite nanoparticles for ferrofluid preparation: study on thermal–magnetic properties. *Journal of magnetism and magnetic materials*, 298(2):83–94.
- Aziz, A. and Khan, W. (2012). Natural convective boundary layer flow of a nanofluid past a convectively heated vertical plate. *International Journal of Thermal Sciences*, 52:83–90.
- Baag, S., Mishra, S., and Nayak, B. (2017). Buoyancy effects on free convective mhd flow in the presence of heat source/sink. *Modelling, Measurement and Control B*, 86:14–32.
- Baehr, H. D. and Stephan, K. (2011). Convective heat and mass transfer. single phase flow. In *Heat and Mass Transfer*, pages 275–441. Springer.
- Bahiraee, M. and Hangi, M. (2015). Flow and heat transfer characteristics of magnetic nanofluids: a review. *Journal of Magnetism and Magnetic Materials*, 374:125–138.
- Bakar, S. A., Arifin, N. M., Nazar, R., Ali, F. M., and Pop, I. (2016). Forced convection boundary layer stagnation-point flow in darcy-forchheimer porous medium past a shrinking sheet. *Frontiers in Heat and Mass Transfer*, 7:38.
- Bergman, T. L., Incropera, F. P., DeWitt, D. P., and Lavine, A. S. (2011). *Fundamentals of heat and mass transfer*. John Wiley & Sons.

- Bhattacharyya, K. (2013). Heat transfer in boundary layer stagnation-point flow towards a shrinking sheet with non-uniform heat flux. *Chinese Physics B*, 22(7):074705.
- Bhattacharyya, K., Mukhopadhyay, S., and Layek, G. (2011). Slip effects on boundary layer stagnation-point flow and heat transfer towards a shrinking sheet. *International Journal of Heat and Mass Transfer*, 54(1-3):308–313.
- Bhatti, M., Abbas, T., and Rashidi, M. (2017). A new numerical simulation of mhd stagnation-point flow over a permeable stretching/shrinking sheet in porous media with heat transfer. *Iranian Journal of Science and Technology, Transactions A: Science*, 41(3):779–785.
- Blake, L. R. (1959). Electro-magnetic pumps for liquid metals. *Journal of Nuclear Energy. Part B. Reactor Technology*, 1(2):65–IN1.
- Blasius, H. (1907). *Grenzschichten in Flüssigkeiten mit kleiner Reibung*. Druck von BG Teubner.
- Blums, E. (2002). Heat and mass transfer phenomena. In *Ferrofluids*, pages 124–139. Springer.
- Bohra, S. et al. (2017). Heat and mass transfer over a three-dimensional inclined non-linear stretching sheet with convective boundary conditions. *Indian Journal of Pure & Applied Physics (IJPAP)*, 55(12):847–856.
- Buongiorno, J. (2006). Convective transport in nanofluids. *J. Heat Tran.*, 128:240–250.
- Cengel, Y. A. and Ghajar, A. J. (2007). Heat and mass transfer. *A practical approach*.
- Chamkha, A. J. and Ismael, M. A. (2013). Conjugate heat transfer in a porous cavity filled with nanofluids and heated by a triangular thick wall. *International Journal of Thermal Sciences*, 67:135–151.
- Chand, R. (2017). *Nanofluid Technologies and Thermal Convection Techniques*. IGI Global.
- Choi, S. U. and Eastman, J. A. (1995). Enhancing thermal conductivity of fluids with nanoparticles. Technical report, Argonne National Lab., IL (United States).
- Chu, Y.-M., Rehman, M. I. U., Khan, M. I., Nadeem, S., Kadry, S., Abdelmalek, Z., and Abbas, N. (2020). Transportation of heat and mass transport in hydromagnetic stagnation point flow of carreau nanomaterial: Dual simulations through runge-kutta fehlberg technique. *International Communications in Heat and Mass Transfer*, 118:104858.

- Crane, L. J. (1970). Flow past a stretching plate. *Zeitschrift für angewandte Mathematik und Physik ZAMP*, 21(4):645–647.
- Das, M., Mahanta, G., and Shaw, S. (2020a). Heat and mass transfer effect on an unsteady mhd radiative chemically reactive casson fluid over a stretching sheet in porous medium. *Heat Transfer*, 49(8):4350–4369.
- Das, S., Ali, A., and Jana, R. (2020b). Darcy–forchheimer flow of a magneto-radiated couple stress fluid over an inclined exponentially stretching surface with ohmic dissipation. *World Journal of Engineering*.
- Dash, G., Tripathy, R., Rashidi, M., and Mishra, S. (2016). Numerical approach to boundary layer stagnation-point flow past a stretching/shrinking sheet. *Journal of Molecular Liquids*, 221:860–866.
- Davidson, P. A. (2002). *An introduction to magnetohydrodynamics*. American Association of Physics Teachers.
- Dessie, H. and Kishan, N. (2014). Mhd effects on heat transfer over stretching sheet embedded in porous medium with variable viscosity, viscous dissipation and heat source/sink. *Ain shams engineering journal*, 5(3):967–977.
- Dzulkifli, N. F., Bachok, N., Yacob, N. A., Pop, I., Arifin, N., and Rosali, H. (2022). Stability solution of unsteady stagnation-point flow and heat transfer over a stretching/shrinking sheet in nanofluid with slip velocity effect. *CFD Letters*, 14(1):66–86.
- Eid, M. R. and Makinde, O. (2018). Solar radiation effect on a magneto nanofluid flow in a porous medium with chemically reactive species. *International Journal of Chemical Reactor Engineering*, 16(9).
- Faires, J. D. and Burden, R. L. (2012). *Numerical methods, 4th*. Cengage Learning.
- Falthammar, C.-G. (1997). Plasma physics from laboratory to cosmos-the life and achievements of hannes alfven. *IEEE transactions on plasma science*, 25(3):409–414.
- Freidoonimehr, N., Rashidi, M., and Jalilpour, B. (2016). Mhd stagnation-point flow past a stretching/shrinking sheet in the presence of heat generation/absorption and chemical reaction effects. *Journal of the Brazilian Society of Mechanical Sciences and Engineering*, 38(7):1999–2008.
- Gautam, A. K., Verma, A. K., Bhattacharyya, K., and Banerjee, A. (2020). Soret and Dufour effects on MHD boundary layer flow of non-Newtonian Carreau fluid with mixed convective heat and mass transfer over a moving vertical plate. *Pramana - J. Phys.*, 94(1):1–10.

- Griese, R. and Kunisch, K. (2006). Optimal control for a stationary mhd system in velocity-current formulation. *SIAM Journal on Control and Optimization*, 45(5):1822–1845.
- Gupta, D., Kumar, L., and Singh, B. (2014). Finite element solution of unsteady mixed convection flow of micropolar fluid over a porous shrinking sheet. *The scientific world journal*, 2014.
- Gupta, M. (2016a). A review on the improvement in convective heat transfer properties using magnetic nanofluids. *Int J Therm Technol E-ISSN-2277-4114*, 6(1):40–46.
- Gupta, M. (2016b). A review on the improvement in convective heat transfer properties using magnetic nanofluids. *Int J Therm Technol E-ISSN-2277-4114*, 6(1):40–46.
- Gupta, M., Singh, V., and Katyal, P. (2018). Synthesis and structural characterization of  $Al_2O_3$  nanofluids. *Materials Today: Proceedings*, 5(14):27989–27997.
- Haq, R. U., Nadeem, S., Khan, Z. H., and Akbar, N. S. (2015). Thermal radiation and slip effects on mhd stagnation point flow of nanofluid over a stretching sheet. *Physica E: Low-dimensional systems and nanostructures*, 65:17–23.
- Harris, S., Ingham, D., and Pop, I. (2009). Mixed convection boundary-layer flow near the stagnation point on a vertical surface in a porous medium: Brinkman model with slip. *Transport in Porous Media*, 77(2):267–285.
- Hartman, J. (1937). Theory of the laminar flow of an electrically conducting liquid in a homogeneous magnetic field, math. *Fys. Medd*, 15(6).
- Hartman, J. and Lazarus, F. (1937). Experimental investigations on the flow of mercury in a homogeneous magnetic field, k. *Dan. Vidensk. Selsk. Mat. Fys. Meed*, 15:1–45.
- Hayat, T., Haider, F., Muhammad, T., and Alsaedi, A. (2017). Darcy-forchheimer flow due to a curved stretching surface with cattaneo-christov double diffusion: A numerical study. *Results in physics*, 7:2663–2670.
- Hayat, T., Muhammad, T., Al-Mezal, S., and Liao, S. (2016). Darcy-forchheimer flow with variable thermal conductivity and cattaneo-christov heat flux. *International Journal of Numerical Methods for Heat & Fluid Flow*.
- Hiemenz, K. (1911). Die grenzschicht an einem in den gleichformigen flussigkeitsstrom eingetauchten geraden kreiszylinder. *Dinglers Polytech. J.*, 326:321–324.
- Hiergeist, R., Andrä, W., Buske, N., Hergt, R., Hilger, I., Richter, U., and Kaiser, W. (1999). Application of magnetite ferrofluids for hyperthermia. *Journal of magnetism and Magnetic Materials*, 201(1-3):420–422.

- Holman, J. (2009). *Heat Transfer tenth edition, ser.* McGraw-Hill Series in Mechanical Engineering. McGraw Hill Higher Education.
- Ibrahim, W., Shankar, B., and Nandeppanavar, M. M. (2013). Mhd stagnation point flow and heat transfer due to nanofluid towards a stretching sheet. *International journal of heat and mass transfer*, 56(1-2):1–9.
- Ibrahim, W. and Tulu, A. (2019). Magnetohydrodynamic (MHD) Boundary Layer Flow Past a Wedge with Heat Transfer and Viscous Effects of Nanofluid Embedded in Porous Media. *Math. Probl. Eng.*, 2019.
- Ishak, A. (2014). Flow and heat transfer over a shrinking sheet: A stability analysis. *International Journal of Mathematical and Computational Sciences*, 8(5):902–906.
- Ismail, N., Arifin, N., Nazar, R., et al. (2017). The stagnation-point flow and heat transfer of nanofluid over a shrinking surface in magnetic field and thermal radiation with slip effects: a stability analysis. In *Journal of Physics: Conference Series*, volume 890, page 012055. IOP Publishing.
- Jagadha, S. and Amrutha, P. (2019). Mhd boundary layer flow of darcy-forchheimer mixed convection in a nanofluid saturated porous media with viscous dissipation. *Applications and Applied Mathematics: An International Journal (AAM)*, 14(4):10.
- Jamaludin, A., Naganthran, K., Nazar, R., and Pop, I. (2020). Thermal radiation and mhd effects in the mixed convection flow of fe<sub>3</sub>o<sub>4</sub>–water ferrofluid towards a nonlinearly moving surface. *Processes*, 8(1):95.
- Jamaludin, A., Nazar, R., and Pop, I. (2019). Mixed convection stagnation-point flow of a nanofluid past a permeable stretching/shrinking sheet in the presence of thermal radiation and heat source/sink. *Energies*, 12(5):788.
- Jamil, B., Anwar, M. S., Rasheed, A., and Irfan, M. (2020). Mhd maxwell flow modeled by fractional derivatives with chemical reaction and thermal radiation. *Chinese Journal of Physics*, 67:512–533.
- Jan, S. U., Haq, S. U., Shah, S. I. A., and Khan, I. (2019). Heat and mass transfer of free convection flow over a vertical plate with chemical reaction under wall–slip effect. *Arabian Journal for Science and Engineering*, 44(12):9869–9887.
- Jordan, A., Scholz, R., Wust, P., Föhling, H., and Felix, R. (1999). Magnetic fluid hyperthermia (mfh): Cancer treatment with ac magnetic field induced excitation of biocompatible superparamagnetic nanoparticles. *Journal of Magnetism and Magnetic materials*, 201(1-3):413–419.

- Jusoh, R. and Nazar, R. (2018). Mhd stagnation point flow and heat transfer of a nanofluid over a permeable nonlinear stretching/shrinking sheet with viscous dissipation effect. In *AIP Conference Proceedings*, volume 1940, page 020125. AIP Publishing LLC.
- Kakaç, S. and Pramuanjaroenkij, A. (2009). Review of convective heat transfer enhancement with nanofluids. *International journal of heat and mass transfer*, 52(13-14):3187–3196.
- Kamal, F., Zaimi, K., Ishak, A., and Pop, I. (2018). Stability analysis on the stagnation-point flow and heat transfer over a permeable stretching/shrinking sheet with heat source effect. *International Journal of Numerical Methods for Heat & Fluid Flow*.
- Kasaeian, A., Daneshzarian, R., Mahian, O., Kolsi, L., Chamkha, A. J., Wongwises, S., and Pop, I. (2017). Nanofluid flow and heat transfer in porous media: a review of the latest developments. *International Journal of Heat and Mass Transfer*, 107:778–791.
- Kausar, M. S., Hussanan, A., Mamat, M., and Ahmad, B. (2019). Boundary layer flow through darcy–brinkman porous medium in the presence of slip effects and porous dissipation. *Symmetry*, 11(5):659.
- Khushi'ie, N. S., Arifin, N. M., Rashidi, M. M., Hafidzuddin, E. H., and Wahi, N. (2020). Magnetohydrodynamics (mhd) stagnation point flow past a shrinking/stretching surface with double stratification effect in a porous medium. *Journal of Thermal Analysis and Calorimetry*, 139(6):3635–3648.
- Khushi'ie, N. S., Md Arifin, N., Nazar, R., Hafidzuddin, E. H., Wahi, N., and Pop, I. (2019). Mixed convective flow and heat transfer of a dual stratified micropolar fluid induced by a permeable stretching/shrinking sheet. *Entropy*, 21(12):1162.
- Kim, Y., Nakatsuka, K., Fujita, T., and Atarashi, T. (1999). Application of hydrophilic magnetic fluid to oil seal. *Journal of Magnetism and Magnetic Materials*, 201(1-3):361–363.
- Kothandapani, M. and Prakash, J. (2015). Effects of thermal radiation parameter and magnetic field on the peristaltic motion of williamson nanofluids in a tapered asymmetric channel. *International Journal of Heat and Mass Transfer*, 81:234–245.
- Kreith, F., Manglik, R. M., and Bohn, M. S. (2011). Principles of heat transfer, cengage learning. *Inc., USA*.
- Kumar, K. G., Giresha, B. J., Kumara, B., Ramesh, G., and Makinde, O. D. (2017a). Phenomenon of radiation and viscous dissipation on casson nanoliquid flow past a

- moving melting surface. In *Diffusion Foundations*, volume 11, pages 33–42. Trans Tech Publ.
- Kumar, K. G., Ramesh, G., Gireesha, B., and Gorla, R. (2018). Characteristics of joule heating and viscous dissipation on three-dimensional flow of oldroyd b nanofluid with thermal radiation. *Alexandria Engineering Journal*, 57(3):2139–2149.
- Kumar, K. G., Rudraswamy, N., Gireesha, B., and Krishnamurthy, M. (2017b). Influence of nonlinear thermal radiation and viscous dissipation on three-dimensional flow of jeffrey nano fluid over a stretching sheet in the presence of joule heating. *Nonlinear Engineering*, 6(3):207–219.
- Kundu, P. K. and Cohen, I. M. (2002). *Fluid mechanics*.
- Kuzubov, A. and Ivanova, O. (1994). Magnetic liquids for heat exchange. *Journal de Physique III*, 4(1):1–6.
- Lajvardi, M., Moghimi-Rad, J., Hadi, I., Gavili, A., Isfahani, T. D., Zabihi, F., and Sabbaghzadeh, J. (2010). Experimental investigation for enhanced ferrofluid heat transfer under magnetic field effect. *Journal of Magnetism and Magnetic Materials*, 322(21):3508–3513.
- Liu, J. P., Fullerton, E., Gutfleisch, O., and Sellmyer, D. J. (2009). *Nanoscale magnetic materials and applications*. Springer.
- Liu, T., Cheng, Y., and Yang, Z. (2005). Design optimization of seal structure for sealing liquid by magnetic fluids. *Journal of Magnetism and Magnetic Materials*, 289:411–414.
- Lok, Y., Amin, N., and Pop, I. (2006). Non-orthogonal stagnation point flow towards a stretching sheet. *International Journal of Non-Linear Mechanics*, 41(4):622–627.
- Lok, Y., Ishak, A., and Pop, I. (2011). Mhd stagnation-point flow towards a shrinking sheet. *International Journal of Numerical Methods for Heat & Fluid Flow*.
- Lübbe, A. S., Bergemann, C., Brock, J., and McClure, D. G. (1999). Physiological aspects in magnetic drug-targeting. *Journal of Magnetism and Magnetic Materials*, 194(1-3):149–155.
- Mabood, F., Khan, W., and Ismail, A. M. (2015). Mhd stagnation point flow and heat transfer impinging on stretching sheet with chemical reaction and transpiration. *Chemical Engineering Journal*, 273:430–437.
- Mahdi, R. A., Mohammed, H., and Munisamy, K. (2013). Improvement of convection heat transfer by using porous media and nanofluid. *Int. J. Sci. Res.*, 2(8):34–47.

- Mahdi, R. A., Mohammed, H., Munisamy, K., and Saeid, N. (2015). Review of convection heat transfer and fluid flow in porous media with nanofluid. *Renewable and Sustainable Energy Reviews*, 41:715–734.
- Mahdy, A. (2010). Effect of chemical reaction and heat generation or absorption on double-diffusive convection from a vertical truncated cone in porous media with variable viscosity. *Int. Commun. Heat Mass Transf.*, 37(5):548–554.
- Makinde, O. (2008). Effect of arbitrary magnetic Reynolds number on mhd flows in convergent-divergent channels. *International Journal of Numerical Methods for Heat & Fluid Flow*.
- Makinde, O. (2012). Heat and mass transfer by mhd mixed convection stagnation point flow toward a vertical plate embedded in a highly porous medium with radiation and internal heat generation. *Meccanica*, 47(5):1173–1184.
- Makinde, O., Khan, W., and Khan, Z. (2013). Buoyancy effects on mhd stagnation point flow and heat transfer of a nanofluid past a convectively heated stretching/shrinking sheet. *International Journal of Heat and Mass Transfer*, 62:526–533.
- Makinde, O., Khan, W., and Khan, Z. (2017). Stagnation point flow of mhd chemically reacting nanofluid over a stretching convective surface with slip and radiative heat. *Proceedings of the Institution of Mechanical Engineers, Part E: Journal of Process Mechanical Engineering*, 231(4):695–703.
- Makinde, O. D. (2018). Stagnation point flow with heat transfer and temporal stability of ferrofluid past a permeable stretching/shrinking sheet. In *Defect and Diffusion Forum*, volume 387, pages 510–522. Trans Tech Publ.
- Makinde, O. D. and Aziz, A. (2011). Boundary layer flow of a nanofluid past a stretching sheet with a convective boundary condition. *International Journal of Thermal Sciences*, 50(7):1326–1332.
- Makinde, O. D. and Eegunjobi, A. S. (2016). Entropy analysis of thermally radiating magnetohydrodynamic slip flow of Casson fluid in a microchannel filled with saturated porous media. *Journal of Porous Media*, 19(9).
- Mansur, S. and Ishak, A. (2016). Unsteady boundary layer flow of a nanofluid over a stretching/shrinking sheet with a convective boundary condition. *Journal of the Egyptian Mathematical Society*, 24(4):650–655.
- Menni, Y., Chamkha, A. J., and Azzi, A. (2019). Nanofluid transport in porous media: a review. *Special Topics & Reviews in Porous Media: An International Journal*, 10(1).

- Merkin, J. (1986). On dual solutions occurring in mixed convection in a porous medium. *Journal of engineering Mathematics*, 20(2):171–179.
- Miklavčič, M. and Wang, C. (2006). Viscous flow due to a shrinking sheet. *Quarterly of Applied Mathematics*, 64(2):283–290.
- Mody, V. V., Cox, A., Shah, S., Singh, A., Bevins, W., and Parihar, H. (2014). Magnetic nanoparticle drug delivery systems for targeting tumor. *Applied Nanoscience*, 4(4):385–392.
- Mohamed, M. K. A., Ismail, N. A., Hashim, N., Shah, N. M., and Salleh, M. Z. (2019). Mhd slip flow and heat transfer on stagnation point of a magnetite (fe<sub>3</sub>o<sub>4</sub>) ferrofluid towards a stretching sheet with newtonian heating. *CFD Letters*, 11(1):17–27.
- Mondal, H., De, P., Goqo, S., and Sibanda, P. (2020). A numerical study of nanofluid flow over a porous vertical plate with internal heat generation and nonlinear thermal radiation. *Journal of Porous Media*, 23(6).
- Mortuja Sarkar, G. and Sahoo, B. (2021). Dual solutions of a magnetohydrodynamic stagnation point flow of a non-newtonian fluid over a shrinking sheet and a linear temporal stability analysis. *Proceedings of the Institution of Mechanical Engineers, Part E: Journal of Process Mechanical Engineering*, 235(2):527–535.
- Motlagh, S. Y., Taghizadeh, S., and Soltanipour, H. (2016). Natural convection heat transfer in an inclined square enclosure filled with a porous medium saturated by nanofluid using buongiorno’s mathematical model. *Advanced Powder Technology*, 27(6):2526–2540.
- Muhammad, T., Alsaedi, A., Hayat, T., and Shehzad, S. A. (2017). A revised model for darcy-forchheimer three-dimensional flow of nanofluid subject to convective boundary condition. *Results in physics*, 7:2791–2797.
- Mukhopadhyay, S. (2012). Upper-convected maxwell fluid flow over an unsteady stretching surface embedded in porous medium subjected to suction/blowing. *Zeitschrift Für Naturforschung A*, 67(10-11):641–646.
- Mustafa, I., Abbas, Z., Arif, A., Javed, T., and Ghaffari, A. (2020). Stability analysis for multiple solutions of boundary layer flow towards a shrinking sheet: Analytical solution by using least square method. *Physica A: Statistical Mechanics and Its Applications*, 540:123028.
- Mustafa, M., Khan, J. A., Hayat, T., and Alsaedi, A. (2017). Buoyancy effects on the mhd nanofluid flow past a vertical surface with chemical reaction and activation energy. *International Journal of Heat and Mass Transfer*, 108:1340–1346.

- Najib, N., Bachok, N., Arifin, N. M., and Ishak, A. (2014). Stagnation point flow and mass transfer with chemical reaction past a stretching/shrinking cylinder. *Scientific reports*, 4(1):1–7.
- Nazar, R., Jaradat, M., Arifin, N., and Pop, I. (2011). Stagnation-point flow past a shrinking sheet in a nanofluid. *Open Physics*, 9(5):1195–1202.
- Nazari, M., Mahmoudi, Y., and Hooman, K. (2019). Introduction to fluid flow and heat transfer in porous media. In *Convective Heat Transfer in Porous Media*, pages 3–18. CRC Press.
- Nguyen, N.-T., Wereley, S. T., and Shaegh, S. A. M. (2019). *Fundamentals and applications of microfluidics*. Artech house.
- Nield, D. A. and Bejan, A. (2017). Mechanics of fluid flow through a porous medium. In *Convection in porous media*, pages 1–35. Springer.
- Nield, D. A., Bejan, A., et al. (2006). *Convection in porous media*, volume 3. Springer.
- Nisar, A., Afzulpurkar, N., Mahaisavariya, B., and Tuantranont, A. (2008). Membrane-based micropumps in drug delivery and biomedical applications. *Sensors and Actuators B: Chemical*, 130(2):917–942.
- Noghrehabadi, A., Behseresht, A., Ghalambaz, M., and Behseresht, J. (2013). Natural-convection flow of nanofluids over vertical cone embedded in non-darcy porous media. *Journal of thermophysics and heat transfer*, 27(2):334–341.
- Obalalu, A. M., Ajala, A. O., Akindele, A. O., Oladapo, O. A., Akintayo, O. O., and Jimoh, O. M. (2022). Computational study of magneto-convective non-newtonian nanofluid slip flow over a stretching/shrinking sheet embedded in a porous medium. *Computers & Mathematics with Applications*.
- Odenbach, S. (2003). Ferrofluids-magnetically controlled suspensions. *Colloids and Surfaces A: Physicochemical and Engineering Aspects*, 217(1-3):171–178.
- Odenbach, S. (2004). Recent progress in magnetic fluid research. *Journal of physics: condensed matter*, 16(32):R1135.
- Ogulu, A. and Makinde, O. D. (2008). Unsteady hydromagnetic free convection flow of a dissipative and radiating fluid past a vertical plate with constant heat flux. *Chemical Engineering Communications*, 196(4):454–462.
- Pal, D. (2009). Heat and mass transfer in stagnation-point flow towards a stretching surface in the presence of buoyancy force and thermal radiation. *Meccanica*, 44(2):145–158.

- Pal, D. and Mondal, H. (2012). Hydromagnetic convective diffusion of species in darcy–forchheimer porous medium with non-uniform heat source/sink and variable viscosity. *International Communications in Heat and Mass Transfer*, 39(7):913–917.
- Prasad, K., Vajravelu, K., Vaidya, H., and Datti, P. (2017). Axisymmetric flow over a vertical slender cylinder in the presence of chemically reactive species. *International Journal of Applied and Computational Mathematics*, 3(2):663–678.
- Prasad, R. V., Reddy, B. N., and Muthucumaraswamy, R. (2006). Transient radiative hydromagnetic free convection flow past an impulsively started vertical plate with uniform heat and mass flux. *Theoretical and Applied Mechanics*, 33(1):31–63.
- Raj, K., Moskowitz, B., and Casciari, R. (1995). Advances in ferrofluid technology. *Journal of magnetism and magnetic materials*, 149(1-2):174–180.
- Rashad, A., Chamkha, A., RamReddy, C., and Murthy, P. (2014). Influence of viscous dissipation on mixed convection in a non-darcy porous medium saturated with a nanofluid. *Heat Transfer-Asian Research*, 43(5):397–411.
- Rashidi, M., Ganesh, N. V., Hakeem, A. A., and Ganga, B. (2014). Buoyancy effect on mhd flow of nanofluid over a stretching sheet in the presence of thermal radiation. *Journal of Molecular Liquids*, 198:234–238.
- Raza, J., Rohni, A. M., and Omar, Z. (2016). Rheology of micropolar fluid in a channel with changing walls: Investigation of multiple solutions. *Journal of Molecular Liquids*, 223:890–902.
- Rehman, K. U., Khan, A. A., Malik, M., and Makinde, O. (2017). Thermophysical aspects of stagnation point magnetonanofluid flow yields by an inclined stretching cylindrical surface: a non-newtonian fluid model. *Journal of the Brazilian Society of Mechanical Sciences and Engineering*, 39(9):3669–3682.
- Rosali, H., Badlilshah, M. N., Johari, M. A. M., and Bachok, N. (2020). Unsteady boundary layer stagnation point flow and heat transfer over a stretching sheet in a porous medium with slip effects. *CFD Letters*, 12(10):52–61.
- Roşca, A. V. and Pop, I. (2013). Flow and heat transfer over a vertical permeable stretching/shrinking sheet with a second order slip. *International Journal of Heat and Mass Transfer*, 60:355–364.
- Ryabinin, A. and Khozhainov, A. (1967). Exact and approximate formulations of problems for unsteady flows of conducting fluids in mhd channels. *Fluid Dynamics*, 2(4):107–109.

- Safwa Khashi'ie, N., Md Arifin, N., Hafidzuddin, E. H., and Wahi, N. (2019). Dual stratified nanofluid flow past a permeable shrinking/stretching sheet using a non-fourier energy model. *Applied Sciences*, 9(10):2124.
- Sakiadis, B. C. (1961). Boundary-layer behavior on continuous solid surfaces: I. boundary-layer equations for two-dimensional and axisymmetric flow. *AIChE Journal*, 7(1):26–28.
- Salman, B., Mohammed, H., and Kherbeet, A. S. (2014). Numerical and experimental investigation of heat transfer enhancement in a microtube using nanofluids. *International Communications in Heat and Mass Transfer*, 59:88–100.
- Sarojini, K. K., Manoj, S. V., Singh, P. K., Pradeep, T., and Das, S. K. (2013). Electrical conductivity of ceramic and metallic nanofluids. *Colloids and Surfaces A: Physicochemical and Engineering Aspects*, 417:39–46.
- Scherer, C. and Figueiredo Neto, A. M. (2005). Ferrofluids: properties and applications. *Brazilian journal of physics*, 35(3A):718–727.
- Schlichting, H. and Gersten, K. (2003). *Boundary-layer theory*. Springer Science & Business Media.
- Sehra, Haq, S. U., Shah, S. I. A., Nisar, K. S., Jan, S. U., and Khan, I. (2021). Convection heat mass transfer and MHD flow over a vertical plate with chemical reaction, arbitrary shear stress and exponential heating. *Sci. Rep.*, 11(1):1–11.
- Seth, G. S. and Mandal, P. K. (2018). Hydromagnetic rotating flow of casson fluid in darcy-forchheimer porous medium. In *MATEC Web of Conferences*, volume 192, page 02059. EDP Sciences.
- Seth, G. S., Sharma, R., Kumbhakar, B., and Chamkha, A. J. (2016). Hydromagnetic flow of heat absorbing and radiating fluid over exponentially stretching sheet with partial slip and viscous and joule dissipation. *Engineering Computations*.
- Sharma, P., Sinha, S., Yadav, R., and Filippov, A. N. (2018). Mhd mixed convective stagnation point flow along a vertical stretching sheet with heat source/sink. *International Journal of Heat and Mass Transfer*, 117:780–786.
- Sharma, R., Ishak, A., and Pop, I. (2014). Stability analysis of magnetohydrodynamic stagnation-point flow toward a stretching/shrinking sheet. *Computers & Fluids*, 102:94–98.
- Sheikholeslami, M. and Ganji, D. D. (2016). *External magnetic field effects on hydrothermal treatment of nanofluid: numerical and analytical studies*. William Andrew.

- Sheikholeslami, M. and Ganji, D. D. (2017). *Applications of nanofluid for heat transfer enhancement*. William Andrew.
- Shen, C.-Y. and Liou, S.-Y. (2008). Surface acoustic wave gas monitor for ppm ammonia detection. *Sensors and Actuators B: Chemical*, 131(2):673–679.
- Shen, M., Wang, F., and Chen, H. (2015). Mhd mixed convection slip flow near a stagnation-point on a nonlinearly vertical stretching sheet. *Boundary value problems*, 2015(1):1–15.
- Singh, G. and Makinde, O. (2013). Mhd slip flow of viscous fluid over an isothermal reactive stretching sheet. *Annals of the Faculty of Engineering Hunedoara*, 11(2):41.
- Sivakumar, N., Prasad, P. D., Raju, C., Varma, S., and Shehzad, S. (2017). Partial slip and dissipation on mhd radiative ferro-fluid over a non-linear permeable convectively heated stretching sheet. *Results in physics*, 7:1940–1949.
- Soid, S. K., Ishak, A., and Pop, I. (2018). Mhd stagnation-point flow over a stretching/shrinking sheet in a micropolar fluid with a slip boundary. *Sains Malaysiana*, 47(11):2907–2916.
- Steg, L. and Sutton, G. W. (1960). The prospects of mhd power generation. *Astronautics*, 5.
- Stoian, F. D., Pop, G., Bica, D., Stoica, V., Marinică, O., and Vékás, L. (2003). A fundamental study regarding the control of nucleate boiling in a complex magnetizable fluid by an applied magnetic field, in microgravity conditions. In *AIP conference proceedings*, volume 654, pages 149–156. American Institute of Physics.
- Sulochana, C., Kumar, T. P., Uma, M., and Thulasi, L. (2021). MHD darcy-forchheimer hybrid nanofluid flow past a nonlinear stretching surface: Numerical study. *IOP Conference Series: Materials Science and Engineering*, 1145(1):012042.
- Sun, Q. and Pop, I. (2014). Free convection in a tilted triangle porous cavity filled with cu-water nanofluid with flush mounted heater on the wall. *International Journal of Numerical Methods for Heat & Fluid Flow*.
- Sun, S. and Zeng, H. (2002). Size-controlled synthesis of magnetite nanoparticles. *Journal of the American Chemical Society*, 124(28):8204–8205.
- Takenouchi, K. (1985). Transient magnetohydrodynamic channel flow with axial symmetry at a supersonic speed. *Journal of the Physical Society of Japan*, 54(4):1329–1338.

- Thompson, P. A. and Troian, S. M. (1997). A general boundary condition for liquid flow at solid surfaces. *Nature*, 389(6649):360–362.
- Toosi, M. H. and Siavashi, M. (2017). Two-phase mixture numerical simulation of natural convection of nanofluid flow in a cavity partially filled with porous media to enhance heat transfer. *Journal of Molecular Liquids*, 238:553–569.
- Tynjälä, T., Bozhko, A., Bulychev, P., Putin, G., and Sarkomaa, P. (2006). On features of ferrofluid convection caused by barometrical sedimentation. *Journal of Magnetism and Magnetic Materials*, 300(1):e195–e198.
- Upreti, H., Pandey, A. K., Kumar, M., and Makinde, O. (2020). Ohmic heating and non-uniform heat source/sink roles on 3d darcy–forchheimer flow of cnts nanofluids over a stretching surface. *Arabian Journal for Science and Engineering*, 45(9):7705–7717.
- Veera Krishna, M. (2020). Heat transport on steady mhd flow of copper and alumina nanofluids past a stretching porous surface. *Heat Transfer*, 49(3):1374–1385.
- Waini, I., Ishak, A., and Pop, I. (2019). Hybrid nanofluid flow and heat transfer past a permeable stretching/shrinking surface with a convective boundary condition. In *Journal of Physics: Conference Series*, volume 1366, page 012022. IOP Publishing.
- Waini, I., Ishak, A., and Pop, I. (2020). Hybrid nanofluid flow towards a stagnation point on an exponentially stretching/shrinking vertical sheet with buoyancy effects. *International Journal of Numerical Methods for Heat & Fluid Flow*.
- Wang, C. (2008). Stagnation flow towards a shrinking sheet. *International Journal of Non-Linear Mechanics*, 43(5):377–382.
- Weidman, P., Kubitschek, D., and Davis, A. (2006). The effect of transpiration on self-similar boundary layer flow over moving surfaces. *International journal of engineering science*, 44(11-12):730–737.
- Yasin, M. H. M., Ishak, A., and Pop, I. (2016). Mhd heat and mass transfer flow over a permeable stretching/shrinking sheet with radiation effect. *Journal of Magnetism and Magnetic Materials*, 407:235–240.
- Zaimi, K. and Ishak, A. (2016). Stagnation-point flow towards a stretching vertical sheet with slip effects. *Mathematics*, 4(2):27.
- Zakaria, K., Sirwah, M. A., and Alkharashi, S. (2009). Instability through porous media of three layers superposed conducting fluids. *European Journal of Mechanics-B/Fluids*, 28(2):259–270.

Zeitoun, O., Ali, M., and Al-Ansary, H. (2013). The effect of particle concentration on cooling of a circular horizontal surface using nanofluid jets. *Nanoscale and microscale thermophysical engineering*, 17(2):154–171.

# Appendix A

## Mathematical Preliminaries and Fluid Flow Models

In this appendix, essential theorems and fluid flow model are given.

### A.1 Mathematical Preliminaries

#### A.1.1 Reynold's Transport Theorem(RTT)

Let  $V(t)$  be an arbitrary volume with boundary surface  $S(t)$ , which moves at the velocity  $\vec{q}$ . The exterior normal to the boundary is denoted by  $n$ . Then

$$\frac{d}{dt} \int_{V(t)} \phi(x,t) dV = \int_{V(t)} \frac{\partial \phi(x,t)}{\partial t} dV + \int_{S(t)} \phi(x,t) \vec{q} \cdot n dS.$$

Where  $\phi(x,t)$  is any quantity to be conserved.

#### A.1.2 Gauss Divergence Theorem

Let  $E$  be a simple solid region and  $S$  is the boundary surface of  $E$  with positive orientation. Let  $\vec{F}$  be a vector field whose components have continuous first order partial derivatives. Then

$$\int_E \nabla \cdot \vec{F} dV = \int_S \vec{F} \cdot d\vec{S}.$$

## A.2 Fluid Flow Model

### A.2.1 Buongiorno Convective Transport Model

In the pioneering nanofluid model introduced by Buongiorno, he considers Brownian motion and the thermophoresis on the heat transfer characteristics to study behaviour of nanofluids. The nanofluid is treated as a two-component mixture (base fluid and nanoparticles) with the following assumptions: incompressible flow, no chemical reactions, negligible external forces, dilute mixture ( $\phi \ll 1$ ), negligible viscous dissipation, negligible radiative heat transfer, and nanoparticle and base fluid locally in thermal equilibrium. Invoking these assumptions, the following equations represent the mathematical formulation of the governing equations as formulated by Buongiorno (Buongiorno, 2006).

The continuity equation for the nanofluid is:

$$\nabla \cdot v = 0,$$

where  $v$  is the velocity.

The continuity equation for the nanoparticles is:

$$\frac{\partial C}{\partial t} + v \cdot \nabla C = \nabla \cdot \left[ D_B \nabla C + D_T \frac{\nabla T}{T} \right],$$

where  $C$  is the nanoparticle volume fraction,  $D_B$  is the Brownian diffusion coefficient and  $D_T$  is the thermophoretic diffusion coefficient.

The momentum equation for the nanofluid with negligible external forces is:

$$\rho \left[ \frac{\partial v}{\partial t} + v \cdot \nabla v \right] = -\nabla P - \nabla \cdot \tau,$$

where  $P$  is the pressure  $\tau$  is the stress tensor.

The energy equation for the nanofluid with negligible external forces is:

$$\rho c \left[ \frac{\partial T}{\partial t} + v \cdot \nabla T \right] = -\nabla \cdot k \nabla T + \rho_p c_p \left[ D_B \nabla C \cdot \nabla T + D_T \frac{\nabla T \cdot \nabla T}{T} \right],$$

where  $c$  is the nanofluid specific heat capacity,  $T$  is the nanofluid temperature,  $h_p$  is the specific enthalpy of the nanoparticle material ( $J/Kg$ ) and  $k$  is the nanofluid thermal conductivity.

## Appendix B

### B.1 Maple Codes for Problem given in Chapter 4

% This code solves velocity, temperature and concentration

```
with(plots)
M:=0.1:Pr:=6.2:Da:=1:Nr:=0.1:Le:=0.1:Nt:=0.1:Nb:=0.5:Nc:=0.1:N:=0.1:Ra:=0.1:
L:=0.1:r:=0.1:Ec:=0.1:
fcns:={S(y),T(y),f(y)}:
sys:=diff(S(y),y$3)-(M+1/Da)*(diff(S(y),y)-1)+(3*S(y)*diff(S(y),y$2)-
2*diff(S(y),y)*diff(S(y),y)+2)/(4*Pr)+T(y)-Nr*f(y)=0,(1+4*Ra/3)*diff(T(y),y$2)+
3*S(y)*diff(T(y),y)/4+Ec*Pr*(diff(S(y),y$2)*diff(S(y),y$2)+
(M+1/Da)*(diff(S(y),y)-1)*(diff(S(y),y)-1))+Nb*diff(f(y),y)*diff(T(y),y)+
Nt*diff(T(y),y)*diff(T(y),y)=0,diff(f(y),y$2)+
Nt*diff(T(y),y$2)/Nb+3*Le*diff(f(y),y)*S(y)/4=0:
p1:=dsolve({sys,S(0)=r,D(S)(0)=L,D(T)(0)=-Nc*(1-T(0)),D(f)(0)=-N*(1-f(0)),
D(S)(10)=1,T(10)=0,f(10)=0},fcns,type=numeric,method=bvp[midrich],abserr=1e-10):
p1u:=odeplot(p1,[y,diff(S(y),y)],0..10,numpoints=100,labels=["y","u"],style=line,
color=black):
p1t:=odeplot(p1,[y,T(y)],0..10,numpoints=100,labels=["y","T"],style=line,color=
black):
p1f:=odeplot(p1,[y,f(y)],0..10,numpoints=100,labels=["y","f"],style=line,color
=black):
-----
with(plots):
M:=0.1:Pr:=6.2:Da:=1:Nr:=0.5:Le:=0.1:Nt:=0.1:Nb:=0.5:Nc:=0.1:N:=0.1:Ra:=0.1:
L:=0.1:r:=0.1:Ec:=0.1:
fcns:={S(y),T(y),f(y)}:
sys:=diff(S(y),y$3)-(M+1/Da)*(diff(S(y),y)-1)+(3*S(y)*diff(S(y),y$2)-
2*diff(S(y),y)*diff(S(y),y)+2)/(4*Pr)+T(y)-Nr*f(y)=0,(1+4*Ra/3)
*diff(T(y),y$2)+3*S(y)*diff(T(y),y)/4+Ec*Pr*(diff(S(y),y$2)*diff(S(y),y$2)+
(M+1/Da)*(diff(S(y),y)-1)*(diff(S(y),y)-1))+Nb*diff(f(y),y)*diff(T(y),y)
+Nt*diff(T(y),y)*diff(T(y),y)=0,diff(f(y),y$2)+Nt*diff(T(y),y$2)/Nb
+3*Le*diff(f(y),y)*S(y)/4=0:
p2:=dsolve({sys,S(0)=r,D(S)(0)=L,D(T)(0)=-Nc*(1-T(0)),D(f)(0)=-N*(1-f(0)),
D(S)(10)=1,T(10)=0,f(10)=0},fcns,type=numeric,method=bvp[midrich],abserr=1e-10):
p2u:=odeplot(p2,[y,diff(S(y),y)],0..10,numpoints=100,labels=["y","u"],style=line,
color=red):
p2t:=odeplot(p2,[y,T(y)],0..10,numpoints=100,labels=["y","T"],style=line,color=
```

```

red):
p2f:=odeplot(p2, [y, f(y)], 0..10, numpoints=100, labels=["y", "f"], style=line, color=
red):
-----

with(plots):
M:=0.1:Pr:=6.2:Da:=1:Nr:=1:Le:=0.1:Nt:=0.1:Nb:=0.5:Nc:=0.1:N:=0.1:Ra:=0.1:
L:=0.1:r:=0.1:Ec:=0.1:
fcns:={S(y), T(y), f(y)}:
sys:=diff(S(y), y$3)-(M+1/Da)*(diff(S(y), y)-1)+(3*S(y)*diff(S(y), y$2)-
2*diff(S(y), y)*diff(S(y), y)+2)/(4*Pr)+T(y)-Nr*f(y)=0, (1+4*Ra/3)*diff(T(y), y$2)+
3*S(y)*diff(T(y), y)/4+Ec*Pr*(diff(S(y), y$2)*diff(S(y), y$2)+
(M+1/Da)*(diff(S(y), y)-1)*(diff(S(y), y)-1))+Nb*diff(f(y), y)*diff(T(y), y)+
Nt*diff(T(y), y)*diff(T(y), y)=0, diff(f(y), y$2)+Nt*diff(T(y), y$2)/Nb
+3*Le*diff(f(y), y)*S(y)/4=0:\\
p3:=dsolve({sys, S(0)=r, D(S)(0)=L, D(T)(0)=-Nc*(1-T(0)), D(f)(0)=-N*(1-f(0)),
D(S)(10)=1, T(10)=0, f(10)=0}, fcns, type=numeric, method=bvp[midrich], abserr=1e-10):
p3u:=odeplot(p3, [y, diff(S(y), y)], 0..10, numpoints=100, labels=["y", "u"], style=line,
color=blue):
p3t:=odeplot(p3, [y, T(y)], 0..10, numpoints=100, labels=["y", "T"], style=line, color=
blue):
p3f:=odeplot(p3, [y, f(y)], 0..10, numpoints=100, labels=["y", "f"], style=line, color=
blue):
-----

with(plots):
M:=1:Pr:=6.2:Da:=1:Nr:=0.1:Le:=0.1:Nt:=0.1:Nb:=0.5:Nc:=0.1:N:=0.1:Ra:=0.1:
L:=0.1:r:=0.1:Ec:=0.1:
fcns:={S(y), T(y), f(y)}:
sys:=diff(S(y), y$3)-(M+1/Da)*(diff(S(y), y)-1)+(3*S(y)*diff(S(y), y$2)-
2*diff(S(y), y)*diff(S(y), y)+2)/(4*Pr)+T(y)-Nr*f(y)=0, (1+4*Ra/3)*diff(T(y), y$2)+
3*S(y)*diff(T(y), y)/4+Ec*Pr*(diff(S(y), y$2)*diff(S(y), y$2)+
(M+1/Da)*(diff(S(y), y)-1)*(diff(S(y), y)-1))+Nb*diff(f(y), y)*diff(T(y), y)+
Nt*diff(T(y), y)*diff(T(y), y)=0, diff(f(y), y$2)+Nt*diff(T(y), y$2)/Nb+
3*Le*diff(f(y), y)*S(y)/4=0:
p4:= dsolve({sys, S(0)=r, D(S)(0)=L, D(T)(0)=-Nc*(1-T(0)), D(f)(0)=-N*(1-f(0)),
D(S)(10)=1, T(10)=0, f(10)=0}, fcns, type=numeric, method=bvp[midrich], abserr=1e-10):
p4u:=odeplot(p4, [y, diff(S(y), y)], 0..10, numpoints=100, labels=["y", "u"], style=line,
color=green):
p4t:=odeplot(p4, [y, T(y)], 0..10, numpoints=100, labels=["y", "T"], style=line, color=
green):

```

```
p4f:=odeplot(p4,[y,f(y)],0..10,numpoints=100,labels=["y","f"],style=line,color=green):
```

```
-----
with(plots):
M:=1:Pr:=6.2:Da:=1:Nr:=0.5:Le:=0.1:Nt:=0.1:Nb:=0.5:Nc:=0.1:N:=0.1:Ra:=0.1:
L:=0.1:r:=0.1:Ec:=0.1:
fcns:={S(y),T(y),f(y)}:
sys:=diff(S(y),y$3)-(M+1/Da)*(diff(S(y),y)-1)+(3*S(y)*diff(S(y),y$2)-
2*diff(S(y),y)*diff(S(y),y)+2)/(4*Pr)+T(y)-Nr*f(y)=0,(1+4*Ra/3)*diff(T(y),y$2)+
3*S(y)*diff(T(y),y)/4+Ec*Pr*(diff(S(y),y$2)*diff(S(y),y$2)+
(M+1/Da)*(diff(S(y),y)-1)*(diff(S(y),y)-1))+Nb*diff(f(y),y)*diff(T(y),y)+
Nt*diff(T(y),y)*diff(T(y),y)=0,diff(f(y),y$2)+Nt*diff(T(y),y$2)/Nb+
3*Le*diff(f(y),y)*S(y)/4=0:
p5:=dsolve({sys,S(0)=r,D(S)(0)=L,D(T)(0)=-Nc*(1-T(0)),D(f)(0)=-N*(1-f(0)),
D(S)(10)=1,T(10)=0,f(10)=0},fcns,type=numeric,method=bvp[midrich],abserr=1e-10):
p5u:=odeplot(p5,[y,diff(S(y),y)],0..10,numpoints=100,labels=["y","u"],style=line,
color=purple):
p5t:=odeplot(p5,[y,T(y)],0..10,numpoints=100,labels=["y","T"],style=line,color=
purple):
p5f:=odeplot(p5,[y,f(y)],0..10,numpoints=100,labels=["y","f"],style=line,color=
purple):
```

```
-----
with(plots):
M:=1:Pr:=6.2:Da:=1:Nr:=1:Le:=0.1:Nt:=0.1:Nb:=0.5:Nc:=0.1:N:=0.1:Ra:=0.1:
L:=0.1:r:=0.1:Ec:=0.1:
fcns:={S(y),T(y),f(y)}:
sys:=diff(S(y),y$3)-(M+1/Da)*(diff(S(y),y)-1)+(3*S(y)*diff(S(y),y$2)-
2*diff(S(y),y)*diff(S(y),y)+2)/(4*Pr)+T(y)-Nr*f(y)=0,(1+4*Ra/3)*diff(T(y),y$2)+
3*S(y)*diff(T(y),y)/4+Ec*Pr*(diff(S(y),y$2)*diff(S(y),y$2)+
(M+1/Da)*(diff(S(y),y)-1)*(diff(S(y),y)-1))+Nb*diff(f(y),y)*diff(T(y),y)+
Nt*diff(T(y),y)*diff(T(y),y)=0,diff(f(y),y$2)+Nt*diff(T(y),y$2)/Nb+
3*Le*diff(f(y),y)*S(y)/4=0:
p6:= dsolve({sys,S(0)=r,D(S)(0)=L,D(T)(0)=-Nc*(1-T(0)),D(f)(0)=-N*(1-f(0)),
D(S)(10)=1,T(10)=0,f(10)=0},fcns,type=numeric,method=bvp[midrich],abserr=1e-10):
p6u:=odeplot(p6,[y,diff(S(y),y)],0..10,numpoints=100,labels=["y","u"],style=line,
color=yellow):
p6t:=odeplot(p6,[y,T(y)],0..10,numpoints=100,labels=["y","T"],style=line,color=
yellow):
p6f:=odeplot(p6,[y,f(y)],0..10,numpoints=100,labels=["y","f"],style=line,color=
```

```

yellow) :
plots[display] ({p1u,p2u,p3u,p4u,p5u,p6u});
plots[display] ({p1t,p2t,p3t,p4t,p5t,p6t});
plots[display] ({p1f,p2f,p3f,p4f,p5f,p6f});

```

## B.2 Maple Codes for Problem given in Chapter 5

```

% This code solves Skin friction
with(plots):
Iron Oxide
cps:=670: hs:=5180: ks:=9.7: as:=(2.5)×106 :
Water
cpf := 4179 : hf := 997.1 : kf := 0.613 : af := (5.0)×10-6 :
M := 0.1 : d1 := 1 : Da := 0.5 : Fn := 1 : r := 0 :
a1 := as/af :
m := (1 - r)2.5 :
A1 := (1 - r + r * hs/hf) * m :
A2 := m * (1 + 3 * (a1 - 1) * r / ((a1 + 2) - (a1 - 1) * r)) :
A3 := m :
i := 1 :
R := array(1..352) : SK := array(1..352) :
for L from -1.25435 by 0.005 to 0.2 do
FF := m * m * Da * G * G + m * A1 * Da * d1 * (L - 1) * G - (L - 1) * (L - 1) * (A3 * Da *
Fn * (L - 1) + A1 * Da * (L + 1) + A2 * Da * M + 1) = 0 :
FF1 := fsolve(FF,G) :
SK[i] := FF1[2] :
R[i] := L :
i := i + 1 :
od :
L := ' L' :
points := seq([R[j],SK[j]],j = 1..291) :
pcf1 := pointplot(points,labels = ["L", "Cf"],style = line,color = black) :
with(plots) :
IronOxide
cps := 670 : hs := 5180 : ks := 9.7 : as := (2.5) * 106 :
Watercpf := 4179 : hf := 997.1 : kf := 0.613 : af := 5.5 * 10-6 :
M := 0.1 : d1 := 1 : Da := 0.5 : Fn := 1 : r := 0 :
a1 := as/af :
m := (1 - r)(2.5) :

```

```

A1 := (1 - r + r * hs/hf) * m :
A2 := m * (1 + 3 * (a1 - 1) * r / ((a1 + 2) - (a1 - 1) * r)) :
A3 := m :
i := 1 :
R := array(1..352) : SK := array(1..352) :
for L from -1.25435 by 0.005 to -1.10435 do
FF := m * m * Da * G * G + m * A1 * Da * d1 * (L - 1) * G - (L - 1) * (L - 1) * (A3 * Da *
Fn * (L - 1) + A1 * Da * (L + 1) + A2 * Da * M + 1) = 0 :
FF1 := fsolve(FF, G) :
SK[i] := FF1[1] :
R[i] := L :
i := i + 1 :
od :
L := ' L' :
points := seq([R[j], SK[j]], j = 1..31) :
pcf2 := pointplot(points, labels = ["L", "Cf"], style = point, linestyle = dot, thickness =
3, color = black) :
plots[display](pcf1, pcf2);
-----
%EigenvalueProblem
with(plots) :
IronOxide
cps := 670 : hs := 5180 : ks := 9.7 : as := (2.5) * 106 :
Water
cpf := 4179 : hf := 997.1 : kf := 0.613 : af := (5.0) * 10(-6) :
M := 0.1 : d1 := 1 : Da := 0.5 : Fn := 1 : r := 0 :
a1 := as/af :
m := (1 - r)(2.5) :
A1 := (1 - r + r * hs/hf) * m :
A2 := m * (1 + 3 * (a1 - 1) * r / ((a1 + 2) - (a1 - 1) * r)) :
A3 := m :
G := 0.503809 : L := -1.14 :
n := (G * m) / (1 - L) :
F1 := d1 + y + (1 - L) * (exp(-n * y) - 1) / n :
fcns := F(y) :
sys := diff(F(y), y3) + A1 * F1 * diff(F(y), y2) + A1 * diff(F1, y2) * F(y) + (b * A1 - A2 * M
- 2 * A1 * diff(F1, y) - (1/Da) - 2 * A3 * Fn * (diff(F1, y) - 1)) * diff(F(y), y) = 0:
p1 := dsolve(sys, D(F)(0) = 0, F(0) = 0, D(D(F))(0) = 1, D(F)(10) = 0, fcns, type = numeric,
method = bvp[midrich], abserr = 1e - 10) :

```

---

```

with(plots):
% Velocity Profiles
r:=0.05: G:=2.548:L:=-1.30: m:=((1-r)(2.5)): n := (G*m)/(1-L) :
Fy1 := 1 - (1 - L) * exp(-n * y) :
pv1 := plot(Fy1, y = 0..20, style = line, thickness = 3, colour = black) :
%VelocityProfiles
r := 0.05 :
G := 0.1134 : L := -1.30 :
m := ((1 - r)(2.5)) :
n := (G * m) / (1 - L) :
Fy2 := 1 - (1 - L) * exp(-n * y) :
pv2 := plot(Fy2, y = 0..20, style = line, linestyle = dot, thickness = 3, colour = black) :
%VelocityProfiles
r := 0.08 :
G := 2.8148 : L := -1.30 :
m := ((1 - r)(2.5)) :
n := (G * m) / (1 - L) :
Fy3 := 1 - (1 - L) * exp(-n * y) :
pv3 := plot(Fy3, y = 0..20, style = line, thickness = 3, color = red) :
%VelocityProfiles
r := 0.08 :
G := 0.257 : L := -1.30 :
m := ((1 - r)(2.5)) :
n := (G * m) / (1 - L) :
Fy4 := 1 - (1 - L) * exp(-n * y) :
pv4 := plot(Fy4, y = 0..20, style = line, linestyle = dot, thickness = 3, colour = red) :
%VelocityProfiles
r := 0.1 :
G := 3.2098 : L := -1.30 :
m := ((1 - r)(2.5)) :
n := (G * m) / (1 - L) :
Fy5 := 1 - (1 - L) * exp(-n * y) :
pv5 := plot(Fy5, y = 0..20, style = line, thickness = 3, colour = blue) :
%VelocityProfiles
r := 0.1 :
G := 0.0833 : L := -1.30 :
m := ((1 - r)(2.5)) :
n := (G * m) / (1 - L) :

```

```

Fy6 := 1 - (1 - L) * exp(-n * y) :
pv6 := plot(Fy6, y = 0..20, style = line, linestyle = dot, thickness = 3, colour = blue) :
plots[display](pv1, pv2, pv3, pv4, pv5, pv6);

```

---

```

%Nusseltnumber

```

```

with(plots) :

```

```

IronOxide

```

```

cps := 670 : hs := 5180 : ks := 9.7 : as := (2.5) * 106 : r := 0.1 :

```

```

Water

```

```

cpf := 4179 : hf := 997.1 : kf := 0.613 : af := 5.5 * 10(-6) :

```

```

M := 0.1 : Pr := 6.2 : Ec := 0.1 : Bi := 0.1 : d1 := 1 : Da := 0.5 : Fn := 1 :

```

```

m := ((1 - r)(2.5)) :

```

```

a1 := as/af :

```

```

M1 := (ks + 2 * kf + r * (kf - ks)) / (ks + 2 * kf - 2 * r * (kf - ks)) :

```

```

A7 := (ks + 2 * kf + r * (kf - ks)) / (ks + 2 * kf - 2 * r * (kf - ks)) :

```

```

A6 := M1 * (1 + 3 * (a1 - 1) * r) / ((a1 + 2) - (a1 - 1) * r) :

```

```

A5 := M1 / ((1 - r)(2.5)) :

```

```

A4 := M1 * (1 - r + r * (hs * cps) / (hf * cpf)) :

```

```

A3 := m :

```

```

A2 := m * (1 + 3 * (a1 - 1) * r) / ((a1 + 2) - (a1 - 1) * r) :

```

```

A1 := (1 - r + r * hs / hf) * m :

```

```

i := 1 :

```

```

R := array(1..352) : SK := array(1..352) :

```

```

for L from -1.464 by 0.02 to 0.2 do

```

```

FF := m * m * Da * G * G + m * A1 * Da * d1 * (L - 1) * G - (L - 1) * (L - 1) * (A3 * Da *
Fn * (L - 1) + A1 * Da * (L + 1) + A2 * Da * M + 1) = 0 :

```

```

FF1 := fsolve(FF, G) :

```

```

%NotethatFF1[2]givesupper solution, FF1[1]givesthelowersolution

```

```

cf := FF1[2] :

```

```

n := cf * m / (1 - L) :

```

```

NN := (A4 * A72 * Bi * Da * Pr * d1 - A4 * A72 * Da * L * Pr + A72 * Bi2 * Da) * H2 +
(-A5 * A7 * Bi * Da * Ec * L2 * Pr * n2 - A72 * Bi * Da * Ec * Fn * L3 * Pr + 2 * A5 * A7 *
Bi * Da * Ec * L * Pr * n2 - A6 * A7 * Bi * Da * Ec * L2 * M * Pr + 3 * A72 * Bi * Da * Ec *
Fn * L2 * Pr - A5 * A7 * Bi * Da * Ec * Pr * n2 + 2 * A6 * A7 * Bi * Da * Ec * L * M * Pr -
3 * A72 * Bi * Da * Ec * Fn * L * Pr - A4 * A7 * Bi2 * Da * Pr * d1 - A5 * A7 * Bi * Ec *
L2 * Pr - A6 * A7 * Bi * Da * Ec * M * Pr + A72 * Bi * Da * Ec * Fn * Pr + 2 * A4 * A7 *
Bi * Da * L * Pr + 2 * A5 * A7 * Bi * Ec * L * Pr - A5 * A7 * Bi * Ec * Pr) * H + A5 * Bi2 *
Da * Ec * L2 * Pr * n2 + A7 * Bi2 * Da * Ec * Fn * L3 * Pr - 2 * A5 * Bi2 * Da * Ec * L *
Pr * n2 + A6 * Bi2 * Da * Ec * L2 * M * Pr - 3 * A7 * Bi2 * Da * Ec * Fn * L2 * Pr + A5 *

```

```

Bi2*Da*Ec*Pr*n2 - 2*A6*Bi2*Da*Ec*L*M*Pr + 3*A7*Bi2*Da*Ec*Fn*
L*Pr + A5*Bi2*Ec*L2*Pr + A6*Bi2*Da*Ec*M*Pr - A7*Bi2*Da*Ec*Fn*
Pr - A4*Bi2*Da*L*Pr - 2*A5*Bi2*Ec*L*Pr + A5*Bi2*Ec*Pr = 0 :
NN1 := solve(NN,H) :
Nt := max(NN1[1],NN1[2]) :
SK[i] := evalc(abs(Nt)) :
R[i] := L :
i := i + 1 :
od :
L :=' L' :
points := seq([R[j],SK[j]],j = 1..200);
pNu1 := pointplot(points,labels = ["L", "Nu"],style = line,thickness = 3,color = black) :

%Nusseltnumber
with(plots) :
IronOxide
cps := 670 : hs := 5180 : ks := 9.7 : as := (2.5)*106 : r := 0.1 :
Water
cpf := 4179 : hf := 997.1 : kf := 0.613 : af := 5.5*10(-6) :
M := 0.1 : Pr := 6.2 : Ec := 0.1 : Bi := 0.1 : d1 := 1 : Da := 0.5 : Fn := 1 :
m := ((1-r)(2.5)) :
a1 := as/af :
M1 := (ks + 2*kf + r*(kf - ks))/(ks + 2*kf - 2*r*(kf - ks)) :
A7 := (ks + 2*kf + r*(kf - ks))/(ks + 2*kf - 2*r*(kf - ks)) :
A6 := M1*(1 + 3*(a1 - 1)*r)/((a1 + 2) - (a1 - 1)*r) :
A5 := M1/((1-r)(2.5)) :
A4 := M1*(1 - r + r*(hs*cps)/(hf*cpf)) :
A3 := m :
A2 := m*(1 + 3*(a1 - 1)*r)/((a1 + 2) - (a1 - 1)*r) :
A1 := (1 - r + r*hs/hf)*m :
i := 1 :
R := array(1..352) : SK := array(1..352) :
forLfrom -1.464by0.02to0.2do
FF := m*m*Da*G*G + m*A1*Da*d1*(L-1)*G - (L-1)*(L-1)*(A3*Da*
Fn*(L-1) + A1*Da*(L+1) + A2*Da*M+1) = 0 :
FF1 := fsolve(FF,G) :
%NotethatFF1[2]givesuppersolution,FF1[1]givesthelowersolution
cf := FF1[1] :
n := cf*m/(1-L) :

```

```

NN := (A4 * A7^2 * Bi * Da * Pr * d1 - A4 * A7^2 * Da * L * Pr + A7^2 * Bi^2 * Da) * H^2 +
(-A5 * A7 * Bi * Da * Ec * L^2 * Pr * n^2 - A7^2 * Bi * Da * Ec * Fn * L^3 * Pr + 2 * A5 * A7 *
Bi * Da * Ec * L * Pr * n^2 - A6 * A7 * Bi * Da * Ec * L^2 * M * Pr + 3 * A7^2 * Bi * Da * Ec *
Fn * L^2 * Pr - A5 * A7 * Bi * Da * Ec * Pr * n^2 + 2 * A6 * A7 * Bi * Da * Ec * L * M * Pr -
3 * A7^2 * Bi * Da * Ec * Fn * L * Pr - A4 * A7 * Bi^2 * Da * Pr * d1 - A5 * A7 * Bi * Ec *
L^2 * Pr - A6 * A7 * Bi * Da * Ec * M * Pr + A7^2 * Bi * Da * Ec * Fn * Pr + 2 * A4 * A7 *
Bi * Da * L * Pr + 2 * A5 * A7 * Bi * Ec * L * Pr - A5 * A7 * Bi * Ec * Pr) * H + A5 * Bi^2 *
Da * Ec * L^2 * Pr * n^2 + A7 * Bi^2 * Da * Ec * Fn * L^3 * Pr - 2 * A5 * Bi^2 * Da * Ec * L *
Pr * n^2 + A6 * Bi^2 * Da * Ec * L^2 * M * Pr - 3 * A7 * Bi^2 * Da * Ec * Fn * L^2 * Pr + A5 *
Bi^2 * Da * Ec * Pr * n^2 - 2 * A6 * Bi^2 * Da * Ec * L * M * Pr + 3 * A7 * Bi^2 * Da * Ec * Fn *
L * Pr + A5 * Bi^2 * Ec * L^2 * Pr + A6 * Bi^2 * Da * Ec * M * Pr - A7 * Bi^2 * Da * Ec * Fn *
Pr - A4 * Bi^2 * Da * L * Pr - 2 * A5 * Bi^2 * Ec * L * Pr + A5 * Bi^2 * Ec * Pr = 0 :
NN1 := solve(NN, H) :
Nt := min(NN1[1], NN1[2]) :
SK[i] := evalc(abs(Nt)) :
R[i] := L :
i := i + 1 :
od :
L :=' L' :
points := seq([R[j], SK[j]], j = 1..200);
pNu11 := pointplot(points, labels = ["L", "Nu"], style = line, linestyle = dot, thickness =
3, colour = black) :
plots[display](pNu1, pNu11);
-----
%Temperatureprofiles :
with(plots) :
IronOxide
cps := 670 : hs := 5180 : ks := 9.7 : as := (2.5) * 10^6 : r := 0.1 :
Water
cpf := 4179 : hf := 997.1 : kf := 0.613 : af := 5.5 * 10^(-6) :
M := 0.1 : Pr := 6.2 : Ec := 0.1 : Bi := 0.1 : d1 := 1 : Da := 0.5 : Fn := 1 :
m := ((1 - r)^(2.5)) :
a1 := as/af :
M1 := (ks + 2 * kf + r * (kf - ks))/(ks + 2 * kf - 2 * r * (kf - ks)) :
A7 := (ks + 2 * kf + r * (kf - ks))/(ks + 2 * kf - 2 * r * (kf - ks)) :
A6 := M1 * (1 + 3 * (a1 - 1) * r)/((a1 + 2) - (a1 - 1) * r) :
A5 := M1/((1 - r)^(2.5)) :
A4 := M1 * (1 - r + r * (hs * cps)/(hf * cpf)) :
A3 := m :

```

```

A2 := m*(1+3*(a1-1)*r/((a1+2)-(a1-1)*r)):
A1 := (1-r+r*hs/hf)*m:
%inputthetstretchingorshrinkingparametervalue)
L := -1.44:
FF := m*m*Da*G*G+m*A1*Da*d1*(L-1)*G-(L-1)*(L-1)*(A3*Da*
Fn*(L-1)+A1*Da*(L+1)+A2*Da*M+1)=0:
FF1 := fsolve(FF,G):
%NotethatFF1[2]givesuppersolution,FF1[1]givesthelowersolution
cf := FF1[2]:
n := cf*m/(1-L):
NN := (A4*A7^2*Bi*Da*Pr*d1-A4*A7^2*Da*L*Pr+A7^2*Bi^2*Da)*H^2+
(-A5*A7*Bi*Da*Ec*L^2*Pr*n^2-A7^2*Bi*Da*Ec*Fn*L^3*Pr+2*A5*A7*
Bi*Da*Ec*L*Pr*n^2-A6*A7*Bi*Da*Ec*L^2*M*Pr+3*A7^2*Bi*Da*Ec*
Fn*L^2*Pr-A5*A7*Bi*Da*Ec*Pr*n^2+2*A6*A7*Bi*Da*Ec*L*M*Pr-
3*A7^2*Bi*Da*Ec*Fn*L*Pr-A4*A7*Bi^2*Da*Pr*d1-A5*A7*Bi*Ec*
L^2*Pr-A6*A7*Bi*Da*Ec*M*Pr+A7^2*Bi*Da*Ec*Fn*Pr+2*A4*A7*
Bi*Da*L*Pr+2*A5*A7*Bi*Ec*L*Pr-A5*A7*Bi*Ec*Pr)*H+A5*Bi^2*
Da*Ec*L^2*Pr*n^2+A7*Bi^2*Da*Ec*Fn*L^3*Pr-2*A5*Bi^2*Da*Ec*L*
Pr*n^2+A6*Bi^2*Da*Ec*L^2*M*Pr-3*A7*Bi^2*Da*Ec*Fn*L^2*Pr+A5*
Bi^2*Da*Ec*Pr*n^2-2*A6*Bi^2*Da*Ec*L*M*Pr+3*A7*Bi^2*Da*Ec*Fn*
L*Pr+A5*Bi^2*Ec*L^2*Pr+A6*Bi^2*Da*Ec*M*Pr-A7*Bi^2*Da*Ec*Fn*
Pr-A4*Bi^2*Da*L*Pr-2*A5*Bi^2*Ec*L*Pr+A5*Bi^2*Ec*Pr=0:
NN1 := solve(NN,H):
Nt := max(NN1[1],NN1[2]):
v := evalc(abs(Nt*A7*Bi/(Bi-A7*Nt))):
Tm := Bi*exp(-v*y)/(v+Bi):
pt1 := plot(Tm,y=0..20,style=line,thickness=3,color=black):
%Temperatureprofiles:
with(plots):
IronOxide
cps := 670:hs := 5180:ks := 9.7:as := (2.5)*10^6:r := 0.1:
Water
cpf := 4179:hf := 997.1:kf := 0.613:af := 5.5*10^(-6):
M := 0.1:Pr := 6.2:Ec := 0.1:Bi := 0.1:d1 := 1:Da := 0.5:Fn := 1:
m := ((1-r)^(2.5)):
a1 := as/af:
M1 := (ks+2*kf+r*(kf-ks))/(ks+2*kf-2*r*(kf-ks)):
A7 := (ks+2*kf+r*(kf-ks))/(ks+2*kf-2*r*(kf-ks)):
A6 := M1*(1+3*(a1-1)*r/((a1+2)-(a1-1)*r)):

```

```

A5 := M1/((1-r)^(2.5)) :
A4 := M1*(1-r+r*(hs*cps)/(hf*cpf)) :
A3 := m :
A2 := m*(1+3*(a1-1)*r/((a1+2)-(a1-1)*r)) :
A1 := (1-r+r*hs/hf)*m :
%inputthestretchingorshrinkingparametervalue)
L := -1.44 :
FF := m*m*Da*G*G+m*A1*Da*d1*(L-1)*G-(L-1)*(L-1)*(A3*Da*
Fn*(L-1)+A1*Da*(L+1)+A2*Da*M+1)=0 :
FF1 := fsolve(FF,G) :
NotethatFF1[2]givesuppersolution,FF1[1]givesthelowersolution
cf := FF1[1] :
n := cf*m/(1-L) :
NN := (A4*A7^2*Bi*Da*Pr*d1-A4*A7^2*Da*L*Pr+A7^2*Bi^2*Da)*H^2+
(-A5*A7*Bi*Da*Ec*L^2*Pr*n^2-A7^2*Bi*Da*Ec*Fn*L^3*Pr+2*A5*A7*
Bi*Da*Ec*L*Pr*n^2-A6*A7*Bi*Da*Ec*L^2*M*Pr+3*A7^2*Bi*Da*Ec*
Fn*L^2*Pr-A5*A7*Bi*Da*Ec*Pr*n^2+2*A6*A7*Bi*Da*Ec*L*M*Pr-
3*A7^2*Bi*Da*Ec*Fn*L*Pr-A4*A7*Bi^2*Da*Pr*d1-A5*A7*Bi*Ec*
L^2*Pr-A6*A7*Bi*Da*Ec*M*Pr+A7^2*Bi*Da*Ec*Fn*Pr+2*A4*A7*
Bi*Da*L*Pr+2*A5*A7*Bi*Ec*L*Pr-A5*A7*Bi*Ec*Pr)*H+A5*Bi^2*
Da*Ec*L^2*Pr*n^2+A7*Bi^2*Da*Ec*Fn*L^3*Pr-2*A5*Bi^2*Da*Ec*L*
Pr*n^2+A6*Bi^2*Da*Ec*L^2*M*Pr-3*A7*Bi^2*Da*Ec*Fn*L^2*Pr+A5*
Bi^2*Da*Ec*Pr*n^2-2*A6*Bi^2*Da*Ec*L*M*Pr+3*A7*Bi^2*Da*Ec*Fn*
L*Pr+A5*Bi^2*Ec*L^2*Pr+A6*Bi^2*Da*Ec*M*Pr-A7*Bi^2*Da*Ec*Fn*
Pr-A4*Bi^2*Da*L*Pr-2*A5*Bi^2*Ec*L*Pr+A5*Bi^2*Ec*Pr=0 :
NN1 := solve(NN,H) :
Nt := min(NN1[1],NN1[2]) :
v := evalc(abs(Nt*A7*Bi/(Bi-A7*Nt))) :
Tm := Bi*exp(-v*y)/(v+Bi) :
pt11 := plot(Tm,y=0..20,style=line,linestyle=dot,thickness=3,colour=red) :
plots[display](pt1,pt11);
-----

```